**Title**
Regulation of metastatic phenotypes by autophagy



**Author**
Kenific, Candia Marie

**Publication Date**
2015

Regulation of metastatic phenotypes by autophagy

by

Candia Marie Kenific

DISSERTATION

Submitted in partial satisfaction of the requirements for the degree of

DOCTOR OF PHILOSOPHY

in

Biomedical Sciences

in the

GRADUATE DIVISION

of the

UNIVERSITY OF CALIFORNIA, SAN FRANCISCO

**Acknowledgements**

The past several years have been incredible. Despite the frustrations, the sporadic hopelessness, and the tireless efforts research seems to always demand, I would not go back in time and choose a different course, and that is in large part due to the support of many people around me. This support has come in many forms. Although it is usually difficult to convey in words the extent of one's own gratitude, I will attempt to do so here. These are the people I would like to thank.

I want to thank my thesis advisor, Jay Debnath, for putting up with me for so many years. As he has alluded to, my occasional insubordinate tendencies perhaps did not always make me the most agreeable mentee. That being said, I am enormously grateful to Jay, not only for letting me join his lab to work on exciting projects, but also for creating an atmosphere in which I could be comfortably and confidently independent. I was never scared to share any new idea or pursue a new experiment, and I knew that I could always count on Jay for honest feedback, good or bad. In retrospect, I probably chewed off more than I could swallow over the past few years, but Jay has been constantly supportive, never stifling my ambition or curiosity. This support goes beyond my work in the lab. He taught me how to write a fellowship, has allowed me to mentor many undergrads and rotation students, and has encouraged me to attend and present at conferences, all of which have been important and necessary experiences for me. I admire the way Jay runs his lab; taking note of how he always has a good group of people leading a wide range of interesting projects, I have come to understand a bit about what it takes to be a successful PI. Thanks to this type of mentorship from Jay, I have learned more than I ever thought I would when this all started, both technically and intellectually, and as a result, regardless of the ultimate outcome of the work, my goals for graduate school have been accomplished. I leave with no regrets and feeling completely prepared for what is next. Thanks, Jay!

I am also grateful to the members of my thesis committee, Zena Werb, Dean Sheppard, and Diane Barber. Through their distinct mentoring styles, I always received well-rounded insight, whether it be related to the details of my research project or advice on progressing through graduate school and moving on to my post-doc. Their liveliness and enthusiasm, as well as their honesty and criticism, created for productive, albeit long, thesis committee meetings from which I would come away confident in the course I had taken up to those points and excited for the next directions I would pursue. I am particularly thankful to my committee chair, Zena, for emphasizing the need to see the big picture, not just for my project, but for my career. Through her guidance, I was reminded to pursue what I am interested in and to keep in mind where I intend to go, not just where I am now, and these are things I hope not to forget as I move on and begin to plan for the next stage of my career beyond my post-doc. In addition to their outpouring of wisdom, I am thankful to all of my committee members for any time they took to write me letters of reference, meet with me one-on-one, and reply to my many emails regarding thesis committee meeting scheduling.

Thanks also to all the members of the Debnath Lab that I have worked with over the years. First, I would like to especially acknowledge Rebecca Lock, who allowed me to be a part of her work during my rotation and to contribute some of my results to her paper during my early years in the lab; she probably had the biggest role in helping me get a handle on cell biological techniques for studying autophagy. I would also like to particularly thank our lab managers Ed Salas and Jordan Ye for keeping the lab running smoothly, as well as Fanya Rostker, our mouse technician for taking care of the breeding and genotyping of all my mice and assisting with laborious mouse procedures. I am also grateful to all the other members of the Debnath Lab. They have provided feedback and shared helpful information, and they are all ready to help at anytime. They have all been great company, in and out of the lab.

I need to write special thank you to one member of the lab, Lyndsay Murrow, who has come to be my best friend in San Francisco. We became instant friends our first year at UCSF

and when she rotated in the lab after me, I put in my best efforts to ensure she would join. Thank you Lyndsay for being way smarter than me; not only could I count on you for sound advice on my experiments and data, but I have to think that spending so much time with you also made me a little bit more intelligent. Thanks for letting me bug you, even when you were clearly busy working, and for entertaining many of my ideas (including my proposal that we start our own secret language). We have so many memories together, inside and outside of the lab; I sincerely believe that the past few years would not have been as great without you.

I also want to thank my UC Berkeley undergraduate volunteers Nathalie Faure, Kimberley Woo, and Jordan Ye for contributing and lending a helping hand over the years. They all definitely made some days easier, by helping with mouse experiments, running Westerns, or analyzing data.

There have been a few people outside of the Debnath Lab that have had important roles in my work. First, Torsten Wittmann and his post-doc, Samantha Stehbens, showed me how to perform the focal adhesion turnover studies and spent so much time providing feedback on experiments and data. Without their help, some of this work would not have been possible. I want to thank Jonathan Chou, a classmate of mine in Zena's lab, who was so selfless with his time in helping me learn so much about how to study metastasis. He was a constant source of knowledge, shared so many protocols, and taught me techniques, such as the fat pad transplantation procedure. A post-doc in Zena's lab, Amy-Jo, has also been so helpful in sharing information and protocols. Thanks also to Daniel Garcia, a former student in the Evan Lab, who taught me how to do tail vein injections.

Finally, I want to thank my family for all of their support during my entire life. In particular, thanks to my parents for raising their kids right. I learned a few key things from them that I know have been necessary in ensuring I have had the stamina and resiliency required to get through grad school and beyond. The first is that it is important to prioritize my education; the number one rule in our house was that when you got home from school you had to sit down and do your

homework before going out to play in the street. In addition, we were expected to work hard, to the best of our abilities, in and out of the classroom, and to not whine when things did not go our way. Finally, we have always been encouraged to pursue what makes us happy. These values have led me down a path in which I have found something I really enjoy and will work very hard at through the good and bad days. I am grateful for this upbringing. In addition, I am particularly thankful to my Mom for ensuring I did not go broke or go without clothes on my back. Even against my will, she constantly sent me cards with money and always took me shopping when I was home. On my trips back home I have been excitedly welcomed back with open arms; thanks to everyone for this hospitality. My sister and her husband have been especially tremendous hosts on all my trips back home. They invite me over to their house before I am barely off the plane and it has always been so great to have them be so excited to hang out with me. I also want to acknowledge my best friend, Laura, who I grew up with. She and her family have visited me here in San Francisco a few times, and even when they were living in Seattle, I made a few trips up there to visit them. They have been so thoughtful and generous, and I am lucky to have such good friends.

I have tried my best to express my gratitude here, but words are never enough. Thanks, everyone.

**Regulation of metastatic phenotypes by autophagy**

**by**

**Candia Marie Kenific**

## Abstract

Metastasis, the process by which primary tumor cells disseminate throughout the body and colonize distant organs, continues to be the principal cause of cancer-associated death. Although our understanding of the biology underlying metastasis has advanced significantly in recent years, there is still a lack of effective therapies available for treating this disease. In light of this unmet clinical need, my thesis has focused on establishing whether autophagy, a cellular stress response pathway, may be a novel therapeutic target for treating cancer metastasis.

Autophagy is an evolutionarily conserved process that involves the formation of a double-membrane vesicle, the autophagosome, which consumes cellular constituents and delivers them to the lysosome for degradation. Autophagy is well-recognized to be a crucial regulator of tumorigenesis. The use of *in vivo* transplant models, as well as genetically engineered mouse models of cancer have shown key roles for autophagy in regulating tumor metabolism, growth, and survival. Moreover, autophagy has also been implicated in the regulation of metastasis. Through the use of elegant and physiologically relevant *in vitro* models of tissue morphogenesis and cancer progression, roles for autophagy in supporting adhesion-independent growth and survival, as well as tumor cell invasion and migration have emerged. However, the mechanisms underlying regulation of these phenotypes by autophagy are poorly understood, and it is not known precisely how autophagy regulates *in vivo* cancer metastasis.

Here, I investigate the cell biological mechanisms through which autophagy regulates cell migration. I find that autophagy is required for the efficient assembly and disassembly, or turnover, of integrin-based cell-matrix focal adhesions (FAs) at the leading edge of motile cells.

Additionally, autophagosomes localize to dynamic FAs with extreme temporal specificity during FA disassembly, suggesting autophagy-dependent FA turnover proximally mediates FA destabilization. Finally, I uncover that the autophagy cargo receptor NBR1, which mediates targeting of autophagosomes to their substrates, acts as a key mediator of cell migration and autophagy-dependent FA disassembly and, like autophagosomes, localizes to FAs. Collectively, these findings point to a molecular mechanism of NBR1-mediated selective autophagy in directly regulating FA turnover during migration.

I also explored the role of autophagy during *in vivo* cancer metastasis. Despite extensive data suggesting autophagy would function to promote metastasis, I find that autophagy functions as a metastasis suppressor. In addition, autophagy does not impact growth or viability of established metastatic tumors, suggesting it regulates stages of metastasis prior to overt secondary tumor growth. Finally, I identify the autophagy cargo receptor, NBR1, as a novel metastasis promoter. Because NBR1 is itself degraded by autophagy, overall, these results hint at an unexpected model in which NBR1 accumulation upon autophagy inhibition drives metastasis.

## Table of Contents

## List of Tables

### Chapter 1



## List of Figures

### Chapter 1



### Chapter 2



### Chapter 3

**Appendix A**



**Appendix B**

**Appendix C**

# CHAPTER 1

## Introduction

**Content in the following chapter was modified from these publications:**

1. **Kenific, C.M.** and Debnath, J. Cellular and metabolic functions for autophagy in cancer cells. *Trends in Cell Biology* **25**, 1 (2015).

   **Contributions**: I was primarily responsible for writing the content in the first draft of this manuscript and Jay Debnath supervised this project. Together we edited and revised subsequent drafts.

2. **Kenific, C.M.**, Thorburn, A., and Debnath, J. Autophagy and metastasis: another double-edged sword. *Current Opinion in Cell Biology* **22,** 2 (2010).

   **Contributions**: I was primarily responsible for writing the content in the first draft of this manuscript, Andrew Thorburn provided critical comments, and Jay Debnath supervised this project. Together we all edited and revised subsequent drafts.

**Overcoming barriers to metastasis**

Metastasis, the process by which cancer cells spread from the primary tumor and colonize distant organs, is well-recognized to be the primary cause of death in cancer patients[1-2]. For example, less than 5% of patients who develop metastatic breast cancer are likely to survive[3]. Despite intense study, our understanding of the extremely complex biology governing metastasis is far from complete, as evidenced by our inability to effectively treat this lethal disease. Therefore, ongoing work is necessary to successfully translate basic research findings into effective anti-metastasis therapies.

Development of metastasis is generally characterized by a series of events that begins with phenotypic changes at the primary tumor leading to acquisition of traits that promote local invasion and migration of cancer cells[4] (Fig. 1 A). Upon mobilization, these migratory tumor cells gain access to the vasculature and enter the circulation through intravasation[5]. Circulating tumor cells (CTCs) disseminate systemically and will eventually lodge in the capillaries of organs away from the primary tumor[6]. The disseminated tumor cells (DTCs) seed the distant organ by extravasating out of the vasculature where they then may persist in a dormant solitary state or as small clusters of cells, termed micrometastases, until they acquire the ability to grow out into established secondary tumors, or macrometastases[5, 7-8].

Undoubtedly, due to the obvious complexity of the metastatic cascade, countless cell biological phenotypes are necessary for the completion of metastasis. In particular, cancer cells must cope with diverse environmental and cellular stresses inherent to seemingly every step of metastatic progression. At the primary tumor, hypoxia, metabolic stress, and anti-tumor inflammation all serve as barriers that tumor cells must overcome to successfully initiate metastasis[9-11]. Additionally, metastasizing tumor cells must acquire the ability to survive and grow in the absence of proper cell-extracellular matrix (ECM) contact while traversing the systemic circulation or occupying the foreign microenvironment of the target organ[12]. Furthermore, during dormancy at the metastatic site, tumor cells must survive in the absence of

sufficient nutrients, while enduring tumor suppressive immune modulation[7-8]. In addition to surviving these constant stresses, the ability of tumor cells to invade and migrate is also required during multiple stages of metastatic progression. This mobility allows tumor cells to access the vasculature for dissemination and to exit the circulation at metastatic sites[5]. Overall, given their importance in supporting development of metastases, cellular pathways regulating these traits associated with survival, growth, and motility may act as critical determinants of cancer metastasis, and, as such, may serve as attractive therapeutic targets to treat metastatic disease. One such pathway is macroautophagy (referred to as autophagy), an adaptive pathway most well known for promoting the metabolic fitness of tumor cells that also supports viability during many of the stresses encountered by metastasizing tumor cells and that functions to regulate invasion and migration (Fig. 1 B).

**Overview of autophagy and tumorigenesis**

Autophagy is an evolutionarily conserved pathway of lysosomal-mediated cellular self-digestion. It involves the formation of a double-membrane vesicle, the autophagosome, which engulfs cytoplasmic components and delivers them to the lysosome for degradation (Fig. 2 A). Landmark studies in yeast have identified over 30 autophagy-related genes (*atg*s) that control autophagosome formation and maturation through a series of distinct steps. Initiation of autophagosome formation is regulated by the unc-51-like kinase (ULK) and class III phosphatidylinositol (PI3K) complexes (Fig. 2 B). The class III PI3K complex becomes activated by the ULK complex and functions to generate phosphatidylinositol 3-phosphate (PI3P) at the site of early autophagosome formation for recruitment of additional ATGs that will subsequently mediate elongation and closure of the autophagosome membrane. Elongation and closure is controlled by two ubiquitin-like conjugation pathways that conjugate ATG12 to ATG5 and LC3 to the lipid phosphatidylethanolamine (PE)[13] (Fig. 2 C). Conjugation of ATG12 to ATG5 is regulated by the E1- and E2-like activities of ATG7 and ATG10, respectively. LC3 is conjugated

to PE by ATG7 and the E2-like enzyme ATG3. PE is inserted into the autophagosome membrane, and LC3-PE is localized to both the inner and outer membranes. Importantly, these core ATGs that directly control elongation of the autophagosome membrane are commonly targeted for experimental purposes, either by genetic deletion or RNAi-mediated depletion, to conduct functional studies of autophagy during tumorigenesis. Additionally, LC3-PE (also termed LC3-II) is regularly used as a marker of autophagosomes to monitor the induction or inhibition of autophagy[14]. Ultimately, the autophagosome fuses with endocytic and lysosomal compartments, leading to formation of the autolysosome (Fig. 2 A). Autophagic cargo is then degraded through the activity of lysosomal proteases.

In response to stress and starvation, numerous signaling pathways impinge on ATGs to induce autophagy. The resulting lysosomal digestion and recycling of cellular contents is proposed to refuel cells with metabolic building blocks and energy in the form of ATP that are critical for survival during stress[15-17]. Additionally, during normal cellular homeostasis, autophagy functions as a primary route of degradation for a variety of cellular cargo, including damaged organelles and protein aggregates[18]. Because of these conserved functions in eukaryotic cells, autophagy has been proposed to act as a crucial cellular adaptation pathway that promotes tumorigenesis by promoting the fitness of cancer cells under duress[19-21].

Nonetheless, over the last decade, studies of how autophagy impacts cancer development have yielded conflicting results. Initial studies demonstrating that loss of the essential autophagy regulator *beclin1* (*atg6*) results in increased tumorigenesis in mice provided genetic evidence that autophagy serves tumor suppressive functions[22-23]. Further support for a role for autophagy in limiting tumorigenesis came from elegant studies in which the deletion of *atg5* or *atg7* led to spontaneous development of premalignant liver tumors due to accumulation of oxidative stress and activation of genome damage responses[24-25]. However, as tumor progression requires cancer cells to thrive in untoward environments, tumor-supporting functions for autophagy have been uncovered[21]. Now, we appreciate that autophagy serves

dual roles during tumorigenesis; its homeostatic function limits genome-damaging events that would otherwise favor tumor initiation, while its ability to help cells mitigate stress facilitates advanced tumor progression[19-20] (Fig. 1 B). Importantly, studies in genetically engineered mouse models (GEMMs) of cancer have provided additional support for these opposing functions of autophagy; during oncogene activation, genetic deletion of ATGs enhances early tumor development but impairs advanced tumorigenesis[26-28] (Table 1).

**Control of tumor cell metabolism by autophagy**

Rapidly proliferating tumor cells have increased anabolic demands, which are met by metabolic changes induced upon activation of oncogenes and loss of tumor suppressors[29]. At its most fundamental level, autophagy couples catabolic breakdown of cellular content with anabolic pathways of macromolecule synthesis by supplying the cell with intracellular metabolites generated via lysosomal-mediated degradation. Despite this salient feature of autophagy, its importance in tumor cell metabolism was not appreciated until recently.

Studies of oncogenic Ras-transformation were the first to demonstrate a role for autophagy in supporting tumor cell proliferation and in maintaining metabolic function in the context of oncogene activation. In mouse embryonic fibroblasts (MEFs) transformed with oncogenic HRas and MDA-MB-231 human breast carcinoma cells, which harbor oncogenic KRas, genetic autophagy inhibition reduced anchorage-independent transformation, slowed proliferation, and decreased glycolysis[30]. Similar results were obtained in a transgenic model of breast tumorigenesis driven by the polyoma middle T (PyMT) oncogene; deletion of *FIP200*, which is essential for autophagy initiation, impaired glycolysis in these tumor cells *in vitro* and reduced mammary tumorigenesis *in vivo*[31]. An additional requirement for autophagy in cancer cell metabolism was subsequently shown using HRas-transformed immortalized baby mouse kidney (iBMK) cells and pancreatic ductal adenocarcinoma (PDAC) cell lines with activated Ras[32-33]. Remarkably, despite conventional thinking that pro-growth pathways suppress

autophagy, these studies described an increase in autophagy with oncogenic activation of Ras, suggesting that sustained autophagy allows Ras-transformed tumor cells to meet their high metabolic demands. Accordingly, inhibiting autophagy in these models led to multiple defects in mitochondrial metabolism, including decreased production of TCA cycle intermediates, reduced mitochondrial respiration, and diminished ATP production. Although these various studies of Ras-transformation uncovered different requirements for autophagy during glycolysis versus mitochondrial metabolism, collectively, they demonstrated that autophagy is important for supporting the diverse metabolic demands of different tumor types.

The role of autophagy in sustaining Ras-regulated metabolism has also been explored extensively in lung cancer GEMMs driven by oncogenic KRas or the Ras effector, Braf (Table 1). Deletion of *atg5* or *atg7* in an oncogenic KRas-induced lung cancer model led to diminished overall lung tumor burden; notably, autophagy-deficient tumors exhibited oncocytic differentiation, marked by the accumulation of abnormal mitochondria within tumor cells[26, 34-35]. In the absence of the tumor suppressor p53, this loss of mitochondrial homeostasis resulted in defective fatty acid oxidation and, consequently, impaired lipid metabolism when *atg7* was deleted[34]. Based on these results, the authors concluded that reduced lipid catabolism compromises the ability of autophagy-deficient tumor cells to cope with nutrient deprivation. In a Braf-driven lung cancer model, advanced tumor progression was similarly reduced by *atg7* deletion[28]. Autophagy deficient cell lines derived from these tumors harbored aberrant mitochondria and addition of the metabolite glutamine rescued defects in mitochondrial metabolism, suggesting that autophagy-inhibited tumor cells exhibit slowed growth due to increased metabolic stress associated with a lack of intermediates that drive mitochondrial metabolic pathways. Defects in lipolysis were not observed here as in the KRas lung model, but these studies nonetheless corroborated the importance of autophagy in regulating metabolic homeostasis by broadly controlling proper mitochondrial function. Furthermore, autophagy inhibition also reduced growth and survival of central nervous system tumor cells with activated

Braf; while the impact of autophagy on metabolism was not investigated here, the results obtained in the Braf lung model intimate an underlying mechanism by which autophagy may impact Braf-driven growth across multiple tumor types[36].

Though these studies demonstrate that maintaining metabolic fitness of cancer cells appears to be the principal and most well characterized role for autophagy in regulating tumor progression, much remains to be learned with regard to the precise mechanisms of autophagy-dependent metabolism. While specific enzymes involved in glycolysis have been shown to regulate autophagy, no such regulation by autophagy on particular steps of the glycolytic pathway has been uncovered[37-38]. Additionally, although accumulation of abnormal mitochondria due to decreased mitophagy may explain the defects associated with mitochondrial metabolism upon autophagy inhibition, impaired mitophagy was not observed in autophagy-deficient PDAC cell lines that exhibited diminished oxidative phosphorylation[33]. This discrepancy suggests that there are mitophagy-independent pathways through which autophagy controls mitochondrial metabolism and that engagement of these various regulatory mechanisms may be context-dependent. Moreover, in most studies, these metabolic defects have been characterized using tumor cell lines in culture; while this method certainly facilitates a detailed analysis of metabolic parameters, it may not accurately recapitulate the metabolic state of tumors *in vivo*. *In vivo* application of established NMR-based technologies to assay glycolysis during tumor formation or use of methods to measure metabolism in freshly isolated mitochondria from tumors will provide further insight into the role of autophagy in cancer metabolism[39-40].

Nevertheless, these studies illustrate the clear requirement for autophagy in sustaining tumor cell metabolism and raise the question of whether autophagy is similarly necessary for the metabolic fitness of metastasizing tumor cells. Metastatic cells must adapt to metabolic stress for survival and they also require energy to complete tasks that are necessary for metastasis. For example, migration is controlled by cellular pathways requiring chemical energy to support the activity of the various enzymes essential for motility, including kinases and

GTPases. Accordingly, in metastasizing tumor cells, catabolic, energy generating pathways may be as equally important as the anabolic pathways that are upregulated by tumor cells to support enhanced growth. In agreement with this idea, recent work focused directly on understanding the metabolic demands of metastasizing tumor cells uncovered an essential role for PGC-1$\alpha$-mediated mitochondrial biogenesis and oxidative phosphorylation during invasion and metastasis, but not primary tumor growth[41]. Compared to primary tumor cells, CTCs exhibited an increase in expression of genes associated with mitochondrial biogenesis and a concomitant increase in oxidative phosphorylation and ATP production. Based on these findings and the aforementioned studies describing a function for autophagy in promoting tumor cell oxidative phosphorylation, autophagy may also metabolically support metastasis phenotypes by maintaining energy production through mitochondrial respiration.

Additionally, it has long been established that hypoxic tumor microenvironments activate cellular pathways that stimulate invasion and migration at the primary tumor site, while also inducing glycolysis to cope with this lack of oxygen[9]. More recently, it has also been shown that at certain metastatic organs, such as liver, colon cancer DTCs must cleverly exploit glycolysis-independent pathways of energy generation to cope with the unique metabolic challenges imposed on them by the hypoxic liver microenvironment for successful metastasis[42]. Autophagy is also robustly upregulated by hypoxia, and this supports the vitality of oxygen deprived tumor cells[43-44]. This pro-survival function of autophagy may be due to its ability to promote glycolysis, as well as to directly generate ATP through lysosomal breakdown of cellular material. Thus the above studies support that by promoting both glycolysis-dependent and –independent ATP synthesis to enable optimal metabolic fitness during hypoxia, autophagy-dependent energy production may ultimately be critical for tumor cells to survive at the primary tumor and metastatic organ, as well as to also fully co-opt invasion-promoting pathways downstream of hypoxia responsive factors to enable metastasis. Further work clarifying the metabolic requirements of tumor cells during all stages of metastatic progression and in specific metastatic

microenvironments may elucidate multiple roles for autophagy in facilitating metabolism of disseminating tumor cells. Given the apparently important and possible context-dependent roles of both oxidative phosphorylation and glycolysis in regulating metastasis, rewiring of tumor cell metabolism by modulation of autophagy may serve to enhance or attenuate metastasis.

**Regulation of tumorigenesis by selective autophagy cargo receptors**

While autophagy is often described as a process involving non-specific bulk degradation of cytoplasmic material, during normal cellular homeostasis, it actually functions at a basal level as a highly selective pathway of cellular degradation in which specific cargo is sequestered by the autophagosome. This cargo typically consists of content that may compromise cell viability, such as damaged organelles, protein aggregates, and pathogens (Fig. 3 A). Indeed, the importance of this role for autophagy in maintaining cellular quality control has been clearly demonstrated *in vivo* where neuronal specific deletion of *atgs* is sufficient to cause neurodegeneration associated with accumulation of abnormal mitochondria, protein aggregates, and inclusion bodies[45-46].

Selective autophagy is principally mediated by autophagy cargo receptors, which regulate degradation of autophagy substrates by promoting their recruitment into growing autophagosomes. This recruitment generally occurs through interaction of receptors with ubiquitin-tagged cargo through an ubiquitin binding domain and with LC3 via an LC3 interacting region (LIR)[47-48] (Fig. 3 A). Importantly, in addition to this crucial function for cargo receptors in regulating capture of substrates by autophagosomes, they also serve autophagy-independent functions. Accordingly, because these receptors themselves are degraded by autophagy due to their interaction with LC3, inhibition of autophagy promotes their accumulation and results in aberrant regulation of their downstream pathways (Fig. 3 B). Therefore, the regulation of autophagy cargo receptors themselves by autophagy may have crucial implications for

tumorigenesis, as illustrated by studies demonstrating direct tumor-promoting functions for the archetypal autophagy cargo receptor p62/SQSTM1[49-50].

p62/SQSTM1 is a versatile, multi-domain adapter that regulates several signaling pathways to promote tumorigenesis[49-50] (Fig. 3 B). Among these, NFκB-mediated control of pro-inflammatory signaling and regulation of the anti-oxidant response by Nrf2 have been most strongly linked to tumorigenesis in the context of autophagy inhibition. Through interaction with TRAF6, p62 promotes NFκB signaling, and this p62-mediated activation of NFκB is required for Ras-induced lung and pancreatic tumorigenesis. Similarly, regulation of the transcription factor Nrf2 by p62 is also important for tumorigenesis. p62 inhibits degradation of Nrf2, a key regulator of the oxidative stress response, by binding to Keap1, an adaptor for the E3 ubiquitin ligase that promotes Nrf2 degradation[51]. The ability of p62 to support tumor growth by activating Nrf2 is necessary for the spontaneous development of liver tumors due to *atg5* or *atg7* knockout[24-25, 52].

p62 also controls additional pro-tumorigenic pathways, including those regulated by mTORC1 and ERK. mTORC1 regulates tumor cell growth, and p62 activates mTORC1 by potentiating its ability to complex with Rag GTPases and TRAF6 and by facilitating its recruitment to lysosomes; this regulation of mTORC1 by p62 supports cell proliferation *in vitro* and tumor growth *in vivo*[53-54]. p62 overexpression can also enhance the growth of PI3K-transformed MCF10A cells in 3D culture[55]. In this model, p62-induced proliferation correlates with activation of mitogenic ERK signaling. These studies collectively point to a pro-tumorigenic function for p62 and highlight the varied regulatory roles of p62 during tumorigenesis.

In addition to p62, other cargo receptors, such as NDP52, OPTN, and NBR1, mediate selective autophagy[47]. Similar to p62, NDP52 has been implicated in regulation of NFκB signaling in lung cancer cells[56]. Although this regulation was proposed to occur through NDP52-mediated selective autophagy, the precise mechanism is unknown. Moreover, OPTN can inhibit NFκB signaling, but how this regulation affects tumor development has not been investigated[57].

While formal evidence for NBR1 in mediating tumor progression is also lacking, it is noteworthy that NBR1 can support Nrf2 anti-oxidant signaling to potentially impact cancer[58]. Additionally, NBR1 regulates selective autophagic clearance of midbodies that form during cell division, and midbody accumulation contributes to increased growth of tumor cells *in vitro*[59]. Collectively, because of their ability to select autophagy cargo and their autophagy-independent functions, cargo receptors may impact tumorigenesis through diverse mechanisms.

Intriguingly, while the potential role of the autophagy cargo receptors in regulating metastasis has not been investigated, their downstream pathways appear to have specific functions in controlling metastatic phenotypes. For example, platelet-induced activation of NFκB in CTCs can synergize with TGFβ signaling to promote invasion and metastasis[60]. Similarly, mTORC1 can support motility, invasion, and *in vivo* metastasis of colorectal cancer cells, whereas ERK appears to be an important pro-growth pathway for establishment of macrometastases[61-62]. Thus, in addition to supporting primary tumor growth, p62 may also promote metastasis by activating these pathways. Similarly, NBR1 has been found to inhibit p38 MAPK signaling to regulate osteoblast differentiation, and p38 MAPK restricts growth of metastases by promoting dormancy[63-64]. These findings broach the hypothesis that accumulation of NBR1 downstream of autophagy inhibition may promote outgrowth of macrometastases by limiting quiescence. Further work establishing the contribution of these selective autophagy regulators to tumorigenesis and metastasis remains an important topic for future study.

**Detachment-induced autophagy and anoikis resistance**

In normal cells, the lack of proper ECM attachment leads to apoptosis, termed anoikis[65-66]. Anoikis maintains homeostasis in developing and adult tissues; for example, anoikis promotes the clearance of epithelial cells detached from the surrounding basement membrane

during ductal elongation in the mouse mammary gland[67]. For tumor cells to survive and metastasize, they must activate mechanisms to resist anoikis; this adhesion independence is crucial during ECM detachment, which may occur while tumor cells are in the circulation or at the metastatic site where they cannot fully engage the foreign ECM[12 65]. In a model of gastric cancer, cells that demonstrate enhanced adhesion independent growth *in vitro* due to anti-apoptotic factor overexpression also exhibit enhanced peritoneal dissemination *in vivo*[68]. Moreover, the neurotrophic tyrosine kinase receptor, TrkB, has been identified as a potent anoikis suppressor. Importantly, TrkB overexpression in non-malignant cells facilitates the robust formation of lung and heart metastases following intravenous injection, indicating that anoikis resistance is both necessary and sufficient for metastasis[69]. As exemplified by this study, the aberrant activation of growth factor pathways is a common mechanism utilized by cancerous cells to evade anoikis.

Recent work indicates that autophagy is another mechanism that protects matrix-detached epithelial cells from anoikis[70-71]. Autophagy was first shown to promote the survival of non-transformed mammary epithelial cells during ECM detachment; subsequent studies revealed that detachment-induced autophagy is critical for adhesion-independent transformation[30, 72] (Fig. 4 A). Multiple Ras-transformed human cancer cell lines upregulate autophagy upon detachment, and autophagy inhibition compromises adhesion-independent growth and survival of cells harboring activated Ras. Similarly, when oncogenic PI3K-transformed MCF10A cells were grown in three-dimensional (3D) culture, autophagy inhibition led to increased apoptosis of luminal cells deprived of ECM contact[55].

There is limited evidence demonstrating a role for detachment-induced autophagy during metastasis *in vivo*. Recent work suggests autophagy-dependent anoikis resistance is necessary for metastasis of hepatocellular carcinoma (HCC) cells[73]. Autophagy inhibition attenuated pulmonary metastasis of HCC cells following orthotopic transplantation into nude mice, and this defect correlated with increased anoikis of autophagy deficient HCC cells *in vitro*. However, in

the absence of data specifically demonstrating that autophagy supports survival of HCC cells *in vivo*, additional work is necessary to rigorously test a direct function for autophagy in promoting adhesion-independent survival of tumor cells during *in vivo* cancer metastasis.

Currently, the precise mechanism through which detachment-induced autophagy protects cells from anoikis remains unclear. Integrin engagement amplifies signals transmitted by growth factor receptor pathways, which together coordinate proper nutrient uptake and metabolism[74-76]. Similar to its role in starvation, autophagy in ECM-detached cells may compensate for the loss of extrinsic signals promoting nutrient and energy metabolism[71]. Alternatively, since autophagy is initially upregulated in stressed regions of primary tumors, sustained self-eating may further enable the pro-metastatic phenotype as primary tumor cells receive microenvironmental signals stimulating ECM detachment and migration. A better understanding of how autophagy supports adhesion-independent growth and survival may offer a better mechanistic understanding of how autophagy can regulate metastasis.

**Regulation of cellular invasion and migration by autophagy**

Autophagy has also emerged as a regulator of cellular invasion and migration, suggesting it may be important in facilitating intravasation or seeding of the metastatic organ (Fig. 4 B). In an organotypic model of invasion through a collagen matrix, knockdown of the essential autophagy regulator, ATG12, decreased invasive capacity of glioma cells[77]. Although this study did not delineate the mechanism of autophagy-mediated invasion, other studies have demonstrated multiple routes by which autophagy controls invasion. For example, in glioblastoma (GBM) stem cells, autophagy inhibition or knockdown of the autophagy regulator, p62, decreased invasion and migration *in vitro* and led to metabolic defects[78]. Based on previous evidence indicating that glycolysis is important for GBM invasion, the authors proposed a model in which p62-dependent autophagy impacts metabolism to control invasion[79].

Further roles for autophagy in regulating invasion have been uncovered in other models. Invasion of HCC cells during starvation was shown to be autophagy-dependent, due to the ability of autophagy to stimulate TGFβ and promote epithelial-to-mesenchymal transition (EMT), a well established transcriptional program that supports metastasis[80]. A similar requirement for autophagy in controlling invasion and migration was observed in Ras-transformed epithelial cells in 3D culture[81]. Autophagy inhibition attenuated invasion and caused a partial reversion of EMT. Additionally, impaired autophagy led to decreased secretion of multiple pro-invasive cytokines, including interleukin-6 (IL-6). Notably, decreased invasion upon autophagy inhibition was partly restored with IL-6 re-addition, demonstrating a specific need for the autophagy pathway in controlling secretion of this cytokine. Finally, autophagy-deficient Ras-transformed cells exhibited reduced pulmonary metastases. Overall, these findings uncovered a new role for autophagy during cancer cell invasion by promoting secretion and suggested that autophagy-dependent secretion may be important for metastasis *in vivo*. An additional report showed that induction of autophagy by toll-like receptors (TLRs) promotes secretion of pro-invasive factors, including IL-6, in lung cancer cells, further corroborating a role for autophagy as a determinant of pro-invasive secretion[82].

The mechanism by which autophagy controls secretion during invasion remains poorly defined. Although these phenotypes may be secondary to autophagic turnover of secretory regulators, autophagy has been directly implicated in promoting both conventional and unconventional secretion in other contexts[83]. During TLR mediated invasion, autophagy upregulates signaling pathways, such as NFκB and MAPK, that promote secretion, but how autophagy controls these pathways in this model is unclear[82]. Furthermore, IL-6 can promote EMT and stimulate TGFβ signaling, which argues that autophagy-dependent secretion may also be important for HCC cell invasion[84].

**Autophagy and dormancy**

Dormancy describes the remarkable ability of disseminated tumor cells (DTCs) to subsist for years to decades at distant sites without giving rise to secondary tumors. The dormant cell population may constitute only a small fraction of cells that disseminate from the primary tumor and harbor the ability to form metastases. These cells usually go undetected upon diagnosis and remain refractive to common treatments targeting proliferating cells at the primary tumor[85-86]. Hence, understanding the mechanisms governing dormancy is critical for identifying treatments to eliminate these cells.

Notably, the inability of DTCs to form strong and stable ECM contacts with a new microenvironment has been proposed to induce tumor dormancy[85]. Specifically, suppression of β1 integrin signaling, a known inducer of autophagy, induces dormancy in the MMTV-PyMT model of breast cancer[70, 87]. Thus, it is possible that since DTCs cannot efficiently engage a foreign ECM, impaired integrin signaling may stimulate autophagy for survival and maintenance of dormancy. Moreover, solitary dormant cells must also resist extrinsic apoptotic stimuli. In breast cancer metastases to bone, where DTCs remain dormant in the bone marrow for extended periods of time, TRAIL is abundantly expressed in the bone marrow microenvironment and can kill dormant cells. Mechanisms involving Src mediated TRAIL resistance promote the survival of dormant cells in the bone marrow[88]. Because autophagy can protect cells from TRAIL-induced apoptosis, it may similarly promote the survival of dormant cells in the bone marrow[89-90].

Tumor cell dormancy likely reflects a mechanism of evolutionary adaptation that DTCs use to survive when exposed to an inhospitable microenvironment[85]. In *C. elegans,* a precedent for stress-induced dormancy has already been established during dauer formation, a stage of developmental growth arrest and quiescence that occurs when larvae are exposed to hostile environments. Importantly, autophagy has been shown to be essential for this process; RNAi against ATGs decreases dauer survival[91]. These findings lend support to a conserved

mechanism by which autophagy promotes survival during quiescent states. Accordingly, pathways leading to $G_0$ arrest induce both dormancy and autophagy; a pro-survival role for autophagy during $p27^{Kip1}$ induced quiescence has been demonstrated and breast cancer cell lines that typically exhibit dormant behavior *in vivo* have upregulated levels of $p27^{Kip1\ 92\text{-}93}$.

Nonetheless, the exact biological role for autophagy during quiescence remains largely unknown. If autophagy is required for growth suppression in quiescent cells, one can alternatively hypothesize that it may also limit the outgrowth of dormant cells into macro-metastases. A direct link between autophagy and tumor cell dormancy was recently uncovered in ovarian cancer cells. The tumor suppressor aplasia Ras homolog member I (ARHI), induces autophagy and promotes *in vivo* survival of dormant cells in the context of a tumor microenvironment[94]. Though limited *in vivo* models of dormancy exist, the pharmacological or genetic manipulation of autophagy during the aforementioned studies may reveal a more defined role for autophagy during dormancy.

**Establishing the functional and mechanistic contributions of autophagy to metastasis**

Overall, our current understanding of autophagy-dependent tumor growth and regulation of metastatic phenotypes strongly support the hypothesis that autophagy acts as a critical determinant of *in vivo* cancer metastasis. Although these functions of autophagy have been well-documented *in vitro* and the role of autophagy in mediating primary tumor growth has been extensively studied, the exact functional and mechanistic contributions of autophagy to *in vivo* cancer metastasis remain very poorly defined. Moreover, because the abovementioned studies on metabolism, autophagy cargo receptors, and autophagy-dependent anoikis resistance, invasion, migration, and dormancy suggest that autophagy may functionally enhance or impede cancer metastasis, it is important to mechanistically define how autophagy regulates metastatic traits and to also establish the contributions of autophagy to each stage of metastatic progression. Such an understanding may offer a more specific avenue for therapeutically

targeting particular autophagy-dependent phenotypes and improve our comprehension of how targeting autophagy may affect metastasis overall. To that end, the goal of my thesis work has been to identify mechanisms by which autophagy regulates cell migration and to establish if and how autophagy regulates *in vivo* metastasis.

In Chapter 2, I present data establishing a mechanistic role for NBR1-dependent selective autophagy in mediating the dynamic turnover of cell-matrix focal adhesions during cellular migration, a phenotype essential for metastasis. In Chapter 3, I describe findings demonstrating an unexpected role for autophagy in functioning as a metastasis suppressor *in vivo,* potentially through autophagy-independent functions of NBR1. In Chapter 4, I propose open questions for future study motivated by the findings in Chapters 2 and 3 and suggest how these results and such further investigation may improve our understanding of multiple areas of cell and cancer biology including: 1) regulation and functions of selective autophagy, 2) control of focal adhesions and cell migration, and 3) autophagy-dependent cancer metastasis. In addition, Appendix A describes the development and validation of *in vivo* syngeneic mouse models to study the genetic requirement for autophagy upon deletion of the essential autophagy regulator, *atg12*, during MMTV-PyMT driven breast cancer metastasis and derivation of a tumor cell line from these mice. Finally, Appendices B and C include publications from our lab to which I contributed demonstrating roles for autophagy in supporting metabolism, anchorage-independent growth and survival, and invasion of transformed cells.

**Figure 1**

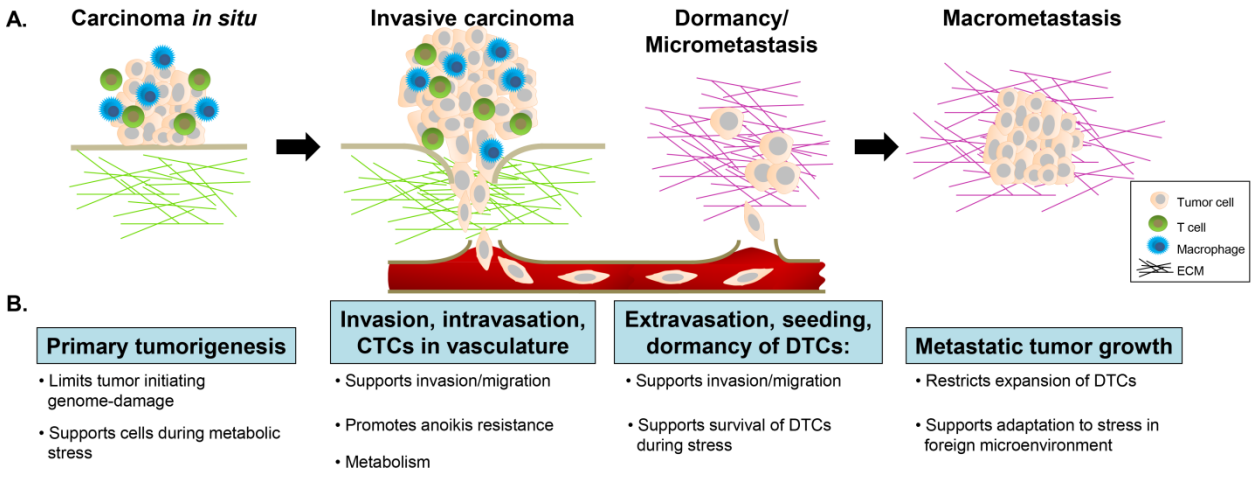


**Figure 1: Potential roles of autophagy during tumor progression and metastasis.** (A) Metastasis is a multistep process in which primary tumor cells acquire the ability to locally invade and migrate. They then enter the systemic circulation to disseminate to metastatic organ sites, where they extravasate and seed the parenchyma of the distant site. After a period of dormancy, which may involve quiescence of single cells and/or balanced proliferation and death of small clusters of cells, overt metastatic tumors will form. Immune cells known to be required for local invasion and migration at the primary tumor are also depicted. (B) Autophagy may serve multiple pro-tumorigenic and anti-tumorigenic roles during primary tumor formation and metastasis. These potentially diverse functions (which are discussed in detail throughout the text) are noted for the primary tumor and each step of the metastatic cascade.

**Figure 2**

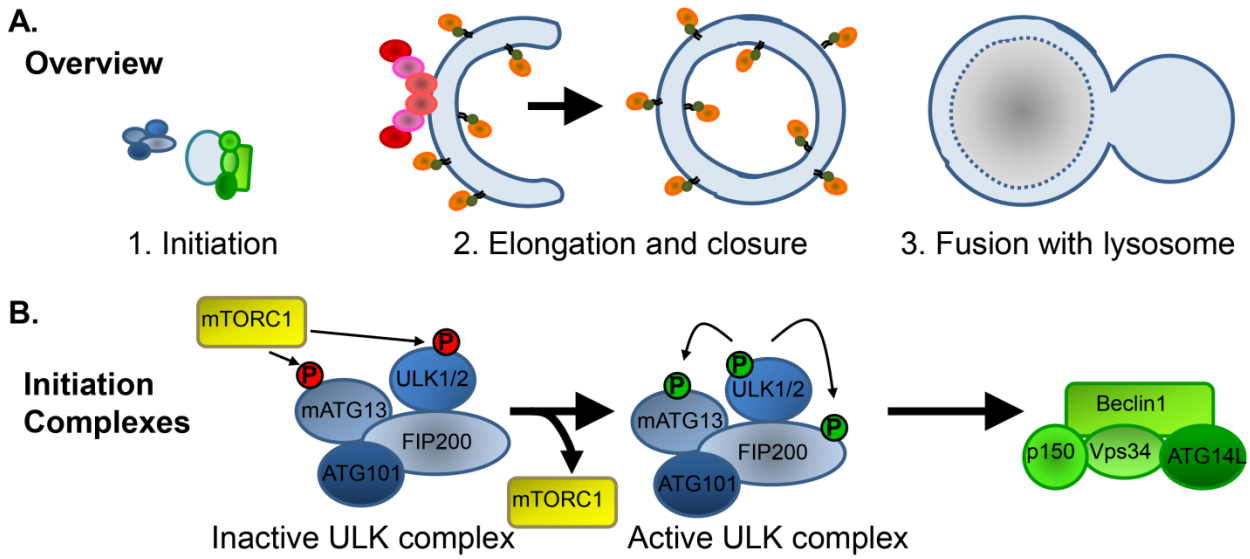
A.
Overview
1. Initiation
2. Elongation and closure
3. Fusion with lysosome
B.
Initiation Complexes
mTORC1
ULK1/2
mATG13
FIP200
ATG101
mTORC1
Inactive ULK complex
Active ULK complex
Beclin1
p150
Vps34
ATG14L
C.
Elongation Pathways
ATG12
ATG7
ATG10
ATG16
ATG5
LC3
ATG3
PE

**Figure 2: The autophagy pathway of lysosomal-mediated cellular degradation.** (A) Autophagy begins with the initiation of autophagosome biogenesis. The growing autophagosome engulfs cellular constituents and eventually fuses with the lysosome for degradation of contents via lysosomal proteases. (B) Initiation of autophagy is regulated by two complexes, the ULK complex and the class III PI3K complex. Following suppression of pro-growth signals, most notably mTORC1, inhibition of the ULK complex is relieved. ULK1/2 phosphorylates its binding partners, mATG13 and FIP200, leading to full activation of the ULK complex, which then activates the class III PI3K complex to generate phosphatidylinositol 3-phosphate at the site of early autophagosome formation for recruitment of additional ATGs that regulate autophagosomal membrane elongation and closure. (C) Elongation of the autophagosomal membrane is regulated by two ubiquitin-like conjugation pathways resulting in the conjugation of ATG12 to ATG5 and LC3 to the lipid phosphatidylethanolamine (PE). Both complexes localize to the autophagosomal membrane to promote elongation and closure.

**Figure 3**

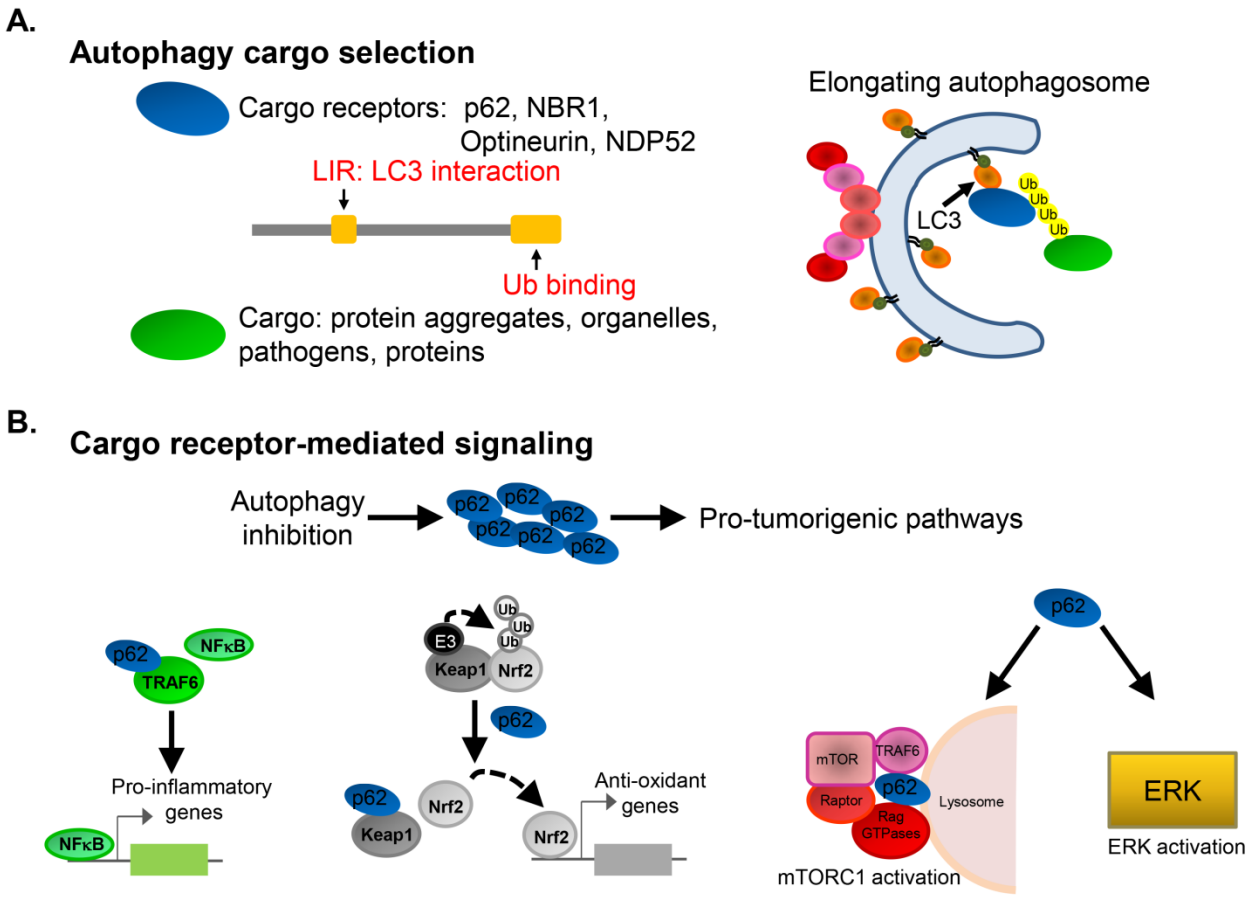


**Figure 3: Functions of autophagy cargo receptors.** (A) Selective autophagy is regulated by autophagy cargo receptors. Encapsulation of cargo into the autophagosome is principally mediated by binding of the cargo receptor to ubiquitinated (Ub) substrates through an ubiquitin binding domain (e.g. UBA) and interaction with LC3 on the autophagosome through an LC3 interacting region (LIR). Cargo receptors also harbor additional protein domains. Notable cargo includes protein aggregates, organelles, pathogens, and proteins. (B) Upon autophagy inhibition, autophagy cargo receptors accumulate and this could impact downstream signaling pathways that may regulate tumorigenesis. For example, p62 can promote tumorigenesis by activating NFκB pro-inflammatory gene regulation and Nrf2 anti-oxidant gene regulation. In addition, p62 can activate additional pro-tumorigenic pathways, such as mTORC1 and ERK.

**Figure 4**

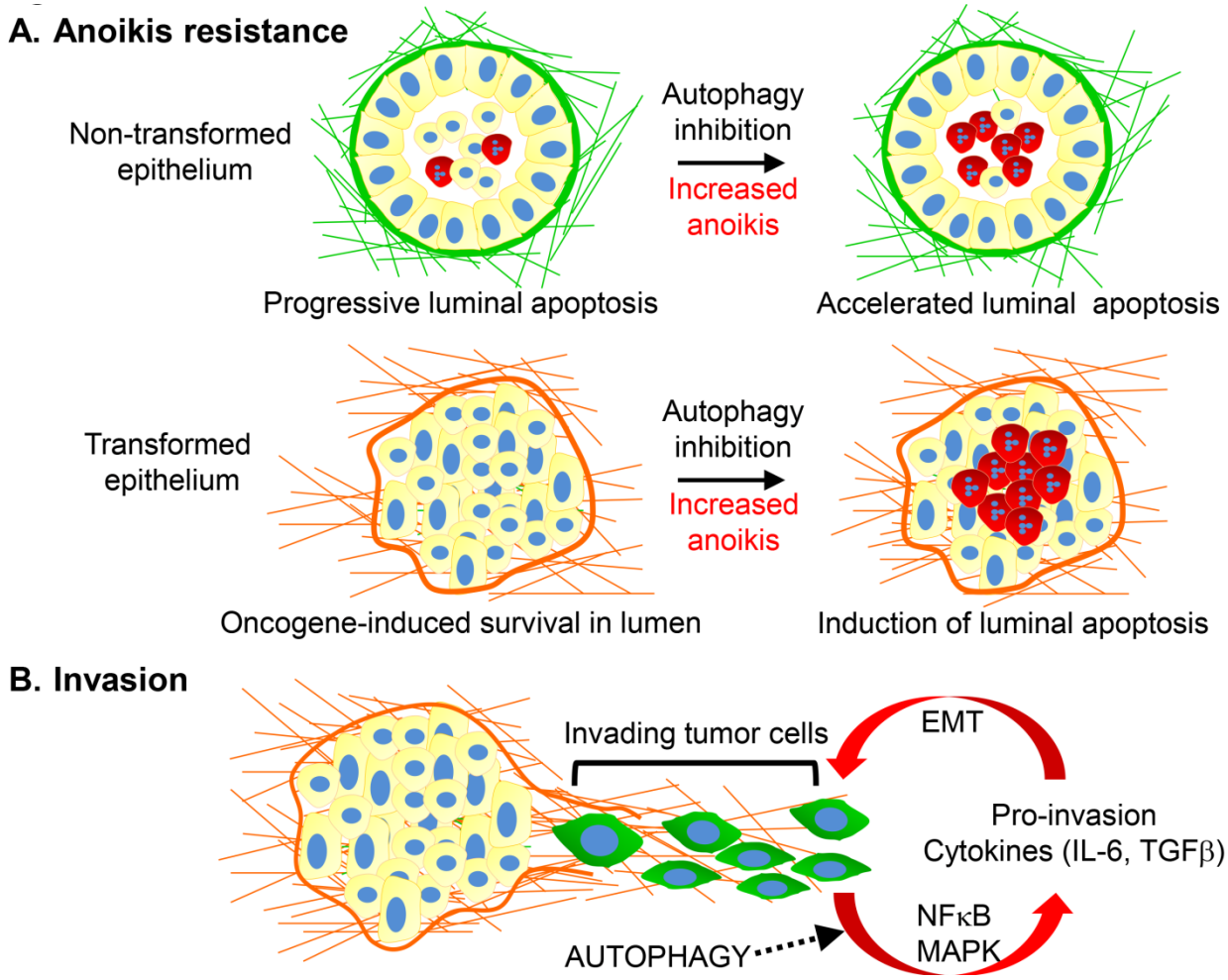
A. Anoikis resistance
Non-transformed epithelium
Autophagy inhibition
Increased anoikis
Progressive luminal apoptosis
Accelerated luminal apoptosis
Transformed epithelium
Autophagy inhibition
Increased anoikis
Oncogene-induced survival in lumen
Induction of luminal apoptosis
B. Invasion
Invading tumor cells
EMT
Pro-invasion Cytokines (IL-6, TGFβ)
NFκB MAPK
AUTOPHAGY

**Figure 4: Autophagy promotes anoikis resistance and tumor cell invasion *in vitro.*** (A) Three-dimensional (3D) culture of MCF10A cells leads to the formation of acini with hollow lumens. Luminal clearance occurs through anoikis of central cells (depicted in red) lacking extracellular matrix (ECM) contact. Oncogene activation protects luminal cells from anoikis, leading to the formation of structures with filled lumens. Autophagy promotes the survival of both normal and transformed epithelial cells deprived of ECM contact; therefore, inhibiting autophagy leads to increased anoikis. (B) Autophagy promotes tumor cell invasion by facilitating the secretion of multiple pro-invasive cytokines. Activation of the NFκB and MAPK pathways by autophagy has been shown to contribute to the increased production of these secreted factors. In turn, these cytokines may augment a pro-invasive gene signature program through the induction of epithelial-to-mesenchymal transition (EMT).

**Table 1: Effects of *atg* deletion on tumor progression and metabolism in cancer GEMMs**

| GEMM | | *Atg* deletion[a] | Phenotype upon autophagy inhibition | | Ref |
|---|---|---|---|---|---|
| Cancer type | Genotype | | Tumor progression[b] | Tumor cell metabolism[c] | |
| Mammary carcinoma | *MMTV-PyMT* | *FIP200* (MMTV-Cre) | Decreased initiation and progression | Impaired glycolysis | [31] |
| Non-small cell lung cancer | *lox-stop-lox-Kras$^{G12D}$; Tp53$^{flox/flox}$* | *Atg7* (intranasal adenoviral Cre) | Decreased progression, oncocytoma formation | Impaired mitochondrial metabolism and fatty acid oxidation, lipid accumulation | [34] |
| Non-small cell lung cancer | *lox-stop-lox-Kras$^{G12D}$* | *Atg5* (intranasal adenoviral Cre) | Increased initiation, decreased progression, oncocytoma formation | Impaired mitochondrial metabolism | [26] |
| Non-small cell lung cancer | *frt-stop-frt-Kras$^{G12D}$; Tp53$^{frt/frt}$* | *Atg7* (Ubc-CreERT2) | Decreased progression, oncocytoma formation | Lipid accumulation | [35] |
| Non-small cell lung cancer | *Braf$^{V600E}$; Tp53$^{flox/flox}$* | *Atg7* (intranasal adenoviral Cre) | Increased initiation, decreased progression, oncocytoma formation | Impaired mitochondrial glutamine metabolism | [28] |
| Pancreatic cancer | *lox-stop-lox-Kras$^{G12D}$; Tp53$^{flox/+}$; Pdx-cre* | *Atg5* (Pdx-Cre) | Increased initiation, decreased progression | ND | [27] |

[a]Method of cre-recombinase mediated deletion is indicated in parentheses. MMTV-Cre expression is mammary epithelial cell specific, Ubc-CreERT2 expression is ubiquitous and tamoxifen-inducible, and Pdx-Cre is exocrine and endocrine pancreatic specific.

[b]Effects on tumor initiation are related to tumor onset and development of early stage tumors. Effects on progression are related to advanced tumorigenesis.

[c]ND indicates metabolic phenotype was not determined in the context of *atg* deletion.

# CHAPTER 2

## NBR1 enables autophagy-dependent focal adhesion turnover

**This chapter is a manuscript currently in revision.**

**Contributions:** I performed all the experiments and analyzed all the data with the following exceptions. Nathalie Faure contributed experimental repeats to the data in Figure S1F and S1G. Jordan Ye assisted with the quantification shown in Figure 1E and generated the immunoblot for wild-type MCF10A cells in Supplemental Figure 1A. In addition, Juliet Goldsmith contributed to validation of knockdown reagents and antibodies for data in Figure 5A, 5B, and S2A and performed the p62 immunoblot in Figure S2A. Andrew Leidal helped with site-directed mutagenesis to generate the autophagy-deficient NBR1 mutant cDNA. Samantha Stehbens and Torsten Wittmann developed methods for imaging and analysis of focal adhesion turnover and were a constant source of critical advice on experimental design and data interpretation and analysis. Jay Debnath supervised the entire project.

**ABSTRACT**

Autophagy is a catabolic pathway involving the sequestration of cellular contents into a double-membrane vesicle, the autophagosome. Although recent studies demonstrate that autophagy supports cell migration, the underlying mechanisms remain unknown. Using live-cell imaging, we uncover that autophagy promotes optimal migratory rate and facilitates the dynamic assembly and disassembly of cell-matrix focal adhesions (FAs), which is essential for efficient motility. Additionally, our studies reveal that autophagosomes associate with FAs primarily during disassembly, suggesting autophagy locally facilitates the destabilization of cell-matrix contact sites. Furthermore, we identify the selective autophagy cargo receptor Neighbor of BRCA1 (NBR1) as a key mediator of autophagy-dependent FA remodeling. NBR1 depletion impairs FA turnover, and overexpression of autophagy-competent, but not autophagy-defective, NBR1 enhances FA disassembly and reduces FA lifetime during migration. Our findings provide mechanistic insight into how autophagy promotes migration by revealing a requirement for NBR1-mediated selective autophagy in enabling FA disassembly in motile cells.

## INTRODUCTION

Cell migration is essential for tissue morphogenesis during development, immune function, and wound healing and is deregulated during pathological processes such as cancer [95-96]. Migration is a highly integrated process involving tight spatiotemporal control of signaling and structural networks throughout the cell. Chief among these are integrin-based focal adhesions (FAs) through which cells engage in adhesive contacts with the surrounding extracellular matrix (ECM). In addition to integrins, FAs are comprised of signaling and adapter proteins allowing them to serve as large, macromolecular biochemical and physical scaffolds linking the ECM to the intracellular actin cytoskeleton [97-98]. As such, FAs direct migration in part by mechanically generating forces for movement. Specifically, rapid cycles of FA assembly and disassembly, or turnover, at the leading edge of migrating cells are necessary for productive migration. FA assembly allows cells to establish traction for forward movement, while subsequent disassembly of FAs enables efficient displacement of the advancing cell [97-99].

Given the prominent role of cell migration in many physiological and pathological processes, understanding the regulation of FA dynamics is a topic of intense study. It is well established that FA assembly involves hierarchical recruitment of FA proteins due to phosphorylation and tension-induced conformational changes that progressively enable protein-protein interactions, but it is not completely certain how these events are regulated [99]. Although FA disassembly has also been shown to require phosphorylation of FA proteins [100] and recent work demonstrates that microtubule-induced FA disassembly involves extracellular proteolysis [101], how FA disassembly is spatiotemporally coordinated at the leading edge of migrating cells remains unclear.

Autophagy is an evolutionarily conserved process of cellular self-degradation that involves formation of a double membrane vesicle, the autophagosome, which sequesters cytoplasmic material for delivery to lysosomes [102]. Though traditionally viewed as a vital

pathway supporting cellular homeostasis and adaptation to stress, autophagy is implicated in a growing list of cellular functions [18]. Recent studies demonstrate that autophagy inhibition impacts cell migration [78, 81-82, 103]. However, apart from establishing a genetic requirement for essential autophagy regulators (ATGs) in mediating these phenotypes, the mechanistic basis of autophagy-dependent motility is not known.

Therefore, we sought to establish how the autophagy pathway regulates motility and demonstrate here that autophagy facilitates leading edge FA turnover during migration. We demonstrate that ATG depletion reduces migratory rate and stabilizes FAs, as evidenced morphologically by enlarged leading edge FAs and kinetically by longer-lived FAs that have decreased rates of FA assembly and disassembly. We also show that autophagosomes localize to dynamic leading edge FAs, and temporally, this association occurs principally during FA disassembly. Finally, our studies uncover an important role for the selective autophagy cargo receptor, Neighbor of BRCA1 (NBR1), in supporting both cell motility and autophagy-dependent FA turnover. Because autophagy cargo receptors mediate sequestration of substrates into autophagosomes, we propose a model in which NBR1 facilitates autophagic targeting of FAs, thereby driving FA turnover to optimize migration.

## RESULTS

### Autophagy-deficient cells exhibit reduced migration rates and increased FA size

We previously demonstrated that autophagy supports the migration of $HRas^{V12}$-transformed MCF10A (MCF10A-Ras) cells and the mutant KRas-transformed human breast cancer cell line, MDA-MB-231 [81]. To extend these findings, we evaluated the role of autophagy during migration of additional epithelial cells in which autophagy was inhibited via genetic loss-of-function of multiple ATGs essential for autophagosome formation. Stable knockdown of ATG7 or ATG12 in wild-type MCF10A mammary epithelial cells or polyoma middle T (PyMT) mouse mammary tumor cells impaired autophagy, as evidenced by the reduced lipidation of LC3 (LC3-II), a biochemical marker of autophagosome formation (Fig. S1, A and B). Similarly, autophagy was eliminated in immortalized baby mouse kidney (iBMK) cells derived from *Atg5-/-* mice (Fig. S1 C). Consistent with previous results, autophagy inhibition due to ATG depletion impaired the motility of both MCF10A cells and PyMT cells during *in vitro* scratch-wound healing assays (Fig. S1, D-G). Likewise, *Atg5-/-* iBMK cells exhibited reduced migration compared to *Atg5+/+* cells (Fig. S1, H and I). These data corroborate that autophagy promotes the motility of multiple cell types.

Next, we used MCF10A-Ras cells to precisely establish how autophagy regulates migration. Using live-cell imaging to track individual migrating cells over 3 h during wound healing, we found that autophagy-deficient cells, due to stable ATG7 or ATG12 depletion, failed to move as far as control cells, resulting in an approximately 40% reduction in migration speed upon ATG depletion (Figs. 1, A-C and S1 A; and Video 1). Because FAs generate force for movement and anchor cells to their substratum, they are established as critical determinants of migration rate in diverse cell types [95, 104-108]. Therefore, we analyzed FAs at the leading edge of wound edge cells by immunofluorescence for endogenous paxillin, a marker of FAs, to determine if cell-ECM adhesion is affected by autophagy deficiency. Measurements of FA area

showed that ATG-depletion resulted in significantly increased FA size, indicating that FAs may be stabilized in autophagy-deficient cells (Fig. 1, D and E). We similarly observed that FAs in autophagy-inhibited PyMT cells were larger than FAs in control cells (Fig. S1 J). Since optimal migration rate is achieved at intermediate levels of integrin-mediated adhesion strength [104-108], these data indicate that enhanced cell-ECM adhesion resulting from FA stabilization upon autophagy inhibition possibly contributes to reduced migration by impeding productive movement.

**Autophagy inhibition impairs FA turnover**

Because FAs are highly dynamic during migration, the FA defects observed upon autophagy inhibition may result from perturbations in FA assembly or disassembly. To establish if autophagy impacts specific aspects of FA turnover, we generated control and ATG knockdown cells expressing paxillin-mCherry, an established reporter of dynamic FAs, and used live-cell spinning disk confocal microscopy to analyze leading edge FAs during migration [101, 109]. Similar to endogenous paxillin immunostaining (Fig. 1, D and E), paxillin-mCherry-labeled FAs appeared larger in autophagy-inhibited cells, and fewer cycles of FA assembly and disassembly were apparent at the leading edge of ATG-depleted cells in comparison to autophagy-competent controls (Fig. 2 A; and Videos 2 and 3). To quantify differences in FA dynamics, we employed established methods in which fluorescence intensity profiles of paxillin-mCherry over time were fitted with a logistic function and a single exponential decay function to determine rate constants for assembly and disassembly, respectively; FA lifetime was calculated as the amount of time paxillin-mCherry fluorescence intensity remained above half its maximal value (Fig. 2 B) [100-101, 109-110]. This analysis showed that in comparison to controls, the rate of assembly was reduced by 30% and 37% for ATG7 and ATG12 knockdown, respectively, and disassembly rates decreased by 48% and 42% upon ATG7 and ATG12 depletion, respectively (Fig. 2 C). Overall, these changes led to stabilization of FAs in autophagy-deficient cells in which lifetimes

were significantly increased by 86% with ATG7 depletion and 68% with ATG12 depletion (Fig. 2 C). These results substantiate that autophagy is required for efficient leading edge FA turnover in migrating cells.

**Autophagy-deficient cells exhibit enhanced cell spreading**

In addition to affecting motility, increased stabilization of FAs is also associated with enhanced cell spreading [95, 111]. Accordingly, we performed cell spreading assays to further assess the functional impact of FA stabilization upon autophagy inhibition. We generated control and ATG knockdown cells expressing ZsGreen for tracking purposes, and using live-cell imaging, we monitored the spreading of cells upon replating over 3 h. These assays revealed that autophagy-deficient cells underwent prolonged spreading, resulting in an increased cell area compared to controls (Fig. 3 A). Quantification of the area of ZsGreen-expressing cells fixed at 1 h post-replating further confirmed that ATG-depleted cells exhibited a significant increase in cell area compared to autophagy-competent cells (Fig. 3, B and C). Together with our quantitative analysis of FAs in migrating cells, these findings point to a broader role for autophagy in modulating adhesion-dependent phenotypes.

**Autophagosomes localize to FAs during disassembly in migrating cells**

Typically, autophagy functions through the local and direct sequestration of cellular material into the forming autophagosome, which eventually fuses with lysosomes for cargo degradation [18, 102]. Accordingly, we reasoned that autophagy-dependent FA turnover may involve the close local apposition of autophagosomes with dynamic FAs during migration. To test this prediction, we generated cells co-expressing paxillin-mCherry and GFP-LC3, which marks autophagosomes, and observed that autophagosomes localized throughout the leading edge of migrating cells (Fig. 4 A; and Video 4). We enumerated adhesions targeted by GFP-LC3, defined as GFP-LC3 puncta in direct contact with paxillin-mCherry-labeled FAs, and found

that 40% of dynamic FAs were directly targeted by autophagosomes (Fig. 4, B-E; and Videos 5 and 6). Of note, these experiments may underestimate the actual number of targeted FAs due to the rapid intracellular dynamics of GFP-LC3-labeled vesicles. Additionally, during cell spreading, we similarly observed GFP-LC3 puncta to be associated with dynamic FAs throughout the periphery of the cell, further confirming that autophagosomes are locally targeted to FAs (Fig. 4 F).

To better understand the functional implication of FA-associated autophagosomes, we next determined if autophagosome targeting to FAs proceeds in a temporally specific manner. Interestingly, a limited number of targeting events occurred during FA assembly or when FAs were relatively stable, but rather, the vast majority of GFP-LC3 targeting events occurred during FA disassembly (Fig. 4, D, E, and G; and Video 6). Together with our data showing that autophagy is functionally required for FA turnover, these results suggest that autophagy impacts leading edge FAs by proximally facilitating disassembly. This autophagy-dependent FA remodeling may involve the local sequestration of FA components into the autophagosome to promote FA destabilization and disassembly.

**The selective autophagy cargo receptor NBR1 promotes cell migration and FA turnover**

Given the highly specific targeting of autophagosomes to FAs during disassembly and because FA turnover is highly coordinated to optimize migration and adhesion [97-99], we hypothesized that a tightly-controlled mechanism would be necessary to direct autophagic targeting of FAs. Additionally, given the importance of FAs in regulating growth and survival, such a mechanism would be necessary for limiting excessive autophagic targeting of FAs. Notably, FAs are large protein complexes [112], and autophagy has been shown to target large intracellular macromolecular assemblies, such as iron-containing ferritin complexes [48, 113] and midbody derivatives during the final stages of cytokinesis [59, 114]. The autophagic targeting of these structures is mediated by autophagy cargo receptors, which promote the selective

degradation of cellular substrates [47, 115]. These molecules bind cargo marked with degradation signals, most commonly ubiquitin, through their ubiquitin binding domains [116] and typically possess an LC3 interacting region (LIR) motif, which allows them to bind to LC3 and other ATG8 isoforms present on developing autophagosomes [117]. Because of these unique characteristics that allow autophagy cargo receptors to specify targeting of autophagosomes to cellular substrates, we sought to determine if they support migration and FA dynamics.

To initially establish if individual autophagy cargo receptors regulate migration, we performed scratch-wound healing assays with cells transiently depleted for several of the major known receptors, including p62/SQSTM1 (p62), NBR1, optineurin (OPTN), and nuclear dot protein 52 (NDP52). We identified NBR1 as the only cargo receptor whose knockdown significantly attenuated wound closure (Figs. 5, A and B and S2 A). To verify this result, we generated stable pools of cells with shRNA against NBR1 (Fig. S2 B). In agreement with our findings using transient, siRNA-mediated depletion, stable NBR1 knockdown also significantly inhibited migration (Fig. 5, C and D). Importantly, in contrast to ATG knockdown, NBR1 depletion did not affect basal autophagy levels (Fig. S2 C).

To further dissect the role of NBR1 in motility, we measured FA dynamics in paxillin-mCherry-expressing cells following stable NBR1 knockdown. Similar to ATG depletion, NBR1 loss-of-function decreased the rates of FA assembly and disassembly by 32% and 41%, respectively, leading to an overall 81% increase in FA lifetime compared to controls (Fig. 5, E and F; and Videos 7 and 8). Consistent with this role for NBR1 in facilitating FA turnover, endogenous NBR1 co-localized with anti-paxillin-labeled FAs, and GFP-NBR1 associated with dynamic leading edge FAs in live migrating cells (Fig. S2, D and E; and Video 9). Furthermore, NBR1-depleted ZsGreen-expressing cells underwent prolonged spreading compared to control cells and exhibited increased cell area at 1 h post-replating (Fig. S3, A-C). Collectively, these results demonstrate that NBR1 loss-of-function phenocopies the effects of autophagy inhibition on both FA turnover and adhesion-dependent processes, indicating NBR1 and autophagy may

coordinately facilitate FA remodeling through a common pathway of NBR1-mediated selective autophagy. Further, we uncover that NBR1, like autophagosomes, localizes to FAs, suggesting that NBR1-mediated selective autophagy proximally impacts FA remodeling.

**NBR1-dependent selective autophagy promotes FA disassembly**

Because NBR1 is a multidomain scaffold protein that may serve autophagy-independent functions, we next used a gain-of-function approach to better ascertain if NBR1-mediated FA turnover is associated with its role in selective autophagy. We generated cells overexpressing wild-type GFP-NBR1 or a mutant NBR1 lacking the LIR (GFP-NBR1 ΔLIR) required for binding to LC3/ATG8, thereby rendering it autophagy-incompetent [118-119] (Fig. 6 A). In contrast to wild-type GFP-NBR1, GFP-NBR1 ΔLIR was resistant to nutrient starvation-induced autophagic degradation, confirming this mutant to be autophagy-incompetent (Fig. 6 B). GFP-NBR1 was overexpressed in paxillin-mCherry cells to test if increased NBR1 was sufficient to enhance FA turnover. Compared to GFP alone, expression of GFP-NBR1 significantly increased FA turnover. Although GFP-NBR1 did not impact FA assembly, it significantly enhanced FA disassembly by 49% leading to an overall 35% decrease in FA lifetime (Fig. 6, C and D; and Video 10). In parallel, we assayed the effects of GFP-NBR1 ΔLIR expression on leading edge FA dynamics in order to interrogate whether this phenotype required the ability of NBR1 to facilitate selective autophagy. Unlike wild-type GFP-NBR1 overexpression, GFP-NBR1 ΔLIR did not significantly affect FA assembly, disassembly, or lifetime (Fig. 6, C and D; and Video 10). These results delineate a specific role for NBR1-mediated selective autophagy in regulating FA turnover by promoting FA disassembly in migrating cells. Furthermore, given the essential role of NBR1 in selectively directing substrates for autophagic targeting and our findings that autophagosomes preferentially localize to FAs during disassembly, these results corroborate a model in which autophagosomes locally sequester FA components to enable FA disassembly.

**Figure 1**

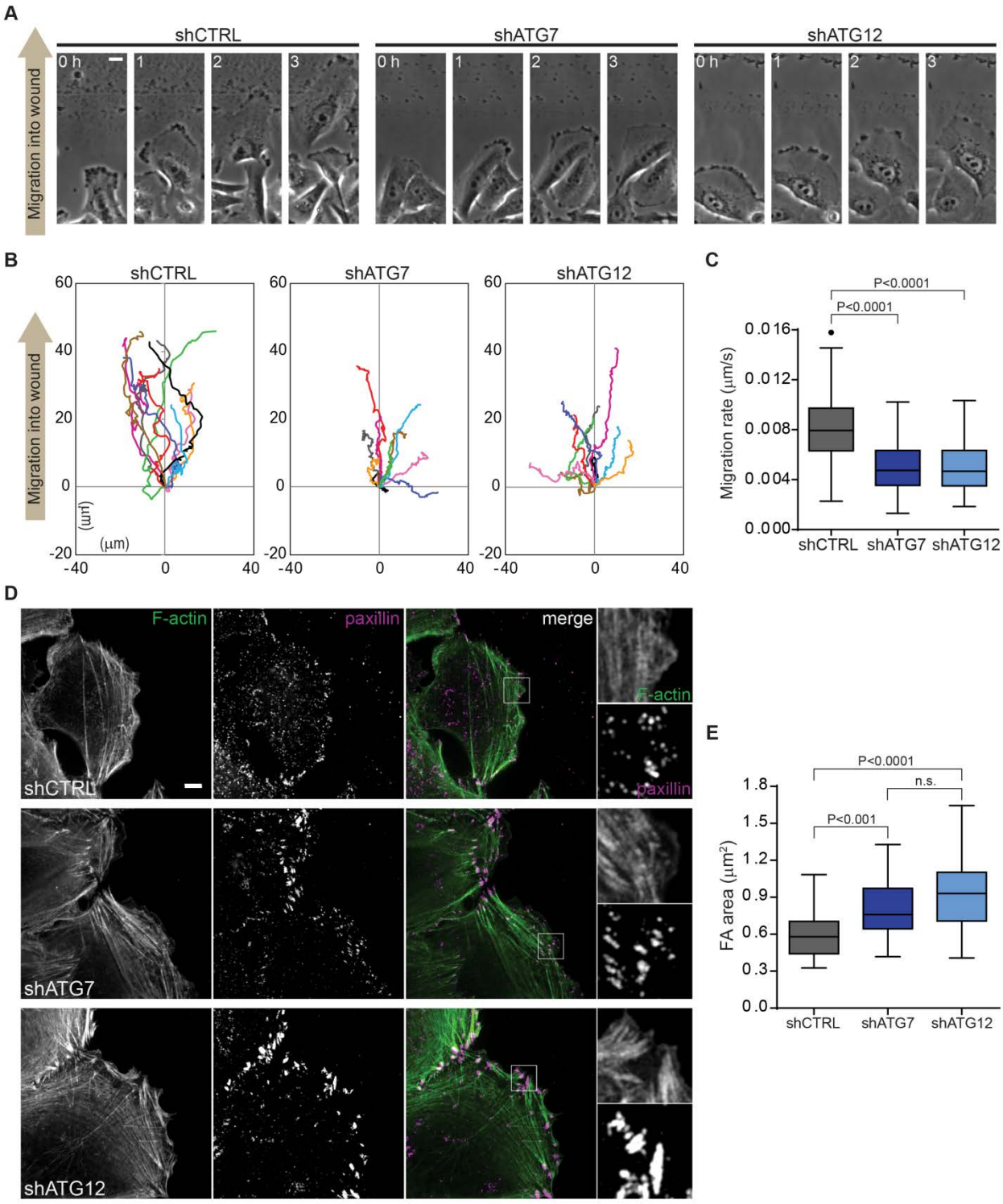
A
shCTRL
shATG7
shATG12
0 h
1
2
3
Migration into wound
B
shCTRL
shATG7
shATG12
Migration into wound
(μm)
(μm)
C
P<0.0001
P<0.0001
Migration rate (μm/s)
0.016
0.012
0.008
0.004
0.000
shCTRL
shATG7
shATG12
D
F-actin
paxillin
merge
shCTRL
shATG7
shATG12
E
P<0.0001
n.s.
P<0.001
FA area (μm²)
1.8
1.5
1.2
0.9
0.6
0.3
0.0
shCTRL
shATG7
shATG12

**Figure 1: Impaired migration rate and increased FA size in autophagy-deficient cells.** (A) Representative phase contrast microscopy time-lapse sequences of single cells expressing shCTRL (left), shATG7 (middle), or shATG12 (right) tracked over 3 h following wounding. Elapsed time (h) in top left of images. Bar, 10 μm. These images correspond to Video 1. (B) Migration paths of individual shCTRL (left), shATG7 (middle), or shATG12 (right) cells showing total distance traveled over 3 h. Cell position over time was used to generate paths and was determined by manually tracking cell nucleoli in each frame over the course of the time-lapse. n=10 representative cells shown per condition and each colored track represents an independent cell. The starting position for each cell was normalized to 0 μm, 0 μm on the x, y axes. (C) Quantification of migration rate of individual tracked cells determined as total distance traveled divided by the total time of migration ($d/t_f$-$t_0$). Data presented as median (line), first and third quartile (box), and whiskers extend to +/- 1.5 times the interquartile range. n=155 cells for shCTRL, n=121 cells for shATG7, and n=115 cells for shATG12, pooled from three independent experiments. P values calculated using a non-parametric Kruskall-Wallis test followed by Dunn's post-test. n.s.=not significant. (D) Representative immunofluorescence images of migrating wound edge cells expressing shCTRL (top), shATG7 (middle), or shATG12 (bottom) stained for endogenous F-actin (green) and paxillin (magenta) to mark FAs. Right panels show enlarged insets of boxed region in merged images. Bar, 5 μm. (E) Quantification of the area of leading edge FAs in migrating wound edge cells determined by manually outlining anti-paxillin-labeled FAs. Data presented as median (line), first and third quartile (box), and whiskers extend to +/- 1.5 times the interquartile range. n=713 FAs for shCTRL, n= 511 FAs for shATG7, and n=430 FAs for shATG12, pooled from two independent experiments. P values calculated using a non-parametric Kruskall-Wallis test followed by Dunn's post-test. n.s.=not significant.

**Figure 2**

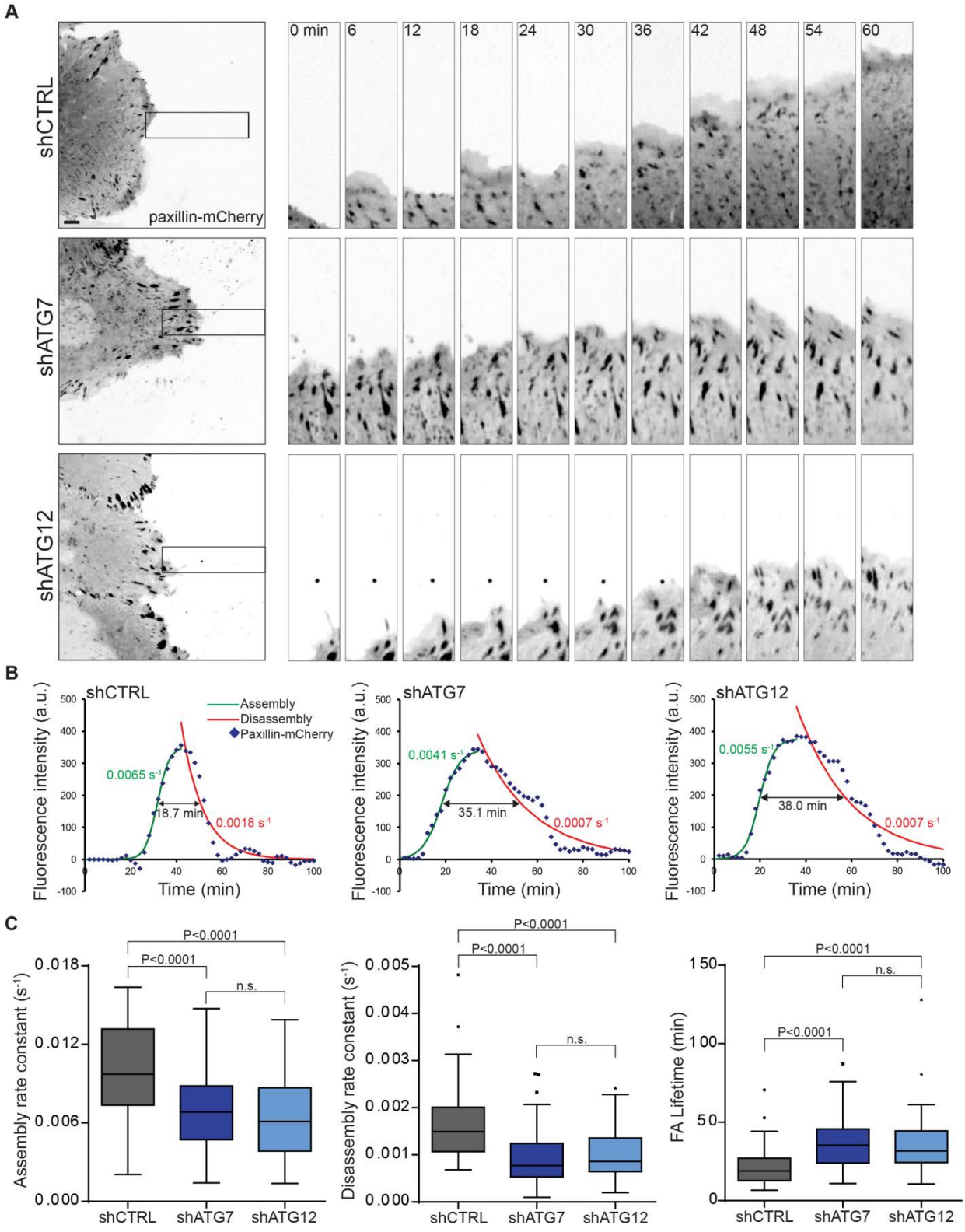
A
shCTRL
shATG7
shATG12
paxillin-mCherry
0 min
6
12
18
24
30
36
42
48
54
60
B
shCTRL
shATG7
shATG12
Assembly
Disassembly
Paxillin-mCherry
Fluorescence intensity (a.u.)
Time (min)
0.0065 s⁻¹
18.7 min
0.0018 s⁻¹
0.0041 s⁻¹
35.1 min
0.0007 s⁻¹
0.0055 s⁻¹
38.0 min
0.0007 s⁻¹
C
Assembly rate constant (s⁻¹)
Disassembly rate constant (s⁻¹)
FA Lifetime (min)
P<0.0001
n.s.
shCTRL
shATG7
shATG12

**Figure 2: Autophagy promotes FA turnover in migrating cells.** (A) Spinning disk confocal microscopy time-lapse sequences of migrating cells expressing paxillin-mCherry (black) to monitor FA dynamics. Left panels show representative cells expressing shCTRL (top), shATG7 (middle), or shATG12 (bottom). Image sequences of boxed regions have been rotated such that the cell edge with dynamic FAs is moving upwards vertically. Elapsed time (min) shown in top left. Bar, 5 μm. These images correspond to Videos 2 and 3. (B) Example plots of paxillin-mCherry fluorescence intensity (y-axis) over time (x-axis) for shCTRL (left), shATG7 (middle), and shATG12 (right) cells used for calculating FA turnover parameters in (C). Plots generated by manually tracking individual FAs over time, and each data point is a three-frame running average of intensity value. The green line represents FA assembly fitted with a logistic function, and the red line represents FA disassembly fitted with an exponential decay function. The lifetime is the time spent above half-maximum fluorescence intensity (double arrow). The values of each parameter are indicated for the specific curves shown (assembly rate constant in green, disassembly rate constant in red, and lifetime in black). (C) Quantification of assembly rate constants (left), disassembly rate constants (middle), and lifetime (right) for FAs in cells expressing shCTRL, shATG7, or shATG12. Data presented as median (line), first and third quartile (box), and whiskers extend to +/- 1.5 times the interquartile range. n=64 FAs for shCTRL, n=62 FAs for shATG7, and n=51 FAs for shATG12, pooled from four independent experiments. P values calculated using a non-parametric Kruskall-Wallis test followed by Dunn's post-test. n.s.=not significant.

**Figure 3**

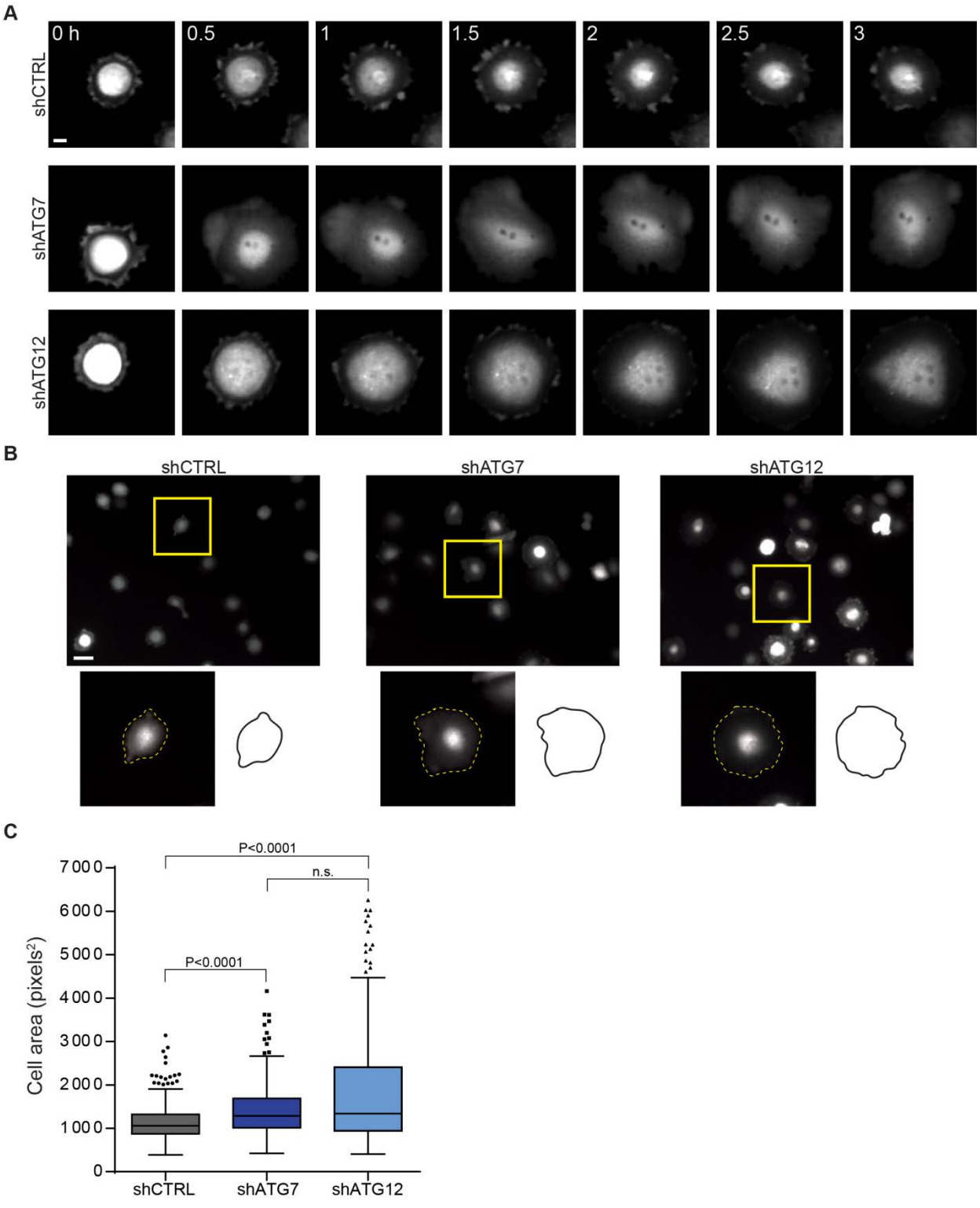
A
0 h
0.5
1
1.5
2
2.5
3
shCTRL
shATG7
shATG12
B
shCTRL
shATG7
shATG12
C
P<0.0001
n.s.
P<0.0001
Cell area (pixels²)
7000
6000
5000
4000
3000
2000
1000
0
shCTRL
shATG7
shATG12

**Figure 3: Autophagy inhibition results in enhanced cell spreading.** (A) Spinning disk confocal microscopy time-lapse sequences of cells expressing ZsGreen during spreading after replating. Representative shCTRL (top), shATG7 (middle), or shATG12 (bottom) cells shown over a 3 h time course. Elapsed time (h) indicated in top left of images. Bar, 10 μm. (B) Representative images of ZsGreen expressing cells fixed 1 h post-replating used for quantification of cell area in (C). Whole field images shown with enlarged boxed insets of individual cells at bottom left. Tracing of individual cell in inset shown at bottom right. Bar, 50 μm. (C) Quantification of area of cells fixed 1 h post-replating. Area determined by manually outlining individual ZsGreen-expressing cell borders. Data presented as median (line), first and third quartile (box), and whiskers extend to +/- 1.5 times the interquartile range. n=315 cells for shCTRL, n=351 cells for shATG7, and n=306 cells for shATG12, pooled from three independent experiments. P values were calculated using a non-parametric Kruskall-Wallis test followed by Dunn's post-test. n.s.=not significant.

**Figure 4**

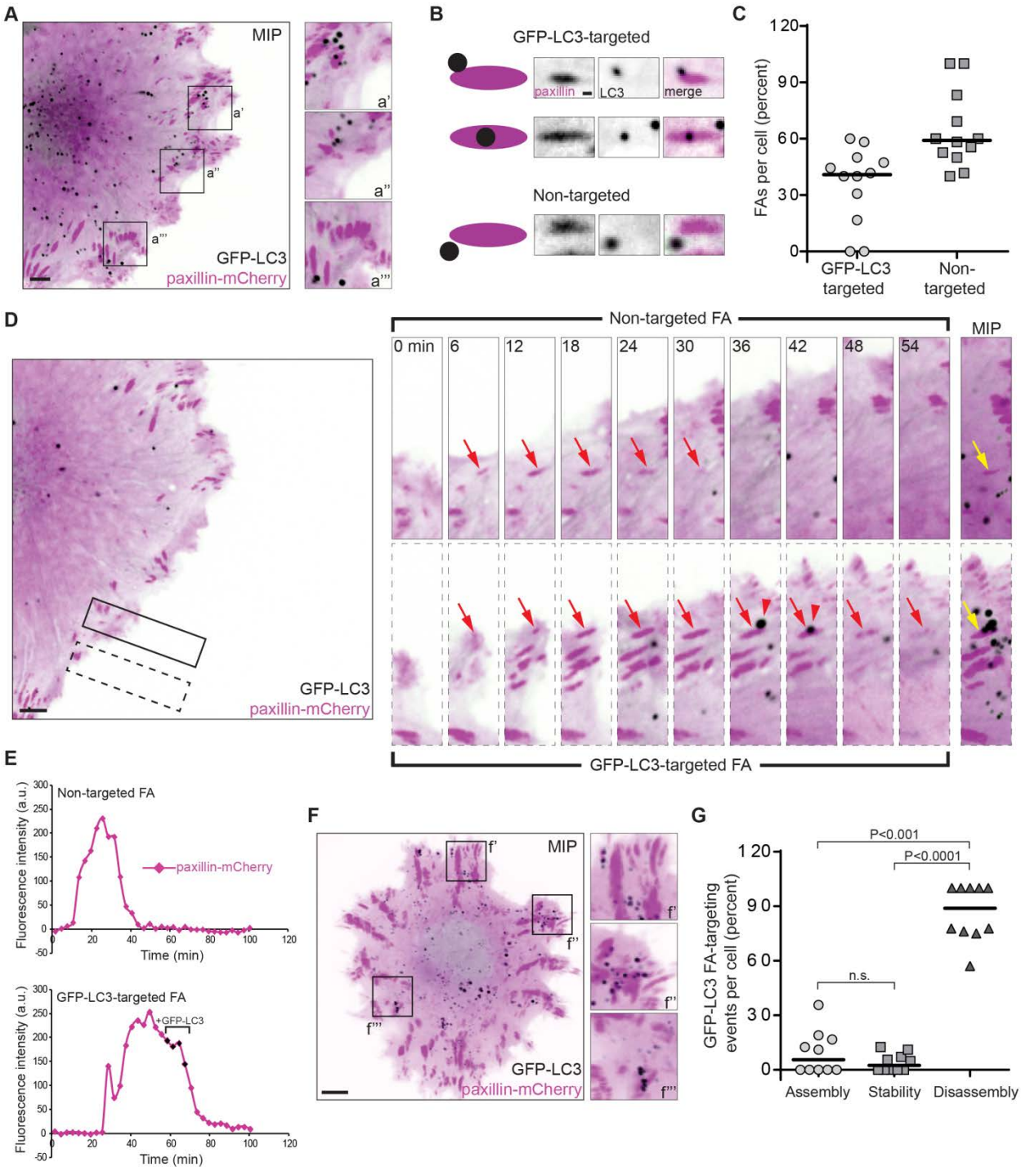
A
MIP
a'
a''
a'''
GFP-LC3
paxillin-mCherry
B
GFP-LC3-targeted
paxillin
LC3
merge
Non-targeted
C
FAs per cell (percent)
120
90
60
30
0
GFP-LC3 targeted
Non-targeted
D
GFP-LC3
paxillin-mCherry
Non-targeted FA
MIP
0 min
6
12
18
24
30
36
42
48
54
GFP-LC3-targeted FA
E
Non-targeted FA
Fluorescence intensity (a.u.)
paxillin-mCherry
Time (min)
GFP-LC3-targeted FA
+GFP-LC3
F
MIP
f'
f''
f'''
GFP-LC3
paxillin-mCherry
G
P<0.001
P<0.0001
n.s.
GFP-LC3 FA-targeting events per cell (percent)
Assembly
Stability
Disassembly

**Figure 4: Autophagosomes associate with dynamic FAs.** (A) Spinning disk confocal microscopy of a migrating cell expressing GFP-LC3 (black) to label autophagosomes and paxillin-mCherry (magenta) to label FAs. Left panel shows maximum intensity projection (MIP) of a cell over 21 min illustrating multiple associations between autophagosomes and FAs. Boxed inset areas are enlarged in right panel. Bar, 5 μm. (B) Criteria for distinguishing GFP-LC3-targeted FAs versus non-targeted FAs used for the analysis in (C). Left illustration depicts a representation of targeted-FAs (top and middle) and non-targeted FAs (bottom). Right images are examples of targeted- and non-targeted FAs. Bar, 0.5 μm. (C) Quantification of the percentage of dynamic leading edge FAs per cell targeted by autophagosomes. FAs were randomly chosen independent of the GFP-channel and then manually tracked from their appearance to disappearance for evidence of direct contact by GFP-LC3 vesicles. Scatter plots show individual single cells (n=12 total cells) and median (line), representing n=129 total FAs analyzed from two independent experiments. (D) Spinning disk confocal microscopy time-lapse sequences of representative targeted (box with dotted border, bottom) and non-targeted (box with solid border, top) FAs. Insets rotated such that leading edge is moving upwards vertically. Arrows track single FAs over time, with autophagosome targeting indicated by arrowheads. Elapsed time (min) shown in top left of images. Right-most panels show MIP for each FA (arrow) shown in the corresponding time-lapse sequence. Bar, 5 μm. (E) Representative paxillin-mCherry fluorescence intensity (y-axis) plots over time (x-axis) for the FAs shown in (D). Frames in which GFP-LC3 was in direct contact with FAs are indicated by black data points and bracketing (bottom plot). (F) Spinning disk confocal microscopy of a spreading cell expressing GFP-LC3 (black) and paxillin-mCherry (magenta). Left panel shows MIP of a cell over 40 min to show autophagosomes near dynamic FAs throughout the cell periphery during spreading. Boxed inset areas are shown enlarged at right. Bar, 5 μm. (G) Temporal analysis of GFP-LC3 targeting to FAs. The phase during which GFP-LC3 associated with FAs was determined by

counting the total number of GFP-LC3 targeting events in (C) and determining when during FA turnover each event occurred; if FAs were targeted multiple times during their lifetime, each event was independently counted. Scatter plots show individual cells (n=12 total cells) and median (line), representing n=114 total targeting events analyzed from two independent experiments. P values were calculated using a non-parametric Kruskall-Wallis test followed by Dunn's post-test. n.s.=not significant. Images throughout this figure correspond to Videos 4-6.

**Figure 5**

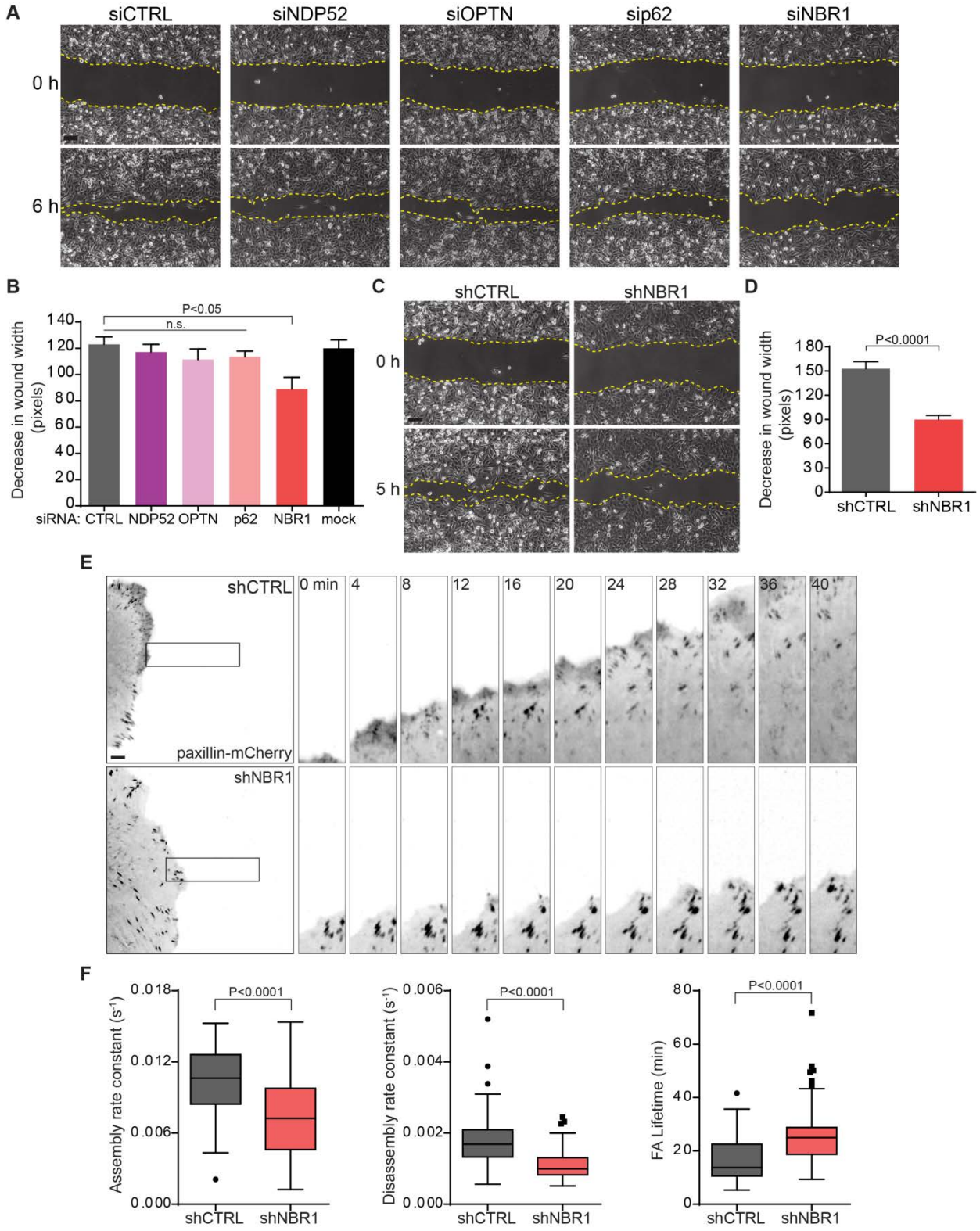
A
siCTRL
siNDP52
siOPTN
sip62
siNBR1
0 h
6 h
B
P<0.05
n.s.
Decrease in wound width (pixels)
140
120
100
80
60
40
20
0
siRNA: CTRL NDP52 OPTN p62 NBR1 mock
C
shCTRL
shNBR1
0 h
5 h
D
P<0.0001
Decrease in wound width (pixels)
180
150
120
90
60
30
0
shCTRL
shNBR1
E
shCTRL
paxillin-mCherry
shNBR1
0 min
4
8
12
16
20
24
28
32
36
40
F
P<0.0001
Assembly rate constant (s⁻¹)
0.018
0.012
0.006
0.000
shCTRL
shNBR1
P<0.0001
Disassembly rate constant (s⁻¹)
0.006
0.004
0.002
0.000
shCTRL
shNBR1
P<0.0001
FA Lifetime (min)
80
60
40
20
0
shCTRL
shNBR1

**Figure 5: NBR1 facilitates cell migration and FA turnover.** (A) Representative phase contrast microscopy images at time of wounding (0 h) and 6 h post-wounding for cells expressing control siRNA (CTRL) or siRNA against NDP52, OPTN, p62, or NBR1. Dashed yellow lines highlight wound boundaries. Bar, 100 μm. (B) Quantification of wound closure over 6 h by cells expressing indicated siRNAs (mean+s.e.m.). The decrease in wound width was determined by subtracting the final width at 6 h from the initial width at 0 h. n=8 wounds for siCTRL, n=8 wounds for siNDP52, n=8 wounds for siOPTN, n=6 wounds for sip62, n=6 wounds for siNBR1, and n=5 wounds for mock (no siRNA), pooled from four independent experiments. P values calculated using one-way ANOVA followed by Tukey's post-test. n.s.=not significant. (C) Representative phase contrast microscopy images of cells expressing shCTRL or shNBR1 at time of wounding (0 h) and at 5 h post-wounding. Dashed yellow lines highlight wound boundaries. Bar, 100 μm. (D) Quantification of wound closure over 5 h by shCTRL and shNBR1 cells (mean+s.e.m.). n=12 wounds for shCTRL and n=15 wounds for shNBR1, pooled from three independent experiments. P value determined using Student's unpaired t-test. (E) Spinning disk confocal microscopy time-lapse sequences of cells expressing paxillin-mCherry (black) to monitor FA dynamics. Left panels show representative cells expressing shCTRL (top) or shNBR1 (bottom). Image sequences of boxed regions on the right have been rotated such that the cell edge with dynamic FAs is moving upwards vertically. Elapsed time (min) in top left of images. Bar, 5 μm. These images correspond to Videos 7 and 8. (F) Quantification of FA assembly rate constants (left), disassembly rate constants (middle), and lifetime (right) for FAs in shCTRL or shNBR1 cells. Data presented as median (line), first and third quartile (box), and whiskers extend to +/- 1.5 times the interquartile range. P value calculated using a non-parametric Mann-Whitney test. n=53 FAs for shCTRL and n=58 FAs for shNBR1, pooled from three independent experiments.

**Figure 6**

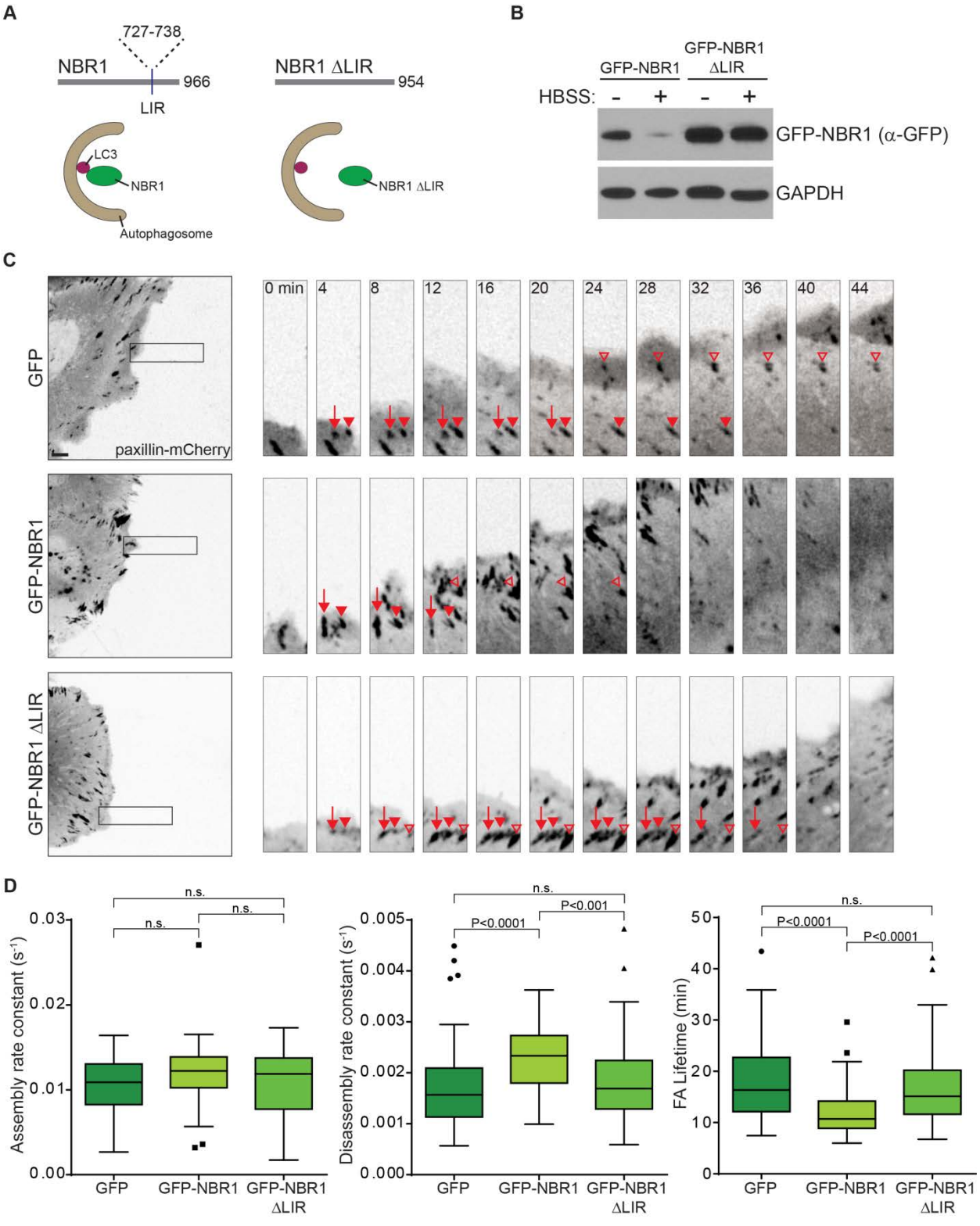
A
727-738
NBR1
966
LIR
LC3
NBR1
Autophagosome
NBR1 ΔLIR
954
NBR1 ΔLIR
B
GFP-NBR1
GFP-NBR1 ΔLIR
HBSS: - + - +
GFP-NBR1 (α-GFP)
GAPDH
C
GFP
paxillin-mCherry
GFP-NBR1
GFP-NBR1 ΔLIR
0 min
4
8
12
16
20
24
28
32
36
40
44
D
Assembly rate constant (s⁻¹)
0.03
0.02
0.01
0.00
n.s.
n.s.
n.s.
GFP
GFP-NBR1
GFP-NBR1 ΔLIR
Disassembly rate constant (s⁻¹)
0.005
0.004
0.003
0.002
0.001
0.000
n.s.
P<0.001
P<0.0001
FA Lifetime (min)
50
40
30
20
10
0
n.s.
P<0.0001
P<0.0001

**Figure 6: NBR1-mediated selective autophagy promotes FA disassembly.** (A) Schematic of wild-type NBR1 (left) and autophagy-defective NBR1 (NBR1 ΔLIR, right) resulting from deletion of the LIR (amino acids 727-738, depicted as vertical line). Bottom diagram demonstrates inability of NBR1 ΔLIR to bind LC3 (right) and be recruited into autophagosomes, unlike wild-type NBR1 (left). (B) Nutrient-starved (Hanks buffered saline solution (HBSS), 4 h) HEK-293T cells ectopically expressing wild-type GFP-NBR1 or GFP-NBR1 ΔLIR. GAPDH is loading control. (C) Spinning disk confocal microscopy time-lapse sequences of paxillin-mCherry-labeled FAs (black) in migrating cells. Left panels show representative cells expressing GFP control (top), GFP-NBR1 (middle) or GFP-NBR1 ΔLIR (bottom). Image sequences of boxed regions on the right have been rotated such that the cell edge with dynamic FAs is moving upwards vertically. Arrows, closed arrowheads, and open arrowheads track individual FAs over time. Elapsed time (min) shown in top left of images. Bar, 5 μm. These images correspond to Video 10. (D) Quantification of FA assembly rate constants (left), disassembly rate constants (middle), and lifetime (right) for FAs in cells expressing GFP control, GFP-NBR1, or GFP-NBR1 ΔLIR. Data presented as median (line), first and third quartile (box), and whiskers extend to +/- 1.5 times the interquartile range. n=67 FAs for GFP control, n=62 FAs for GFP-NBR1, and n=62 for GFP-NBR1 ΔLIR, pooled from two independent experiments. P values calculated using a non-parametric Kruskall-Wallis test followed by Dunn's post-test. n.s.=not significant.

## Figure S1

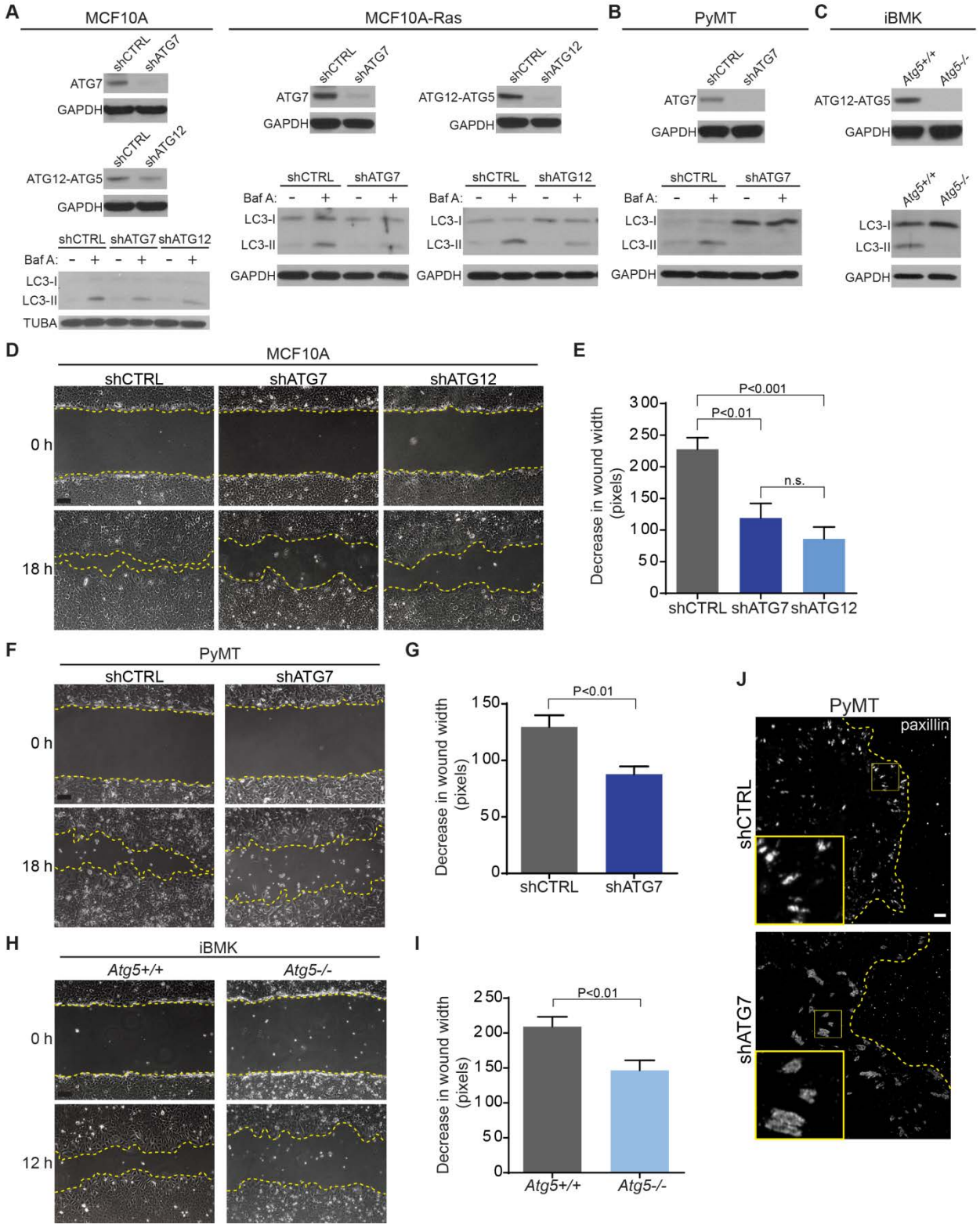
A
MCF10A
MCF10A-Ras
B
PyMT
C
iBMK
shCTRL
shATG7
shATG12
ATG7
GAPDH
ATG12-ATG5
Baf A:
LC3-I
LC3-II
TUBA
Atg5+/+
Atg5-/-
D
MCF10A
0 h
18 h
E
Decrease in wound width (pixels)
P<0.001
P<0.01
n.s.
F
PyMT
G
P<0.01
H
iBMK
12 h
I
J
paxillin

**Figure S1: Autophagy enables migration of multiple cell types.** (A) Stable shRNA-mediated depletion of ATG7 or ATG12 inhibits autophagy in wild-type MCF10A (left) and MCF10A-Ras (right) cells. ATG12 knockdown results in decrease of the ATG12-ATG5 complex required for autophagosome formation. Autophagy inhibition in ATG7- or ATG12-depleted cells shown by reduced LC3-II turnover in the presence versus absence of the lysosomal inhibitor bafilomycin A (Baf A, 20 nM for 30 min). GAPDH or TUBA ($\alpha$-tubulin) used as loading control. (B) shRNA-mediated depletion of ATG7 inhibits autophagy in PyMT cells. LC3-II turnover was assessed as in (A). GAPDH is the loading control. (C) Absence of ATG12-ATG5 and loss of autophagy (LC3-II) in iBMK cells derived from *Atg5-/-* mice but not *Atg5+/+* controls. GAPDH used as loading control. (D) Representative phase contrast microscopy images of MCF10A cells expressing indicated shRNAs at time of wounding (0 h) and at 18 h. Dashed yellow lines highlight wound boundaries. Bar, 100 $\mu$m. (E) Quantification of wound closure over 18 h for MCF10A cells (mean+s.e.m.). Decrease in wound width determined by subtracting the final width at 18 h from the initial width at 0 h. n=12 wounds for shCTRL, n=12 wounds for shATG7, and n=8 wounds for shATG12, pooled from six independent experiments. P values determined using a one-way ANOVA followed by Tukey's post-test. n.s.=not significant. (F) Representative phase contrast microscopy images of PyMT cells expressing shCTRL or shATG7 at time of wounding (0 h) and 18 h. Dashed yellow lines highlight wound boundaries. Bar, 100 $\mu$m. (G) Quantification of wound closure over 18 h for PyMT cells (mean+s.e.m.). n=16 wounds for shCTRL and n=20 wounds for shATG7, pooled from eight independent experiments. P value determined using Student's unpaired t-test. (H) Representative phase contrast microscopy images of *Atg5+/+* and *Atg5-/-* iBMK cells at time of wounding (0 h) and 12 h. Dashed yellow lines highlight wound boundaries. Bar, 100 $\mu$m. (I) Quantification of wound closure over 12 h for iBMK cells (mean+s.e.m.). n=10 wounds each for *Atg5+/+* and *Atg5-/-*, pooled from four independent experiments. P value determined using Student's unpaired t-test. (J) Representative immunofluorescence images of

wound edge PyMT cells expressing shCTRL (top) or shATG7 (bottom) stained for endogenous paxillin to mark FAs. Cell edges outlined with dotted yellow line. Enlarged insets of boxed regions are shown. Bar, 5 μm.

**Figure S2**

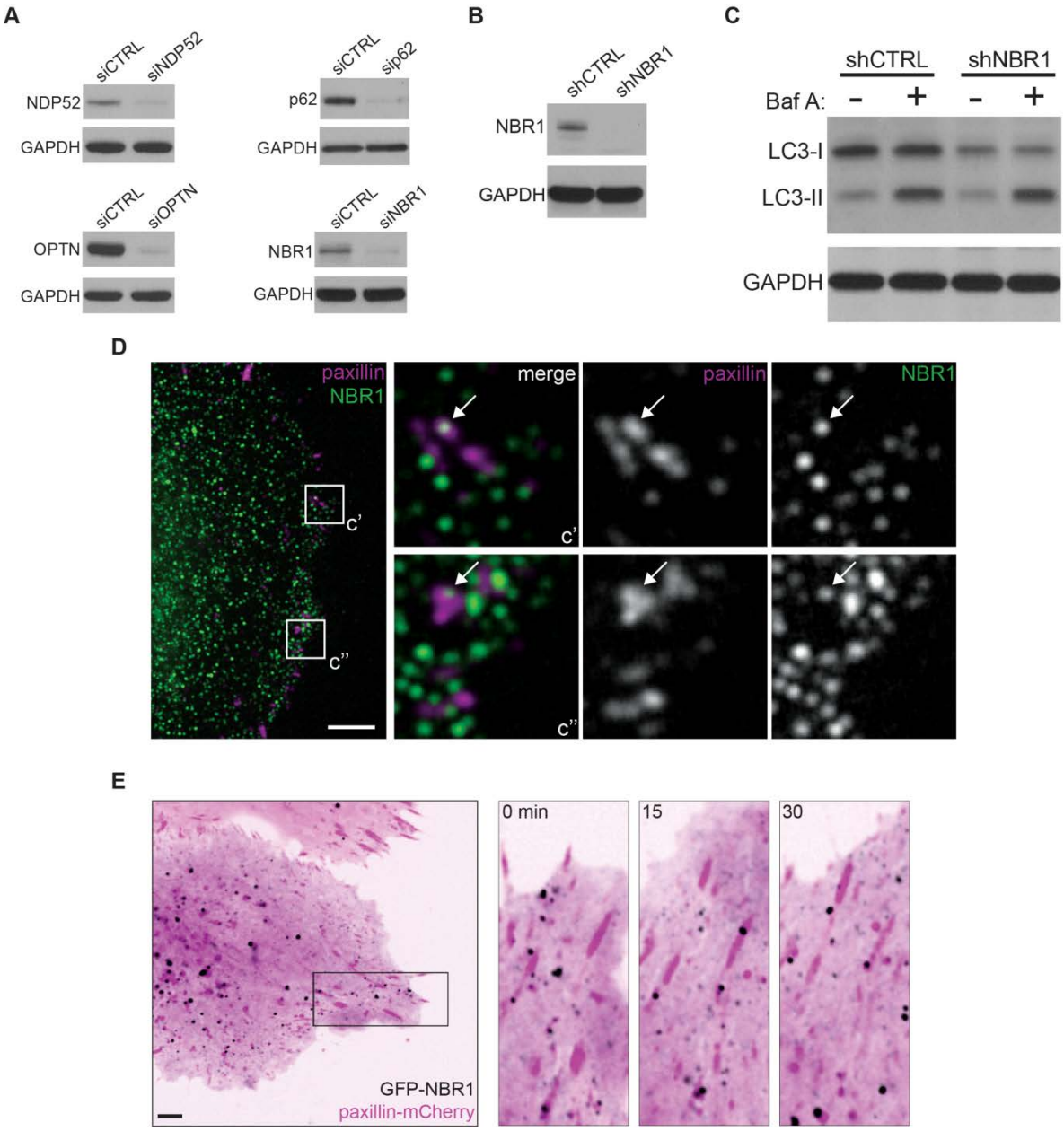
A
siCTRL
siNDP52
NDP52
GAPDH
siCTRL
sip62
p62
GAPDH
siCTRL
siOPTN
OPTN
GAPDH
siCTRL
siNBR1
NBR1
GAPDH
B
shCTRL
shNBR1
NBR1
GAPDH
C
shCTRL
shNBR1
Baf A:
- + - +
LC3-I
LC3-II
GAPDH
D
paxillin
NBR1
c'
c''
merge
paxillin
NBR1
c'
c''
E
GFP-NBR1
paxillin-mCherry
0 min
15
30

**Figure S2: Regulation of migration and FAs by the autophagy cargo receptor NBR1.** (A) siRNA-mediated depletion of the indicated autophagy cargo receptors used for scratch-wound closure assays. GAPDH is loading control. (B) shRNA knockdown of NBR1. (C) LC3-II turnover in the absence or presence of bafilomycin A (Baf A, 20 nM for 30 min). GAPDH is loading control. (D) Representative immunofluorescence images of wound edge cells stained for endogenous paxillin (magenta) to mark FAs and endogenous NBR1 (green). Whole cell merged image shown at left and enlarged boxed insets of merged and single-channel paxillin and NBR1 images shown at right. Arrow points to co-location in insets. Bar, 5 μm. (E) Spinning disk confocal microscopy of a migrating cell expressing GFP-NBR1 (black) and paxillin-mCherry (magenta). Boxed region is shown as enlarged insets to the right rotated such that the cell edge is moving upwards vertically. Elapsed time (min) indicated in top left of images. Bar, 5 μm. These images correspond to Video 9.

**Figure S3**

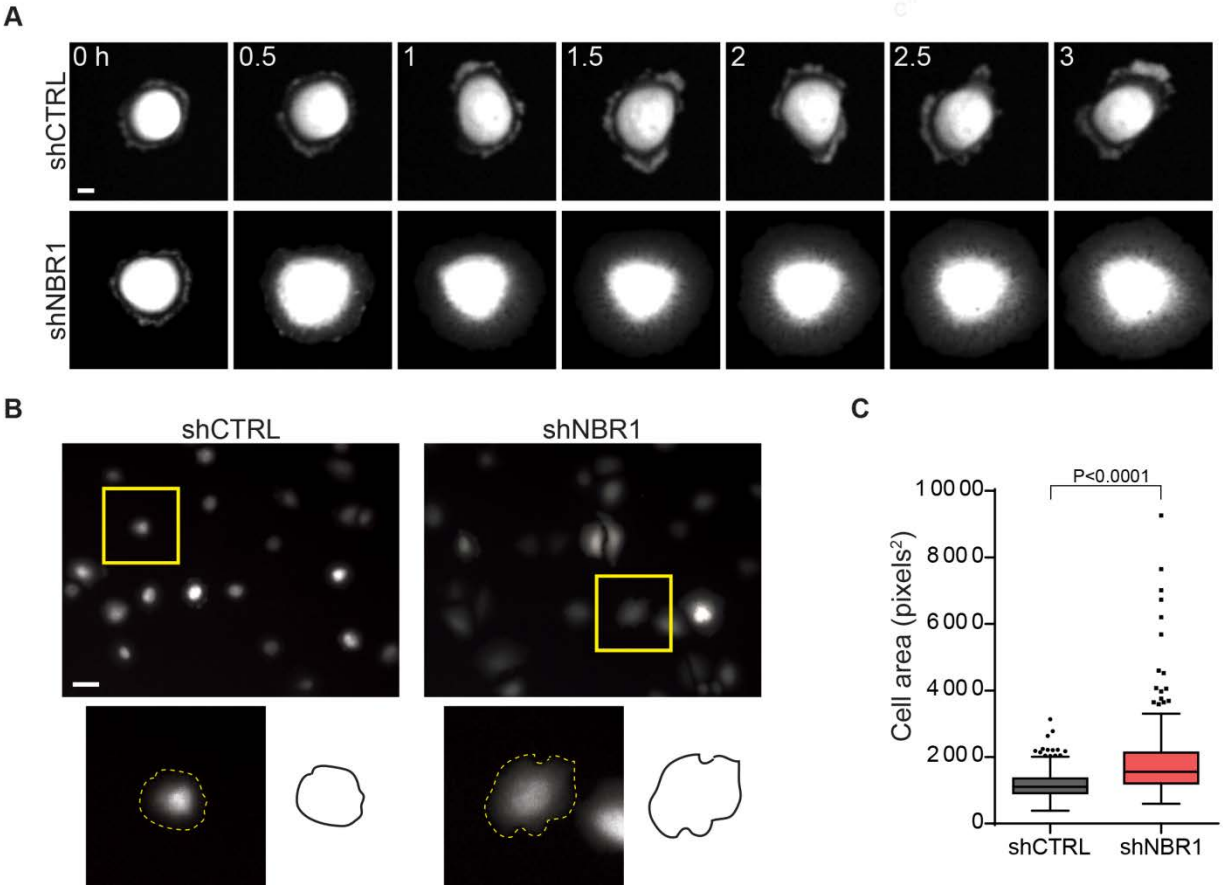
A
0 h
0.5
1
1.5
2
2.5
3
shCTRL
shNBR1
B
shCTRL
shNBR1
C
P<0.0001
Cell area (pixels²)
100 00
8 000
6 000
4 000
2 000
0
shCTRL
shNBR1

**Figure S3: NBR1 knockdown leads to enhanced cell spreading.** (A) Spinning disk confocal microscopy time-lapse sequences of cells expressing ZsGreen during spreading after replating. Representative images of shCTRL (top) and shNBR1 (bottom) cells are shown over 3 h. Elapsed time (h) indicated at top left. Bar, 10 μm. (B) Representative images of ZsGreen-labeled cells fixed at 1 h post-replating. Whole field images shown with boxed insets of individual cells enlarged at bottom left. Tracing of individual cell in inset at bottom right. Bar, 50 μm. (C) Quantification of area of shCTRL- and shNBR1-expressing cells fixed 1 h post-replating. Area determined by manually outlining individual ZsGreen-expressing cell borders. Data presented as median (line), first and third quartile (box), and whiskers extend to +/- 1.5 times the interquartile range. n=211 cells for shCTRL and n=195 cells for shNBR1, pooled from two independent experiments. Note that these experiments were run in conjunction with two out of the three experimental repeats in Fig. 3, B and C; thus, quantitative data for shCTRL from those experiments are also included as part of Fig. S3 C. P values were calculated using a non-parametric Kruskall-Wallis test followed by Dunn's post-test.

**Supplemental Video Legends**

**Video 1: Single-cell tracking of migrating shCTRL-, shATG7-, and shATG12-expressing cells.** Phase contrast microscopy of single-cell migration of shCTRL- (top), shATG7- (middle), and shATG12-expressing (bottom) cells. Images were acquired every 3 min. The video plays at 24 frames per second and is accelerated 4320 times. This video is related to Fig. 1.

**Video 2: FA dynamics in shCTRL-, shATG7-, and shATG12-expressing cells.** Spinning disk confocal microscopy of FA turnover dynamics in shCTRL- (left), shATG7- (middle), and shATG12-expressing (right) cells. FAs are marked by paxillin-mCherry (black). Images were acquired every 2 min. The video plays at 6 frames per second and is accelerated 720 times. This video is related to Fig. 2.

**Video 3: FA dynamics at the leading edge of shCTRL-, shATG7-, and shATG12-expressing cells.** Spinning disk confocal microscopy of FA turnover dynamics at the leading edge of shCTRL- (left), shATG7- (middle), and shATG12-expressing (right) cells. These are insets from the same cells shown in Video 2. FAs are marked by paxillin-mCherry (black). Images were acquired every 2 min. The video plays at 6 frames per second and is accelerated 720 times. This video is related to Fig. 2.

**Video 4: Migrating cell co-expressing GFP-LC3 and paxillin-mCherry.** Spinning disk confocal microscopy of a migrating cell expressing GFP-LC3 (black) to mark autophagosomes and paxillin-mCherry (magenta) to mark FAs. Images were acquired every 3 min. The video plays at 2 frames per second and is accelerated 360 times. This video is related to Fig. 4.

**Video 5: Dynamics of a non-targeted FA.** Spinning disk confocal microscopy of a leading edge non-targeted FA from a cell expressing GFP-LC3 (black) and paxillin-mCherry (magenta). This is an inset from the cell in Video 4. Images were acquired every 3 min. The video plays at 2 frames per second and is accelerated 360 times. This video is related to Fig. 4.

**Video 6: Dynamics of a GFP-LC3-targeted FA.** Spinning disk confocal microscopy of a leading edge GFP-LC3-targeted FA from a cell expressing GFP-LC3 (black) and paxillin-mCherry (magenta). This is an inset from the cell in Video 4. Images were acquired every 3 min. The video plays at 2 frames per second and is accelerated 360 times. This video is related to Fig. 4.

**Video 7: FA dynamics in shCTRL- and shNBR1-expressing cells.** Spinning disk confocal microscopy of FA turnover dynamics in shCTRL- (left) and shNBR1-expressing (right) cells. FAs are marked by paxillin-mCherry (black). Images were acquired every 2 min. The video plays at 6 frames per second and is accelerated 720 times. This video is related to Fig. 5.

**Video 8: FA dynamics at the leading edge of shCTRL- and shNBR1-expressing cells.** Spinning disk confocal microscopy of FA turnover dynamics at the leading edge of shCTRL- (left) and shNBR1-expressing (right) cells. These are insets from the same cells shown in Video 7. FAs are marked by paxillin-mCherry (black). Images were acquired every 2 min. The video plays at 6 frames per second and is accelerated 720 times. This video is related to Fig. 5.

**Video 9: Migrating cell co-expressing GFP-NBR1 and paxillin-mCherry.** Spinning disk confocal microscopy of the leading edge of a migrating cell expressing GFP-NBR1 (black) and paxillin-mCherry (magenta). Images were acquired every 1.5 min. The video plays at 2 frames per second and is accelerated 180 times. This video is related to Fig. S2.

**Video 10: FA dynamics at the leading edge of cells expressing GFP, GFP-NBR1, or GFP-NBR1 ΔLIR.** Spinning disk confocal microscopy of FA turnover dynamics at the leading edge of cells expressing GFP control (left), GFP-NBR1 (middle), or GFP-NBR1 ΔLIR (right). FAs are marked by paxillin-mCherry (black). Images were acquired every 2 min. The video plays at 2 frames per second and is accelerated 240 times. This video is related to Fig. 6.

## MATERIALS AND METHODS

### Cell culture

MCF10A and MCF10A-Ras mammary epithelial cells were cultured in DMEM/F12 supplemented with 5% horse serum, 20 ng/ml EGF, 0.5 μg/ml hydrocortisone, 100 ng/ml cholera toxin, 10 μg/ml insulin, penicillin, and streptomycin. PyMT mammary carcinoma cells (R221A clone [120]; a gift from Barbara Fingleton, Vanderbilt University) and HEK-293T cells were cultured in DMEM with 10% FBS, penicillin, and streptomycin. Eileen White (Rutgers University) kindly provided immortalized baby mouse kidney (iBMK) epithelial cells derived from isogenic *Atg5+/+* and *Atg5-/-* littermates [121], which were cultured in DMEM with 10% FBS, penicillin, and streptomycin. For experiments, MCF10A-Ras cells were routinely incubated in assay media (DMEM/F12, 2% horse serum, 0.5 μg/ml hydrocortisone, 100 ng/ml cholera toxin, 10 μg/ml insulin, penicillin, and streptomycin) [122]; 20 mM HEPES was added to the culture medium during live-cell imaging experiments.

### cDNA constructs and retroviral and lentiviral vectors

pBabeneo-HRas$^{V12}$, pBabepuro-GFP-LC3 (Addgene #22405), and pLenti6blast-paxillin-mCherry have been previously described [72, 81, 101, 123]. pMXsIP-GFP-NBR1 was a gift from Noboru Mizushima (Addgene #38283). pHIV-ZsGreen was provided by Bryan Welm (Addgene #18121). To generate pMXspuro-GFP, pMXspuro-GFP-NBR1, and pMXspuro-GFP-NBR1 ΔLIR, GFP alone and GFP-NBR1 were first amplified from pMXsIP-GFP-NBR1 and cloned into pcDNA3 (Life Technologies). Site directed mutagenesis was then performed for deletion of amino acids 727-738 in NBR1 (NBR1 ΔLIR); GFP, GFP-NBR1, and GFP-NBR1 ΔLIR were subsequently amplified from pcDNA3 and subcloned into BamHI/XhoI sites of pMXspuro for

retroviral expression [124]. VSV-G pseudotyped retrovirus and lentivirus were generated, and cells were infected as previously described [72].

**RNA interference:**

For stable RNA interference, pLKO.1puro lentiviral plasmids with non-targeting shRNA or shRNA against ATG7 (human: NM_006395, mouse: NM_028835), human ATG12 (NM_004707), and human NBR1 (NM_031858) were purchased from Sigma Aldrich. The target sequence for shRNA against human ATG7 (TRCN0000007587) is: CCCAGCTATTGGAACACTGTA, against human ATG12 (TRCN0000007394) is: TGGAACTCTCTATGAGTGTTT, against mouse ATG7 (TRCN0000092163) is: CCAGCTCTGAACTCAATAATA, and against human NBR1 (TRCN0000123161) is: GCCAGGAACCAAGTTTATCAA. shRNA lentivirus was produced and pools of stable shRNA-expressing cell lines were generated as previously described [81].

For siRNA-mediated knockdown, ON-TARGETplus SMARTpool siRNAs against human SQSTM1/p62 (L-010230-00), human NBR1 (L-010522-00), human OPTN (L-016269-00), and human CALCOCO2/NDP52 (L-010637-00) were purchased from Dharmacon. The Amaxa Nucleofector device (Lonza) was used to transfect cells using program T-024 and nucleofector kit V according to manufacturer's instructions.

**Antibodies, immunoblotting, and immunofluorescence**

The following antibodies were used for immunoblotting: anti-ATG7 for human (Santa Cruz Biotechnology sc-8668, 1:200), anti-ATG12 for human (Cell Signaling 2010, 1:500), anti-ATG7 for mouse (Cell Signaling 2631, 1:500), anti-ATG12 for mouse (Cell Signaling 2011, 1:500), anti-p62/SQSTM1 (Progen Biotechnik GP62-C, 1:1000), anti-NBR1 (Abnova H00004077-A01, 1:500), anti-OPTN (Abcam ab23666, 1:1000), anti-CALCOCO2/NDP52 (Abcam 68588, 1:500), anti-GFP (Santa Cruz Biotechnology 390394, 1:500), anti-TUBA (Sigma

Aldrich T6199, 1:5000), and anti-GAPDH (Millipore AB2302, 1:5000). A rabbit polyclonal antibody against MAP1LC3 has been previously described [72] and is now commercially available (Millipore ABC232, 1:1000).

For immunoblot analysis, cells were lysed in RIPA buffer (1% Triton X-100, 1% sodium deoxycholate, 0.1% SDS, 25 mM Tris, pH 7.6, 150 mM NaCl) plus protease inhibitor cocktail (Sigma Aldrich), 10 mM NaF, 10 mM β-glycerophosphate, 1 mM $Na_3VO_4$, 10 nM calyculin A, 0.5 mM PMSF, 10 μg/ml E64d, and 10 μg/ml pepstatin A. Lysates were freeze-thawed at -80°C, cleared by centrifugation for 30 min at 4°C, boiled in sample buffer, resolved by SDS-PAGE, and transferred to PVDF membrane. Membranes were blocked for 1 h in 5% milk in PBS with 0.1% Tween 20 (PBST), incubated in primary antibody overnight at 4°C, washed, incubated for 1 h at room temperature with HRP-conjugated secondary antibodies (Jackson Immunoresearch, 1:5000), washed, and visualized via enhanced chemiluminescence (Thermo Scientific).

For immunofluorescence, anti-paxillin (BD Biosciences 610619, 1:200) and anti-NBR1 (Novus 71703, 1:200) were used. Alexa Fluor 488-conjugated phalloidin (Life Technologies A12379, 1:200) was used for imaging the F-actin cytoskeleton. Cells were fixed with 4% PFA for 20 min at room temperature, permeabilized with 0.5% Triton X-100 in PBS, rinsed with PBS-glycine, and blocked overnight at 4°C in blocking buffer (10% goat serum and 0.2% Triton X-100 in PBS). Cells were incubated with primary antibodies for 1 h at room temperature, washed, incubated with Alexa Fluor-conjugated secondary antibodies (Life Technologies, 1:500) for 40 min at room temperature, washed, and mounted using Prolong Gold Anti-Fade mounting medium (Life Technologies).

**Microscopy**

Static phase contrast and epi-fluorescence images were obtained using an Axiovert 200 microscope (Carl Zeiss) with a 10x (NA: 0.25) or 20x (NA: 0.4) objective, Spot RT camera

(Diagnostic Instruments), and mercury lamp. Images were acquired using MetaMorph software (v6.0). Phase contrast microscopy time-lapse sequences were acquired on a TE 2000 inverted microscope stand (Nikon) with a CoolSNAP HQ2 scientific grade interline CCD camera (Photometrics) and a 40x (NA: 0.6) objective (CFI Plan Fluor ELWD DM, Nikon) housed in an environmentally controlled chamber at 37$^{o}$C. Microscope hardware and image acquisition were controlled by NIS-Elements software (Nikon).

Spinning disk confocal imaging was performed as previously described [101, 109] using an environmentally controlled Nikon TI inverted microscope stand (Nikon) equipped with a Borealis-modified Yokogawa CSU-X1 confocal head (Spectral Applied Research), solid-state 488 nm and 561 nm lasers, and a Clara cooled scientific grade interline CCD camera (Andor). Intracellular fluorescent-tagged protein dynamics in live cells were imaged at 37°C using a 60x (NA: 1.49) objective (CFI Apochromat TIRF; Nikon) and immunofluorescence images were acquired using a 100x (NA: 1.49) objective (CFI Aprochromat, Nikon). Live-cell spreading of ZsGreen cells was imaged at 37°C using a 10x (NA: 0.45) objective (CFI Plan Apochromat, Nikon). Microscope hardware was controlled with NIS-Elements.

For analysis of all microscopy images, raw image data were used. Details of image analysis for each experimental technique are described in the sections below.

**Scratch-wound healing migration assay**

For assessment of wound healing by different cell types, monolayers were grown to confluency and incubated in the following media: assay media supplemented with 5 ng/ml EGF for wild-type MCF10A cells, DMEM with 2% FBS, 50 ng/ml EGF, penicillin, and streptomycin for PyMT cells, and DMEM with 2% FBS, penicillin, and streptomycin for iBMK cells. The proliferation inhibitor mitomycin C (1 μg/ml) was added to the cultures during assays. Confluent monolayers were wounded using a 200 μl pipette tip, washed several times to remove cell

debris, and imaged at time of wounding (0 h) and the indicated time points. Wound widths were determined using MetaMorph software and were taken as the average of 6-9 measurements across the wound; to account for differences in starting wound width, data is reported as the decrease in wound width calculated by subtracting the final width from the initial width.

For live-cell phase contrast imaging of migrating MCF10A-Ras cells, cells were grown to confluency on 3.5 cm glass bottom dishes (Mattek), incubated in assay media, and wounded. Image fields were randomly chosen along the length of the wound, and images were acquired every 3 min for 3 h. Single-cell tracking analysis was performed in NIS-Elements by randomly choosing 1-2 cells per image field and using the "Tracking" feature to manually track cell nucleoli (discerned as dark spots in nucleus) for each frame over the time course; time and position data were then used to create single-cell migration paths and calculate migration speed as the total distance traveled divided by total time ($d/t_f$-$t_0$) for each cell over 3 h.

**Cell spreading assay**

Coverslips in 24-well dishes and glass bottom 6-well dishes (Mattek) were prepared by coating overnight at 4$^o$C with 10 μg/ml fibronectin in PBS and then blocking with 1% BSA in DMEM/F12 for 30 min at 37$^o$C. Subconfluent monolayers of MCF10A-Ras cells expressing ZsGreen were incubated overnight in assay media, harvested with fresh aliquots of 0.05% trypsin/EDTA diluted 1:1 with PBS, and sparsely plated in assay media. To synchronize attachment and initiation of spreading, plates were spun at 300 rpm in a swinging bucket rotor for 5 min immediately upon plating cells. For live-cell confocal imaging of spreading, cells in 6-well dishes were imaged every 5 min for 3 h. Cells on coverslips were incubated for 1 h, fixed in 4% PFA for 20 min at room temperature, and stored in PBS for imaging; epi-fluorescence images of ZsGreen-expressing cells were used to quantify cell area using Image J by manually outlining cell borders. For each experiment, two coverslips per condition were plated and four

random fields per coverslip were imaged. All cells entirely present in each image field were measured.

**Focal adhesion size analysis**

MCF10A-Ras cells were plated at confluency in assay media on coverslips coated with 10 μg/ml fibronectin, wounded, and fixed 4-6 h post-wounding for anti-paxillin immunostaining. Confocal images of migrating cells were acquired randomly along the wound edge, and FAs at the leading edge of cells were manually outlined for area measurements using NIS-Elements. FAs from 1-3 cells were measured in each field and the average area of FAs per field was determined and plotted.

**Focal adhesion turnover assay and analysis**

Analysis of dynamic FA turnover in live cells was performed as previously described [101, 109]. Briefly, MCF10A-Ras cells expressing paxillin-mCherry were plated at confluency in assay media on 3.5 cm glass bottom dishes coated with 10 μg/ml fibronectin and wounded. 15-25 image fields were taken along the wound edge, and cells were imaged every 2-3 minutes for 1.5-3 h. For analysis, FAs were randomly chosen and 3-5 FAs were measured per cell; only FAs that could be tracked completely from their appearance through disappearance were measured. To track FAs, the Bezier ROI tool was used to manually outline individual FAs and was redrawn in each frame as necessary over time if the FA significantly changed in size or location. The “Time Measurement” feature in NIS-Elements was used to generate fluorescence intensity data for each tracked FA, and background intensity was similarly determined using a duplicated ROI placed adjacent to the FA. Background corrected intensity values were then used to generate smoothed fluorescence intensity curve plots of paxillin-mCherry for calculation

of FA assembly rate constant, disassembly rate constant, and lifetime as detailed previously [101, 109].

**Analysis of GFP-LC3 targeting to focal adhesions in live cells**

MCF10A-Ras cells co-expressing GFP-LC3 and paxillin-mCherry were imaged every 3 min during migration as described above for analysis of FA turnover. For enumeration of GFP-LC3 targeting to FAs, 5-10 FAs were first randomly chosen per cell independent of the GFP-channel, and then, the number of GFP-LC3 vesicles that associated with each FA was counted. Note that targeting was strictly defined as observable physical contact of GFP-LC3 vesicles with FAs (Fig. 4 B). Multiple targeting events were counted if the FA was targeted more than once over its lifetime or by multiple vesicles at the same time. Then, FAs were tracked and measured as described above for generation of paxillin-mCherry fluorescence intensity plots to delineate assembly, stability, and disassembly phases of each targeted FA to determine the phase during which GFP-LC3 targeting events occurred. Qualitative live-cell analysis of GFP-LC3 association with dynamic FAs during spreading was performed by imaging cells within 30 min of plating at 1 min intervals.

**Image processing**

All image analysis was performed on raw image data; however, for presentation purposes, images were processed using established methods [101]. In NIS-Elements, 14-bit spinning disk confocal microscopy time-lapse sequences of paxillin-mCherry were corrected for photobleaching over time using the “Equalize Intensity in Time” tool, and reduction of pixel noise and enhancement of contrast were performed using a low pass filter and unsharp mask, respectively. Images were then linearly adjusted as needed for brightness and contrast and converted to 8 bit. “Complement Colors” was used to contrast invert images for visualization of

black FAs on a white background. Throughout figures, leading edge inset areas are cropped and rotated for closer visualization of FA dynamics.

To generate two-color black/magenta images as previously described [101] of GFP-LC3 and paxillin-mCherry or GFP-NBR1 and paxillin-mCherry, the GFP and mCherry channels were first separated and processed individually to 8 bit images as detailed above. Next, the images were added using ND Image Arithmetics: GFP + mCherry, and subsequently combined by merging channels (Red: GFP, Green: GFP+mCherry (from ND Arithmetics), Blue: GFP). The merged image was then contrast inverted using "Complement Colors" to create black/magenta overlays with magenta FAs and black vesicles on a white background.

Fixed dual color immunofluorescence images of FAs and F-actin or NBR1 were processed to 8 bit as described above, and green/magenta overlays were created in NIS-Elements using merge channels (Red: 561 nm, Green: 488 nm, Blue: 561 nm). Finally, both phase contrast and epi-fluorescence images were linearly brightness and contrast adjusted to better discern cell bodies and outlines in MetaMorph or Image J.

**Statistical analysis**

All statistical analyses were performed using GraphPad Prism 6. The normality of the distribution of data sets was determined by a Shapiro-Wilk normality test ($P<0.05$ indicating a non-normal distribution); for data sets in which the sample size was not large enough ($n\leq6$) for determination of normality, a normal distribution was assumed. For normal distributions, groups were compared using Student's unpaired t-test or one-way ANOVA followed by Tukey's post-test for multiple comparisons. For non-parametric statistics, a Mann-Whitney test or Kruskall-Wallis test followed by Dunn's post-test for multiple comparisons was used. $P<0.05$ was considered to be significant for all tests.

**ACKNOWLEDGEMENTS**

Confocal microscopy and image analysis were performed in the Biological Imaging Development Center at UCSF. We thank Dean Sheppard and Nilgun Reed for advice on spreading adhesion assays. Grant support to J.D. includes NIH (CA126792, CA188404), DOD BCRP (W81XWH-11-1-0130 and W81XWH-12-1-0505), and Samuel Waxman Cancer Research Foundation. Grant support to T.W. includes NIH (GM079139 and S10 RR26758). C.M.K. is supported by NIH pre-doctoral fellowship F31CA167905, and J.G. is supported by NSF Graduate Student Fellowship (DGE-1144247). The authors declare no competing financial interests.

# CHAPTER 3

## Autophagy suppresses metastasis

**The following chapter describes unpublished work.**

**Contributions:** I performed all the mouse experiments presented in this chapter. In addition, Kimberly Woo performed the H&E quantification, as well as immunostaining and analysis of proliferation and apoptosis for experiments in Figures 2 and 4. I generated all other data shown here. The Mouse Pathology Core provided support for sectioning and H&E staining of lung tissue. Jay Debnath supervised the project.

## INTRODUCTION

The metastatic cascade involves a complex series of events that culminate in the growth of secondary tumors, or metastases, at organ sites distant from the primary tumor. Contrary to traditional thought, it is now widely appreciated that dissemination of tumor cells likely begins early, even before primary tumors exhibit an overtly invasive phenotype. In multiple mouse models of breast cancer and during human breast cancer, DTCs can be detected in lung and bone marrow during atypical ductal hyperplasia and ductal carcincoma *in situ* stages[125]. Additionally, cultivation of a pre-metastatic niche by tumor-derived secreted factors at the metastatic organ also begins during the earliest phases of primary tumorigenesis[126]. Indeed, these seminal findings have engendered the more contemporary school of thought that understanding these events associated with the evolution of metastases at the distant organ is critically important for therapeutically targeting metastatic disease.

Given our additional knowledge that clinically, metastatic disease may not present for years to even decades following primary tumor detection and treatment, these findings that preparations for metastasis begin early implicate processes associated with metastatic seeding and eventual outgrowth as arguably some of the most crucial for the success of metastasis. In fact, these particular steps have even been proposed to be the most rate-limiting during the formation of metastasis[127-128]. Accordingly, while these events are certainly not solely responsible for completion of metastasis, there is a compelling rationale for focusing on clinical targeting of these steps of the metastatic cascade. For example, though targeting of primary tumor invasion is without a doubt necessary to halt dissemination, therapeutically intervening at this stage alone may prove futile if CTCs and DTCs have already spread throughout the body.

Although there is abundant evidence suggesting autophagy may be important throughout the entire metastatic process, based on this potential promise that therapies targeting disseminated disease may hold to treat metastasis, we sought to determine how

autophagy would functionally impact establishment of macrometastases specifically at the metastatic site. We demonstrate that inhibition of autophagy potentiates, rather than attenuates, lung metastasis of mammary carcinoma tumor cells. In addition, we find that overall, the growth and survival of macrometastases is not affected by autophagy, indicating that, functionally, autophagy regulates lung colonization events preceding the rapid growth phase of overt lung tumors, such as those associated with metastatic seeding and/or the ability of DTCs to initiate outgrowth. Finally, we propose that this increase in metastasis by autophagy-deficient cells may be mechanistically linked to the accumulation of the autophagy cargo receptor NBR1 upon autophagy inhibition.

## RESULTS

### Autophagy supports metastatic phenotypes of mouse mammary carcinoma cells *in vitro*

To investigate the contribution of autophagy to metastasis, we utilized a previously established cell line (clone R221A) derived from a spontaneous MMTV-polyoma middle T (PyMT)-driven mammary tumor[120]. The MMTV-PyMT mouse model of breast cancer has been well characterized to mimic progression of human disease, and because it is one of the few models in which tumor cells robustly metastasize to lung, it has been used extensively for studies of breast cancer metastasis, making it an appropriate model for studies of autophagy-dependent metastasis[129-130]. Stable knockdown of ATG7, an essential autophagy gene, in these cells led to inhibition of autophagy as shown by decreased formation of LC3-II, a marker of autophagosomes (Chapter 2, Fig. S1 B and Fig. 1 A).

Because the role of autophagy during MMTV-PyMT metastasis is unknown, we first verified whether autophagy is required for metastatic phenotypes in these cells. In agreement with our previous findings, we found that autophagy is potently induced in R221A cells upon substratum detachment[30, 55, 72]. Compared to adherent cultures, suspended R221A cells have increased levels of LC3-II in the presence of lysosomal inhibitors, indicating increased autophagosome formation and autophagic flux during adhesion-independent culture (Fig. 1 A). To determine if autophagy is required for resistance to anoikis of detached R221A cells, we assessed apoptosis in suspended cultures of autophagy-competent and –deficient cells and found that ATG7 depletion compromised the survival of R221A cells, as shown by increased levels of the apoptosis marker cleaved caspase-3 (Fig. 1 B). As expected, this correlated with a marked reduction in autophagy induction during suspension in ATG7-depleted cells (Fig. 1 A). Furthermore, as described in Chapter 2, autophagy inhibition slows the motility of these cells, which is associated with the formation of enlarged FAs (Chapter 2, Fig. S1, F-G and J). Since resistance to anoikis, migration, and adhesion may all be critical for seeding, survival, and

growth at the metastatic organ, collectively, these results corroborating that autophagy supports multiple metastatic phenotypes of PyMT mammary tumor cells hint at a critical role for autophagy in dictating their capacity for metastatic colonization.

**Autophagy inhibits lung metastasis**

Experimental models of metastasis in which tumor cells are intravenously inoculated into the host circulation to bypass the earliest steps of metastasis associated with primary tumor invasion and migration are commonly utilized to robustly assess events associated with colonization of the metastatic organ, such as extravasation and survival and growth of DTCs. Accordingly, we employed an experimental model of lung metastasis to test the prediction that autophagy impacts lung metastasis of R221A cells following injection into the lateral tail vein (Fig. 2 A). Analysis of lung metastases in mice injected with control or ATG7 knockdown R221A cells at two weeks post-injection showed that autophagy inhibition enhanced metastasis (Fig. 2 B). Quantification of lung H&E revealed an increase in both the number and size of metastases arising from autophagy-deficient cells (Fig. 2, C and D). Additionally, we verified that ATG7-depleted cells cultured *ex vivo* from lung metastases maintained autophagy inhibition (Fig. 2 E). Thus, despite evidence suggesting that autophagy functions largely to support metastasis promoting phenotypes, this unexpected result demonstrates that autophagy acts as a metastasis inhibitor.

Furthermore, to confirm the relevance of this finding to the overall process of metastasis, we also determined if autophagy attenuates spontaneous lung metastasis from the primary tumor site (Fig. 3 A). Control and autophagy-deficient cells were orthotopically transplanted into the mammary fat pad of wild-type, syngeneic FVB/n hosts and metastasis was quantified. Similar to our findings using the experimental metastasis model, we found that during spontaneous metastasis, ATG7-depleted cells gave rise to an increased number of lung metastases (Fig. 3, B and C). Of note, no differences in primary tumor growth were noted

among control and ATG7 knockdown cells, supporting that the increased metastasis was not secondary to changes in primary tumor growth (Fig. 3 E). In addition, both lung tumor cells cultured *ex vivo* and *in vivo* mammary tumors exhibited decreased autophagy with ATG7 knockdown (Fig. 3, D and F). Importantly, these findings further substantiate that autophagy functions as a metastasis suppressor in a more pathological context.

**Autophagy does not impact growth or viability of macrometastases**

We hypothesized that differences in the metastatic potential of autophagy-competent and autophagy-inhibited cells might be due to decreased viability, enhanced growth, or both of ATG7 knockdown cells during experimental metastasis. Therefore, we assessed proliferation and apoptosis in macrometastases at two weeks post-injection from representative lung sections of mice injected with control or ATG7-depleted cells by immunostaining for phospho-histone H3 to assess proliferation and cleaved caspase-3 to measure apoptosis (Fig. 4, A and C). However, quantification of the percentage of proliferative or apoptotic cells per metastatic lung lesion showed that there were no differences in the growth or survival of these cells (Fig. 4, B and D). These findings indicate that autophagy deficiency may functionally promote metastasis during stages prior to sustained growth of established macrometastases, such as seeding or initiation of outgrowth.

**NBR1 supports lung metastasis**

Cell-matrix adhesion is a well established promoter of metastasis. In particular, activation of ERK downstream of integrin receptors and FAK induces pro-growth signals that drive metastatic colonization[62, 131]. Moreover, integrin-mediated adhesion can facilitate metastasis by promoting attachment to platelets and the endothelium, thereby enabling seeding[5, 60]. Therefore, we reasoned that enhanced cell-matrix adhesion upon autophagy

inhibition in R221A cells (reported in Chapter 2) could mechanistically lead to enhanced metastasis.

We identified NBR1 as a key regulator of autophagy-dependent focal adhesion regulation. Similar to autophagy inhibition, knockdown of NBR1 also stabilizes cell-matrix adhesion, and this is dependent on its role in mediating selective autophagy (Chapter 2, Fig. 5). Thus, to address the possibility that regulation of adhesion by autophagy impacts lung metastasis of R221A cells, we focused on determining if, like autophagy, NBR1 also suppresses experimental lung metastasis. NBR1 was depleted from R221A cells via stable expression of two independent shRNAs, and then control and NBR1 knockdown cells were inoculated into the lateral tail vein (Fig. 5 A). Upon quantification of lung H&E two weeks post-injection, surprisingly, we found that unlike autophagy inhibition, NBR1 loss-of-function, significantly inhibited metastasis (Fig. 5 B). This was characterized by a decrease in both the size and number of metastases (Fig. 5, C and D). These data demonstrate that NBR1 functions to promote metastasis.

Intriguingly, NBR1 can inhibit p38 MAPK signaling, which is a known promoter of metastatic dormancy[63-64]. Although we cannot rule out that NBR1 does not regulate cell-matrix adhesion in R221A cells or that autophagy-dependent regulation of integrin-based adhesion does not mediate *in vivo* metastasis, in conjunction with the finding that autophagy inhibition exacerbates metastasis, these preliminary results point to a model in which NBR1 accumulation upon autophagy inhibition may be sufficient to enhance metastasis, potentially through downregulation of p38 MAPK signaling. In agreement, we have observed that NBR1 levels are elevated in autophagy-deficient R221A cells (Fig. 5 E). This possible model is further supported by our cell fate analyses demonstrating that autophagy most likely functionally impacts earlier phases of metastatic colonization, which could include escape from quiescence or dormancy upon lung seeding. Ongoing work is now testing this unexpected role for NBR1 in functioning as

a novel pro-metastatic factor to define the molecular basis of metastasis suppression by autophagy.

**Figure 1**

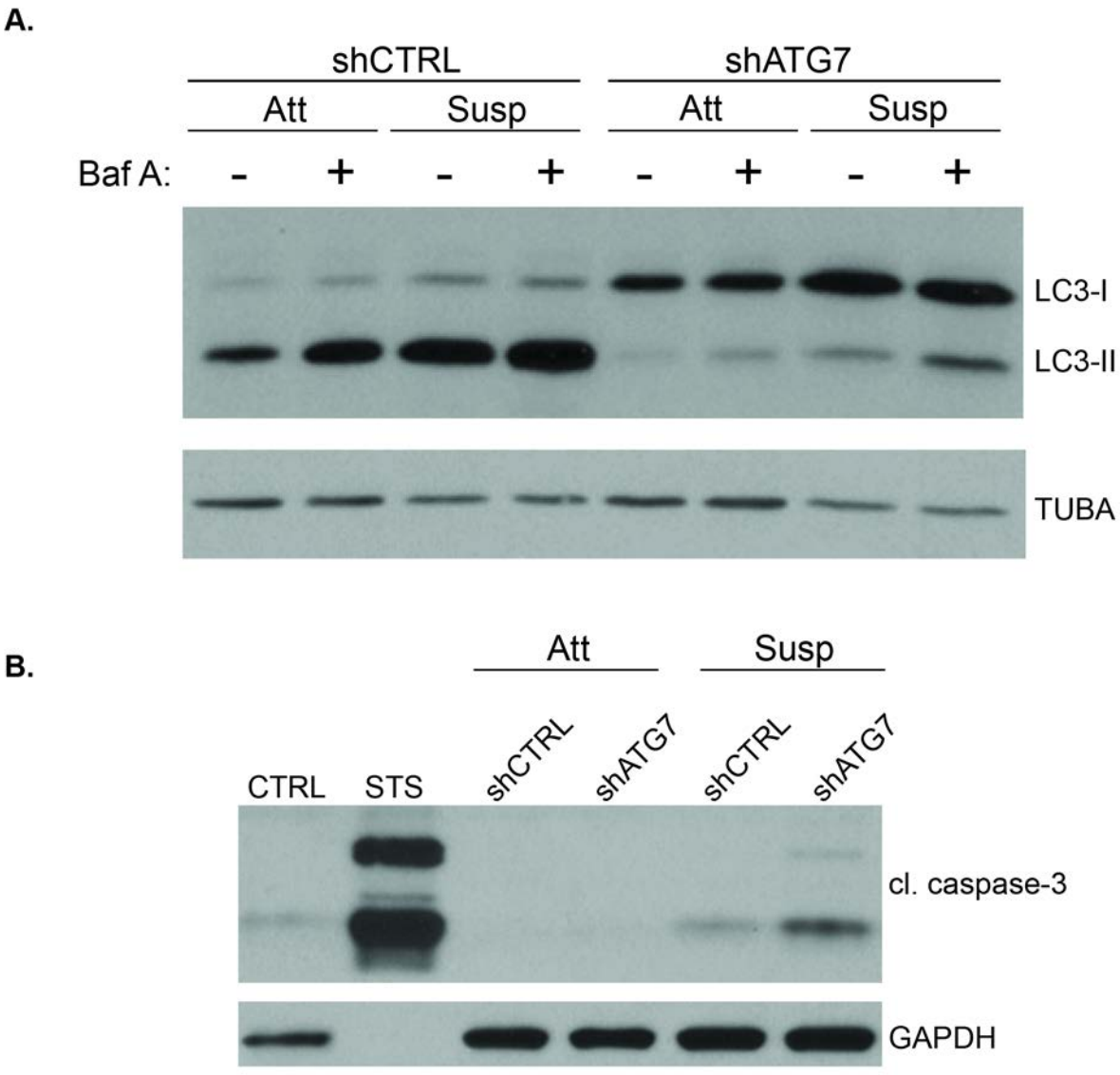
A.
shCTRL
shATG7
Att
Susp
Att
Susp
Baf A:
-
+
-
+
-
+
-
+
LC3-I
LC3-II
TUBA
B.
Att
Susp
CTRL
STS
shCTRL
shATG7
shCTRL
shATG7
cl. caspase-3
GAPDH

**Figure 1: Autophagy supports adhesion-independent survival of PyMT mammary carcinoma cells.** (A) R221A cells expressing control non-targeting shRNA or shRNA against ATG7 were grown attached (Att) or suspended (Susp) for 24 h. Induction of autophagy is indicated by an increase in lipidated LC3 (LC3-II) in the presence of the lysosomal inhibitor bafilomycin A (Baf A, 20 nM for 30 min). Impaired autophagy induction in ATG7-depleted cells is shown by decreased levels of LC3-II in suspended cultures. TUBA ($\alpha$-tubulin) used as the loading control. (B) Autophagy supports viability of detached cells. R221A cells expressing control shRNA or shRNA against ATG7 were cultured in suspension for 24 h and apoptosis was assessed via immunoblot for the presence of cleaved caspase-3. Staurosporine (STS) treatment was used as a control for induction of cell death. GAPDH is the loading control.

**Figure 2**

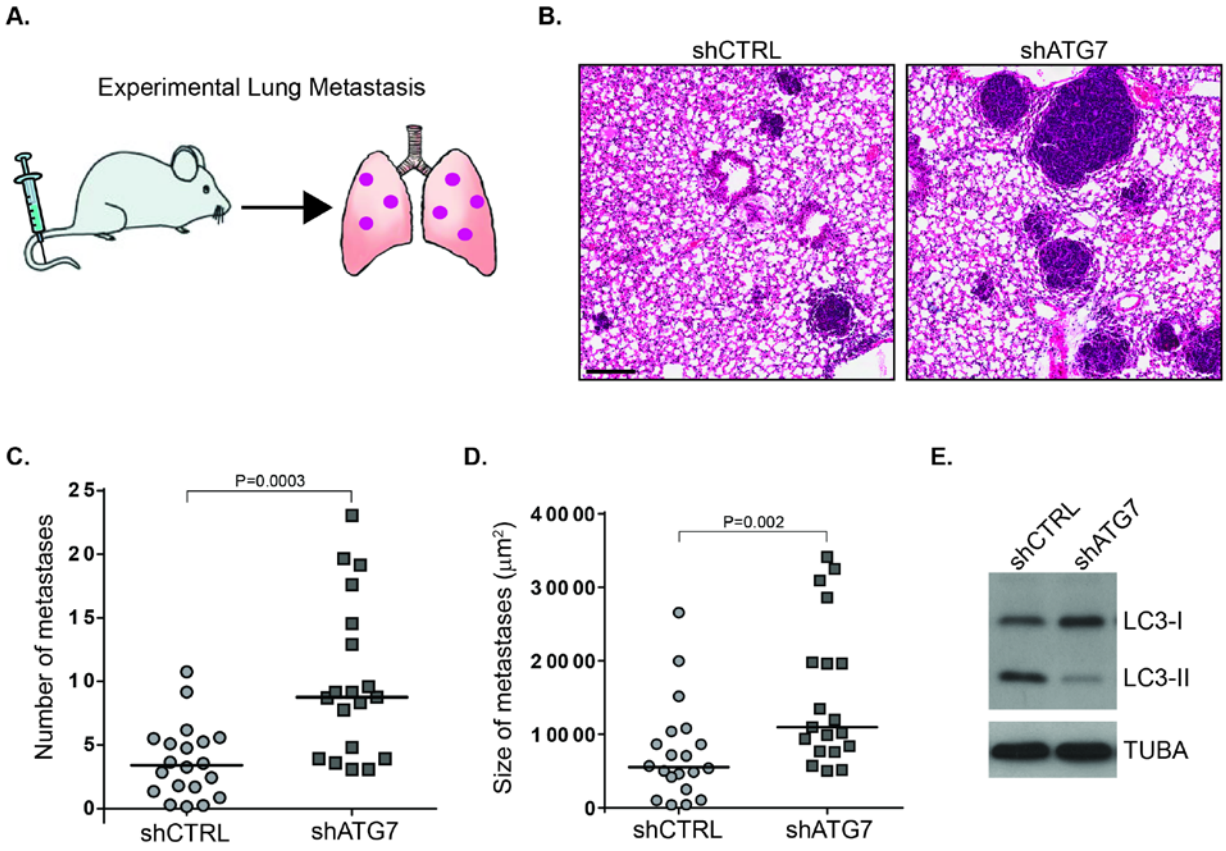
A.
Experimental Lung Metastasis
B.
shCTRL
shATG7
C.
P=0.0003
Number of metastases
25
20
15
10
5
0
shCTRL
shATG7
D.
P=0.002
Size of metastases (µm²)
400 00
300 00
200 00
100 00
0
shCTRL
shATG7
E.
shCTRL
shATG7
LC3-I
LC3-II
TUBA

**Figure 2: Autophagy inhibition increases experimental lung metastasis.** (A) Schematic illustrating experimental metastasis assay. Cells are injected intravenously through the lateral tail vein and then give rise to lung tumors. (B) Representative H&E staining of lung sections show metastases in mice injected with control R221A cells or ATG7-depleted R221A cells. Bar, 150 μm. (C) Quantification of the number of lung metastases per field shown in B. Four total fields from three sections per mouse were counted. Data is presented as median (line) and each data point represents a single mouse. n=20 mice for shCTRL and n=19 for shATG7 pooled from three independent experiments. P value determined using a non-parametric Mann-Whitney test. (D) Quantification of the size of lung metastases from fields of view shown in B. Four total fields from three sections per mouse were analyzed. Data is presented as median (line) and each data point represents a single mouse. n=20 mice for shCTRL and n=19 for shATG7 pooled from three independent experiments. P value determined using a non-parametric Mann-Whitney test. (E) Immunoblot for LC3 from R221A cells cultured *ex vivo* out of the lung following experimental metastasis. TUBA (α-tubulin) used as the loading control.

**Figure 3**

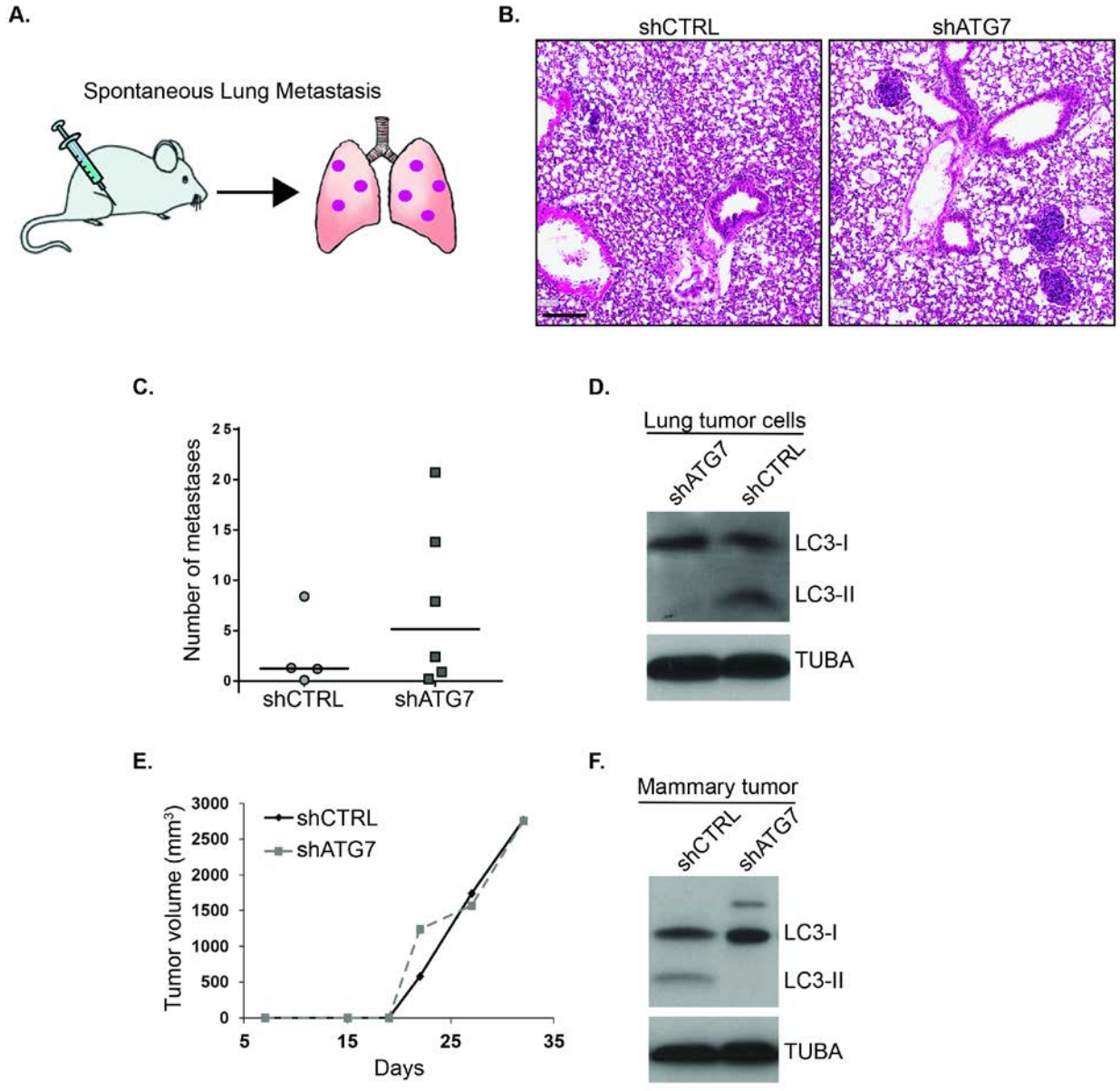
A.
Spontaneous Lung Metastasis
B.
shCTRL
shATG7
C.
Number of metastases
25
20
15
10
5
0
shCTRL
shATG7
D.
Lung tumor cells
shATG7
shCTRL
LC3-I
LC3-II
TUBA
E.
Tumor volume (mm³)
3000
2500
2000
1500
1000
500
0
shCTRL
shATG7
5
15
25
35
Days
F.
Mammary tumor
shCTRL
shATG7
LC3-I
LC3-II
TUBA

**Figure 3: Autophagy inhibition promotes spontaneous lung metastasis and does not affect primary tumor growth of PyMT cells.** (A) Schematic illustrating spontaneous metastasis assay. Cells are transplanted orthotopically into the cleared #4 mammary fat pad and then give rise to primary mammary tumors and metastatic lung tumors. (B) Representative H&E staining of lung sections show metastases in mice transplanted with control R221A cells or ATG7-depleted R221A cells. Bar, 150 μm. (C) Quantification of the number of lung metastases per section. The total number on each of ten sections per mouse was counted. Data is presented as median (line) and each data point represents a single mouse. n=4 mice for shCTRL and n=6 mice for shATG7 from one experiment. (D) Immunoblot for LC3 from R221A cells cultured *ex vivo* out of the lung following spontaneous metastasis. TUBA (α-tubulin) used as the loading control. (E) Tumor growth curves from mice transplanted with R221A cells expressing shCTRL or shATG7. (F) Immunoblot for LC3 from tumors arising from orthotopic transplantation of shCTRL- or shATG7-expressing R221A cells.

**Figure 4**

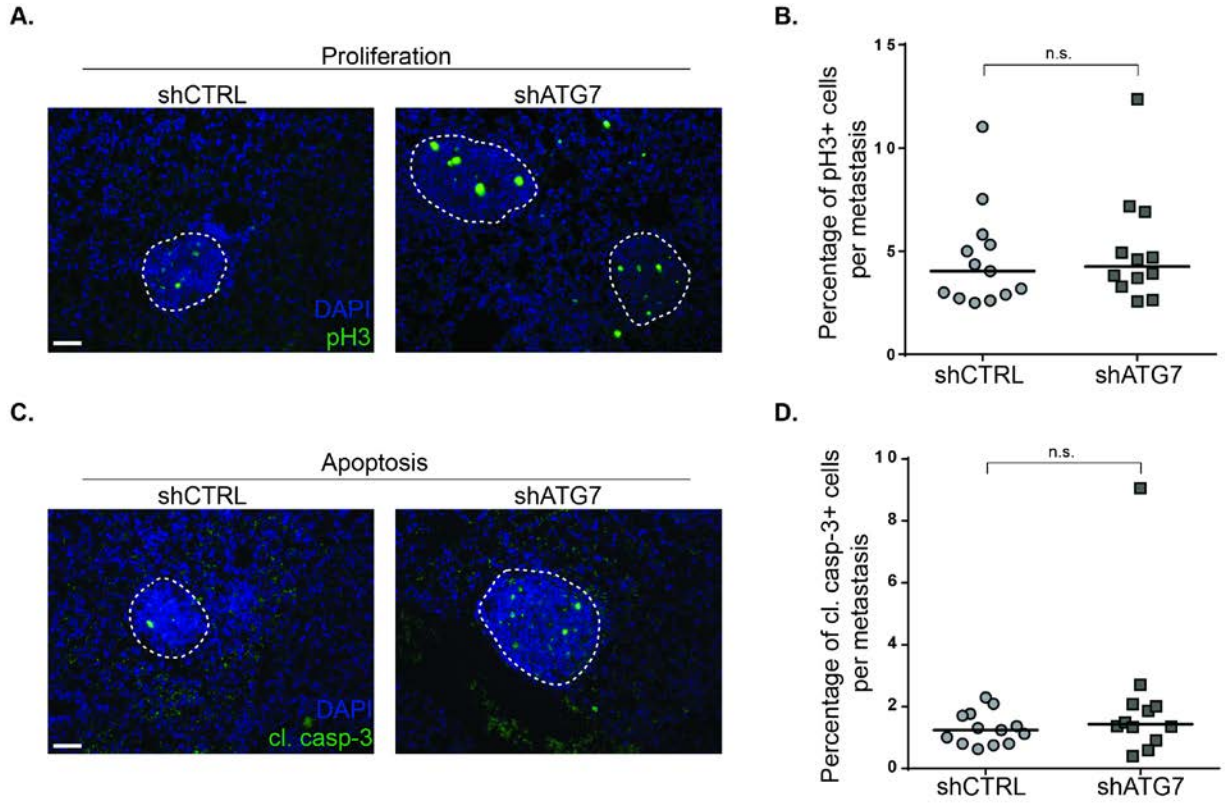
A.
Proliferation
shCTRL
shATG7
DAPI
pH3
B.
Percentage of pH3+ cells per metastasis
n.s.
shCTRL
shATG7
C.
Apoptosis
shCTRL
shATG7
DAPI
cl. casp-3
D.
Percentage of cl. casp-3+ cells per metastasis
n.s.
shCTRL
shATG7

**Figure 4: Autophagy does not regulate proliferation or apoptosis of macrometastases.** (A) Lung sections from mice during experimental metastasis were stained for phospho-Histone H3 (pH3, green) as an indicator of proliferation. DAPI (blue) marks nuclei. Metastases are outlined by dotted white lines. Bar, 50 μm. (B) Quantification of the percent of pH3 positive cells per metastatic tumor in the lung from images in A. Six fields of view were counted from one section per mouse. Data are presented as median (line) and each data point represents one mouse. n=13 mice for shCTRL and n=12 mice for shATG7 pooled from two independent experiments. P value determined using a non-parametric Mann-Whitney test. n.s.=not significant. (C) Lung sections from mice during experimental metastasis were stained for cleaved caspase-3 (cl. casp-3, green) as an indicator of apoptosis. DAPI (blue) marks nuclei. Metastases are outlined by dotted white lines. Bar, 50 μm. (D) Quantification of the percent of cl. casp-3 positive cells per metastatic tumor in the lung from images in C. Six fields of view were counted from one field per mouse. Data are presented as median (line) and each data point represents one mouse. n=13 mice for shCTRL and n=12 mice for shATG7 pooled from two independent experiments. P value determined using a non-parametric Mann-Whitney test. n.s.=not significant.

**Figure 5**

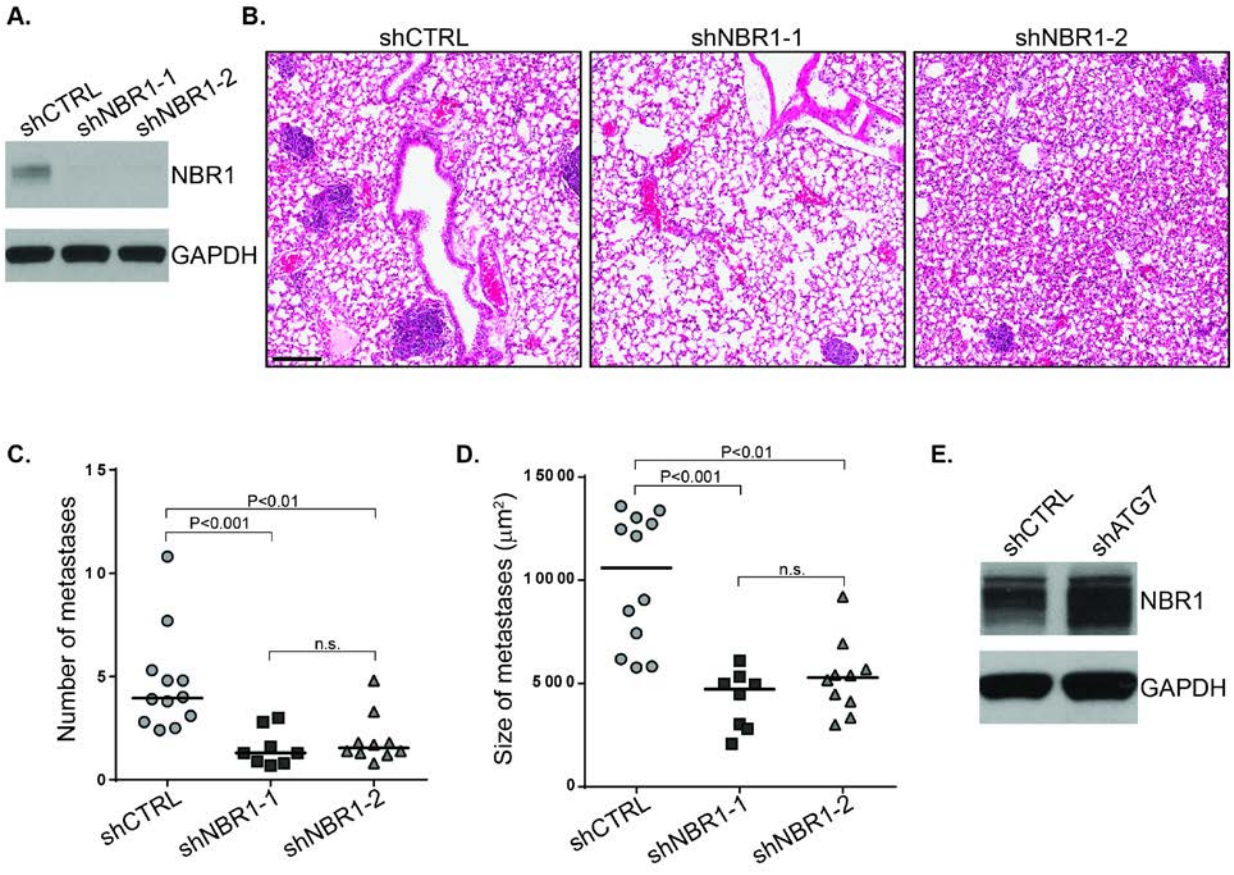
A.
shCTRL
shNBR1-1
shNBR1-2
NBR1
GAPDH
B.
shCTRL
shNBR1-1
shNBR1-2
C.
Number of metastases
15
10
5
0
P<0.01
P<0.001
n.s.
shCTRL
shNBR1-1
shNBR1-2
D.
Size of metastases (μm²)
150 00
100 00
5 000
0
P<0.01
P<0.001
n.s.
shCTRL
shNBR1-1
shNBR1-2
E.
shCTRL
shATG7
NBR1
GAPDH

**Figure 5: NBR1 depletion reduces experimental metastasis.** (A) Immunoblot verifying knockdown of NBR1 in R221A cells using two independent shRNAs. GAPDH is the loading control. (B) Representative lung H&E from experimental metastasis studies in mice injected with cells expressing control shRNA or shRNAs against NBR1. (C) Quantification of the number of lung metastases per field shown in B. Four total fields from three sections per mouse were counted. Data are presented as median (line) and each data point represents a single mouse. n=12 mice for shCTRL, n=8 mice for shNBR1-1, and n=10 mice for shNBR1-2 pooled from two independent experiments. P value determined using a non-parametric Kruskall-Wallis test followed by Dunn's post-test. n.s.=not significant. (D) Quantification of the size of lung metastases from fields of view shown in B. Four total fields from three sections per mouse were analyzed. Data are presented as median (line) and each data point represents a single mouse. n=12 mice for shCTRL, n=8 mice for shNBR1-1, and n=10 mice for shNBR1-2 pooled from two independent experiments. P value determined using a non-parametric Kruskall-Wallis test followed by Dunn's post-test. n.s.=not significant. (E) Immunoblot showing accumulation of NBR1 in cells inhibited for autophagy via knockdown of ATG7. GAPDH is the loading control.

## MATERIALS AND METHODS

### Animal Studies

All animal experiments were performed in accordance with protocols approved by the UCSF IACUC, and mice were housed under pathogen-free conditions in the UCSF barrier facility. Wild-type FVB/n mice for syngeneic transplants were purchased from Jackson Laboratories. For experimental metastasis experiments, 6-7 week old female mice were injected intravenously through the lateral tail vein with $1 \times 10^6$ PyMT tumor cells resuspended in PBS. For primary tumor growth and spontaneous metastasis experiments, $1 \times 10^6$ PyMT tumor cells were resuspended in 1:1 PBS:Matrigel (Corning) and injected into the cleared #4 mammary fat pad of 3 week old mice. Tumors were monitored once weekly until palpable and then measured twice weekly using a caliper. Tumor volume was calculated as: volume = 0.52 x length x $(\text{width})^2$, with the length being the longest diameter and width being the shortest diameter.

### Cell culture

PyMT mammary carcinoma cells (R221A clone; a gift from Barbara Fingleton, Vanderbilt University) were cultured in DMEM with 10% FBS, penicillin, and streptomycin[120]. To establish *ex vivo* cultures of lung tumor cells from mice with experimental or spontaneous metastasis, a portion of lung tissue was minced and then digested in collagenase buffer (DMEM/F12, 2 mg/ml collagenase, 2 mg/ml trypsin, 5% FBS, 50 μg/ml gentamicin, and 5 μg/ml insulin) at 37°C with shaking for approximately 1 h. Cells were pelleted by centrifugation at 1500 rpm for 5 min, DNAse treated, and subjected to red blood cell lysis. The remaining cell pellet was resuspended and plated in growth medium. 24-48 h post-plating, growth medium containing G418 was added to the cells to specifically select out tumor cells from the host lung cells for immunoblot analysis.

**RNA interference:**

For stable RNA interference, pLKO.1puro lentiviral plasmids with non-targeting shRNA or shRNA against mouse ATG7 (NM_028835) and mouse NBR1 (NM_008676) were purchased from Sigma Aldrich. The target sequence for shRNA against mouse ATG7 (TRCN0000092163) is: CCAGCTCTGAACTCAATAATA and against mouse NBR1 (TRCN0000123384 and TRCN0000123388) are: CCTTGAATGTTTCCAAGAATT and GCAGAGGTCAAAGAGCTTAAA. shRNA lentivirus was produced and pools of stable shRNA-expressing cell lines were generated as previously described[81].

**Immunoblotting**

The following antibodies were used for immunoblotting: anti-ATG7 (Cell Signaling 2631, 1:500), anti-NBR1 (Novus NBP1-71703, 1:1000), anti-cleaved caspase-3 (Cell Signaling 9661, 1:200), anti-TUBA (Sigma Aldrich T6199, 1:5000), and anti-GAPDH (Millipore AB2302, 1:5000). A rabbit polyclonal antibody against MAP1LC3 has been previously described and is now commercially available (Millipore ABC232, 1:1000)[72]. For immunoblot analysis, cells were lysed in RIPA buffer (1% Triton X-100, 1% sodium deoxycholate, 0.1% SDS, 25 mM Tris, pH 7.6, 150 mM NaCl) plus protease inhibitor cocktail (Sigma Aldrich), 10 mM NaF, 10 mM β-glycerophosphate, 1 mM $Na_3VO_4$, 10 nM calyculin A, 0.5 mM PMSF, 10 μg/ml E64d, and 10 μg/ml pepstatin A. Lysates were freeze-thawed at -80°C, cleared by centrifugation for 30 min at 4°C, boiled in sample buffer, resolved by SDS-PAGE, and transferred to PVDF membrane. Membranes were blocked for 1 h in 5% milk in PBS with 0.1% Tween 20 (PBST), incubated in primary antibody overnight at 4°C, washed, incubated for 1 h at room temperature with HRP-conjugated secondary antibodies (Jackson Immunoresearch, 1:5000), washed, and visualized via enhanced chemiluminescence (Thermo Scientific).

**Immunofluorescence**

For immunofluorescence, the following antibodies were used: anti-phospho-Histone H3 (Ser 10) (Cell Signaling 9701, 1:100) and anti-cleaved caspase-3 (Cell Signaling 9661, 1:100). Lung tissue was PFA fixed overnight at 4$^{o}$C, paraffin embedded, and sectioned (5 μm). Following antigen retrieval with citrate buffer (Dako Target Retrieval Solution), sections were blocked for 30 min at room temperature in blocking buffer (PBS, 0.1% Tween 20, 10% goat serum), incubated with primary antibodies overnight at 4$^{o}$C, washed, incubated with Alexa Fluor-conjugated secondary antibodies (Life Technologies, 1:200) for 1 h at room temperature, washed, and mounted using Vectashield Antifade Mounting Medium with DAPI (Vector Laboratories).

**Analysis of lung metastases number and size**

PFA-fixed paraffin-embedded lungs were sectioned (5 μm), stained with H&E, and imaged using the ScanScope XT slide scanner (Aperio). For quantification of metastases, four random fields of 8x magnification were chosen from each of three sections per mouse. The number of metastases per field was manually counted and area of metastases was determined by manually outlining all tumors in the field of view using ImageScope analysis software (Aperio). The average number per field and average size per metastasis is plotted for each mouse.

**Proliferation and apoptosis analysis of metastases**

Lung sections were processed and immunostained as described above for phospho-Histone H3 and cleaved caspase-3. Epi-fluorescence images were obtained using an Axiovert 200 microscope (Carl Zeiss) with a 20x (NA: 0.4) objective, Spot RT camera (Diagnostic Instruments), and mercury lamp. Images were acquired using MetaMorph software (v6.0). The

percentages of proliferating and apoptotic cells were counted per tumor mass in six fields from one section per mouse using Image J. The average percent proliferating or apoptotic cells per metastasis are plotted for each mouse.

### *In vitro* suspension assay

Suspension assays were performed as previously described[72]. Briefly, cells were plated in uncoated or poly-HEMA-coated 6-well dishes at a density of 300,000 – 600,000 cells per well in full growth medium for 24 h. For analysis of autophagic flux, cells were treated with 20 nM bafilomycin A during the final 30 min of culture. Cells were harvested and lysed as described above for biochemical analysis of LC3-II conversion and apoptosis by immunoblot.

### Statistical analysis

All statistical analyses were performed using GraphPad Prism 6. The normality of the distribution of data sets was determined by a Shapiro-Wilk normality test ($P<0.05$ indicating a non-normal distribution); for data sets in which the sample size was not large enough ($n\leq6$) for determination of normality, a normal distribution was assumed. For normal distributions, groups were compared using Student's unpaired t-test or one-way ANOVA followed by Tukey's post-test for multiple comparisons. For non-parametric statistics, a Mann-Whitney test or Kruskall-Wallis test followed by Dunn's post-test for multiple comparisons was used. $P<0.05$ was considered to be significant for all tests.

# CHAPTER 4

# Discussion

## CRUCIAL FUNCTIONS FOR AUTPOHAGY IN CANCER PROGRESSION

Over the past decade, autophagy has unquestionably emerged as a principle determinant of cancer development. From the earliest studies demonstrating that autophagy may function to merely support survival of tumor cells exposed to chemotherapies to our now considerably in depth realizations that it may itself underlie the functional basis of many phenotypes involved in tumor initiation and progression, there exists a sound base of evidence rationalizing therapeutic targeting of autophagy for treatment of cancer. Now, it is also increasingly apparent that roles for autophagy in promoting cancer cell fitness during primary tumorigenesis may also be critical for metastasis, and recent studies of invasion and migration have begun to illuminate novel functions for autophagy in tumor cells. Though these new findings indicate pharmacological modulation of autophagy may prove efficacious in treating metastasis, without detailed knowledge of the mechanisms underlying autophagy-dependent control of these phenotypes or a basic understanding of how autophagy inhibition affects metastasis in relevant *in vivo* mouse models, the potential outcome of autophagy-targeted therapies in treatment of patients with metastatic disease remains unclear.

In this thesis, I present work that attempts to address these issues by exploring the mechanistic basis of autophagy-dependent motility and by investigating the role of autophagy during *in vivo* breast cancer metastasis. I identify a new and previously unexplored function for selective autophagy in regulating FA turnover to support cell migration and provide evidence that autophagy unexpectedly functions as a metastasis suppressor. Intriguingly, although these results seem disparate, distinct functions for the selective autophagy cargo receptor, NBR1, may in part underlie the molecular basis of both autophagy-dependent motility and metastatic colonization. Thus, an additional outcome of this overall work is the potential characterization of cargo receptors as important determinants of autophagy-dependent cell biological phenotypes.

## REGULATION OF FOCAL ADHESION TURNOVER AND CELL MIGRATION BY SELECTIVE AUTOPHAGY

### Mechanisms of autophagy at focal adhesions

We present evidence for autophagy as a mechanism of FA turnover at the leading edge of migrating cells and implicate the selective autophagy cargo receptor, NBR1, as a key mediator of this process. Using live-cell imaging to directly visualize FAs, we uncover that autophagy supports FA turnover and that autophagosomes target FAs during disassembly. Overall, these data suggest a role for autophagy in facilitating FA turnover by locally promoting FA disassembly. Although autophagosomes are found preferentially associated with disassembling FAs, ATG knockdown functionally impairs both FA assembly and disassembly. Therefore, while disassembly may be proximally modulated by autophagy, we cannot rule out that autophagy regulates FA assembly by more indirect mechanisms that do not involve the localization of autophagosomes to FAs. It is also possible that defects in assembly may occur as a consequence of impaired disassembly. For example, the release of FA proteins from a disassembling FA would provide a readily accessible reservoir of building blocks for use during assembly of new adhesions. This local recycling of FA components among neighboring adhesions would be highly efficient for rapid FA dynamics at the leading edge of migrating cells; however, this potential fate of proteins released from disassembling FAs has not been explored. Thus, interrogation into the relationship between FA assembly and disassembly will be necessary to establish how autophagy impacts FA assembly.

There is evidence that autophagy directs the endocytic recycling of β1-integrins. However, the activation of this pathway is only observed during extreme nutrient deprivation conditions in which cells are incubated in Hank's Buffered Saline Solution (HBSS) to induce autophagy. As a result, it remains uncertain if the autophagy pathway alters integrin recycling to impact migration in broader physiological contexts[103]. Moreover, the role of integrin recycling

specifically in leading edge FA turnover remains contentious and inadequately studied, casting further doubt on whether autophagy-dependent integrin recycling is a determinant of rapid FA dynamics during migration[132]. Nevertheless, although autophagy may modulate cell motility through multiple mechanisms, our results here most clearly implicate autophagy in promoting leading edge FA turnover, which functions as a crucial and distinct contributor to migration.

Significantly, our results expand on the growing importance of selective autophagy regulators, namely NBR1, in controlling essential cellular functions. Our findings that loss of NBR1 function phenocopies autophagy deficiency to inhibit migration and leading edge FA turnover, that only autophagy-competent NBR1 is sufficient to specifically enhance FA disassembly, and that NBR1 localizes near dynamic FAs all support that this particular pathway of cargo receptor-mediated autophagy is required for efficient migration by facilitating optimal adhesion site turnover. Like other autophagy cargo receptors, NBR1 enables the selective capture of cellular substrates into autophagosomes. Accordingly, our data indicating that core ATGs and NBR1 function in the same pathway raises the hypothesis that NBR1 interacts with FA proteins to enable association of autophagosomes with FAs via binding of NBR1 to LC3. This recruitment may ultimately trigger sequestration of FA components by autophagosomes, which would be expected to promote FA disassembly. Indeed, selective autophagy is an attractive candidate for mediating turnover of large macromolecular complexes, such as FAs, as it is the major homeostatic pathway through which bulky cellular cargo, such as organelles and protein aggregates, are sequestered and degraded[18]. Similar to our observations, autophagosomes and cargo receptors also localize to these cargoes and the stability of these substrates is increased upon autophagy deficiency, lending precedent to our proposed model that autophagy may function via a similar mechanism of action to regulate FAs.

**Potential origins of focal adhesion-targeted autophagosomes**

Capture of cellular material by autophagy is presumed to occur via growth of the autophagosomal membrane around substrates. This model is supported by ultrastructural electron microscopy data showing opened double membrane structures forming around cellular content, such as mitochondria; obvious evidence for incompletely formed autophagosomes trafficking long distances to their cargo or enclosed autophagosomes re-opening to take up targets is lacking[133]. Based on this current knowledge, our data implies that autophagosome formation occurs locally at the FA and autophagosomes are then trafficked away for fusion with endolysosomal compartments. As LC3 is thought to primarily mark more mature autophagosomes, identification of early autophagosomal markers known to be present in the early stages of autophagosome biogenesis, such as ULK1, ATG14, WIPI1, DFCP1, and ATG12-5-16L, localized near FAs will more directly address this possibility[134].

This putative model raises further questions about the precise nature of autophagosome formation near FAs related to probable sources of membrane and site-specification of autophagosome formation, two poorly understood aspects of autophagosome biogenesis. The source of autophagosome membrane has been a topic of intense debate; numerous reports describe various origins of autophagosomal membrane including endoplasmic reticulum (ER), golgi apparatus, mitochondria, and plasma membrane[135]. Interestingly, ER has been shown to extend out to FA areas and plasma membrane lipids would be readily accessible at FAs, suggesting that either of these compartments can provide lipid for forming autophagosomes.

Additionally, it is not clear how the autophagy machinery may position itself to form autophagosomes at the leading edge. Microtubules (MTs) are well characterized inducers of FA disassembly and are known to undergo a characteristic polarized assembly towards the leading edge of migrating cells[132]. Overall, it appears that temporally specified targeting of MTs to FAs leads to delivery of “relaxation factors” of various natures that promote disassembly. Both LC3 and NBR1 can bind MTs so it may be possible that this targeting of MTs helps to position autophagy machinery for interaction with and capture of FAs by forming autophagosomes[136-137].

Such a mechanism would agree with the temporal specificity with which autophagy and NBR1 affect FAs. Further investigation into these issues will provide a better mechanistic understanding of how the autophagy pathway is regulated to direct FA dynamics and reveal important information about autophagosome formation.

**Regulation of NBR1-dependent selective autophagy at focal adhesions**

Defining the mechanisms that regulate convergence of the autophagy pathway with FAs is a necessary goal for future study. While our data hints at a key role for NBR1 in mediating association of autophagosomes with FAs, it remains unknown how NBR1 itself functions at FAs. Specifically, determining if NBR1 directly interacts with FA proteins and how such interactions are promoted will define the biochemical nature of the observed localization of NBR1 to FAs, as well as reveal the molecular events that initiate autophagy-dependent FA disassembly. During selective autophagy, cargo selection is often specified by ubiquitination of substrates, and E3 ubiquitin ligases constitute an integral arm of the adhesome, suggesting FA proteins can be modified by ubiquitination[99, 138-140]. Thus, one possibility is that the ubiquitin binding domain (UBA) of NBR1 allows for interaction with ubiquitinated FA proteins. Despite being an important pathway for the turnover of ubiquitinated substrates, the role of autophagy in dictating the fate of FAs harboring ubiquitinated proteins has not been interrogated. Additionally, ubiquitin-independent mechanisms of autophagy substrate selection also exist, and FAs consist of hundreds of proteins[112, 116]. NBR1 is a large multi-domain scaffold with the ability to engage in many interactions[118-119, 141-142]. Given these potentially diverse mechanisms of ubiquitin-dependent and –independent cargo recognition, numerous interactions between NBR1 and FAs may exist that could serve to bridge autophagosomes to FAs. Although conventional biochemical approaches are commonly utilized to identify targets of autophagy cargo receptors, employing such strategies to elucidate NBR1 interacting partners at dynamic FAs during migration is hampered by the asynchronous and spatially polarized nature of FA turnover in a

cell, as well as the extreme temporal specificity with which autophagosomes are recruited to FAs during disassembly. Nevertheless, important goals for future study are definitively identifying NBR1 binding partners at FAs and demonstrating that these interactions are required for autophagy-mediated FA turnover during adhesion-dependent processes such as cell migration and spreading.

In addition to investigating whether and how NBR1 directly interacts with FA proteins, it will also be necessary to understand the signals that enable this interaction. Our data showing that autophagosomes associate with disassembling adhesions and that NBR1 enhances FA disassembly indicate that the primary function of such signals may be to dictate this temporal specificity at some level. As mentioned above, the temporal targeting of MTs could have a role in promoting association of autophagy machinery and NBR1 to FAs specifically for disassembly, but once positioned, additional regulatory mechanisms may be in place to ensure that the proper interactions are established for precise spatial fidelity of cargo uptake by the autophagosome. For instance, ubiquitination-dependent interactions may be regulated by specific E3 ligases that act on FA substrates primarily during disassembly. Alternatively, NBR1 itself may be biochemically regulated such that it is primed to bind substrates in an ubiquitin-dependent or –independent manner or interact with LC3 at certain times. Further work addressing precise mechanisms underlying marking of cargo, recognition of substrates by NBR1, and regulation of the interaction between NBR1 and autophagosomes at FAs will clarify the molecular basis of autophagy-dependent FA turnover. Importantly, while much is known about regulatory events that lead to starvation-induced autophagy, how selective autophagy pathways are activated and precisely controlled is only beginning to be studied. Our models of FA turnover during migration and spreading may provide reliable systems to interrogate key aspects of selective autophagy in a physiological setting.

**Functional implications of autophagy-dependent focal adhesion regulation during migration**

Our results demonstrating that FA turnover is partially inhibited in autophagy-deficient cells reinforce that selective autophagic targeting of FAs only serves as one destabilizing mechanism to promote disassembly. Additional pathways including phosphorylation mediated by FAK-Src signaling [100], endocytosis [143-145], calpain cleavage [146-148], and ECM proteolysis [101, 149] have been implicated in FA disassembly. Together with our current results demonstrating that autophagy supports FA turnover, these findings illustrate how cells engage diverse mechanisms to direct adhesion and migration. Given the importance of motility in development, physiology, and disease states, it is not surprising that the cell has evolved multiple mechanisms to ensure migration can occur.

It remains to be determined how this function for autophagy in regulating motility may impact these migration-dependent processes *in vivo*. For instance, there is a lack of insight into the function of autophagy during developmental tissue morphogenesis. However, one study that closely examined the role of autophagy during embryonic cardiac development found that ATG loss-of-function led to defects in cardiac morphogenesis in both zebrafish and mice[150]. In conjunction with our data demonstrating that autophagy regulates the motility of multiple cell types, these findings indicate that autophagy-dependent migration may be of physiological importance. Pathologically, the relevance of autophagy during migration remains uncertain during processes such as metastasis; although our data indicate that autophagy-dependent migration may not be critical for metastasis, without specifically assessing this particular phenotype *in vivo*, the requirement for this function of autophagy in mediating tumor cell dissemination is still an open question. Going forward, future studies illuminating the detailed mechanisms through which autophagy mediates FA turnover during migration will facilitate a better understanding of the functional role for autophagy during multiple migration-dependent processes.

## AUTOPHAGY AND *IN VIVO* CANCER METASTASIS

### Autophagy and metastasis suppression

Mounting evidence has implicated autophagy in the regulation of a variety of phenotypes essential for completion of metastasis. In particular, due to its role in maintaining cellular fitness and promoting processes such as invasion and migration, it has primarily been hypothesized that autophagy would serve a pro-metastatic function. However, little is known about the actual role of autophagy during *in vivo* metastasis. We show here that inhibition of autophagy enhances, rather than inhibits *in vivo* lung metastasis of PyMT mammary carcinoma cells, indicating that autophagy acts to suppress metastasis. Mechanistically, we propose that metastasis suppression by autophagy may be due to its ability to limit expression of the autophagy cargo receptor, NBR1, which may function as a novel metastasis promoter.

### Deciphering stage-specific contributions of autophagy to metastasis

To address the role of autophagy in mediating the potentially most critical and rate-limiting steps of metastasis, we used both experimental and spontaneous models of breast cancer metastasis to lung. Intriguingly, we uncovered that knockdown of the essential autophagy gene, ATG7, leads to increased metastasis in both experimental contexts. These findings indicate that autophagy may determine the malignant potential of tumor cells during stages of metastasis that are common to both models. Such steps, which likely occur at the lung, include extravasation of tumor cells to seed the lung, survival following this initial seeding period, and eventual outgrowth.

To better define how autophagy may impact metastatic colonization at the distant organ, we first asked whether autophagy inhibition altered cell fate of macrometastases during experimental metastasis. In light of multiple pieces of evidence suggesting that autophagy inhibition could promote the growth of metastases, we reasoned that autophagy-deficiency may

confer a proliferative advantage. For instance, integrin-mediated adhesion and ERK signaling provide growth promoting signals to potently induce proliferation of macrometastases, and we have found that autophagy inhibition enhances adhesion of PyMT cells *in vitro*[62, 131]. Similarly, we and others have previously implicated the autophagy cargo receptor p62, which accumulates with autophagy inhibition, in activating growth inducing signals such as ERK and mTORC1[53-55]. Finally, autophagy has also been reported to promote epithelial-mesenchymal transition (EMT), the reversion of which, or mesenchymal-epithelial transition (MET), favors the establishment of metastases[81, 151]. However, despite these multiple functions for autophagy in potentially supporting expansion of metastatic lung tumors, we found that macrometastases arising from autophagy-competent and autophagy-deficient cells exhibited no differences in growth, or viability. Thus, because autophagy appears to have an important function in suppressing metastasis at the distant organ yet this metastasis-inhibiting role of autophagy does not impact the cellular fitness of macrometastases, we suggest that autophagy regulates the earliest events involved in lung colonization, such as seeding and dormancy. Going forward, it will be necessary to establish the precise function of autophagy in directly regulating these particular phenotypes *in vivo*.

These results demonstrate a clear function for autophagy in suppressing breast cancer metastasis to lung. However, in patients, metastasis occurs most commonly to bone, as well as to other sites such as liver and brain[152]. It seems possible that the microenvironments of these different organs may impose unique and distinct demands on tumor cells. For example, liver and bone marrow are characteristically hypoxic. This raises the possibility that the pro-survival functions of autophagy may be most critical in these organs for survival of DTCs, which does not appear to be the case in mouse lung. In support, recent findings have shown that autophagy serves a protective function in adult, quiescent hematopoietic stem cells (HSCs)[153]. Because DTCs in the bone marrow are known to exhibit a long period of dormancy and occupy the same niche as HSCs, these data suggest that autophagy may instead be an essential survival

mechanism for bone DTCs. Future work interrogating the role of autophagy in regulating metastatic organotropism will be critical to address these issues and will raise key questions about how to target autophagy in patients with multi-organ metastatic disease.

Although we have focused on scrutinizing metastasis events occurring specifically at the metastatic site, it is still important to determine if autophagy is critical during earlier stages of metastasis, such as local primary tumor invasion and dissemination in the vasculature. Our published data indicate that autophagy is necessary for local invasion and survival of CTCs. Accordingly, our analysis of spontaneous metastasis, which also demonstrated that autophagy suppresses metastasis, raises the possibility that autophagy may indeed have dual roles throughout the metastatic cascade. For instance, it may function as a metastasis promoter in locally invading primary tumor cells and CTCs; however, due to the rate-limiting nature of steps associated with seeding and colonization, the apparent metastasis suppressing function of autophagy during these latter stages may ultimately prevail. Clarification of the importance of these potentially diametrically opposing functions for autophagy during metastatic progression remains an important goal for future work.

In addition to regulating events such as invasion and migration at the primary tumor, it should be noted that autophagy also has the potential to serve other critical roles during the earliest stages of metastatic development associated with conditioning of the pre-metastatic niche, the formation of which is induced by tumor cell-derived secreted factors, including cytokines and extracellular vesicles, such as exosomes[126, 154]. There is limited evidence demonstrating functions for autophagy in regulating conventional and unconventional secretory pathways[83]. Moreover, we have recently identified functions for autophagy regulators in controlling exosome biogenesis and secretion through modulation of the multi-vesicular body trafficking pathway[155]. These intriguing findings motivate future work aimed at exploring an essential function for autophagy in regulating the earliest stages of pre-metastatic niche formation. Because the full repertoire of autophagy-dependent secretory factors has yet to be

defined and it is not precisely clear if autophagy may regulate packaging of cargo into exosomes, it is possible that autophagy may serve to promote or inhibit metastasis by regulating secretion of these diverse intercellular signaling factors.

Regardless of the stage-specific contributions of autophagy to metastasis, our finding that autophagy inhibition overall enhances metastasis raises key concerns for therapeutically inhibiting autophagy in patients with cancers that characteristically metastasize. The most clinically worrisome implication of these data is the possibility that autophagy inhibition would promote outgrowth of undetectable DTCs. Thus, while further studies may ultimately reveal that autophagy supports local tumor invasion and CTCs, extreme care should be taken when deciding if autophagy inhibition is an appropriate therapeutic course based on what is known about dormant disease or lethal outcome for the metastasis of specific cancers. This particular concern underscores the need for a comprehensive understanding of the mechanistic basis of autophagy-dependent functions during metastasis. Elaborating how autophagy controls metastatic traits *in vivo* will provide more precise avenues to target specific aspects of metastasis, whereas global inhibition of autophagy by targeting upstream, core autophagy regulators may not overall be beneficial.

**NBR1 as a novel metastasis promoter**

In order to mechanistically link autophagy to metastasis suppression, we investigated the role of the autophagy cargo receptor, NBR1, in regulation of metastasis. Although these experiments were originally motivated by our data demonstrating that autophagy and NBR1 coordinately regulate cell-ECM adhesion, we surprisingly found that, unlike autophagy, NBR1 supports metastasis. Very little is known about NBR1, with regard to both its selective autophagy-dependent and –independent functions, but it has been reported to inhibit p38 MAPK signaling. Intriguingly, p38 MAPK signaling is known to promote dormancy during metastasis[64]. Thus, a model in which NBR1 accumulation upon autophagy inhibition would lead to decreased

p38 MAPK activity is in agreement with our findings that functionally, autophagy may regulate dormancy of DTCs. While we have verified that NBR1 does accumulate in ATG7-depleted cells, it remains to be determined if this role for p38 MAPK signaling is critical for dormancy regulation of PyMT cells in our models and if p38 MAPK signaling is indeed altered in autophagy-deficient cells or NBR1 knockdown cells. Finally, though these data establish an exciting correlation between metastasis suppressive functions for autophagy and metastasis promoting functions for NBR1, it will also be necessary to demonstrate causally that accumulation of NBR1 does in fact mediate increased metastasis upon autophagy inhibition. Further interrogation into the functional role of autophagy in suppressing metastasis will facilitate a more specific mechanistic analysis that is necessary to address these issues.

## AUTOPHAGY CARGO RECEPTORS AS DETERMINANTS OF AUTOPHAGY-DEPENDENT PHENOTYPES

Although superficially, the two major findings in this thesis seem contradictory with regards to whether or not autophagy is metastasis-promoting or –inhibiting, collectively, they echo the important and emerging theme that the molecular underpinnings through which autophagy exerts its functions are undoubtedly quite diverse, particularly in the case of cancer progression. Furthermore, they also potentially illuminate how this diversity is endowed, in part, through the function of autophagy cargo receptors, namely NBR1. Apart from their ability to target cargo for autophagic capture or regulate a handful of signaling events, very little is truly known about these molecules. Thus, future research must focus not only on the molecular and biochemical regulation of autophagy cargo receptors and their downstream effectors, but also on the contexts in which they mediate specific outcomes in cell fate. Certainly, the presence of multiple receptors suggests there is functional and contextual specificity with which they act that

has favored their collective evolution. Overall, future studies described above aimed at clarifying how autophagy regulates FAs during migration and *in vivo* metastasis are poised to unveil new, unexpected, and exciting roles for autophagy cargo receptors in mediating tumor progression. Such work will be instrumental in enhancing our current knowledge of cellular processes regulating metastasis and uncovering new opportunities for therapeutic targeting of metastasis.

## References


1. Kang, Y., and Pantel, K. (2013) Tumor cell dissemination: emerging biological insights from animal models and cancer patients. *Cancer Cell* 23, 573-581

2. Brabletz, T.*, et al.* (2013) Roadblocks to translational advances on metastasis research. *Nat Med* 19, 1104-1109

3. Rajeev S. Samant, O.F., Lalita A. Shevde (2007) The genetic control of breast cancer metastasis. In *Metastasis of Breast Cancer*, 7-30, Springer Netherlands

4. Friedl, P., and Alexander, S. (2011) Cancer invasion and the microenvironment: plasticity and reciprocity. *Cell* 147, 992-1009

5. Reymond, N.*, et al.* (2013) Crossing the endothelial barrier during metastasis. *Nat Rev Cancer* 13, 858-870

6. Pantel, K., and Speicher, M.R. (2015) The biology of circulating tumor cells. *Oncogene* Advance online publication doi: 10.1038/onc.2015.192

7. Ghajar, C.M. (2015) Metastasis prevention by targeting the dormant niche. *Nat Rev Cancer* 15, 238-247

8. Sosa, M.S.*, et al.* (2014) Mechanisms of disseminated cancer cell dormancy: an awakening field. *Nat Rev Cancer* 14, 611-622

9. Semenza, G.L. (2015) The hypoxic tumor microenvironment: A driving force for breast cancer progression. *Biochim Biophys Acta*

10. Garber, K. (2006) Energy Deregulation: Licensing Tumors to Grow. *Science* 312, 1158-1159

11. Johansson, M.*, et al.* (2008) Polarized immune responses differentially regulate cancer development. *Immunol Rev* 222, 145-154

12. Paoli, P.*, et al.* (2013) Anoikis molecular pathways and its role in cancer progression. *Biochim Biophys Acta* 1833, 3481-3498

13. Geng, J., and Klionsky, D.J. (2008) The Atg8 and Atg12 ubiquitin-like conjugation systems in macroautophagy. 'Protein modifications: beyond the usual suspects' review series. *EMBO Rep* 9, 859-864

14. Klionsky, D.J.*, et al.* (2012) Guidelines for the use and interpretation of assays for monitoring autophagy. *Autophagy* 8, 445-544

15. Reggiori, F., and Klionsky, D.J. (2013) Autophagic processes in yeast: mechanism, machinery and regulation. *Genetics* 194, 341-361

16. Yang, Z., and Klionsky, D.J. (2010) Mammalian autophagy: core molecular machinery and signaling regulation. *Curr Opin Cell Biol* 22, 124-131

17. He, C., and Klionsky, D.J. (2009) Regulation mechanisms and signaling pathways of autophagy. *Annu Rev Genet* 43, 67-93

18. Murrow, L., and Debnath, J. (2013) Autophagy as a stress-response and quality-control mechanism: implications for cell injury and human disease. *Annu Rev Pathol* 8, 105-137

19. Kimmelman, A.C. (2011) The dynamic nature of autophagy in cancer. *Genes Dev* 25, 1999-2010

20. White, E. (2012) Deconvoluting the context-dependent role for autophagy in cancer. *Nat Rev Cancer* 12, 401-410

21. Guo, J.Y.*, et al.* (2013) Autophagy-mediated tumor promotion. *Cell* 155, 1216-1219

22. Yue, Z.*, et al.* (2003) Beclin 1, an autophagy gene essential for early embryonic development, is a haploinsufficient tumor suppressor. *Proc Natl Acad Sci U S A* 100, 15077-15082

23. Qu, X.*, et al.* (2003) Promotion of tumorigenesis by heterozygous disruption of the beclin 1 autophagy gene. *J Clin Invest* 112, 1809-1820

24. Takamura, A.*, et al.* (2011) Autophagy-deficient mice develop multiple liver tumors. *Genes Dev* 25, 795-800

25. Inami, Y.*, et al.* (2011) Persistent activation of Nrf2 through p62 in hepatocellular carcinoma cells. *J Cell Biol* 193, 275-284

26. Rao, S.*, et al.* (2014) A dual role for autophagy in a murine model of lung cancer. *Nat Commun* 5, 3056

27. Yang, A.*, et al.* (2014) Autophagy is critical for pancreatic tumor growth and progression in tumors with p53 alterations. *Cancer Discov*

28. Strohecker, A.M.*, et al.* (2013) Autophagy sustains mitochondrial glutamine metabolism and growth of BrafV600E-driven lung tumors. *Cancer Discov* 3, 1272-1285

29. Ward, P.S., and Thompson, C.B. (2012) Metabolic reprogramming: a cancer hallmark even warburg did not anticipate. *Cancer Cell* 21, 297-308

30. Lock, R.*, et al.* (2011) Autophagy facilitates glycolysis during Ras-mediated oncogenic transformation. *Mol Biol Cell* 22, 165-178

31. Wei, H.*, et al.* (2011) Suppression of autophagy by FIP200 deletion inhibits mammary tumorigenesis. *Genes Dev* 25, 1510-1527

32. Guo, J.Y.*, et al.* (2011) Activated Ras requires autophagy to maintain oxidative metabolism and tumorigenesis. *Genes Dev* 25, 460-470

33. Yang, S.*, et al.* (2011) Pancreatic cancers require autophagy for tumor growth. *Genes Dev* 25, 717-729

34. Guo, J.Y.*, et al.* (2013) Autophagy suppresses progression of K-ras-induced lung tumors to oncocytomas and maintains lipid homeostasis. *Genes Dev* 27, 1447-1461

35. Karsli-Uzunbas, G.*, et al.* (2014) Autophagy is Required for Glucose Homeostasis and Lung Tumor Maintenance. *Cancer Discov*

36. Levy, J.M.*, et al.* (2014) Autophagy Inhibition Improves Chemosensitivity in BRAFV600E Brain Tumors. *Cancer Discov* 4, 773-780

37. Roberts, D.J.*, et al.* (2014) Hexokinase-II positively regulates glucose starvation-induced autophagy through TORC1 inhibition. *Mol Cell* 53, 521-533

38. Yang, Z.*, et al.* (2013) Phosphofructokinase deficiency impairs ATP generation, autophagy, and redox balance in rheumatoid arthritis T cells. *J Exp Med* 210, 2119-2134

39. Hu, S.*, et al.* (2011) 13C-pyruvate imaging reveals alterations in glycolysis that precede c-Myc-induced tumor formation and regression. *Cell Metab* 14, 131-142

40. Li, Z., and Graham, B.H. (2012) Measurement of mitochondrial oxygen consumption using a Clark electrode. *Methods Mol Biol* 837, 63-72

41. LeBleu, V.S.*, et al.* (2014) PGC-1α mediates mitochondrial biogenesis and oxidative phosphorylation in cancer cells to promote metastasis. *Nat Cell Biol* 16, 992-1003

42. Loo, J.M.*, et al.* (2015) Extracellular metabolic energetics can promote cancer progression. *Cell* 160, 393-406

43. Goldsmith, J.*, et al.* (2014) Autophagy and cancer metabolism. *Methods Enzymol* 542, 25-57

44. Kaur, J., and Debnath, J. (2015) Autophagy at the crossroads of catabolism and anabolism. *Nat Rev Mol Cell Biol* 16, 461-472

45. Hara, T.*, et al.* (2006) Suppression of basal autophagy in neural cells causes neurodegenerative disease in mice. *Nature* 441, 885-889

46. Komatsu, M.*, et al.* (2006) Loss of autophagy in the central nervous system causes neurodegeneration in mice. *Nature* 441, 880-884

47. Rogov, V.*, et al.* (2014) Interactions between autophagy receptors and ubiquitin-like proteins form the molecular basis for selective autophagy. *Mol Cell* 53, 167-178

48. Mancias, J.D.*, et al.* (2014) Quantitative proteomics identifies NCOA4 as the cargo receptor mediating ferritinophagy. *Nature* 509, 105-109

49. Puissant, A.*, et al.* (2012) When autophagy meets cancer through p62/SQSTM1. *Am J Cancer Res* 2, 397-413

50. Komatsu, M.*, et al.* (2012) p62/SQSTM1/A170: physiology and pathology. *Pharmacol Res* 66, 457-462

51. Komatsu, M., *et al.* (2010) The selective autophagy substrate p62 activates the stress responsive transcription factor Nrf2 through inactivation of Keap1. *Nat Cell Biol* 12, 213-223

52. Ichimura, Y., *et al.* (2013) Phosphorylation of p62 activates the Keap1-Nrf2 pathway during selective autophagy. *Mol Cell* 51, 618-631

53. Duran, A., *et al.* (2011) p62 is a key regulator of nutrient sensing in the mTORC1 pathway. *Mol Cell* 44, 134-146

54. Linares, J.F., *et al.* (2013) K63 polyubiquitination and activation of mTOR by the p62-TRAF6 complex in nutrient-activated cells. *Mol Cell* 51, 283-296

55. Chen, N., *et al.* (2013) Autophagy restricts proliferation driven by oncogenic phosphatidylinositol 3-kinase in three-dimensional culture. *Oncogene* 32, 2543-2554

56. Newman, A.C., *et al.* (2012) TBK1 kinase addiction in lung cancer cells is mediated via autophagy of Tax1bp1/Ndp52 and non-canonical NF-kappaB signalling. *PLoS One* 7, e50672

57. Zhu, G., *et al.* (2007) Optineurin negatively regulates TNFalpha- induced NF-kappaB activation by competing with NEMO for ubiquitinated RIP. *Curr Biol* 17, 1438-1443

58. Rubio, N., *et al.* (2014) p38(MAPK)-regulated induction of p62 and NBR1 after photodynamic therapy promotes autophagic clearance of ubiquitin aggregates and reduces reactive oxygen species levels by supporting Nrf2-antioxidant signaling. *Free Radic Biol Med* 67, 292-303

59. Kuo, T.C., *et al.* (2011) Midbody accumulation through evasion of autophagy contributes to cellular reprogramming and tumorigenicity. *Nat Cell Biol* 13, 1214-1223

60. Labelle, M., *et al.* Direct Signaling between Platelets and Cancer Cells Induces an Epithelial-Mesenchymal-Like Transition and Promotes Metastasis. *Cancer Cell* 20, 576-590

61. Gulhati, P., *et al.* (2011) mTORC1 and mTORC2 Regulate EMT, Motility, and Metastasis of Colorectal Cancer via RhoA and Rac1 Signaling Pathways. *Cancer Research* 71, 3246-3256

62. Shibue, T., *et al.* (2012) The outgrowth of micrometastases is enabled by the formation of filopodium-like protrusions. *Cancer Discov* 2, 706-721

63. Whitehouse, C.A., *et al.* (2010) Neighbor of Brca1 gene (Nbr1) functions as a negative regulator of postnatal osteoblastic bone formation and p38 MAPK activity. *Proceedings of the National Academy of Sciences* 107, 12913-12918

64. Bragado, P., *et al.* (2013) TGF-beta2 dictates disseminated tumour cell fate in target organs through TGF-beta-RIII and p38alpha/beta signalling. *Nat Cell Biol* 15, 1351-1361

65. Chiarugi, P., and Giannoni, E. (2008) Anoikis: A necessary death program for anchorage-dependent cells. *Biochemical Pharmacology* 76, 1352-1364

66. Frisch, S., and Francis, H. (1994) Disruption of epithelial cell-matrix interactions induces apoptosis. *J. Cell Biol.* 124, 619-626

67. Mailleux, A.A.*, et al.* (2007) BIM Regulates Apoptosis during Mammary Ductal Morphogenesis, and Its Absence Reveals Alternative Cell Death Mechanisms. *Developmental Cell* 12, 221-234

68. Yawata, A.*, et al.* (1998) Prolonged cell survival enhances peritoneal dissemination of gastric cancer cells. *Oncogene* 16, 2681-2686

69. Douma, S.*, et al.* (2004) Suppression of anoikis and induction of metastasis by the neurotrophic receptor TrkB. *Nature* 430, 1034-1039

70. Fung, C.*, et al.* (2008) Induction of Autophagy during Extracellular Matrix Detachment Promotes Cell Survival. *Mol. Biol. Cell* 19, 797-806

71. Lock, R., and Debnath, J. (2008) Extracellular matrix regulation of autophagy. *Current Opinion in Cell Biology* 20, 583-588

72. Fung, C.*, et al.* (2008) Induction of autophagy during extracellular matrix detachment promotes cell survival. *Mol Biol Cell* 19, 797-806

73. Peng, Y.F.*, et al.* (2013) Autophagy inhibition suppresses pulmonary metastasis of HCC in mice via impairing anoikis resistance and colonization of HCC cells. *Autophagy* 9, 2056-2068

74. Miranti, C.K., and Brugge, J.S. (2002) Sensing the environment: a historical perspective on integrin signal transduction. *Nat Cell Biol* 4, E83-E90

75. Edinger, A.L., and Thompson, C.B. (2002) Akt Maintains Cell Size and Survival by Increasing mTOR-dependent Nutrient Uptake. *Mol. Biol. Cell* 13, 2276-2288

76. Schafer, Z.T.*, et al.* (2009) Antioxidant and oncogene rescue of metabolic defects caused by loss of matrix attachment. *Nature* 461, 109-113

77. Macintosh, R.L.*, et al.* (2012) Inhibition of autophagy impairs tumor cell invasion in an organotypic model. *Cell Cycle* 11, 2022-2029

78. Galavotti, S.*, et al.* (2013) The autophagy-associated factors DRAM1 and p62 regulate cell migration and invasion in glioblastoma stem cells. *Oncogene* 32, 699-712

79. Beckner, M.E.*, et al.* (2010) Identification of ATP citrate lyase as a positive regulator of glycolytic function in glioblastomas. *Int J Cancer* 126, 2282-2295

80. Li, J.*, et al.* (2013) Autophagy promotes hepatocellular carcinoma cell invasion through activation of epithelial-mesenchymal transition. *Carcinogenesis* 34, 1343-1351

81. Lock, R.*, et al.* (2014) Autophagy-dependent production of secreted factors facilitates oncogenic RAS-driven invasion. *Cancer Discov* 4, 466-479

82. Zhan, Z.*, et al.* (2014) Autophagy facilitates TLR4- and TLR3-triggered migration and invasion of lung cancer cells through the promotion of TRAF6 ubiquitination. *Autophagy* 10, 257-268

83. Deretic, V.*, et al.* (2012) Autophagy intersections with conventional and unconventional secretion in tissue development, remodeling and inflammation. *Trends Cell Biol* 22, 397-406

84. O'Reilly, S.*, et al.* (2014) Interleukin-6 (IL-6) trans signaling drives a STAT3-dependent pathway that leads to hyperactive transforming growth factor-beta (TGF-beta) signaling promoting SMAD3 activation and fibrosis via Gremlin protein. *J Biol Chem* 289, 9952-9960

85. Aguirre-Ghiso, J.A. (2007) Models, mechanisms and clinical evidence for cancer dormancy. *Nat Rev Cancer* 7, 834-846

86. Nguyen, D.X.*, et al.* (2009) Metastasis: from dissemination to organ-specific colonization. *Nat Rev Cancer* 9, 274-284

87. White, D.E.*, et al.* (2004) Targeted disruption of [beta]1-integrin in a transgenic mouse model of human breast cancer reveals an essential role in mammary tumor induction. *Cancer Cell* 6, 159-170

88. Zhang, X.H.F.*, et al.* (2009) Latent Bone Metastasis in Breast Cancer Tied to Src-Dependent Survival Signals. *Cancer Cell* 16, 67-78

89. Han, J.*, et al.* (2008) Involvement of Protective Autophagy in TRAIL Resistance of Apoptosis-defective Tumor Cells. *Journal of Biological Chemistry* 283, 19665-19677

90. Herrero-Martin, G.*, et al.* (2009) TAK1 activates AMPK-dependent cytoprotective autophagy in TRAIL-treated epithelial cells. *EMBO J* 28, 677-685

91. Melendez, A.*, et al.* (2003) Autophagy Genes Are Essential for Dauer Development and Life-Span Extension in C. elegans. *Science* 301, 1387-1391

92. Liang, J.*, et al.* (2007) The energy sensing LKB1-AMPK pathway regulates p27kip1 phosphorylation mediating the decision to enter autophagy or apoptosis. *Nat Cell Biol* 9, 218-224

93. Barkan, D.*, et al.* (2008) Inhibition of Metastatic Outgrowth from Single Dormant Tumor Cells by Targeting the Cytoskeleton. *Cancer Res* 68, 6241-6250

94. Lu, Z.*, et al.* (2008) The tumor suppressor gene ARHI regulates autophagy and tumor dormancy in human ovarian cancer cells. *The Journal of Clinical Investigation* 118, 3917-3929

95. Friedl, P., and Wolf, K. (2010) Plasticity of cell migration: a multiscale tuning model. *J Cell Biol* 188, 11-19

96. Ridley, A.J.*, et al.* (2003) Cell migration: integrating signals from front to back. *Science* 302, 1704-1709

97. Gardel, M.L.*, et al.* (2010) Mechanical integration of actin and adhesion dynamics in cell migration. *Annu Rev Cell Dev Biol* 26, 315-333

98. Geiger, B., and Yamada, K.M. (2011) Molecular architecture and function of matrix adhesions. *Cold Spring Harb Perspect Biol* 3

99. Wolfenson, H.*, et al.* (2013) Dynamic regulation of the structure and functions of integrin adhesions. *Dev Cell* 24, 447-458

100. Webb, D.J.*, et al.* (2004) FAK-Src signalling through paxillin, ERK and MLCK regulates adhesion disassembly. *Nat Cell Biol* 6, 154-161

101. Stehbens, S.J.*, et al.* (2014) CLASPs link focal-adhesion-associated microtubule capture to localized exocytosis and adhesion site turnover. *Nat Cell Biol* 16, 561-573

102. Feng, Y.*, et al.* (2014) The machinery of macroautophagy. *Cell Res* 24, 24-41

103. Tuloup-Minguez, V.*, et al.* (2013) Autophagy modulates cell migration and beta1 integrin membrane recycling. *Cell Cycle* 12, 3317-3328

104. DiMilla, P.A.*, et al.* (1991) Mathematical model for the effects of adhesion and mechanics on cell migration speed. *Biophys J* 60, 15-37

105. DiMilla, P.A.*, et al.* (1993) Maximal migration of human smooth muscle cells on fibronectin and type IV collagen occurs at an intermediate attachment strength. *J Cell Biol* 122, 729-737

106. Gupton, S.L., and Waterman-Storer, C.M. (2006) Spatiotemporal feedback between actomyosin and focal-adhesion systems optimizes rapid cell migration. *Cell* 125, 1361-1374

107. Palecek, S.P.*, et al.* (1997) Integrin-ligand binding properties govern cell migration speed through cell-substratum adhesiveness. *Nature* 385, 537-540

108. Huttenlocher, A.*, et al.* (1996) Modulation of cell migration by integrin-mediated cytoskeletal linkages and ligand-binding affinity. *J Cell Biol* 134, 1551-1562

109. Stehbens, S.J., and Wittmann, T. (2014) Analysis of focal adhesion turnover: a quantitative live-cell imaging example. *Methods Cell Biol* 123, 335-346

110. Meenderink, L.M.*, et al.* (2010) P130Cas Src-binding and substrate domains have distinct roles in sustaining focal adhesion disassembly and promoting cell migration. *PLoS One* 5, e13412

111. Cavalcanti-Adam, E.A.*, et al.* (2007) Cell spreading and focal adhesion dynamics are regulated by spacing of integrin ligands. *Biophys J* 92, 2964-2974

112. Geiger, T., and Zaidel-Bar, R. (2012) Opening the floodgates: proteomics and the integrin adhesome. *Curr Opin Cell Biol* 24, 562-568

113. Dowdle, W.E.*, et al.* (2014) Selective VPS34 inhibitor blocks autophagy and uncovers a role for NCOA4 in ferritin degradation and iron homeostasis in vivo. *Nat Cell Biol* 16, 1069-1079

114. Pohl, C., and Jentsch, S. (2009) Midbody ring disposal by autophagy is a post-abscission event of cytokinesis. *Nat Cell Biol* 11, 65-70

115. Johansen, T., and Lamark, T. (2011) Selective autophagy mediated by autophagic adapter proteins. *Autophagy* 7, 279-296

116. Kraft, C.*, et al.* (2010) Selective autophagy: ubiquitin-mediated recognition and beyond. *Nat Cell Biol* 12, 836-841

117. Birgisdottir, A.B.*, et al.* (2013) The LIR motif - crucial for selective autophagy. *J Cell Sci* 126, 3237-3247

118. Kirkin, V.*, et al.* (2009) A role for NBR1 in autophagosomal degradation of ubiquitinated substrates. *Mol Cell* 33, 505-516

119. Waters, S.*, et al.* (2009) Interactions with LC3 and polyubiquitin chains link nbr1 to autophagic protein turnover. *FEBS Lett* 583, 1846-1852

120. Martin, M.D.*, et al.* (2008) Effect of ablation or inhibition of stromal matrix metalloproteinase-9 on lung metastasis in a breast cancer model is dependent on genetic background. *Cancer Res* 68, 6251-6259

121. Mathew, R.*, et al.* (2008) Immortalized mouse epithelial cell models to study the role of apoptosis in cancer. *Methods Enzymol* 446, 77-106

122. Debnath, J.*, et al.* (2003) Morphogenesis and oncogenesis of MCF-10A mammary epithelial acini grown in three-dimensional basement membrane cultures. *Methods* 30, 256-268

123. Hu, K.*, et al.* (2007) Differential transmission of actin motion within focal adhesions. *Science* 315, 111-115

124. Kitamura, T.*, et al.* (2003) Retrovirus-mediated gene transfer and expression cloning: powerful tools in functional genomics. *Exp Hematol* 31, 1007-1014

125. Husemann, Y.*, et al.* (2008) Systemic spread is an early step in breast cancer. *Cancer Cell* 13, 58-68

126. Peinado, H.*, et al.* (2011) The secreted factors responsible for pre-metastatic niche formation: old sayings and new thoughts. *Semin Cancer Biol* 21, 139-146

127. Kouros-Mehr, H.*, et al.* (2008) GATA-3 links tumor differentiation and dissemination in a luminal breast cancer model. *Cancer Cell* 13, 141-152

128. Chambers, A.F.*, et al.* (2002) Dissemination and growth of cancer cells in metastatic sites. *Nat Rev Cancer* 2, 563-572

129. Guy, C.T.*, et al.* (1992) Induction of mammary tumors by expression of polyomavirus middle T oncogene: a transgenic mouse model for metastatic disease. *Molecular and Cellular Biology* 12, 954-961

130. Lin, E.Y.*, et al.* (2003) Progression to Malignancy in the Polyoma Middle T Oncoprotein Mouse Breast Cancer Model Provides a Reliable Model for Human Diseases. *The American Journal of Pathology* 163, 2113-2126

131. Shibue, T., and Weinberg, R.A. (2009) Integrin beta1-focal adhesion kinase signaling directs the proliferation of metastatic cancer cells disseminated in the lungs. *Proc Natl Acad Sci U S A* 106, 10290-10295

132. Stehbens, S., and Wittmann, T. (2012) Targeting and transport: how microtubules control focal adhesion dynamics. *J Cell Biol* 198, 481-489

133. Yla-Anttila, P.*, et al.* (2009) Monitoring autophagy by electron microscopy in Mammalian cells. *Methods Enzymol* 452, 143-164

134. Itakura, E., and Mizushima, N. (2010) Characterization of autophagosome formation site by a hierarchical analysis of mammalian Atg proteins. *Autophagy* 6, 764-776

135. Tooze, S.A., and Yoshimori, T. (2010) The origin of the autophagosomal membrane. *Nat Cell Biol* 12, 831-835

136. Mann, S.S., and Hammarback, J.A. (1994) Molecular characterization of light chain 3. A microtubule binding subunit of MAP1A and MAP1B. *J Biol Chem* 269, 11492-11497

137. Marchbank, K.*, et al.* (2012) MAP1B Interaction with the FW Domain of the Autophagic Receptor Nbr1 Facilitates Its Association to the Microtubule Network. *Int J Cell Biol* 2012, 208014

138. Winograd-Katz, S.E.*, et al.* (2014) The integrin adhesome: from genes and proteins to human disease. *Nat Rev Mol Cell Biol* 15, 273-288

139. Schiller, H.B., and Fassler, R. (2013) Mechanosensitivity and compositional dynamics of cell-matrix adhesions. *EMBO Rep* 14, 509-519

140. Deng, S., and Huang, C. (2014) E3 ubiquitin ligases in regulating stress fiber, lamellipodium, and focal adhesion dynamics. *Cell Adh Migr* 8, 49-54

141. Muller, S.*, et al.* (2006) Crystal structure of the PB1 domain of NBR1. *FEBS Lett* 580, 341-344

142. Whitehouse, C.*, et al.* (2002) NBR1 interacts with fasciculation and elongation protein zeta-1 (FEZ1) and calcium and integrin binding protein (CIB) and shows developmentally restricted expression in the neural tube. *Eur J Biochem* 269, 538-545

143. Ezratty, E.J.*, et al.* (2005) Microtubule-induced focal adhesion disassembly is mediated by dynamin and focal adhesion kinase. *Nat Cell Biol* 7, 581-590

144. Ezratty, E.J.*, et al.* (2009) Clathrin mediates integrin endocytosis for focal adhesion disassembly in migrating cells. *J Cell Biol* 187, 733-747

145. Chao, W.T., and Kunz, J. (2009) Focal adhesion disassembly requires clathrin-dependent endocytosis of integrins. *FEBS Lett* 583, 1337-1343

146. Franco, S.J.*, et al.* (2004) Calpain-mediated proteolysis of talin regulates adhesion dynamics. *Nat Cell Biol* 6, 977-983

147. Chan, K.T.*, et al.* (2010) Regulation of adhesion dynamics by calpain-mediated proteolysis of focal adhesion kinase (FAK). *J Biol Chem* 285, 11418-11426

148. Cortesio, C.L.*, et al.* (2011) Calpain-mediated proteolysis of paxillin negatively regulates focal adhesion dynamics and cell migration. *J Biol Chem* 286, 9998-10006

149. Shi, F., and Sottile, J. (2011) MT1-MMP regulates the turnover and endocytosis of extracellular matrix fibronectin. *J Cell Sci* 124, 4039-4050

150. Lee, E.*, et al.* (2014) Autophagy is essential for cardiac morphogenesis during vertebrate development. *Autophagy* 10, 572-587

151. Tsai, J.H.*, et al.* (2012) Spatiotemporal Regulation of Epithelial-Mesenchymal Transition is Essential for Squamous Cell Carcinoma Metastasis. *Cancer Cell* 22, 725-736

152. Nguyen, D.X.*, et al.* (2009) Metastasis: from dissemination to organ-specific colonization. *Nat Rev Cancer* 9, 274-284

153. Warr, M.R.*, et al.* (2013) FOXO3A directs a protective autophagy program in haematopoietic stem cells. *Nature* 494, 323-327

154. Peinado, H.*, et al.* (2012) Melanoma exosomes educate bone marrow progenitor cells toward a pro-metastatic phenotype through MET. *Nat Med* 18, 883-891

155. Murrow, L.*, et al.* (2015) ATG12-ATG3 interacts with Alix to promote basal autophagic flux and late endosome function. *Nat Cell Biol* 17, 300-310

# APPENDIX A

## Generation of transgenic mice for studies of autophagy gene knockout during metastasis

**The following appendix is unpublished work.**

**Contributions:** I maintained mouse colonies and coordinated and managed the breeding of the mice described here. I generated a bank of primary tumor cells and the mammary tumor line derived from these mice, as well as verified *atg12* deletion methods and syngeneic growth of primary cells and the *atg12 fl/fl* tumor cell line. Fanya Rostker was responsible for mouse husbandry and genotyping, and Kimberley Woo assisted with tumor harvest for isolation of primary tumor cells. The UCSF Genomics Core performed microsatellite genotyping, and the UCSF Mouse Pathology Core provided support for sectioning and H&E staining of tissue. Jay Debnath supervised the study.

## INTRODUCTION

The *MMTV-PyMT* mouse model of mammary carcinoma has proven to be an invaluable and necessary tool for studying breast cancer progression[1-2]. Indeed, countless studies in which *MMTV-PyMT* mice have been crossed to a variety of genetically modified mice have shaped our understanding of essential metastasis traits. Notably, the use of the *MMTV-PyMT* model has the primary advantage of allowing for characterization of metastatic phenotypes in an immune-competent background. Such studies can be performed by directly breeding mice of interest to *MMTV-PyMT* mice and monitoring progression of autochthonous tumors or by transplanting tumor cells derived from *MMTV-PyMT* mice into wild-type syngeneic hosts[3].

Due to the utility of *MMTV-PyMT* in studying in breast cancer progression, we sought to establish *MMTV-PyMT* mice harboring floxed alleles of the essential autophagy regulator *atg12* (*atg12 fl/fl*) for use as an additional tool to interrogate the function of autophagy during breast cancer metastasis. Although I have described in Chapter 3 the use of shRNA against ATG7 to inhibit autophagy in a PyMT cell line, the ability to knockout *atg12* in PyMT tumor cells will allow us to corroborate our results in the context of the loss-of-function of an additional autophagy gene. Because autophagy regulators may have autophagy-independent functions, it is necessary to verify functional roles for autophagy by manipulating multiple ATGs. To date, implementation of shRNA reagents targeting additional ATGs in the PyMT cell line described in Chapter 3 has proven unsuccessful at efficiently inhibiting autophagy, necessitating the use of a knockout strategy for *atg12*. Furthermore, the use of these genetically engineered models provides the additional opportunity to exploit established models of inducible cre-recombinase for a highly specific and temporal analysis of the requirement for autophagy during breast cancer metastasis. While inducible shRNA reagents are increasingly available, those too have been ineffective in our hands for autophagy inhibition.

Here, I describe breeding efforts to generate *atg12 fl/fl; MMTV-PyMT* mice to be used as donors of primary tumor cells for syngeneic spontaneous and experimental metastasis studies. In addition, a cell line was derived from these tumors. Finally, these mice were further bred for incorporation of an inducible cre-recombinase allele (*CAG-CreER*) for inducible deletion of *atg12*.

## RESULTS AND DISCUSSION

The generation of *atg12 fl/fl* mice by our lab has been previously described[4]. To verify its use for functional studies of autophagy-dependent phenotypes, we validated that, similar to knockout of other essential *atgs*, loss of *atg12* leads to neonatal lethality, as well as a complete block in autophagy in primary mouse embryonic fibroblasts following cre-recombinase-mediated deletion of *atg12 in vivo*. These mice were originally generated on a mixed C57Bl/6 background. Therefore, to enable syngeneic transplant studies, *atg12 fl/fl* mice were first backcrossed two generations to wild-type C57Bl/6 mice. Purity following backcrosses was assessed by microsatellite genotyping of approximately 185 alleles for the C57Bl/6 strain compared to other strains. This analysis revealed an increase in purity from 89% to 96% following these backcrosses.

*Atg12 fl/fl* mice were further crossed with *MMTV-PyMT; β-actin-CFP* mice to introduce the PyMT oncogene and facilitate tracking of tumor cells upon transplantation through expression of CFP. The mice were also bred with mice harboring a cre-recombinase reporter allele in which *tdRFP* is preceded by a floxed stop cassette knocked into the *Rosa26* locus (*Rosa26-LSL-tdRFP*) for use as tool to monitor successful activity of cre-recombinase in cells of interest[5]. Both *MMTV-PyMT; β-actin-CFP* mice and *Rosa26-LSL-tdRFP* mice were on a C57Bl/6 background. A large bank of frozen primary tumor cells from *atg12 fl/fl; Rosa26-LSL-tdRFP; MMTV-PyMT; β-actin-CFP* mice has been generated for future use in studies of autophagy-dependent breast cancer tumorigenesis and metastasis.

During the generation of near pure C57Bl/6 *atg12 fl/fl* mice, *atg12 fl/fl; MMTV-PyMT; Rosa26-LSL-RFP* mice on a mixed background were generated to expedite validation of methods for *ex vivo* deletion of *atg12* in primary tumor cells. Advanced stage mammary tumors were harvested from females of this genotype, and primary tumor organoids were isolated using

previously established protocols optimized for enrichment of mammary epithelium[6]. To delete *atg12*, organoids were infected in suspension culture with adenovirus expressing Cre-eGFP or eGFP alone. Imaging of cultures 24 h after infection revealed that cells infected with adenoviral cre-recombinase were both eGFP and tdRFP positive, indicating successful infection and activity of cre-recombinase (Fig. 1 A). In contrast, cells infected with adenoviral eGFP only were eGFP positive but did not express tdRFP (Fig. 1 A). Because sufficient material was not available for immunoblot-based verification of the loss of *atg12* expression in this experiment, PCR-based analysis was used as a preliminary test to directly assess deletion of *atg12*. This demonstrated that cells treated with adenoviral Cre-eGFP harbored the *atg12* null allele, consisting of only exons 1 and 4 (Fig. 1 B). To confirm whether *atg12* deletion can be maintained in tumors following transplantation of infected *atg12 fl/fl; MMTV-PyMT; Rosa26-LSL-RFP* organoids, infected organoids were orthotopically transplanted into the cleared mammary fat pad of nude mice. Immunoblot analysis of tumors arising from these transplants showed that infection of cells with adenoviral cre-recombinase led to efficient deletion of *atg12* and inhibition of autophagy, as shown by a lack of LC3-II (Fig. 1 C). These results confirm that *ex vivo* deletion of *atg12* using adenoviral cre-recombinase is a suitable method for generating autophagy-deficient primary PyMT tumor cells for transplantation studies. Furthermore, due to our interest in establishing the role of autophagy during metastasis, we confirmed that primary tumor cells from near pure C57Bl/6 *atg12 fl/fl; Rosa26-LSL-tdRFP; MMTV-PyMT; β-actin-CFP* mice give rise to lung metastases when injected into the tail vein of wild-type C57Bl/6 mice (Fig. 2).

In addition to generating a frozen bank of primary tumor cells, *atg12 fl/fl; Rosa26-LSL-tdRFP; MMTV-PyMT; β-actin-CFP* primary tumor cells were also plated in culture to generate a cell line. Although initial sub-culturing of primary tumor cells proved that they are in fact quite slow growing and seemingly senescent, after months of culture in which the cells were not

passaged, but culture medium was replaced every few days, we acquired a cell line that spontaneously grew out. Morphologically, these cells appeared epithelial and looked similar to the R221A-PyMT cell line described in Chapter 3 (Fig. 3 A). In addition, infection with adenoviral cre-recombinase leads to deletion of *atg12*, accumulation of the autophagy-specific substrate, p62, and inhibition of autophagy (Fig. 3 B).

We next wanted to determine if this cell line was capable of establishing primary tumors and lung metastases in wild-type C57Bl/6 hosts. Cells were injected into the tail vein or transplanted orthotopically into the cleared mammary fat pad of recipient mice. After five weeks, experimental metastases were detected both by H&E and culturing of lung tumor cells out of digested lung tissue from mice injected into the tail vein with these cells (Fig. 4 A). In addition, this cell line also gave rise to orthotopic tumors, and lung DTCs were detected in cultures of lung cells from orthotopically-transplanted mice (Fig. 4 B). However, due to the potentially small amount of lung DTCs, we could not confidently identify lung metastases by H&E during spontaneous metastasis. Nevertheless, these results demonstrate that this cell line can be used to assess the requirement for autophagy in regulating *in vivo* breast cancer metastasis. Furthermore, derivatives of this cell line have been cultured out from the experimental lung metastases and orthotopic tumor; these sublines may be better suited for rapid *in vivo* growth and are currently being used to assess this possibility.

Finally, *atg12 fl/fl; Rosa26-LSL-tdRFP; MMTV-PyMT; β-actin-CFP* have been further bred to *CAG-CreER* mice for introduction of a tamoxifen-inducible cre-recombinase[7]. Studies in which tumor cells from these mice are transplanted will allow for a temporal dissection of the role of autophagy during metastasis. We have verified that *ex vivo* treatment of primary tumor cells from these mice with 4-hydroxytamoxifen leads to *atg12* deletion, accumulation of the autophagy substrate p62, and inhibition of autophagy (Fig. 5). This mouse continues to be used by others in the lab who have demonstrated that *in vivo* treatment with 4-hydroxytamoxifen also successfully leads to autophagy inhibition.

In summary, we have generated multiple *in vivo* tools for genetic manipulation of autophagy during metastasis. In addition to RNAi-based methods described in Chapter 3, we now have various ways to delete *atg12* in PyMT tumor cells. These methods include *ex vivo* viral introduction of cre-recombinase into primary tumor cells, deletion of *atg12* in stable cell lines, and *ex vivo* or *in vivo* tamoxifen-induced *atg12* deletion. Additionally, we have also bred *atg5 fl/fl* mice to *MMTV-PyMT* mice to allow for genetic knockout of an additional *atg*. Overall, we are well equipped to comprehensively study the contribution of autophagy to *in vivo* cancer metastasis.

**Figure 1**

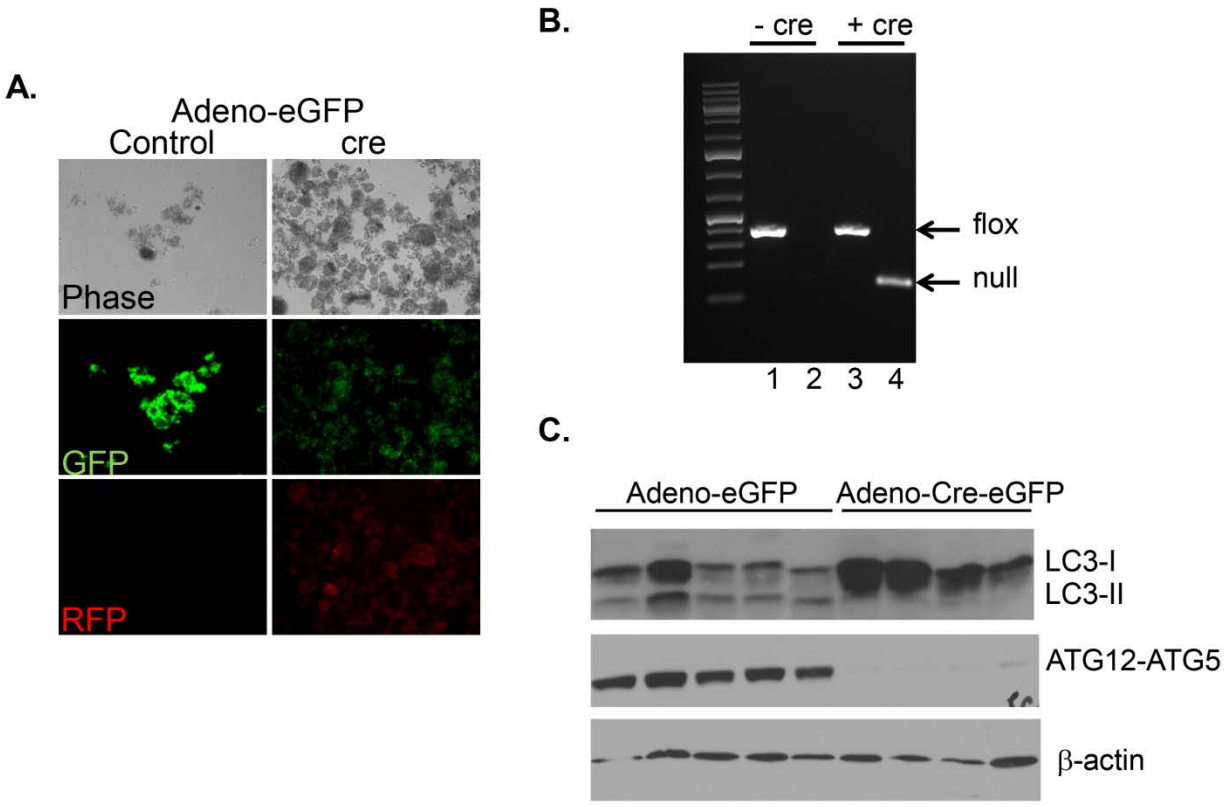


**Figure 1: Validation of *atg12* deletion and autophagy inhibition in *atg12 fl/fl* primary tumor cells.** (A) Images of primary tumor organoids in suspension culture following infection with adenovirus. (B) PCR analysis of primary tumor organoids to verify cre-recombinase mediated recombination of *atg12* allele. In lanes 1 and 3, PCR was performed for the floxed allele, and in lanes 2 and 4, PCR was performed for the null allele. (C) Immunoblot of lysates from tumors arising from *atg12 fl/fl; Rosa26-LSL-tdRFP; MMTV-PyMT* primary cells to verify loss of ATG12 protein expression and inhibition of autophagy, as shown by a lack of LC3-II. β-actin is the loading control.

**Figure 2**

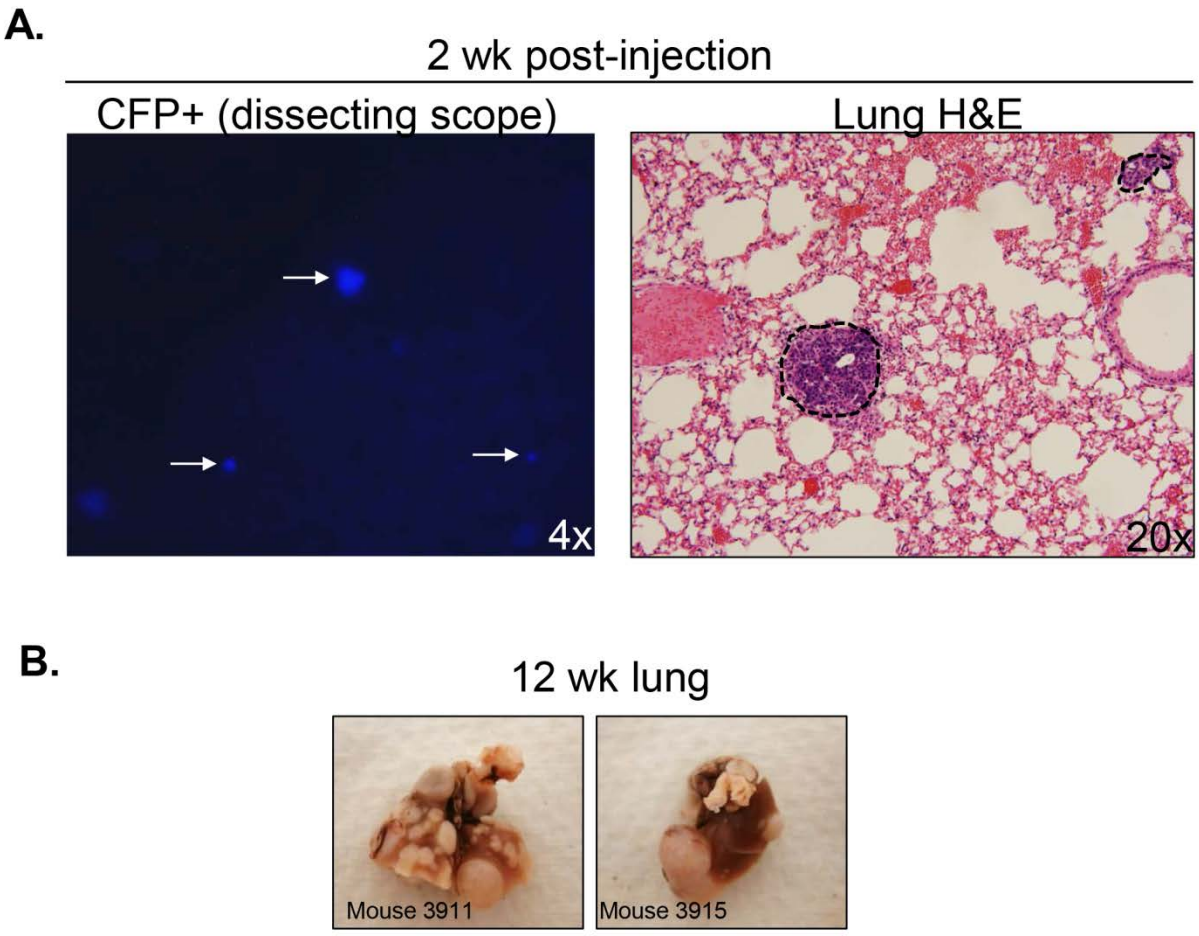


**Figure 2: Growth of experimental metastases following tail vein injection of primary tumor cells.** (A) *atg12 fl/fl; Rosa26-LSL-tdRFP; MMTV-PyMT; β-actin-CFP* primary tumor cells were injected into the lateral tail vein of wild-type C57Bl/6 mice and metastases were assessed at two weeks post-injection by the presence of CFP-expressing tumor cells in the lung and the growth of metastases by H&E staining of lung sections. (B) At 12 weeks post-injection, surface metastases were grossly visible on excised lungs.

**Figure 3**

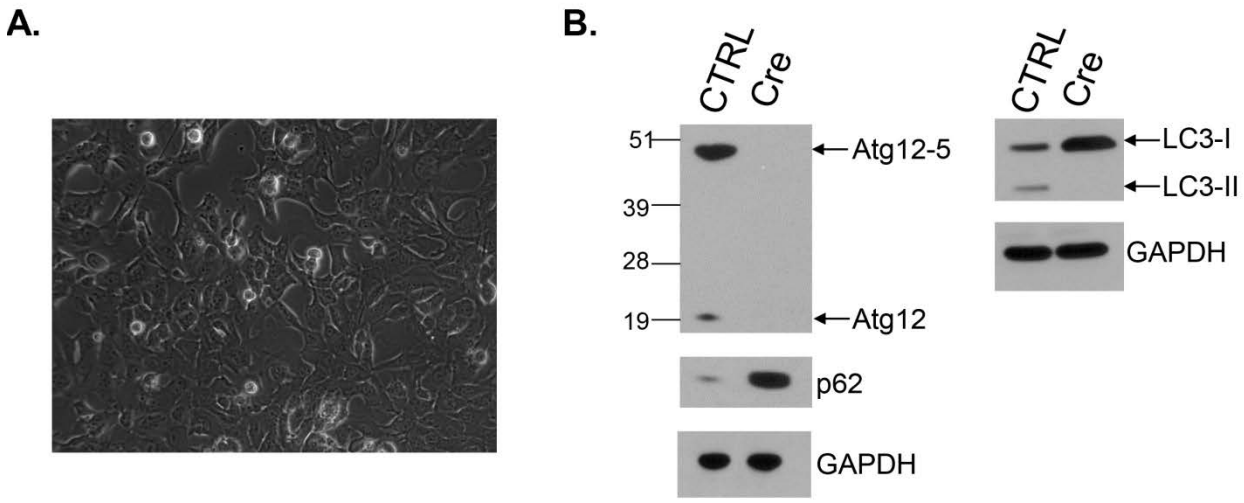


**Figure 3: Generation of an *atg12 fl/fl; Rosa26-LSL-tdRFP; MMTV-PyMT; β-actin-CFP* mammary tumor cell line.** (A) Morphology of cells in monolayer culture by phase-contrast microscopy. (B) Immunoblot of cell lysates to verify loss of ATG12 protein expression and inhibition of autophagy, as shown by an accumulation of p62 and a lack of LC3-II, with adenoviral cre-recombinase. GAPDH is the loading control.

**Figure 4**

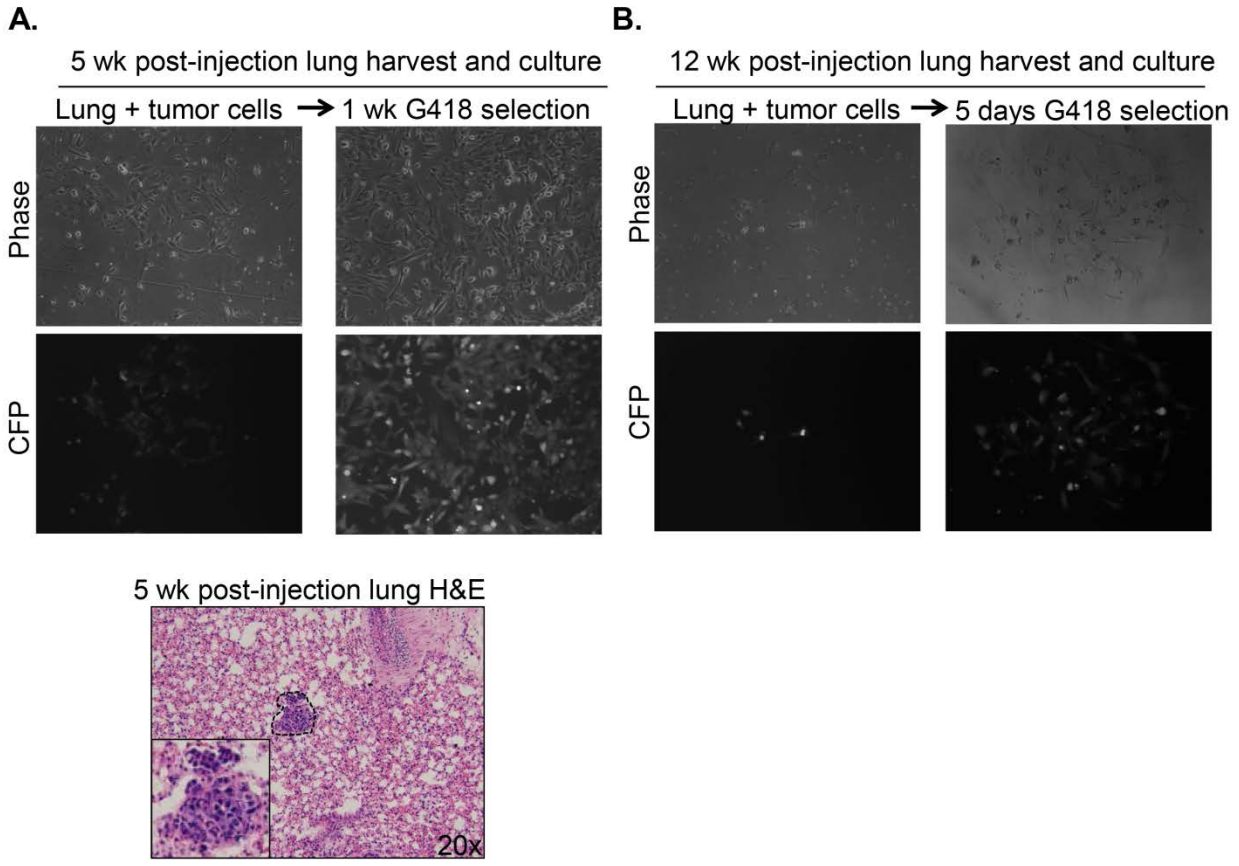


**Figure 4: Establishment of metastases by *atg12 fl/fl; Rosa26-LSL-tdRFP; MMTV-PyMT; β-actin-CFP* mammary tumor cell line in syngeneic hosts.** (A) The presence of tumor cells in the lung was assessed by culture of lung cells and metastases were observed by lung H&E following tail vein injection of cells. (B) The presence of lung DTCs during spontaneous metastasis was assessed by culture of lung cells. In both (A) and (B) tumor cells were selected for by G418 selection.

**Figure 5**

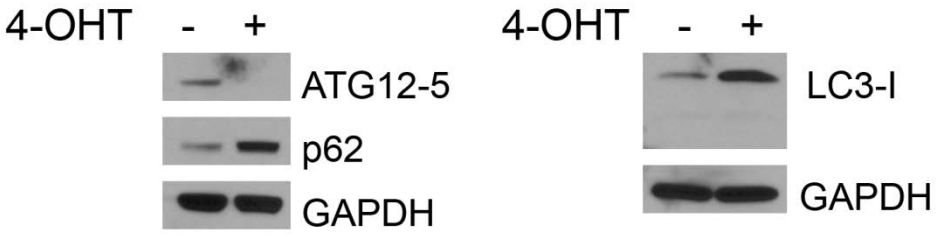


**Figure 5: Deletion of *atg12* with tamoxifen-inducible cre-recombinase.** *atg12 fl/fl; Rosa26-LSL-tdRFP; MMTV-PyMT; β-actin-CFP*; *CAG-CreER* primary tumor cells were treated *in vitro* with 4-hydroxytamoxifen (4-OHT). Immunoblot of ATG12, p62, and LC3 demonstrates autophagy inhibition. GAPDH is the loading control. Note that LC3-II was not visible in these blots; however, accumulation of LC3-I, as can be seen here, typically occurs with *atg* knockout.

## MATERIALS AND METHODS

### Animal Studies

All animal experiments were performed in accordance with protocols approved by the UCSF IACUC, and mice were housed under pathogen-free conditions in the UCSF barrier facility. C57Bl/6 *MMTV-PyMT; β-actin-CFP* mice were generously provided by Zena Werb. *Rosa26-LSL-tdRFP* mice were kindly provided by Mark Ansel. *CAG-CreER* mice were from Scott Seeley. Wild-type C57Bl/6 mice for syngeneic transplants were purchased from Jackson Laboratories. For experimental metastasis experiments, 6-7 week old female mice were injected intravenously through the lateral tail vein with 1 x $10^6$ tumor cells (primary and cell line) resuspended in PBS. For primary tumor growth and spontaneous metastasis experiments, 1 x $10^6$ tumor cells (primary and cell line) were resuspended in 1:1 PBS:Matrigel (Corning) and injected into the cleared #4 mammary fat pad of 3 week old mice. Tumors were monitored once weekly until palpable and then measured twice weekly using a caliper. Tumor volume was calculated as: volume = 0.52 x length x $(\text{width})^2$, with the length being the longest diameter and width being the shortest diameter.

### Cell culture

Primary tumor organoids were harvested as previously described[6]. Briefly, tumors were harvested and minced with a scalpel. They were then digested in collagenase buffer (DMEM/F12, 2 mg/ml collagenase, 2 mg/ml trypsin, 5% FBS, 50 μg/ml gentamicin, and 5 μg/ml insulin) at 37$^o$C with shaking for approximately 1 h. Cells were pelleted by centrifugation at 1500 rpm for 10 min and DNase treated. Following several rounds of differential centrifugation to remove single-cells for isolation of epithelial organoids, cells were frozen for later use in 100% FBS/10% DMSO.

For *ex vivo* adenoviral infection, primary tumor organoids were thawed in growth medium (DMEM/F12 supplemented with 1 μg/ml hydrocortisone, 50 ng/ml EGF, 10 μg/ml insulin, 10% FBS, penicillin, and streptomycin) and plated at low density in 24-well ultra-low attachment plates. Cells were infected overnight with adenoviral eGFP or Cre-eGFP (University of Iowa Viral Vector Core Facility) and then viral media was washed out. 48 h post-infection, cells were analyzed for *atg12* deletion or sorted for GFP+ cells and then orthotopically injected. Adenoviral infection of the cell line was performed similarly, except adherent cultures of cells were infected. Treatment with 4-hydroxytamoxifen was performed at a dose of 1 μM for three to five days.

To establish *ex vivo* cultures of lung tumor cells from mice with experimental or spontaneous metastasis, a portion of lung tissue was minced and then digested in collagenase buffer (DMEM/F12, 2 mg/ml collagenase, 2 mg/ml trypsin, 5% FBS, 50 μg/ml gentamicin, and 5 μg/ml insulin) at 37$^{o}$C with shaking for approximately 1 h. Cells were pelleted by centrifugation at 1500 rpm for 5 min, DNAse treated, and subjected to red blood cell lysis. The remaining cell pellet was resuspended and plated in growth medium. 24-48 h post-plating, growth medium containing G418 was added to the cells to specifically select out tumor cells from the host lung cells for immunoblot analysis.

**PCR analysis**

To assess *atg12* deletion by PCR, DNA from the Triton X-100 insoluble pellet was genotyped for the presence of floxed and null alleles. The following three primer reaction is used for detecting the floxed allele (originally from a protocol for detecting both floxed and wild-type alleles): 5'- ATG TGA ATC AGT CCT TTG CCC-3', 5'- ACT CTG AAG GCG TTC ACG GC-3', and 5'- CTC TGA AGG CGT TCA CAA CA-3'. The following primer pair detects the null allele: 5'- ACT CTG AAG GCG TTC ACG GC-3' and 5'-CAC CCT GCT TTT ACG AAG CCC A-3'.

**Immunoblotting**

The following antibodies were used for immunoblotting: anti-ATG12 (Cell Signaling 2011, 1:200), anti-p62/SQSTM1 (Progen Biotechnik GP62-C, 1:1000), anti-β-actin (Abcam, 1:1000), and anti-GAPDH (Millipore AB2302, 1:5000). A rabbit polyclonal antibody against MAP1LC3 has been previously described and is now commercially available (Millipore ABC232, 1:1000)[8]. For immunoblot analysis, cells were lysed in RIPA buffer (1% Triton X-100, 1% sodium deoxycholate, 0.1% SDS, 25 mM Tris, pH 7.6, 150 mM NaCl) plus protease inhibitor cocktail (Sigma Aldrich), 10 mM NaF, 10 mM β-glycerophosphate, 1 mM $Na_3VO_4$, 10 nM calyculin A, 0.5 mM PMSF, 10 μg/ml E64d, and 10 μg/ml pepstatin A. Lysates were freeze-thawed at -80$^{o}$C, cleared by centrifugation for 30 min at 4$^{o}$C, boiled in sample buffer, resolved by SDS-PAGE, and transferred to PVDF membrane. Membranes were blocked for 1 h in 5% milk in PBS with 0.1% Tween 20 (PBST), incubated in primary antibody overnight at 4$^{o}$C, washed, incubated for 1 h at room temperature with HRP-conjugated secondary antibodies (Jackson Immunoresearch, 1:5000), washed, and visualized via enhanced chemiluminescence (Thermo Scientific).

## REFERENCES


1. Guy, C.T.*, et al.* (1992) Induction of mammary tumors by expression of polyomavirus middle T oncogene: a transgenic mouse model for metastatic disease. *Molecular and Cellular Biology* 12, 954-961

2. Lin, E.Y.*, et al.* (2003) Progression to Malignancy in the Polyoma Middle T Oncoprotein Mouse Breast Cancer Model Provides a Reliable Model for Human Diseases. *The American Journal of Pathology* 163, 2113-2126

3. Khanna, C., and Hunter, K. (2005) Modeling metastasis in vivo. *Carcinogenesis* 26, 513-523

4. Malhotra, R.*, et al.* (2015) Loss of Atg12, but not Atg5, in pro-opiomelanocortin neurons exacerbates diet-induced obesity. *Autophagy* 11, 145-154

5. Luche, H.*, et al.* (2007) Faithful activation of an extra-bright red fluorescent protein in "knock-in" Cre-reporter mice ideally suited for lineage tracing studies. *European Journal of Immunology* 37, 43-53

6. Fata, J.E.*, et al.* (2007) The MAPK(ERK-1,2) pathway integrates distinct and antagonistic signals from TGFalpha and FGF7 in morphogenesis of mouse mammary epithelium. *Dev Biol* 306, 193-207

7. Hayashi, S., and McMahon, A.P. (2002) Efficient recombination in diverse tissues by a tamoxifen-inducible form of Cre: a tool for temporally regulated gene activation/inactivation in the mouse. *Dev Biol* 244, 305-318

8. Fung, C.*, et al.* (2008) Induction of autophagy during extracellular matrix detachment promotes cell survival. *Mol Biol Cell* 19, 797-806

# APPENDIX B

## Autophagy facilitates glycolysis during Ras-mediated oncogenic transformation

**The following appendix is published work:**

Lock, R., Roy, S., **Kenific, C.M.,** Su, J.S., Salas, E., Ronen, S.M., and Debnath, J. Autophagy facilitates glycolysis during Ras-mediated oncogenic transformation. *Molecular Biology of the Cell* **22**, 2 (2011).

**Contributions:** The following work was performed primarily by Rebecca Lock, a former graduate student in the lab. I contributed to data in Figure 1 demonstrating that autophagy can be induced during suspension of oncogene expressing cells. Jay Debnath supervised this project.

**ABSTRACT**

The pro-tumorigenic functions for autophagy are largely attributed to its ability to promote cancer cell survival in response to diverse stresses. Here, we demonstrate an unexpected connection between autophagy and glucose metabolism that facilitates adhesion-independent transformation driven by a strong oncogenic insult--mutationally active Ras. In cells ectopically expressing oncogenic HRas as well as human cancer cell lines harboring endogenous KRas mutations, autophagy is induced following extracellular matrix detachment. Inhibiting autophagy due to the genetic deletion or RNAi-mediated depletion of multiple autophagy regulators (ATGs) attenuates Ras-mediated adhesion-independent transformation and proliferation, as well as reduces glycolytic capacity. Furthermore, in contrast to autophagy competent cells, both proliferation and transformation in autophagy deficient cells expressing oncogenic Ras are insensitive to reductions in glucose availability**.** Overall, increased glycolysis in autophagy-competent cells facilitates Ras-mediated adhesion-independent transformation, suggesting a unique mechanism by which autophagy may promote Ras-driven tumor growth in specific metabolic contexts.

## INTRODUCTION

Macroautophagy (hereafter called autophagy), which serves critical functions in maintaining cellular homeostasis and as an adaptive response to cellular stress, has both anti- and pro-tumor functions (Chen and Debnath, 2010). The tumor suppressor functions for autophagy were originally revealed through genetic studies of Beclin/ATG6 (Liang *et al.*, 1999; Qu *et al.*, 2003; Yue *et al.*, 2003). Subsequently, multiple mechanisms have been uncovered by which autophagy potentially prevents tumor formation; these include the mitigation of genotoxic damage, suppression of a pro-tumorigenic inflammatory response secondary to decreased necrosis, and the induction of oncogene-induced senescence (Degenhardt *et al.*, 2006; Karantza-Wadsworth *et al.*, 2007; Mathew *et al.*, 2007; Mathew *et al.*, 2009; Young *et al.*, 2009). In contrast, the pro-tumorigenic functions for autophagy are almost exclusively attributed to its cytoprotective functions in tumor cells as they encounter common stresses during cancer progression. (Chen and Debnath, 2010). For example, increased autophagy is observed in cells centrally located within solid tumors that lack access to nutrients and oxygen; in such cells, genetic inhibition of autophagy results in the increased death of these stressed tumor cells (Degenhardt *et al.*, 2006).

Autophagy is induced following extracellular matrix (ECM) detachment, which protects cells from detachment-induced cell death (anoikis) (Frisch and Francis, 1994; Fung *et al.*, 2008). Since the ability to overcome anoikis is viewed as a critical hurdle in tumor development, one can hypothesize that detachment-induced autophagy enables the viability and fitness of tumor cells deprived of contact with extracellular matrix. In addition to autophagy, oncogene-mediated activation of growth factor signaling pathways also protects cells from anoikis (Gilmore, 2005); among these oncogenes, one of the most potent suppressors of anoikis is Ras, a small GTPase commonly mutated in a large number of human epithelial cancers (Khwaja *et al.*, 1997).

In addition to its ability to inhibit anoikis, oncogenic Ras promotes glucose metabolism, which is critical for its capacity to support growth and proliferation during oncogenic transformation (Chiaradonna *et al.*, 2006). Indeed, recent studies have begun to highlight the importance of the metabolic switch to aerobic glycolysis (termed the "Warburg effect") that takes place in cancer cells as a critical driver of tumorigenesis (Vander Heiden *et al.*, 2009). Remarkably, two proteins that mitigate cell stress, Oct1 and Hsf1, have both been demonstrated to facilitate tumorigenesis through the enhancement of glucose metabolism (Dai *et al.*, 2007; Shakya *et al.*, 2009). These studies broach important interconnections between stress pathways and cancer cell metabolism.

Surprisingly, although autophagy is similarly viewed as a salvage mechanism that affords basic components to sustain core metabolic functions during starvation or stress, the relationship between autophagy and metabolism remains largely unclear. Along with our previous work demonstrating that detachment-induced autophagy promotes cell survival during anoikis, the aforementioned studies highlighting the importance of stress pathways in modulating glucose metabolism motivated us to delineate the biological contributions of autophagy to Ras-mediated adhesion-independent transformation. Our experiments point to an unexpected requirement for autophagy competence in facilitating glycolysis, which promotes adhesion independent transformation driven by oncogenic Ras.

## MATERIALS AND METHODS

### Cell Culture

Dr. Noburu Mizushima (Tokyo Medical and Dental University) generously provided *atg5*+/+ and *atg5*-/- MEFs (simian virus 40 T antigen immortalized). Dr. Masaaki Komatsu (Tokyo Metropolitan Institute) generously provided *atg7*+/+ and *atg7*-/-, *atg3*+/+ and *atg3*-/- MEFs

(simian virus 40 T antigen immortalized). All mouse fibroblasts were cultured in DMEM containing 25mM glucose (Invitrogen) supplemented with 10% FBS, penicillin, and streptomycin. MCF-10A cells were cultured as described previously (Debnath *et al.*, 2003) and MDA-MB-231 cells were grown in DMEM containing 25mM glucose supplemented with 10% FBS, penicillin, and streptomycin. When indicated, MEFs and MDA-MB-231 cells were grown in DMEM containing 25mM, 5.5mM, 2.8mM or 1.4mM glucose supplemented with 10% dialyzed FBS, penicillin, and streptomycin.

**Antibodies and Chemicals**

A peptide corresponding to the N-terminus common to human, mouse, and rat MAP1LC3 was used to create α-LC3 rabbit polyclonal antibody (Fung *et al.*, 2008). Other antibodies used included the following: α-p62 (Progen Biotechnik); α-phospho-ERK1/2 (Biosource); α-ERK1/2 (Invitrogen); α-phopho-ribosomal protein S6 (Ser240/244, Cell Signaling Technology); α-ribosomal protein S6 (Cell Signaling Technology); α-ATG12 (Cell Signaling Technology); α-ATG7 (Santa Cruz Biotechnology); α-ATG5 (Cell Signaling Technology); α-cleaved caspase-3 (Cell Signaling Technology); α-BCL-2 (BD Biosciences); α-LDH-A (Cell Signaling Technology); and α-α-tubulin (Sigma-Aldrich). Chemicals utilized included poly 2-hydroxyethyl methacrylate (poly-HEMA), E64d, and pepstatin A (all from Sigma-Aldrich).

**Generation of Stable Lines**

The following retroviral vectors for stable gene expression have been described previously: pBABEpuro-HRasV12, pBABEneo-HRasV12, pBABEneo-Bcl-2, and pBABEpuroGFP-LC3 (Debnath *et al.*, 2002). For retroviral transduction, VSV-G-pseudotyped retroviruses were generated, and cells were infected and selected as previously described (Debnath *et al.*, 2003).

**RNA Interference**

pLKO.1 lentiviral expression plasmids containing short hairpin RNAs against ATG7 and ATG12 were purchased from Sigma-Aldrich (Mission shRNA), and viral particles were produced using a 3rd generation lentiviral packaging system in HEK293T cells. Following infection and drug selection, early passage stable pools (maximum of 3-5 passages) were utilized because the extended propagation of cells results in the loss of RNAi-mediated ATG silencing and autophagy inhibition. The target sequences for hairpins directed against ATG7 (NM_006395) are: shATG7-1 (TRCN0000007584): GCCTGCTGAGGAGCTCTCCA; and shATG7-2 (TRCN0000007587): CCCAGCTATTGGAACACTGTA; and directed against ATG12 (NM_004707) are: shATG12-1 (TRCN0000007393): TGTTGCAGCTTCCTACTTCAA

**Substratum Detachment Assays**

Tissue culture plates coated with 6 mg/ml poly-HEMA in 95% ethanol were incubated at 37°C until dry. Cells were plated on poly-HEMA–coated plates at a density of 500-750K cells/well in 6-well plates in their appropriate complete growth medium. The lysosomal inhibitors, E64d and pepstatin A, were added directly to the culture media at 10 μg/ml at 4-6h before lysis to evaluate autophagic flux.

**Immunoblotting**

Attached or suspended cells were lysed in RIPA lysis buffer plus 10mM NaF, 10 mM β-glycerophosphate, 1 mM $Na_3VO_3$, 10 nM calyculin A, and protease inhibitors. Lysates were clarified by centrifugation for 15 min at 4°C, and protein concentrations were assessed using a BCA protein assay (Thermo). Samples containing equal amounts of protein were boiled in SDS

sample buffer (15-50µg of total protein per lane), resolved using SDS-polyacrylamide gel electrophoresis (PAGE), and transferred to polyvinylidene difluoride membrane. Membranes were blocked in PBS + 0.1% Tween 20 with 5% nonfat dry milk, incubated with the primary antibodies indicated overnight at 4°C, washed, incubated with horseradish peroxidase-conjugated secondary antibodies, and analyzed by enhanced chemiluminescence.

**Soft Agar Colony Formation Assay**

To evaluate anchorage independent growth, $1x10^4$ HRasV12 MEF cells, $1x10^4$ HRasV12 MCF10A cells, or $2x10^4$ MDA-MB-231 cells were resuspended in 0.35% agarose in growth media. Cells were plated on a solidified bed of 0.5% agarose in growth media in 3.5cm plates. Plates containing HRasV12 MEF and HRasV12 MCF10A cells were fixed and stained with 0.005% crystal violet after 14d, and plates containing MDA-MB-231 cells were fixed following 21d of growth. Brightfield images of HRasV12 MCF10A and MDA-MB-231 colonies were taken using a 4x objective. Plates with HRasV12 MEFs were scanned. The number of colonies per field (for MCF10A and MDA-MB-231 cells) and number of colonies per plate (for MEFs) were counted using MetaMorph (version 6.0).

**Glucose Uptake, Lactate Dehydrogenase Activity and Media Glucose Concentration Analysis**

To measure glucose uptake, cells were incubated with growth media containing 100µM 2-[N-(7-nitrobenz-2-oxa-1,3-diazol-4-yl)amino]-2-deoxyglucose (2-NBDG, Invitrogen) for the indicated timepoints up to 8h, washed 3x with PBS, and detached for FACS analysis. Mean fluorescence intensity of cells was obtained using a Becton Dickinson FACSCalibur flow cytometer and data was analyzed using CellQuest Pro v5.1.1 software. Lactate dehydrogenase activity was measured

using the CytoTox 96 Non-Radioactive Cytotoxicity Assay (Promega). To measure glucose concentrations, conditioned media were collected from cells on the days indicated and assayed using the Amplex Red Glucose/Glucose Oxidase Assay Kit (Invitrogen).

**Cell Cycle Analysis and Growth Assays**

For cell cycle analysis following extracellular matrix detachment, cells were suspended on either poly-HEMA coated plates (suspension) or grown attached on tissue culture plastic for 48h. Cells in suspension were washed and incubated in 0.25% trypsin for 10 minutes at 37ºC to break up cell clumps and generate single cell suspensions. Both suspended and attached cells were collected and fixed in 70% ice cold EtOH. Cells were stained with 20µg/mL PI in 0.1% Triton X-100 in PBS with 200ug/mL RNase A and incubated at 37ºC for 15 minutes. Cell cycle profiles were collected using a Becton Dickinson FACSCalibur flow cytometer and data was analyzed using FlowJo v. 8.8.6 cell cycle analysis software. For cell growth assays, $4x10^4$ MEFs or $1.1x10^5$ MDA-MB-231 cells were plated on 6 cm plates and cells were counted using a hemocytometer every 24h for up to 5d.

***De novo* Protein Translation Analysis**

The indicated cell types were grown either attached or suspended for 24h. Cells were then incubated with methionine-free DMEM (Invitrogen) for 1h, followed by 100µM Click-iT AHA (Invitrogen), a methionine analog, in methionine-free DMEM to pulse-label newly synthesized proteins for 3h. Cells were lysed and incorporated Click-iT AHA was detected using the TAMRA Click-iT Protein Analysis Detection Kit (Invitrogen) following manufacturer's instructions. Total protein levels were measured and equilibrated using BCA assay (Thermo), and 10µg of total protein was loaded per well. Following detection of newly synthesized

proteins, gels were stained with SYPRO Ruby gel stain (Invitrogen) to detect total protein levels. TAMRA fluorescence (newly synthesized proteins) and SYPRO Ruby fluorescence (total protein) were detected using a FLA-5100 imager (FujiFilm) and analyzed using Multi Gauge software v3.X. Newly synthesized protein levels were normalized to total protein levels.

**NMR acquisition and analysis**

Cells were grown in medium containing equal concentrations (12.5 mmol/L) of [1-$^{13}$C] glucose and unlabeled glucose for 24h, after which medium was collected and cell extracts were prepared using the dual-phase extraction method (Tyagi *et al.*, 1996). Briefly, cells were rinsed with ice-cold saline, fixed in 10 ml ice-cold methanol and scraped from the culture flask surface, and vigorously vortexed, upon which 10 ml of ice-cold chloroform was added, followed by 10 ml of ice-cold deionized water to the fixed cells. After phase separation, the aqueous phase was lyophilized, and the protein pellet was air-dried. Protein concentration was determined using the BCA assay. To acquire $^{13}$C spectra, the aqueous fraction was reconstituted in 500 μL deuterium oxide, and NMR spectra were acquired on a 600-MHz INOVA spectrometer (Varian; Palo Alto, CA) using a 30° flip angle, 3.5 s repetition time, and broadband proton decoupling. Analysis of the NMR spectra was performed using ACD/Spec Manager software version 9.15 (Advanced Chemistry Development Inc). The concentrations of metabolites were determined with respect to an external reference, 2,2,3,3-tetradeutero-3-trimethylsilylpropionic acid (TSP), with a known concentration.

**Statistics:** Experimental groups were compared using Student's t test for pairwise comparisons or ANOVA (followed by Tukey's HSD test).

## RESULTS

**Oncogenic Ras does not suppress ECM detachment-induced autophagy.** Several studies demonstrate that constitutive activation of Ras suppresses autophagy induction while others indicate that Ras/MAPK pathway activation can enhance autophagy during nutrient starvation (Pattingre *et al.*, 2003; Furuta *et al.*, 2004; Berry and Baehrecke, 2007). Given these paradoxical results, we first sought to clarify how oncogenic Ras modulates autophagy upon loss of cell-matrix contact, a cardinal stress during adhesion-independent transformation. We generated stable pools of MCF10A human mammary epithelial cells expressing oncogenic HRas (HRasV12) as well as control cells expressing an empty vector (BABE) (Figure 1A, left). We then tested autophagy levels following substratum detachment by plating cells on poly-HEMA coated plates to prevent cell-matrix adhesion. As previously reported, in BABE control cells, we observed an increase in the lysosomal turnover of phosphotidylethanolamine (PE) lipidated LC3/ATG8 (LC3-II), commonly termed autophagic flux, following matrix detachment. (Figure 1A, right). (Fung *et al.*, 2008). Furthermore, MCF10A cells expressing HRasV12 displayed an increase in LC3-II induction and lysosomal turnover following matrix detachment. (Figure 1A, left). To further verify autophagosome induction in HRasV12 transformed MCF10A cells, we stably expressed GFP-LC3 in HRasV12 and vector control cells, and assessed autophagosome formation (punctate GFP-LC3) using fluorescence microscopy. Following detachment, we observed robust induction of GFP-LC3 puncta in both empty vector and RasV12 expressing MCF10A cells in comparison to attached controls (Figure 1B). Because detached epithelial cells exhibit extensive clustering, we were unable to precisely enumerate puncta per cell; nonetheless, we consistently observed similar levels of punctate GFP-LC3 in HRasV12 transformed MCF10A compared to BABE controls.

We next evaluated the effects of HRasV12 on detachment-induced autophagy in immortalized mouse embryonic fibroblasts (MEFs) (Figure 1C). Remarkably, both HRasV12 and control fibroblasts exhibited a high baseline level of LC3-II when grown in attached conditions; upon suspension, LC3-II levels decreased dramatically in the HRasV12 expressing MEFs and to a lesser extent, in vector controls during suspension. Upon addition of E/P, LC3-II levels increased following detachment in both cell types, indicating that both control and RasV12 fibroblasts exhibit LC3-II turnover during matrix detachment (Figure 1C, center). To more conclusively validate these results, we assessed the degradation of p62 (SQSTM), a scaffold protein specifically degraded by autophagy, following detachment (Figure 1C, right). In both vector control and HRasV12 transformed MEFs, we observed significantly reduced p62 levels following 24h of suspension. In contrast, p62 levels remained elevated in both control and HRasV12 transformed *atg5-/-* MEFs, supporting that the degradation of p62 during substratum detachment requires an intact autophagy pathway.

To extend these results, we evaluated detachment-induced autophagy in epithelial cancer cell lines that naturally harbor oncogenic Ras mutations. In three different carcinoma lines that possess activating KRas mutations, MDA-MB-231 breast carcinoma cells, HCT116 colon carcinoma cells, and PANC-1 pancreatic carcinoma cells, both LC3-II induction and turnover increased upon substratum detachment (Figure 1D). In parallel, we examined autophagosome formation (GFP-LC3 puncta) following suspension. Similar to MCF 10A cells, all three carcinoma cell lines displayed an increase in GFP-LC3 puncta following 24 h matrix detachment (Figure 1E). Altogether, our results support the robust induction of autophagy in both epithelial and fibroblast cells expressing HRasV12 as well as in cancer cell lines harboring activating KRas mutations following matrix detachment; hence, Ras activation does not suppress autophagy during ECM detachment.

We next assessed whether constitutive Ras activation was sufficient to maintain activation of downstream signaling pathways following ECM detachment. We first tested if oncogenic activation of Ras sustained activation of the MAPK pathway by examining levels of phosphorylated ERK. Both MCF10A cells and mouse fibroblasts (expressing empty vector) displayed a reduction in phosphorylated ERK1/2 levels following 24h ECM detachment. In contrast, the phosphorylation of ERK1/2 remained elevated in both HRasV12 transformed MCF10As and MEFs during ECM detachment (Figure 2A-B). ERK1/2 phosphorylation was similarly maintained in MDA-MB-231 cells and HCT 116; remarkably, in PANC-1 cells ERK1/2 phosphorylation was increased in matrix-detached cells when compared to attached controls. (Figure 2C).

Sustained activation of mTORC1, the archetypal negative regulator of autophagy, has been proposed to mediate autophagy inhibition downstream of oncogenic Ras (Furuta *et al.*, 2004; Maiuri *et al.*, 2009). Thus, we measured mTORC1 activation in HRasV12 transformed cells following ECM detachment by assessing the phosphorylation status of ribosomal protein S6, a downstream mTOR target. Upon detachment, S6 phosphorylation decreased sharply in control MCF10A cells, supporting reduced activation of the mTORC1 pathway. Notably, S6 phosphorylation was partially decreased in HRasV12-transformed cells following 24h suspension (Figure 2D). In fibroblasts, both control and HRasV12-transformed MCF10A cells demonstrated decreased levels of phosphorylated S6 during suspension (Figure 2E). Similarly, in KRas mutant cancer cells, S6 phosphorylation was reduced following ECM detachment (Figure 2F). Because we observed a partial decrease in S6 phosphorylation during ECM detachment, particularly in HRasV12 MCF10A cells, we treated suspended cells with rapamycin to assess whether robust inhibition of mTORC1 was able to further enhance detachment-induced autophagy. Upon rapamycin treatment, we were unable to detect S6 phosphorylation in

HRasV12 MCF10A cells following 24h suspension; however, we did not observe any further increase in LC3-II induction or turnover upon rapamycin treatment (Figure 2G). This result supports that autophagy can be potently induced in HRasV12 MCF10A cells following extracellular matrix detachment without complete suppression of mTORC1 activity.

**Reduced HRasV12 driven soft agar transformation in autophagy deficient MEFs.** Because autophagy was robustly induced in Ras-transformed cells upon loss of cell-matrix contact, we next interrogated the functional contribution of autophagy to HRasV12 driven anchorage-independent growth. For these experiments, we initially tested how the genetic deletion of three critical autophagy regulators, *atg5, atg7,* and *atg3,* individually influence anchorage-independent transformation by oncogenic Ras. All three proteins are essential components of the ubiquitin-like conjugation pathways that control the early step of autophagosome formation; thus, the genetic deletion of any of these ATGs is sufficient to completely inhibit autophagy (Ohsumi, 2001; Kuma *et al.*, 2004; Komatsu *et al.*, 2005; Sou *et al.*, 2008). We first compared the ability of *atg5*+/+ and *atg5*-/- MEFs transformed with HRasV12 to form colonies in soft agar. HRasV12 transformed *atg5*-/- MEFs displayed an approximate 4-fold decrease in colony formation compared to wild-type autophagy-competent controls (Figure 3A); importantly, both *atg5*+/+ and *atg5*-/- cells expressed equivalent levels of HRasV12 (Figure 1C, left).

To verify that these differences directly resulted from autophagy inhibition upon ATG5 deletion, we constituted *atg5*-/- cells with either wild-type mouse ATG5 or ATG5 K130R, a lysine mutant unable to conjugate to ATG12 and therefore unable to induce autophagy. Rescue of HRasV12 *atg5*-/- MEFs with wild-type ATG5 restored ATG5-ATG12 complex levels whereas expression of ATG5 K130R did not (Figure 3B). This rescue of HRasV12 *atg5*-/- MEFs with wild-type ATG5 restored autophagy induction, indicated by the production of LC3-II

in attached conditions and following suspension. In contrast, both HRasV12 *atg5-/-* MEFs, as well as those expressing ATG5 K130R, were unable to induce autophagy during suspension (Figure 3B). Furthermore, the rescue of HRasV12 transformed *atg5-/-* MEFs with wild-type ATG5, but not ATG5 K130R, was able to restore soft agar colony formation (Figure 3C), further supporting that autophagy competence functionally contributes to Ras-driven transformation. Similarly, soft agar transformation mediated by HRasV12 was also abrogated in *atg7-/-* and *atg3-/-* cells. Colony formation was reduced almost four-fold in HRasV12 *atg7-/-* MEFs compared to wild-type controls (Figure 3D), and HRasV12 *atg3-/-* MEFs displayed the most profound defect in soft agar colony formation, almost 8 fold, compared to wild-type controls (Figure 3E). These results support that the elimination of autophagy in mouse fibroblasts, achieved via the genetic deletion of multiple ATGs, potently inhibits the transformation potential of HRasV12.

**Reduced soft agar transformation upon ATG knockdown in Ras-transformed epithelial cells.** We next determined if the acute reduction of autophagy in the context of preexisting oncogenic Ras activation was similarly able to inhibit adhesion-independent transformation. First, we stably expressed two independent shRNAs against ATG7 (shATG7-1 and shATG7-2) as well as a hairpin directed against ATG12 (shATG12-1) in MDA-MB-231 cells. Analysis of target protein levels by western blot revealed high level knockdown of ATG7 with both shATG7-1 and 2 and reduction of the ATG5-ATG12 complex in shATG12-1 expressing MDA-MB-231 cells (Figure 4A). Of these three hairpins, shATG7-2 gave the most robust reduction in autophagy; based on immunoblotting for LC3-II (data not shown). MDA-MB-231 cells expressing this shRNA exhibited an approximately 50% decrease in both basal and detachment-induced autophagy (Figure 4B). Furthermore, the expression of all three of these shATGs in

MDA-MB-231 cells resulted in a significant decrease in soft agar colony formation, ranging from approximately 50%-90% depending on the shRNA used (Figure 4C).

In parallel, we generated stable pools of HRasV12 MCF10A cells expressing shRNA against ATG7 (shATG7-2). These cells demonstrated potent ATG7 knockdown and decreased LC3-II in both attached and detached conditions (Figure 4D). Colony formation in HRasV12 MCF10A cultures expressing shATG7-2 was reduced by approximately 50% when compared to shCNT expressing cells (Figure 4E); suggesting ATG7 knockdown was sufficient to partially suppress HRasV12 induced soft agar growth in MCF10A cells. Hence, consistent with our data in ATG-deficient fibroblasts, epithelial cells with oncogenic Ras displayed a reduction in soft agar colony formation following RNAi-mediated knockdown of ATGs. Furthermore, it is important to note that although we were able to achieve high levels of ATG knockdown, such perturbations produced partial reductions in autophagic capacity, up to 50% of control. Nonetheless, such levels of autophagy reduction resulted in robust decreases in soft agar colony formation, pointing to a critical role for autophagy in Ras-mediated anchorage-independent transformation.

**Effects of autophagy inhibition on detachment-induced apoptosis (anoikis) in Ras-transformed cells.** Because our previous work indicates that detachment-induced autophagy protects nontransformed MCF10A cells from anoikis, we hypothesized that autophagy may similarly promote the survival of Ras-transformed cells deprived of cell-matrix contact (Fung *et al.*, 2008). To test this prediction, HRasV12 *atg5*+/+ and *atg5*-/- MEFs were either grown attached or suspended for 24-48h and protein lysates were immunoblotted for cleaved caspase-3. Although previous work indicates that fibroblasts do not undergo anoikis, we found that cleaved caspase-3 did indeed increase in HRasV12 autophagy-competent fibroblasts upon ECM

detachment. Furthermore, compared to wild type controls, the levels of cleaved caspase-3 in HRasV12 *atg5*-/- MEFs following suspension were higher. This corroborates that autophagy deficiency leads to increased detachment-induced apoptosis in HRasV12-transformed cells (Figure 5A).

Based on these results, we interrogated if the ectopic expression of the anti-apoptotic molecule Bcl-2 was sufficient to promote adhesion independent growth and survival in HRasV12 *atg5-/-* MEFs. To test this hypothesis, we generated HRasV12 atg5+/+ and *atg5-/-* MEFs stably expressing Bcl-2 (Figure 5B). As Bcl-2 has previously been shown to suppress autophagy in certain cell types via its interaction with Beclin 1, we determined the effects of Bcl-2 expression on detachment-induced autophagy in HRasV12 MEFs, but did not identify any significant effects on LC3-II induction or turnover, or on p62 degradation during ECM detachment (Figure 5C) (Pattingre *et al.*, 2005). In contrast, Bcl-2 potently reduced apoptosis in HRasV12-transformed *atg5*+/+ and *atg5-/-* cells following matrix detachment, as indicated by immunoblotting for cleaved caspase-3, (Figure 5D).

We next evaluated if Bcl-2 expression was sufficient to restore adhesion-independent transformation in HRasV12 *atg5-/-* MEFs. However, we continued to detect reduced levels of HRasV12 driven soft agar growth in Bcl-2-expressing autophagy-deficient cells when compared to wild-type counterparts (Figure 5E). These results indicate that autophagy inhibition in HRasV12 transformed cells can promote anoikis; however, protecting autophagy-deficient cells from apoptosis is not sufficient to restore adhesion-independent transformation, raising the possibility that autophagy facilitates Ras transformation via other mechanisms.

**Autophagy inhibition results in decreased proliferation of Ras-transformed cells.** The aforementioned results motivated us to test the functional contributions of autophagy to the

proliferation of HRasV12 transformed cells. First, we tested the effects of ECM detachment on the proliferation capacity of autophagy competent and deficient MEFs expressing either vector control (BABE) or HRasV12. Cells grown attached or in suspension for 48h were subject to flow cytometric analysis for DNA content corresponding to the S+G2/M phases of the cell cycle (Figure 6A). In vector control (BABE) wild-type MEFs, we observed a decrease in the percentage of cycling cells (S+G2/M), from 67.3% +/-1.3% in attached conditions to 40.7% +/-3.5% after 48h of suspension (Figure 6A, black bar). In contrast, 57.9% +/-1.5% of HRasV12 transformed wild-type (*atg5+/+)* cells remained in S+G2/M following 48h of suspension (Figure 6A, white bar). Thus, HRasV12 transformed cells continue to proliferate upon loss of cell-matrix contact. However, in HRasV12 *atg5-/-* MEFs, incapable of autophagy, the ability of HRasV12 to promote proliferation in the absence of cell-matrix contact was attenuated, with only 47.3% +/-2.1% of cells remaining in cycle following 48h of suspension (Figure 6A, light grey bar). Interestingly, we noted that control (BABE) *atg5-/-* MEFs (dark grey bars) proliferated slightly better than *atg5+/+* cells during detachment; such results are consistent with previous studies demonstrating that reduced autophagy due to Beclin/ATG6 haploinsufficiency or genetic deletion of Ambra1 can promote cell proliferation (Qu *et al.*, 2003; Fimia *et al.*, 2007). Nevertheless, in the context of HRasV12 expression, autophagy inhibition curtailed rather than enhanced proliferation during ECM detachment.

To extend these results, we then measured if HRasV12 transformed *atg5-/-* cells displayed similar defects in proliferation in the absence of the stresses imposed by substratum detachment. Thus, we grew the various cell types in nutrient replete, attached conditions in which only basal levels of autophagy were present. Upon enumerating cell numbers from cultures, we found that nontransformed wild type and *atg5-/-* MEFs exhibited minimal differences in proliferation (Figure 6B). In contrast, upon transformation with HRasV12,

autophagy-deficient cells failed to proliferate as well as controls (Figure 6C). Similarly, acute ATG7 knockdown in MDA-MB-231 cells led to a profound decrease in proliferation compared to controls (Figure 6D). Overall, these results indicate that autophagy induction is necessary for optimal cell proliferation in HRasV12 expressing cells following ECM detachment, and that oncogenic Ras activation engenders an increased reliance on basal autophagy for cell expansion in attached conditions.

**Increased glucose metabolism in autophagy competent cells.** Due to the decreased proliferation observed in Ras-transformed cells upon autophagy inhibition, we hypothesized that the difference in adhesion-independent transformation we observed between Ras-transformed autophagy competent and deficient cells may arise from changes in protein synthesis or in cellular metabolism, two processes that directly impact the capacity for cell growth and proliferation. Both nitrogen-starved, autophagy deficient yeast and early ATG5 deficient embryos display a decrease in *de novo* protein translation compared to wild-type controls (Onodera and Ohsumi, 2005; Tsukamoto *et al.*, 2008). Therefore, we speculated that HRasV12 *atg5-/-* MEFs would exhibit diminished rates of protein synthesis compared to HRasV12 wild-type MEFs in the absence of ECM contact. Although we observed decreased *de novo* protein synthesis in empty vector (BABE) expressing *atg5-/-* MEFs compared to wild-type following 24h detachment, only minor differences were present when we compared HRasV12 expressing wild-type and *atg5-/-* MEFs (Supplemental Figure S1).

Like many oncogenes, HRasV12 enhances glycolysis, which is associated with increased glucose uptake and lactate production; importantly, increased aerobic glycolysis is required for Ras driven tumors to maintain energy production and enhance biosynthetic pathways. Remarkably, we found that glucose uptake, determined by uptake of 2-[N-(7-nitrobenz-2-oxa-

1,3-diazol-4-yl) amino]-2-deoxy-D-glucose (2-NBDG), was significantly reduced in empty vector *atg5-/-* MEFs compared to atg5+/+ controls (Figure 7A). As expected, HRasV12 expression resulted in increased glucose uptake (Supplemental Figure S2A). When we compared glucose uptake between HRasV12 *atg5*+/+ and HRasV12 *atg5-/-* MEFs over an 8h timecourse, we found reduced glucose uptake in HRasV12 *atg5-/-* MEFs compared to HRasV12 atg5+/+ cells at all timepoints examined (Figure 7B). We also observed a decreased level of glucose uptake in HRasV12 *atg5-/-* MEFs following extracellular matrix detachment (Supplemental Figure S2B). Enhanced glucose uptake is often associated with an increase in glycolytic flux, resulting in the enhanced production of lactate. Thus, to determine the glycolytic status of autophagy-proficient and deficient cells, we used $^{13}$C-NMR spectroscopy to assess metabolic fluxes. Cells were labeled with [1-$^{13}$C]-glucose and *de novo* lactate production was monitored. Despite reduced glucose uptake in *atg5-/-* MEFs compared to atg5+/+ controls, there was no concomitant decrease in lactate production in *atg5-/-* MEFs (Figure 7C). In fact, we observed equivalent levels of both intracellular and extracellular lactate production by wild type and *atg5-/-* MEFs. However, upon HRasV12 transformation, both intracellular and extracellular [3-$^{13}$C]-lactate production was decreased in HRasV12 transformed *atg5-/-* cells in comparison to atg5+/+ controls (Figure 7C). Furthermore, compared to *atg5*+/+ controls, HRasV12 *atg5-/-* MEFs exhibited decreased levels of [3-$^{13}$C]-alanine, which is produced via the transamination of the glycolytic end product pyruvate (Supplemental Figure S2C).

Next, we evaluated if defects in glucose metabolism were present in MDA-MB-231 cells upon ATG7 knockdown. Although glucose uptake was not significantly reduced in ATG7 depleted cells (data not shown), they did exhibit a significant decrease in the enzymatic activity of lactate dehydrogenase (LDH), which is required for the conversion of pyruvate to lactate. Furthermore, LDH-A protein levels were also decreased in ATG7 depleted MDA-MB-231 cells

(Supplemental Figure S2D). LDH-A levels were not altered in empty vector *atg5-/-* or HRasV12 *atg5-/-* MEFs compared to wild-type controls (Supplemental Figure S2E). Altogether, these results implicate that reduced autophagy results in a concomitant decrease in glycolytic capacity.

**Autophagy competent cells exhibit increased sensitivity to diminished glucose availability.** Because glycolysis was decreased in Ras-transformed, autophagy deficient cells, we next sought to determine the effects of varying glucose concentrations on autophagy competent versus deficient cells. We first assessed if autophagy is stimulated in response to decreasing media glucose concentrations, since previous studies support that autophagy is induced upon glucose starvation or treatment with 2-deoxy-glucose (Aki *et al.*, 2003; DiPaola *et al.*, 2008). Although we observed a robust induction of autophagy following 9h of complete glucose withdrawal, a similar increase in autophagy was not detected in HRasV12 expressing MEFs upon lowering glucose concentrations from the standard 25mM to 5.5mM for up to 48h (Figure 8A).

Glycolytic cells typically display exquisite sensitivity to diminishing concentrations of glucose; accordingly, we assessed how autophagy competence versus deficiency impacted glucose consumption and proliferation in HRasV12 expressing cells. First, we measured the consumption of glucose in HRasV12 *atg5*+/+ and *atg5-/-* cells grown over 2d in 5.5mM glucose; in accordance with the results above, media glucose concentrations declined more precipitously in HRasV12 wild-type MEF cultures compared to HRasV12 *atg5-/-* cells (Figure 8B). Furthermore, following 4d of culture in 5.5mM glucose, cell numbers in HRasV12 wild-type cultures were reduced by 62.5% in comparison to those grown in 25mM. In contrast, the expansion of HRasV12 *atg5*-/- cells was not as profoundly attenuated by similar reductions in glucose concentration; these cells only exhibited a 40.4% reduction in cell number when cultured in 5.5mM glucose compared to 25mM glucose. This increased sensitivity of HRasV12 *atg5*+/+

MEFs to lower media glucose levels is in accordance with the increases in glycolytic capacity and glucose uptake we observed in HRasV12 *atg5*+/+ MEFs (Figure 8B). To corroborate these results, we performed parallel experiments in MDA-MB-231 cells following acute ATG7 depletion. When grown in 2.8mM glucose, cells expressing shATG7-2 consumed glucose at a lower rate than cells expressing control shRNA (shCNT) (Figure 8C). In addition, the expansion of shATG7-2 cells was not as sensitive to lower glucose concentrations as shCNT cells (Figure 8C).

Based on these results, we hypothesized that declining glucose concentrations would attenuate the rate of adhesion-independent transformation of HRasV12-transformed autophagy competent cells, but have little effect on autophagy-deficient counterparts. Accordingly, we observed a significant reduction in soft agar colony formation in HRasV12 *atg5*+/+ MEFs grown in 5.5mM glucose compared to those grown in 25mM glucose. In contrast, adhesion-independent transformation in HRasV12 *atg5*-/- MEFs was not affected by declining glucose concentrations. Remarkably, at the lower glucose concentration (5.5mM), we observed comparable levels of soft agar colony formation between HRasV12 transformed autophagy-competent and deficient cells (Figure 8D). These results support that the ability of autophagy to promote adhesion independent transformation is highly dependent on glucose levels, and point to a previously unrecognized role for autophagy competence in facilitating glycolysis and proliferation during oncogenic Ras-mediated transformation.

**DISCUSSION**

Overall, our studies demonstrate that in the context of a potent oncogene, mutationally active Ras, autophagy both promotes adhesion independent transformation and facilitates glycolysis. The genetic deletion or RNAi-mediated knockdown of autophagy regulators (ATGs)

causes a potent decrease in anchorage-independent growth in soft agar, indicating that an intact autophagy pathway is required for robust adhesion-independent transformation by oncogenic Ras. Furthermore, autophagy inhibition during Ras transformation results in reduced proliferation and decreased glucose metabolism. The decreased rate of glycolysis found in Ras-transformed autophagy deficient cells correlates with decreased sensitivity to declining glucose concentrations in comparison to autophagy competent counterparts, both in terms of proliferation and adhesion-independent transformation.

In addition, our results indicate that oncogenic Ras does not suppress autophagy during ECM detachment. These data differ from previous reports in both Ras expressing cells *in vitro* as well as Drosophila development *in vivo* (Furuta *et al.*, 2004; Berry and Baehrecke, 2007), both of which demonstrate that Ras activation suppresses autophagy. Ras-mediated suppression of autophagy is proposed to arise secondary to the constitutive activation of the PI3K/mTOR pathway, a negative regulator of autophagy induction. However, upon ECM detachment of several KRas mutant cancer lines, ribosomal protein S6 phosphorylation, an established readout of mTORC1 activity, is rapidly decreased, indicating that Ras is unable to sustain mTORC1 activation in cells deprived of matrix contact. Furthermore, detached MEFs expressing HRasV12 exhibit decreased S6 phosphorylation comparable to non-transformed controls. On the other hand, in HRasV12 transformed MCF10A cells, S6 phosphorylation is only slightly reduced following matrix detachment compared to nontransformed counterparts. Interestingly, although we were able to completely inhibit mTORC1 activity by treating HRasV12 MCF10A cells with rapamycin during suspension, this did not further augment autophagy. This result indicates the enhanced level of mTORC1 activity that persists in HRasV12 MCF10A cells following detachment is not sufficient to suppress autophagy induction. From these results, we speculate that a partial reduction in mTORC1 activity in HRasV12 expressing MCF10A cells may be

sufficient to promote detachment-induced autophagy. Alternatively, other mTORC1-independent pathways may promote autophagy in detached cells expressing oncogenic Ras. Importantly, our results support that oncogenic Ras activation does not inhibit detachment-induced autophagy in mammalian cells.

The mechanisms through which autophagy modulates oncogenic transformation are context dependent (Chen and Debnath, 2010). Here, we demonstrate that autophagy is required for robust Ras-driven transformation; cells deleted or depleted of multiple independent ATGs all exhibit decreased anchorage-independent transformation in soft agar. Recently, we discovered that detachment-induced autophagy protects cells from anoikis, which we proposed to facilitate oncogenic transformation (Fung *et al.*, 2008). However, because the ectopic overexpression of the anti-apoptotic protein Bcl-2 does not enhance soft agar growth in Ras-transformed autophagy deficient cells, the ability of autophagy to facilitate Ras transformation cannot be completely explained by its ability to protect cells from apoptosis during ECM detachment.

These studies point to a previously unrecognized tumor-promoting function for autophagy that manifests during oncogenic Ras transformation. For example, upon matrix detachment, increased numbers of *atg5-/-* cells continue to proliferate compared to *atg5+/+* controls. In fact, the enhanced proliferation of autophagy deficient cells has been proposed as a potential mechanism by which autophagy might exert tumor suppressive effects (Qu *et al.*, 2003; Fimia *et al.*, 2007). However, unlike non-transformed autophagy-deficient cells, *atg5* genetic deletion impedes, rather than enhances, the ability of HRasV12 transformed MEFs to proliferate during ECM detachment. Similarly, when cultured in attached nutrient-rich conditions, Ras-transformed *atg5-/-* cells exhibit a marked decrease in proliferation compared to their autophagy-competent counterparts. In addition, we have also found that MCF10A cells expressing HRasV12 occasionally undergo growth arrest or cell death following lentiviral-driven

introduction of shRNAs against ATGs; in contrast, nontransformed cells consistently remain viable and continue to proliferate upon ATG knockdown (data not shown). These results support that autophagy competence is required for cells to proliferate and expand during oncogenic Ras transformation.

Increasing evidence indicates that stress response pathways play diverse, multifaceted roles necessary for oncogenic transformation. For example, heat shock protein 1 (HSP1), an important mediator of the heat shock response, has been implicated as an important facilitator of Ras transformation, which correlates with its ability to modulate both proliferative capacity and glucose metabolism (Dai *et al.*, 2007). Here, we demonstrate that autophagy similarly supports increased glucose metabolism, suggesting a previously unrecognized mechanism by which autophagy may contribute to tumorigenesis. HRasV12 transformed, autophagy competent MEFs display enhanced glucose uptake compared to their autophagy deficient counterparts. In addition, using $^{13}$C-NMR analysis of glucose metabolism, we observe augmented glycolytic flux in HRasV12 expressing autophagy competent cells as evidenced by increased production of lactate and alanine from glucose. Notably, we have also observed reduced glucose uptake in nontransformed, autophagy deficient cells, but unlike HRasV12-transformed cells, these reductions do not correlate with significant changes in lactate production or in monolayer proliferation. Increased glycolysis in tumors, first observed by Otto Warburg, is crucial to support both the increased energy and synthetic demands required for high rates of proliferation. This metabolic shift in tumor cells is coordinated by upregulating critical components of glycolysis resulting in enhanced glucose uptake and lactate production even in the presence of ample oxygen (Vander Heiden *et al.*, 2009). It is currently unclear whether reduced autophagy specifically elicits changes in glucose metabolism or causes more global metabolic shifts during

Ras transformation. We are presently evaluating whether and how other metabolic pathways are affected by the loss or reduction of autophagy.

Although glucose withdrawal and energy depletion have been shown to be potent activators of autophagy as a survival response, we have unexpectedly found that the reduction or elimination of autophagy competence can actually reduce glycolytic capacity in a Ras-transformed cell. Hence, we speculate that autophagy may promote oncogenic Ras-driven tumor growth in specific metabolic microenvironments. In support, decreasing glucose concentrations inhibits soft agar colony formation in HRasV12 expressing wild-type cells to levels approaching that of HRasV12 autophagy deficient cells. In contrast, both the proliferation and adhesion independent transformation of autophagy deficient cells is relatively insensitive to reductions in glucose availability. These alterations in glucose metabolism in autophagy deficient cells may similarly impact transformation by other oncogenes, such as Myc and PI3K, which orchestrate global metabolic changes that contribute to the transformed phenotype, similar to activating mutations in Ras. Thus, we are presently examining the impact of autophagy inhibition on glucose metabolism and transformation driven by other oncogenes.

**ACKNOWLEDGEMENTS**

We thank Davide Ruggero for critically reading this manuscript and Drs. Noboru Mizushima and Masaaki Komatsu for providing reagents. Grant support includes the NIH (RO1CA126792 to JD and RO1 CA130819 to SR), an UCSF PBBR Integrative Award (to JD and SR), a Culpeper Medical Scholar Award (Partnership For Cures to JD), and the California Tobacco Related Diseases Research Program (18XT-0106 to JD). RL is a DOD BCRP Predoctoral Scholar (W81XWH-08-1-0759).

## REFERENCES


Aki, T., Yamaguchi, K., Fujimiya, T., and Mizukami, Y. (2003). Phosphoinositide 3-kinase accelerates autophagic cell death during glucose deprivation in the rat cardiomyocyte-derived cell line H9c2. Oncogene *22*, 8529-8535.

Berry, D.L., and Baehrecke, E.H. (2007). Growth arrest and autophagy are required for salivary gland cell degradation in Drosophila. Cell *131*, 1137-1148.

Chen, N., and Debnath, J. (2010). Autophagy and tumorigenesis. FEBS Lett *584*, 1427-1435.

Chiaradonna, F., Sacco, E., Manzoni, R., Giorgio, M., Vanoni, M., and Alberghina, L. (2006). Ras-dependent carbon metabolism and transformation in mouse fibroblasts. Oncogene *25*, 5391-5404.

Dai, C., Whitesell, L., Rogers, A.B., and Lindquist, S. (2007). Heat shock factor 1 is a powerful multifaceted modifier of carcinogenesis. Cell *130*, 1005-1018.

Debnath, J., Mills, K.R., Collins, N.L., Reginato, M.J., Muthuswamy, S.K., and Brugge, J.S. (2002). The role of apoptosis in creating and maintaining luminal space within normal and oncogene-expressing mammary acini. Cell *111*, 29-40.

Debnath, J., Muthuswamy, S.K., and Brugge, J.S. (2003). Morphogenesis and oncogenesis of MCF-10A mammary epithelial acini grown in three-dimensional basement membrane cultures. Methods *30*, 256-268.

Degenhardt, K., Mathew, R., Beaudoin, B., Bray, K., Anderson, D., Chen, G., Mukherjee, C., Shi, Y., Gelinas, C., Fan, Y., Nelson, D.A., Jin, S., and White, E. (2006). Autophagy promotes tumor cell survival and restricts necrosis, inflammation, and tumorigenesis. Cancer cell *10*, 51-64.

DiPaola, R.S., Dvorzhinski, D., Thalasila, A., Garikapaty, V., Doram, D., May, M., Bray, K., Mathew, R., Beaudoin, B., Karp, C., Stein, M., Foran, D.J., and White, E. (2008). Therapeutic starvation and autophagy in prostate cancer: a new paradigm for targeting metabolism in cancer therapy. The Prostate *68*, 1743-1752.

Fimia, G.M., Stoykova, A., Romagnoli, A., Giunta, L., Di Bartolomeo, S., Nardacci, R., Corazzari, M., Fuoco, C., Ucar, A., Schwartz, P., Gruss, P., Piacentini, M., Chowdhury, K., and Cecconi, F. (2007). Ambra1 regulates autophagy and development of the nervous system. Nature *447*, 1121-1125.

Frisch, S.M., and Francis, H. (1994). Disruption of epithelial cell-matrix interactions induces apoptosis. The Journal of cell biology *124*, 619-626.

Fung, C., Lock, R., Gao, S., Salas, E., and Debnath, J. (2008). Induction of Autophagy during Extracellular Matrix Detachment Promotes Cell Survival. Mol Biol Cell *19*, 797-806.

Furuta, S., Hidaka, E., Ogata, A., Yokota, S., and Kamata, T. (2004). Ras is involved in the negative control of autophagy through the class I PI3-kinase. Oncogene *23*, 3898-3904.

Gilmore, A.P. (2005). Anoikis. Cell death and differentiation *12 Suppl 2*, 1473-1477.

Karantza-Wadsworth, V., Patel, S., Kravchuk, O., Chen, G., Mathew, R., Jin, S., and White, E. (2007). Autophagy mitigates metabolic stress and genome damage in mammary tumorigenesis. Genes & development *21*, 1621-1635.

Khwaja, A., Rodriguez-Viciana, P., Wennstrom, S., Warne, P.H., and Downward, J. (1997). Matrix adhesion and Ras transformation both activate a phosphoinositide 3-OH kinase and protein kinase B/Akt cellular survival pathway. The EMBO journal *16*, 2783-2793.

Komatsu, M., Waguri, S., Ueno, T., Iwata, J., Murata, S., Tanida, I., Ezaki, J., Mizushima, N., Ohsumi, Y., Uchiyama, Y., Kominami, E., Tanaka, K., and Chiba, T. (2005). Impairment of starvation-induced and constitutive autophagy in Atg7-deficient mice. J Cell Biol *169*, 425-434.

Kuma, A., Hatano, M., Matsui, M., Yamamoto, A., Nakaya, H., Yoshimori, T., Ohsumi, Y., Tokuhisa, T., and Mizushima, N. (2004). The role of autophagy during the early neonatal starvation period. Nature *432*, 1032-1036.
Liang, X.H., Jackson, S., Seaman, M., Brown, K., Kempkes, B., Hibshoosh, H., and Levine, B. (1999). Induction of autophagy and inhibition of tumorigenesis by beclin 1. Nature *402*, 672-676.
Maiuri, M.C., Tasdemir, E., Criollo, A., Morselli, E., Vicencio, J.M., Carnuccio, R., and Kroemer, G. (2009). Control of autophagy by oncogenes and tumor suppressor genes. Cell death and differentiation *16*, 87-93.
Mathew, R., Karp, C.M., Beaudoin, B., Vuong, N., Chen, G., Chen, H.Y., Bray, K., Reddy, A., Bhanot, G., Gelinas, C., Dipaola, R.S., Karantza-Wadsworth, V., and White, E. (2009). Autophagy suppresses tumorigenesis through elimination of p62. Cell *137*, 1062-1075.
Mathew, R., Kongara, S., Beaudoin, B., Karp, C.M., Bray, K., Degenhardt, K., Chen, G., Jin, S., and White, E. (2007). Autophagy suppresses tumor progression by limiting chromosomal instability. Genes & development *21*, 1367-1381.
Ohsumi, Y. (2001). Molecular dissection of autophagy: two ubiquitin-like systems. Nat Rev Mol Cell Biol *2*, 211-216.
Onodera, J., and Ohsumi, Y. (2005). Autophagy is required for maintenance of amino acid levels and protein synthesis under nitrogen starvation. The Journal of biological chemistry *280*, 31582-31586.
Pattingre, S., Bauvy, C., and Codogno, P. (2003). Amino acids interfere with the ERK1/2-dependent control of macroautophagy by controlling the activation of Raf-1 in human colon cancer HT-29 cells. The Journal of biological chemistry *278*, 16667-16674.
Pattingre, S., Tassa, A., Qu, X., Garuti, R., Liang, X.H., Mizushima, N., Packer, M., Schneider, M.D., and Levine, B. (2005). Bcl-2 antiapoptotic proteins inhibit Beclin 1-dependent autophagy. Cell *122*, 927-939.
Qu, X., Yu, J., Bhagat, G., Furuya, N., Hibshoosh, H., Troxel, A., Rosen, J., Eskelinen, E.L., Mizushima, N., Ohsumi, Y., Cattoretti, G., and Levine, B. (2003). Promotion of tumorigenesis by heterozygous disruption of the beclin 1 autophagy gene. The Journal of clinical investigation *112*, 1809-1820.
Shakya, A., Cooksey, R., Cox, J.E., Wang, V., McClain, D.A., and Tantin, D. (2009). Oct1 loss of function induces a coordinate metabolic shift that opposes tumorigenicity. Nature cell biology *11*, 320-327.
Sou, Y.S., Waguri, S., Iwata, J., Ueno, T., Fujimura, T., Hara, T., Sawada, N., Yamada, A., Mizushima, N., Uchiyama, Y., Kominami, E., Tanaka, K., and Komatsu, M. (2008). The Atg8 conjugation system is indispensable for proper development of autophagic isolation membranes in mice. Mol Biol Cell *19*, 4762-4775.
Tsukamoto, S., Kuma, A., Murakami, M., Kishi, C., Yamamoto, A., and Mizushima, N. (2008). Autophagy is essential for preimplantation development of mouse embryos. Science (New York, N.Y *321*, 117-120.
Tyagi, R.K., Azrad, A., Degani, H., and Salomon, Y. (1996). Simultaneous extraction of cellular lipids and water-soluble metabolites: evaluation by NMR spectroscopy. Magn Reson Med *35*, 194-200.
Vander Heiden, M.G., Cantley, L.C., and Thompson, C.B. (2009). Understanding the Warburg effect: the metabolic requirements of cell proliferation. Science (New York, N.Y *324*, 1029-1033.

Young, A.R., Narita, M., Ferreira, M., Kirschner, K., Sadaie, M., Darot, J.F., Tavare, S., Arakawa, S., Shimizu, S., Watt, F.M., and Narita, M. (2009). Autophagy mediates the mitotic senescence transition. Genes & development *23*, 798-803.
Yue, Z., Jin, S., Yang, C., Levine, A.J., and Heintz, N. (2003). Beclin 1, an autophagy gene essential for early embryonic development, is a haploinsufficient tumor suppressor. Proceedings of the National Academy of Sciences of the United States of America *100*, 15077-15082.

**FIGURE LEGENDS**

**Figure 1.** Oncogenic Ras does not suppress ECM detachment-induced autophagy. (A) Left: Ras expression in MCF10A cells expressing empty vector (BABE) or HRasV12. Right: BABE and HRasV12 MCF10A cells were grown attached (A) or suspended (susp) for the indicated times in the presence or absence of E64d and pepstatin A (E/P), lysed, and subject to immunoblotting with antibodies against LC3 and tubulin. (B) GFP-LC3 puncta in MCF10A cells expressing empty vector (BABE) or HRasV12 grown attached or suspended for 24h. (C) Left: Ras expression in *atg5*+/+ (WT) and *atg5*-/- MEFs expressing empty vector or HRasV12. Center: *atg5*+/+ (WT) MEFs expressing empty vector (BABE) and HRasV12 were growth attached (A) or suspended (susp) for 24h in the presence or absence of E64d and pepstatin A (E/P), lysed, and subject to immunoblotting with antibodies against LC3 and tubulin. Right: *atg5*+/+ (WT) and *atg5*-/- MEFs expressing HRasV12 or empty vector (BABE) were grown attached (A) or suspended (susp) for 24h, lysed, and subject to immunobloting with antibodies against p62 and tubulin. (D) MDA-MB-231, HCT 116 and PANC-1 cells were grown attached (A) or suspended (susp) for 24h in the presence or absence of E64d and pepstatin A (E/P) and subject to immunoblotting with antibodies against LC3 and tubulin. (E) GFP-LC3 puncta in MDA-MB-231, HCT 116 and PANC-1 cells that were grown attached or detached for 24h. Bar, 25 μm.

**Figure 2.** Effects of ECM detachment on MAPK and mTORC1 signaling in Ras transformed cells. **(**A-C) Empty vector (BABE) and HRasV12 expressing MCF10A cells (A), *atg5*+/+ (WT) and *atg5*-/- MEFs (B), and K-Ras mutant carcinoma cell lines (C) were grown attached (A) or suspended (susp) for the indicated times, and subject to immunoblotting with antibodies against phosphorylated-ERK1+2 and total ERK1+2 protein. (D-F) Empty vector (BABE) and HRasV12 expressing MCF10A cells (D), *atg5*+/+ (WT) and *atg5*-/- MEFs (E), and K-Ras mutant

carcinoma cell lines (F) were grown attached (A) or suspended (susp) for the indicated times, and subject to immunoblotting with antibodies against phosphorylated-S6 and total ribosomal S6 protein. (G) HRasV12 MCF10A cells were grown attached (A) or suspended (susp) for 24h in the presence or absence of E64d and pepstatin A (E/P) and subject to immunoblotting with antibodies against phosphorylated-S6, S6, LC3, and tubulin. When indicated, cells were treated with 25nM rapamycin for 5h prior to harvest.

**Figure 3.** Decreased anchorage-independent growth in autophagy deficient MEFs expressing HRasV12. **(**A) Soft agar colony formation in HRasV12 expressing *atg5*+/+ (WT) and *atg5*-/- MEFs. (B) *atg5*-/- MEFs reconstituted with wild-type murine ATG5 or ATG5 K130R were subject to immunoblotting with antibodies against ATG12 (to detect the ATG12-ATG5 complex) and tubulin. As indicated, cells were grown attached (A) or suspended for 24h (susp) in the presence or absence of E64d and pepstatin A (E/P) and subject to immunoblotting with antibodies against LC3 and tubulin as a loading control. (C) Soft agar colony formation in HRasV12 expressing *atg5*-/- MEFs expressing ATG5 or ATG5K130R. (D-E) Soft agar colony formation in HRasV12 expressing wild type (WT), *atg7*-/-, and *atg3*-/- MEFs. Above results represent the mean+/-SEM from 3 or more independent experiments. P-value was calculated using Student's t-test.

**Figure 4.** Effects of ATG knockdown on adhesion independent transformation in MDA-MB-231 cells and HRasV12 MCF10A cells. (A) MDA-MB-231 cells transduced with lentiviral vectors encoding shRNAs against the indicated ATGs (shATGs) were subject to immunoblotting with antibodies against ATG7, ATG5 (to detect ATG12-ATG5 complex), and tubulin. (B) MDA-MB-231 cells expressing shATG7-2 or shCNT were grown attached (A) or suspended

(susp) for the indicated times in the presence or absence of E64d and pepstatin A (E/P) and subject to immunoblotting with antibodies against LC3 and tubulin. (C) Representative images and quantification of soft agar colony formation in MDA-MB-231 cells expressing the indicated shATGs. (D) HRasV12 MCF10A cells expressing shCNT or shATG7-2 were grown attached (A) or suspended (susp) for the indicated times in the presence or absence of E64d and pepstatin A (E/P) and subject to immunoblotting with antibodies against ATG7, LC3, and tubulin. (E) Representative images and quantification of soft agar colony formation in HRasV12 MCF10A cells expressing shCNT or shATG7-2. Above results represent the mean+/-SEM from 3 or more independent experiments. P-value was calculated using Student's t-test.

**Figure 5.** Bcl-2 inhibition of apoptosis is not sufficient to restore anchorage-independent growth in autophagy deficient cells. (A) HRasV12 expressing *atg5*+/+ (WT) and *atg5*-/- MEFs were grown attached (A) or suspended (susp) for the indicated times and subject to immunoblotting with antibodies against cleaved capase-3 and tubulin. (B) Bcl-2 expression levels in HRasV12 *atg5*+/+ (WT) and *atg5*-/- MEFs in the presence or absence of stable ectopic expression of Bcl-2. (C) The indicated cell types were grown attached (A) or suspended (susp) for 24h with or without E64d and pepstatin A (E/P) and subject to immunoblotting with antibodies against LC3, p62 and tubulin. (D) The indicated cell types, all expressing HRasV12, were grown attached (A) or suspended for 24h and subject to immunoblotting with antibodies against cleaved caspase-3, and tubulin. (E) Soft agar colony formation of HRasV12 *atg5*+/+ (WT) and *atg5*-/- MEFs stably expressing BCL-2. Results represent the mean+/-SEM from 3 independent experiments. P-value was calculated using Student's t-test.

**Figure 6.** Reduced proliferation upon autophagy inhibition in HRasV12 expressing MEFs and MDA-MB-231 cells. (A) The indicated cell types were grown attached or subject to ECM detachment for 48h and analyzed by flow cytometry to quantify the percent of cells with DNA content corresponding to the S and G2/M (S+G2/M) phases of the cell cycle. Results are the mean+/-SEM from 3 or more independent experiments. Statistical significance was calculated using ANOVA. (B) Proliferation curves of empty vector (BABE) *atg5*+/+ (WT) and *atg5*-/- MEFs cultured in attached, nutrient-rich conditions. (C) Proliferation curves of HRasV12 expressing *atg5*+/+ (WT) and *atg5*-/- MEFs in attached, nutrient-rich conditions. (D) Proliferation curves of MDA-MB-231 cells expressing shCNT or shATG7-2 in attached, nutrient-rich conditions. For (B-D), P-value was calculated at each timepoint using Student's t-test, with statistical significance indicated as follows: * $p<0.05$; ** $p<0.01$.

**Figure 7.** Reduced glucose metabolism in autophagy deficient MEFs. (A) Levels of glucose uptake (2-NBDG uptake, mean fluorescence intensity) in empty vector (BABE) *atg5*+/+ (WT) and *atg5*-/- MEFs following 2.5h incubation. Statistical significance was calculated using Student's t-test. (B) 2-NBDG uptake (mean fluorescence intensity) after 1h (left histogram) and over an 8h timecourse (right graph) in HRasV12 expressing *atg5*+/+ (WT) and *atg5*-/- MEFs. P-value was calculated at each timepoint using Student's t-test, with statistical significance indicated as follows: * $p<0.05$; ** $p<0.01$; ***$p<0.001$. (C) Levels of $^{13}C$ labeled intracellular lactate and extracellular lactate detected by NMR following 24h of labeling with 1-$^{13}C$-glucose. Results represent the mean+/-SEM from 3 independent experiments. Statistical significance was calculated using ANOVA.

**Figure 8.** The proliferation and transformation of autophagy competent cells is more sensitive to diminished glucose availability than autophagy deficient cells. (A) HRasV12 expressing WT MEFs were cultured in media containing 25mM or 5.5mM glucose for 48h, or in the complete absence of glucose (0mM) for 9h. E64d and pepstatin A (E/P) were added when indicated to measure autophagic flux. Cells were lysed and subject to immunoblotting with antibodies against LC3, p62, and tubulin as a loading control. (B) Left: Media glucose levels from cultures of HRasV12 *atg5*+/+ (WT) and *atg5*-/- MEFs grown in 5.5mM glucose over 2d. Right: Relative percentage of viable cells in 5.5mM glucose compared to 25mM glucose following 4d of culture. (C) Left: Media glucose levels from cultures of MDA-MB-231 cells expressing shCNT or shATG7-2 grown in 2.8mM glucose over 2d. Right: Relative percentage of viable cells grown in 2.8mM and 1.4mM glucose media compared to 25mM glucose following 3d of growth. (D) Soft agar colony formation of HRasV12 expressing *atg5*+/+ (WT) and *atg5*-/- MEFs in 25mM and 5.5mM glucose conditions. Results represent the mean+/-SEM from 4 independent experiments. Statistical significance was calculated using ANOVA.

.

**SUPPLEMENTAL FIGURES**

**Figure S1.** *De novo* protein synthesis following ECM detachment. (A) Left: Empty vector (BABE) and HRasV12 expressing wild type and *atg5*-/- MEFs were grown attached (A) or suspended (susp) for 24h and labeled using TAMRA Click-iT Protein Analysis Detection Kit to detect newly translated proteins. Right: Total protein levels from the same SDS-PAGE gel. (B) Quantification of translated protein levels normalized to total protein (middle column) and quantification of the decrease in protein synthesis following suspension expressed as percent of

translated protein relative to the attached condition (right column). Results are representative of three independent experiments.

**Figure S2:** Reduced glucose metabolism in autophagy deficient cells. (A) 2-NBDG uptake (mean fluorescence intensity) in empty vector (BABE) and HRasV12 *atg5*+/+ (WT) MEFs following 2.5h incubation. (B) 2-NBDG uptake (mean fluorescence intensity) in HRasV12 atg5+/+ (WT) and HRasV12 *atg5*-/- MEFs following 7h suspension. (C) Levels of $^{13}C$ labeled intracellular alanine detected by NMR following 24h of labeling with 1-$^{13}C$-glucose. (D) Left: Lactate dehydrogenase (LDH) activity levels in MDA-MB-231 cells expressing shCNT or shATG7-2. Right: MDA-MB-231 cells were subject to immunoblotting with antibodies against LDH-A and tubulin. (E) Empty vector (BABE) and HRasV12 expressing *atg5*+/+ (WT) and *atg5*-/- MEFs were subject to immunoblotting with antibodies against LDH-A and tubulin. Results represent the mean+/-SEM from 3 or more independent experiments. For all panels, statistical significance was calculated using Student's t-test.

**Figure 1**

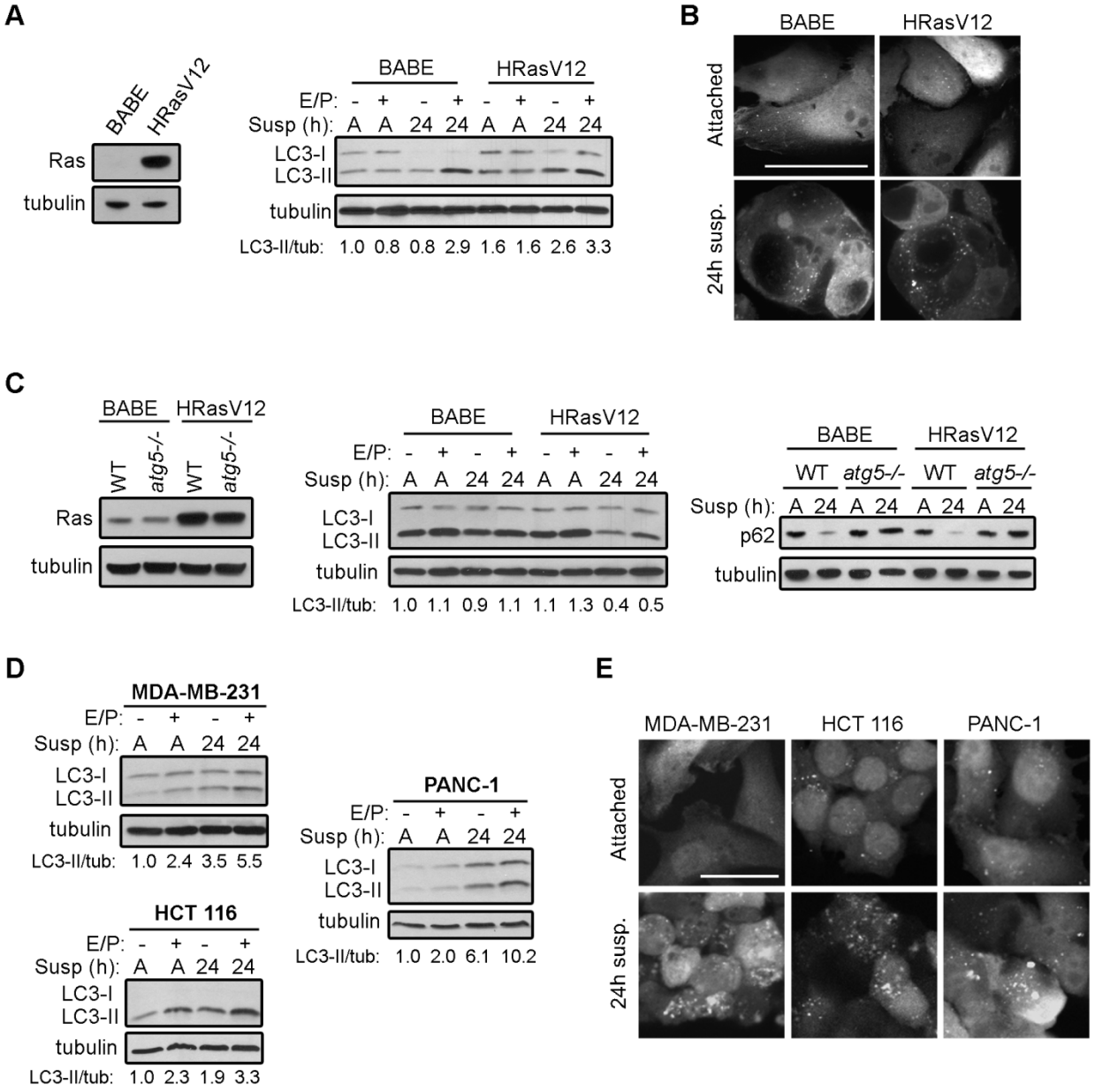
A
BABE
HRasV12
Ras
tubulin
BABE
HRasV12
E/P: - + - + - + - +
Susp (h): A A 24 24 A A 24 24
LC3-I
LC3-II
tubulin
LC3-II/tub: 1.0 0.8 0.8 2.9 1.6 1.6 2.6 3.3
B
BABE
HRasV12
Attached
24h susp.
C
BABE
HRasV12
WT
atg5-/-
WT
atg5-/-
Ras
tubulin
BABE
HRasV12
E/P: - + - + - + - +
Susp (h): A A 24 24 A A 24 24
LC3-I
LC3-II
tubulin
LC3-II/tub: 1.0 1.1 0.9 1.1 1.1 1.3 0.4 0.5
BABE
HRasV12
WT
atg5-/-
WT
atg5-/-
Susp (h): A 24 A 24 A 24 A 24
p62
tubulin
D
MDA-MB-231
E/P: - + - +
Susp (h): A A 24 24
LC3-I
LC3-II
tubulin
LC3-II/tub: 1.0 2.4 3.5 5.5
HCT 116
E/P: - + - +
Susp (h): A A 24 24
LC3-I
LC3-II
tubulin
LC3-II/tub: 1.0 2.3 1.9 3.3
PANC-1
E/P: - + - +
Susp (h): A A 24 24
LC3-I
LC3-II
tubulin
LC3-II/tub: 1.0 2.0 6.1 10.2
E
MDA-MB-231
HCT 116
PANC-1
Attached
24h susp.

**Figure 2**

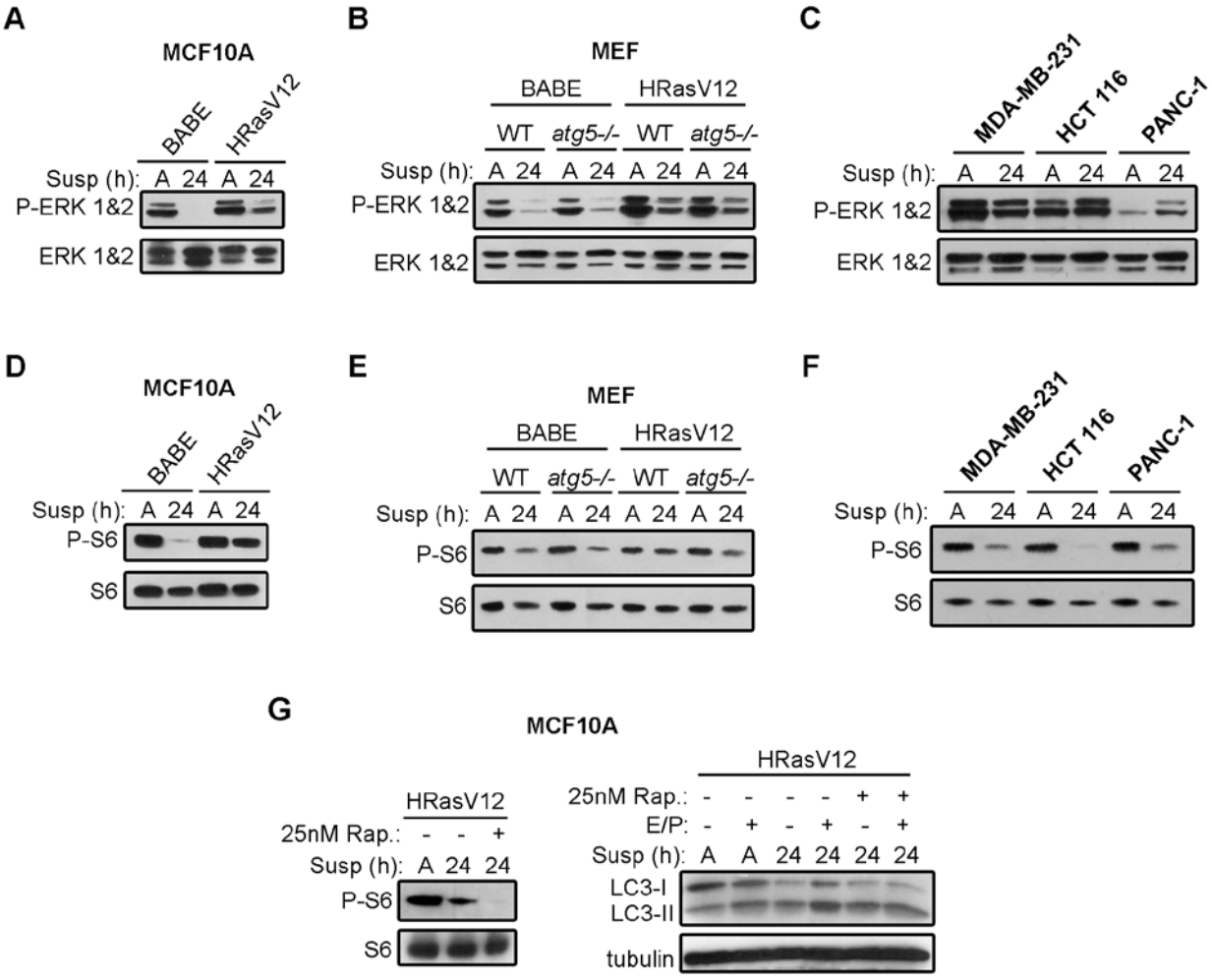
A
MCF10A
BABE
HRasV12
Susp (h): A 24 A 24
P-ERK 1&2
ERK 1&2
B
MEF
BABE
HRasV12
WT
atg5-/-
WT
atg5-/-
Susp (h): A 24 A 24 A 24 A 24
P-ERK 1&2
ERK 1&2
C
MDA-MB-231
HCT 116
PANC-1
Susp (h): A 24 A 24 A 24
P-ERK 1&2
ERK 1&2
D
MCF10A
BABE
HRasV12
Susp (h): A 24 A 24
P-S6
S6
E
MEF
BABE
HRasV12
WT
atg5-/-
WT
atg5-/-
Susp (h): A 24 A 24 A 24 A 24
P-S6
S6
F
MDA-MB-231
HCT 116
PANC-1
Susp (h): A 24 A 24 A 24
P-S6
S6
G
MCF10A
HRasV12
25nM Rap.: - - +
Susp (h): A 24 24
P-S6
S6
HRasV12
25nM Rap.: - - - - + +
E/P: - + - + - +
Susp (h): A A 24 24 24 24
LC3-I
LC3-II
tubulin

**Figure 3**

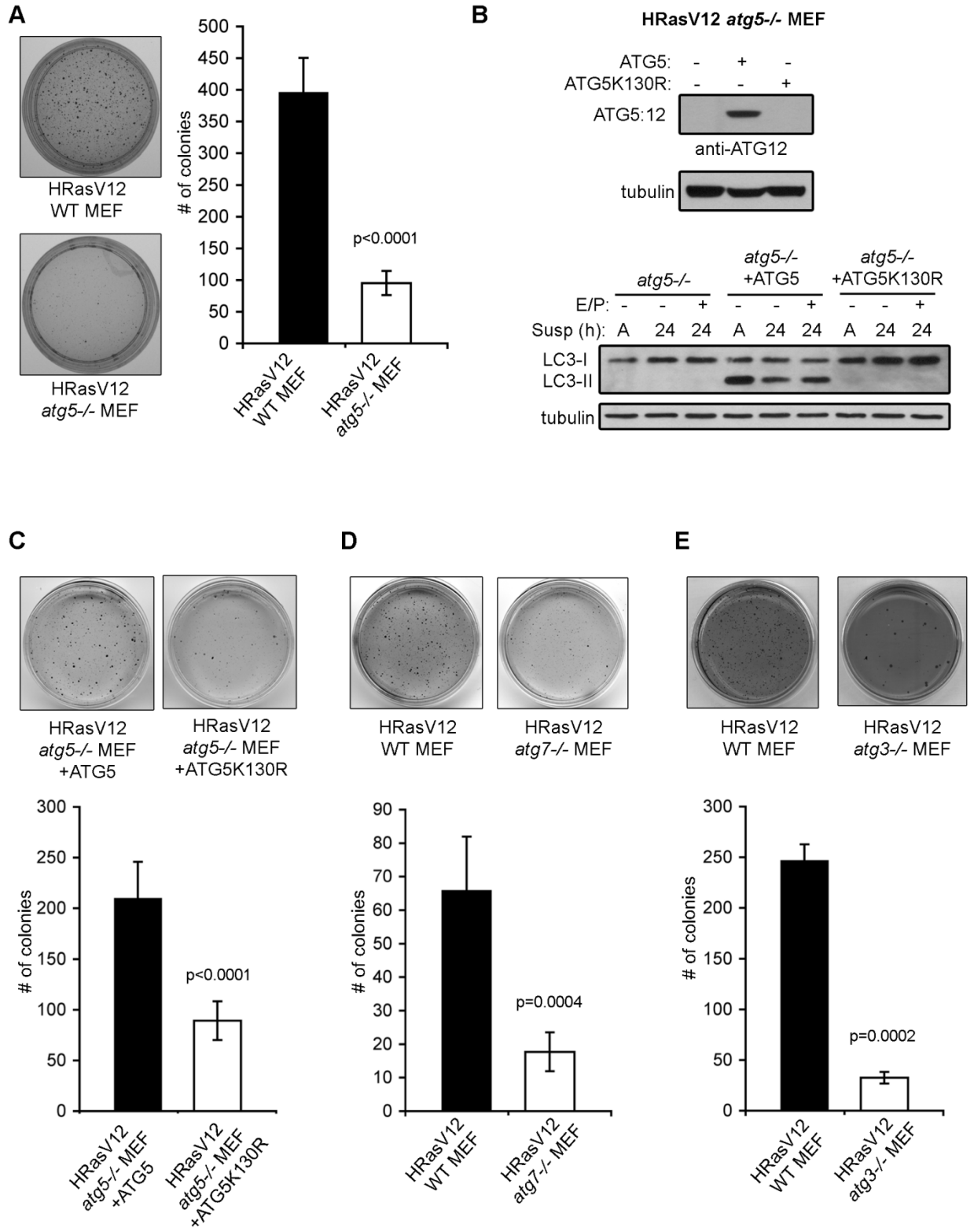
A
HRasV12
WT MEF
HRasV12
atg5-/- MEF
# of colonies
500
450
400
350
300
250
200
150
100
50
0
p<0.0001
HRasV12
WT MEF
HRasV12
atg5-/- MEF
B
HRasV12 atg5-/- MEF
ATG5: - + -
ATG5K130R: - - +
ATG5:12
anti-ATG12
tubulin
atg5-/-
atg5-/-
+ATG5
atg5-/-
+ATG5K130R
E/P: - - + - - + - - +
Susp (h): A 24 24 A 24 24 A 24 24
LC3-I
LC3-II
tubulin
C
HRasV12
atg5-/- MEF
+ATG5
HRasV12
atg5-/- MEF
+ATG5K130R
# of colonies
300
250
200
150
100
50
0
p<0.0001
HRasV12
atg5-/- MEF
+ATG5
HRasV12
atg5-/- MEF
+ATG5K130R
D
HRasV12
WT MEF
HRasV12
atg7-/- MEF
# of colonies
90
80
70
60
50
40
30
20
10
0
p=0.0004
HRasV12
WT MEF
HRasV12
atg7-/- MEF
E
HRasV12
WT MEF
HRasV12
atg3-/- MEF
# of colonies
300
250
200
150
100
50
0
p=0.0002
HRasV12
WT MEF
HRasV12
atg3-/- MEF

**Figure 4**

.

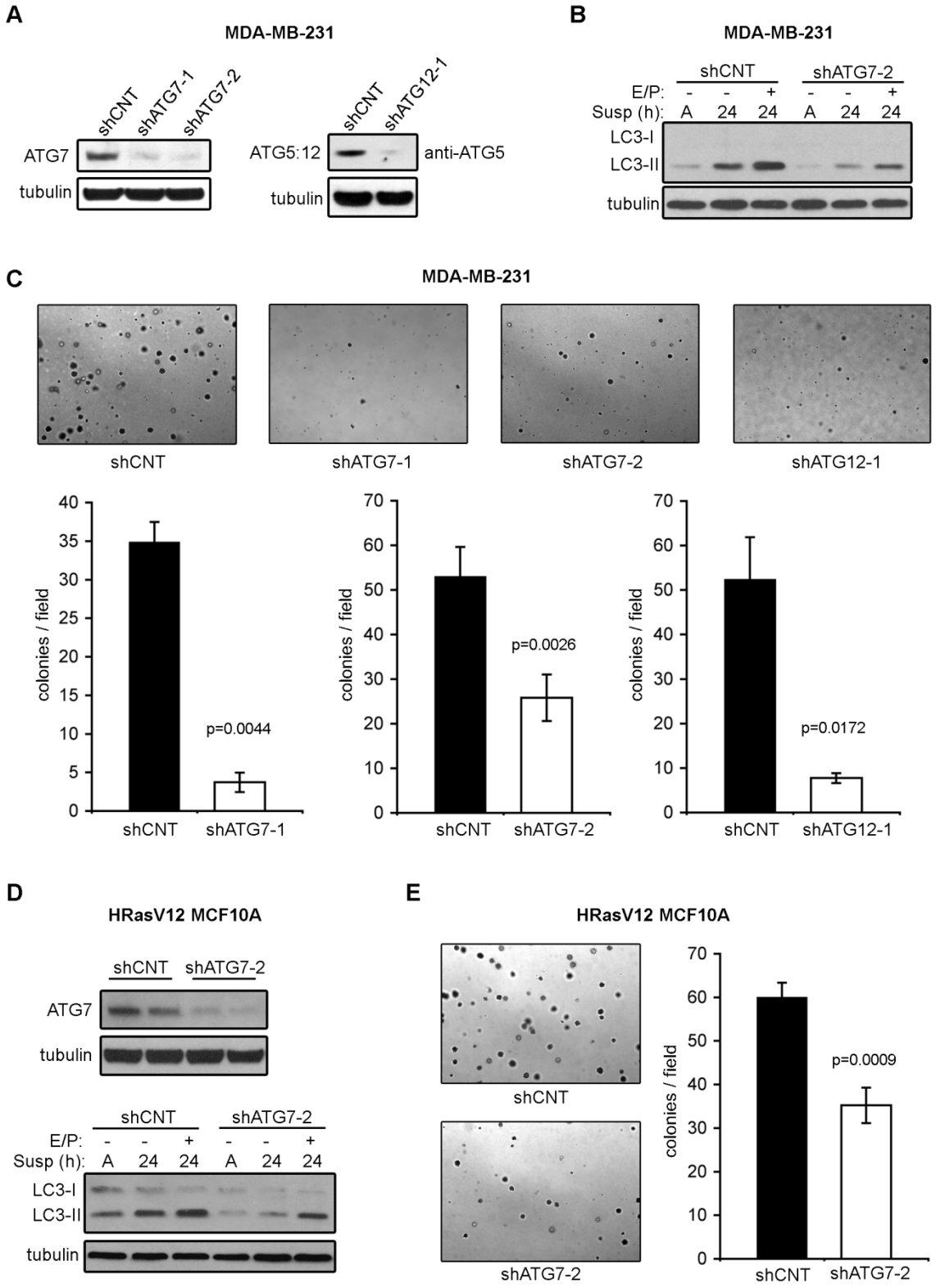
A
MDA-MB-231
shCNT
shATG7-1
shATG7-2
ATG7
tubulin
shCNT
shATG12-1
ATG5:12
anti-ATG5
tubulin
B
MDA-MB-231
shCNT
shATG7-2
E/P: - - + - - +
Susp (h): A 24 24 A 24 24
LC3-I
LC3-II
tubulin
C
MDA-MB-231
shCNT
shATG7-1
shATG7-2
shATG12-1
colonies / field
p=0.0044
shCNT
shATG7-1
p=0.0026
shCNT
shATG7-2
p=0.0172
shCNT
shATG12-1
D
HRasV12 MCF10A
shCNT
shATG7-2
ATG7
tubulin
shCNT
shATG7-2
E/P: - - + - - +
Susp (h): A 24 24 A 24 24
LC3-I
LC3-II
tubulin
E
HRasV12 MCF10A
shCNT
shATG7-2
colonies / field
p=0.0009
shCNT
shATG7-2

**Figure 5**

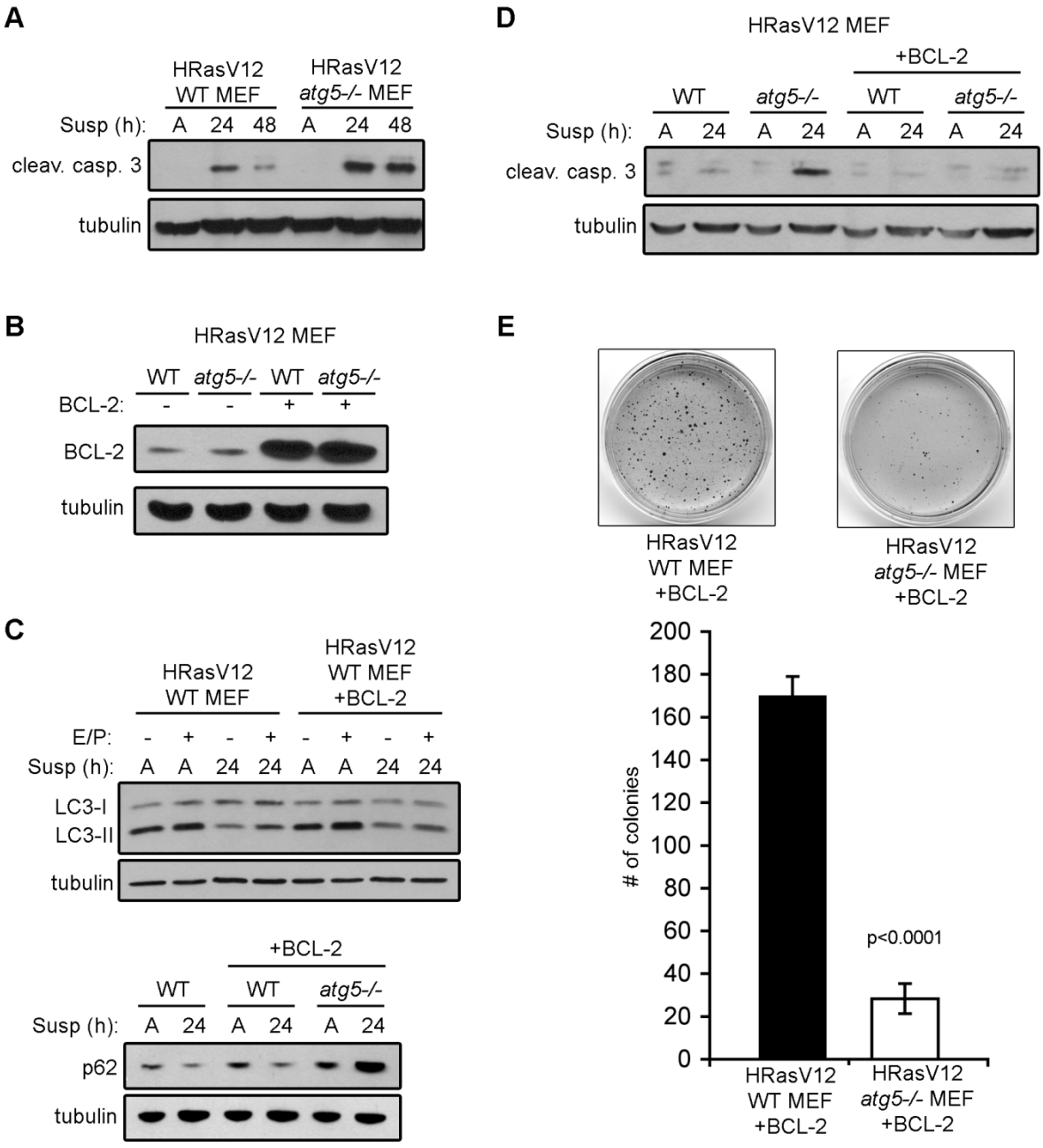
A
HRasV12 WT MEF
HRasV12 atg5-/- MEF
Susp (h): A 24 48 A 24 48
cleav. casp. 3
tubulin
B
HRasV12 MEF
WT atg5-/- WT atg5-/-
BCL-2: - - + +
BCL-2
tubulin
C
HRasV12 WT MEF
HRasV12 WT MEF +BCL-2
E/P: - + - + - + - +
Susp (h): A A 24 24 A A 24 24
LC3-I
LC3-II
tubulin
+BCL-2
WT WT atg5-/-
Susp (h): A 24 A 24 A 24
p62
tubulin
D
HRasV12 MEF
+BCL-2
WT atg5-/- WT atg5-/-
Susp (h): A 24 A 24 A 24 A 24
cleav. casp. 3
tubulin
E
HRasV12 WT MEF +BCL-2
HRasV12 atg5-/- MEF +BCL-2
# of colonies
200
180
160
140
120
100
80
60
40
20
0
p<0.0001
HRasV12 WT MEF +BCL-2
HRasV12 atg5-/- MEF +BCL-2

**Figure 6**

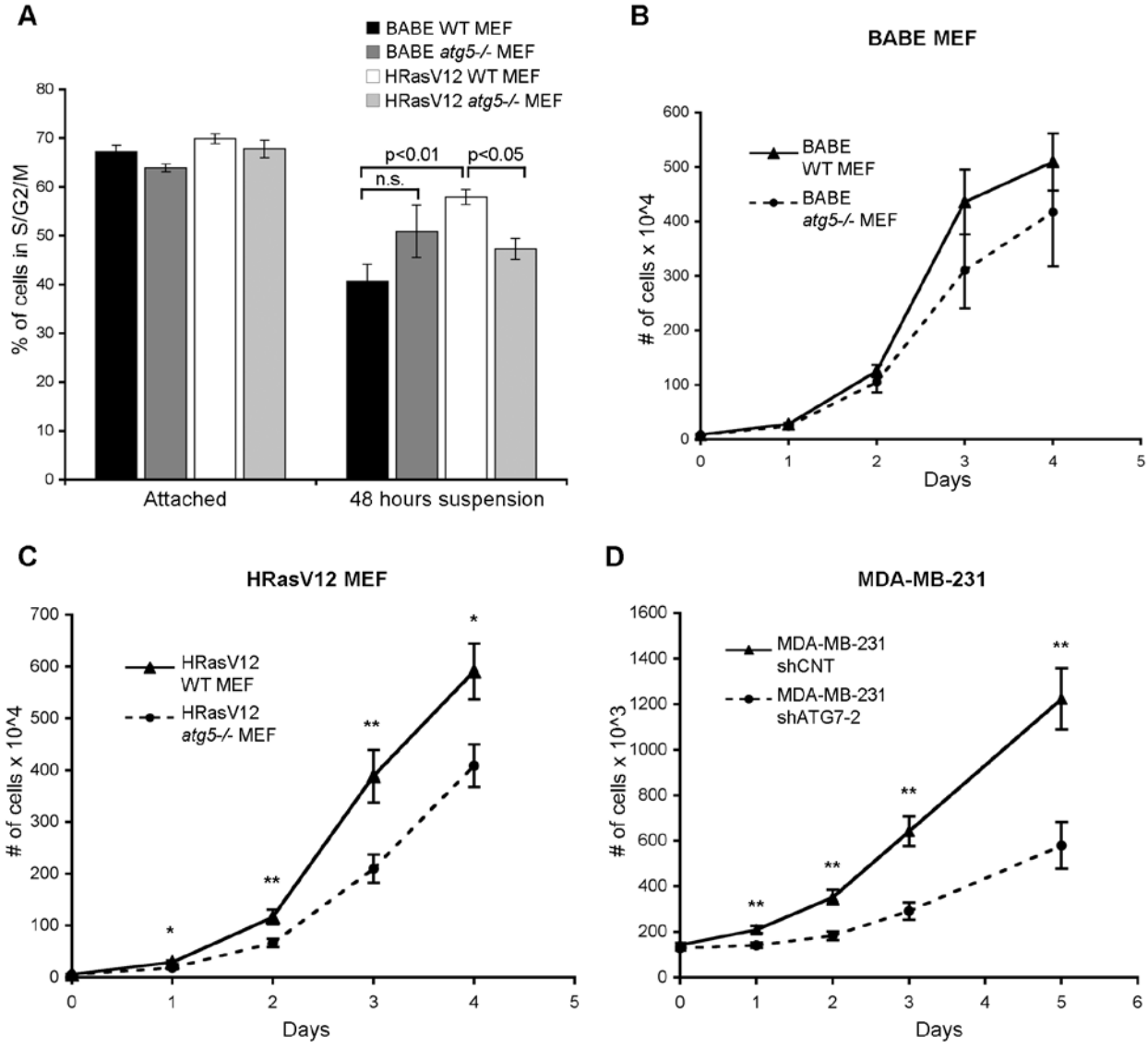
A
BABE WT MEF
BABE atg5-/- MEF
HRasV12 WT MEF
HRasV12 atg5-/- MEF
% of cells in S/G2/M
p<0.01
p<0.05
n.s.
Attached
48 hours suspension
B
BABE MEF
BABE WT MEF
BABE atg5-/- MEF
# of cells x 10^4
Days
C
HRasV12 MEF
HRasV12 WT MEF
HRasV12 atg5-/- MEF
# of cells x 10^4
Days
D
MDA-MB-231
MDA-MB-231 shCNT
MDA-MB-231 shATG7-2
# of cells x 10^3
Days

## Figure 7

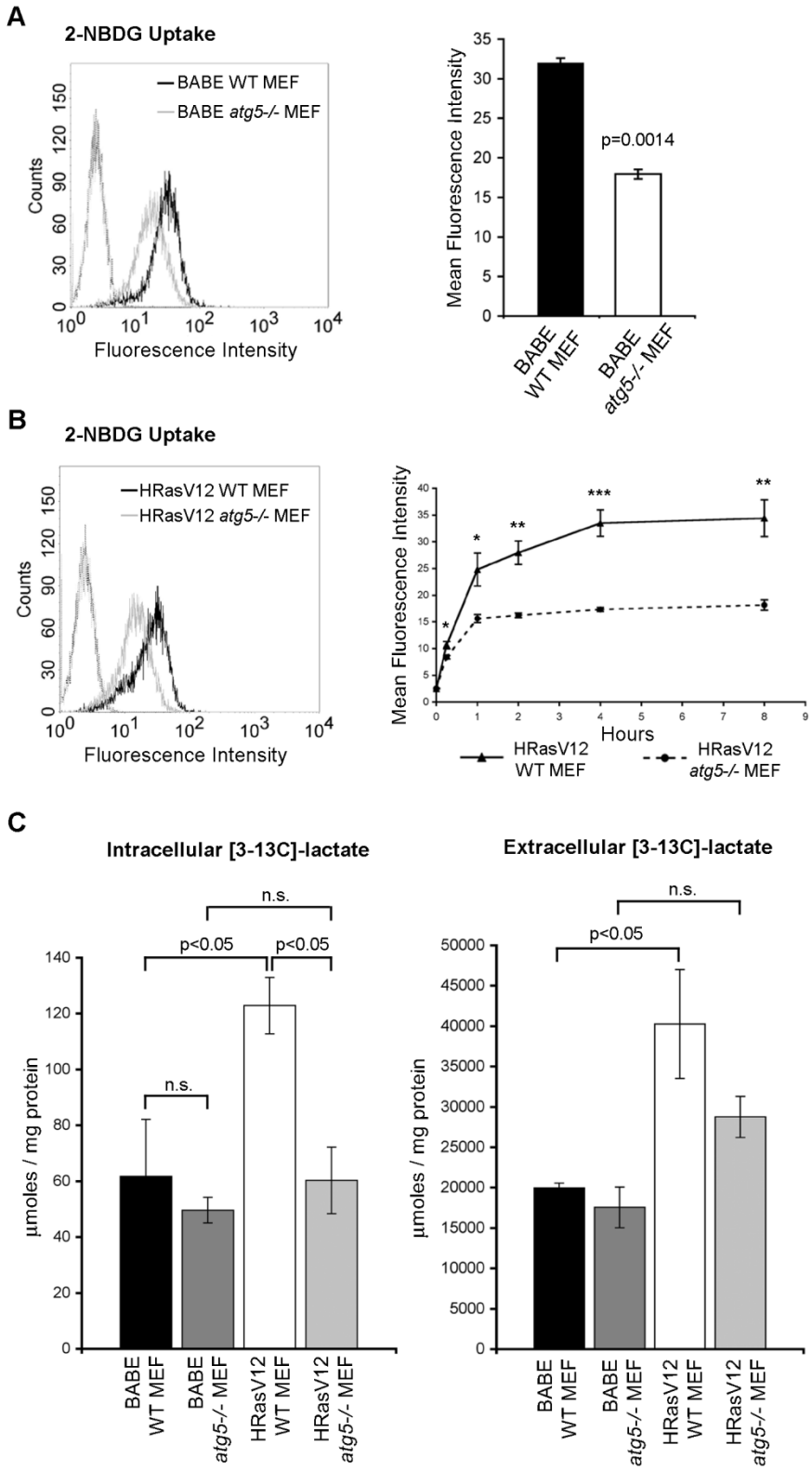
A
2-NBDG Uptake
BABE WT MEF
BABE atg5-/- MEF
Counts
Fluorescence Intensity
Mean Fluorescence Intensity
p=0.0014
BABE WT MEF
BABE atg5-/- MEF
B
2-NBDG Uptake
HRasV12 WT MEF
HRasV12 atg5-/- MEF
Counts
Fluorescence Intensity
Mean Fluorescence Intensity
Hours
HRasV12 WT MEF
HRasV12 atg5-/- MEF
C
Intracellular [3-13C]-lactate
Extracellular [3-13C]-lactate
n.s.
p<0.05
p<0.05
n.s.
µmoles / mg protein
BABE WT MEF
BABE atg5-/- MEF
HRasV12 WT MEF
HRasV12 atg5-/- MEF

**Figure 8**

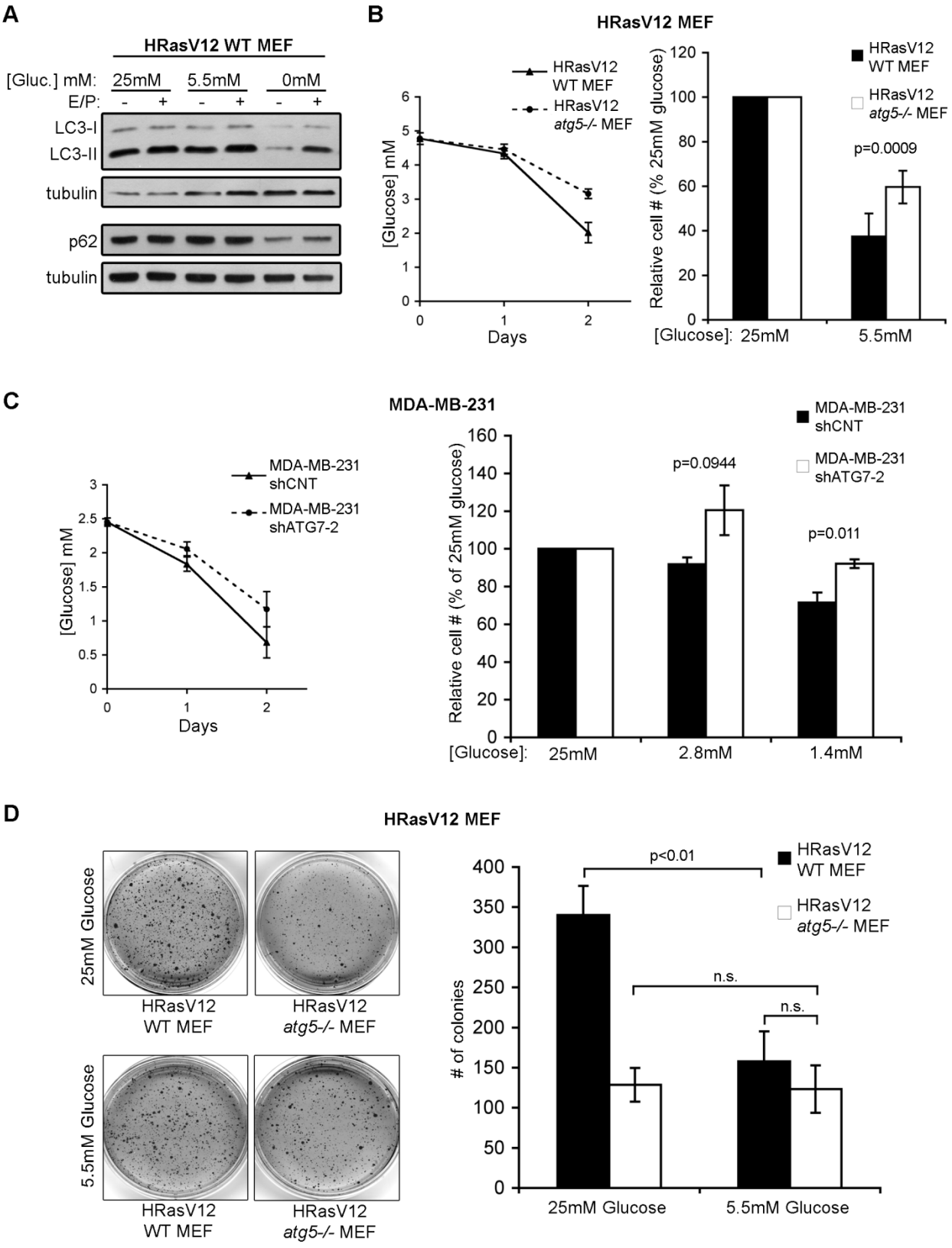
A
HRasV12 WT MEF
[Gluc.] mM: 25mM 5.5mM 0mM
E/P: - + - + - +
LC3-I
LC3-II
tubulin
p62
tubulin
B
HRasV12 MEF
HRasV12 WT MEF
HRasV12 atg5-/- MEF
[Glucose] mM
Days
Relative cell # (% 25mM glucose)
p=0.0009
[Glucose]: 25mM 5.5mM
C
MDA-MB-231
MDA-MB-231 shCNT
MDA-MB-231 shATG7-2
[Glucose] mM
Days
Relative cell # (% of 25mM glucose)
p=0.0944
p=0.011
[Glucose]: 25mM 2.8mM 1.4mM
D
HRasV12 MEF
25mM Glucose
5.5mM Glucose
HRasV12 WT MEF
HRasV12 atg5-/- MEF
p<0.01
n.s.
n.s.
# of colonies
25mM Glucose
5.5mM Glucose

**Figure S1**

**A**

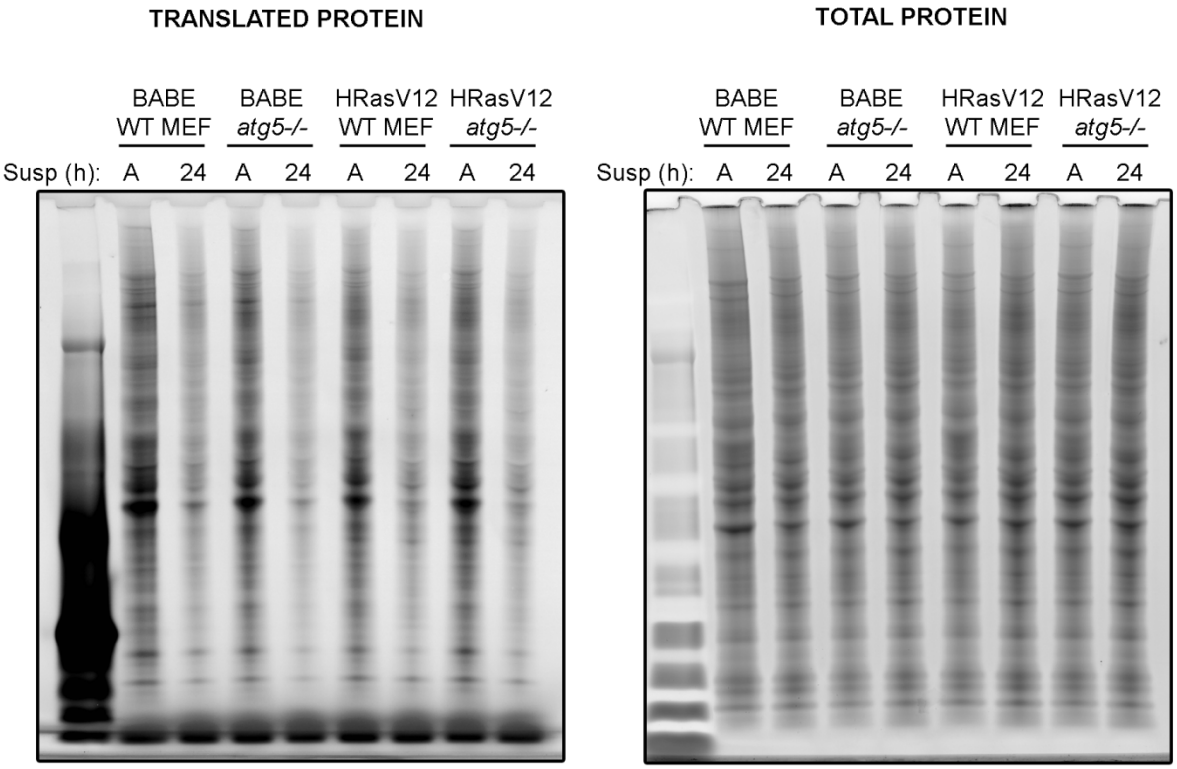


**B**

| | TRANS. PROT. (AU) | % OF ATTACH. |
|---|---|---|
| **BABE WT MEF Attached** | 903101.2 | 100.0 |
| **BABE WT MEF 24hr sus** | 251643.3 | 27.9 |
| **BABE atg5-/- MEF Attached** | 823654.5 | 100.0 |
| **BABE atg5-/- MEF 24hr sus** | 140428.3 | 17.0 |
| **HRasV12 WT MEF Attached** | 731482.6 | 100.0 |
| **HRasV12 WT MEF 24hr sus** | 199562.4 | 27.3 |
| **HRasV12 atg5-/- MEF Attached** | 747440.8 | 100.0 |
| **HRasV12 atg5-/- MEF 24hr sus** | 161101.4 | 21.6 |

**Figure S2**

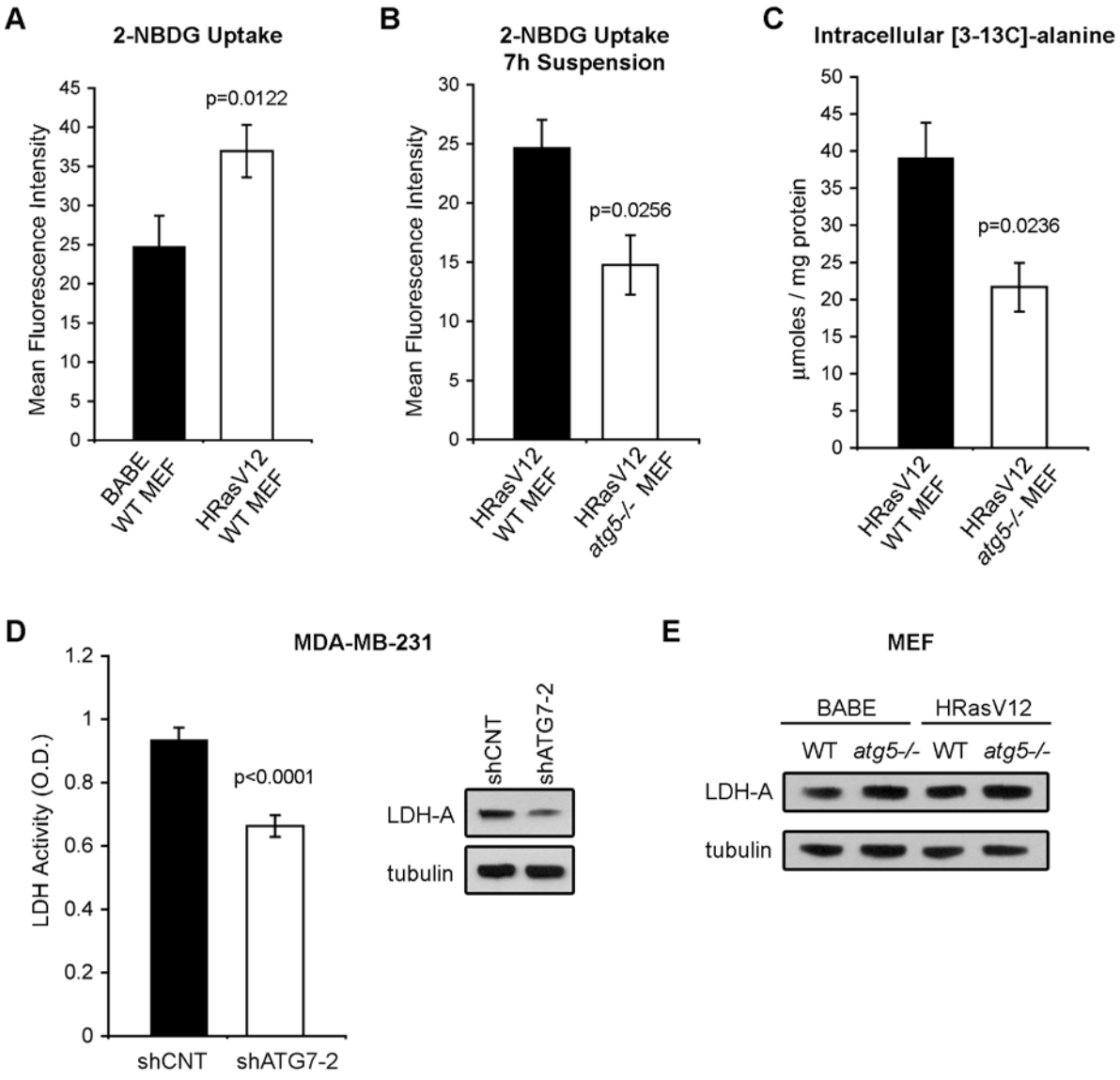
A
2-NBDG Uptake
Mean Fluorescence Intensity
p=0.0122
BABE WT MEF
HRasV12 WT MEF
B
2-NBDG Uptake 7h Suspension
Mean Fluorescence Intensity
p=0.0256
HRasV12 WT MEF
HRasV12 atg5-/- MEF
C
Intracellular [3-13C]-alanine
µmoles / mg protein
p=0.0236
HRasV12 WT MEF
HRasV12 atg5-/- MEF
D
MDA-MB-231
LDH Activity (O.D.)
p<0.0001
shCNT
shATG7-2
shCNT
shATG7-2
LDH-A
tubulin
E
MEF
BABE
HRasV12
WT
atg5-/-
WT
atg5-/-
LDH-A
tubulin

# APPENDIX C

## Autophagy dependent production of secreted factors facilitates oncogenic RAS-driven invasion

**The following appendix is published work:**

Lock, R., **Kenific, C.M.,** Leidal, A.M., Salas, E., and Debnath, J. Autophagy-dependent production of secreted factors facilitates oncogenic RAS-driven invasion. *Cancer Discovery* **4**, 4 (2014).

**Contributions:** The following work was performed primarily by Rebecca Lock, a former graduate student in the lab. I generated data in Figure 4 demonstrating that autophagy supports the migration of transformed cells and experimental pulmonary metastasis of HRasV12-transformed MCF10A cells. Jay Debnath supervised this study.

**ABSTRACT**

The tumor promoting functions of autophagy are primarily attributed to its ability to promote cancer cell survival. However, emerging evidence suggests that autophagy plays other roles during tumorigenesis. Here, we uncover that autophagy promotes oncogenic RAS-driven invasion. In epithelial cells transformed with oncogenic RAS, depletion of autophagy-related genes suppresses invasion in three-dimensional culture, decreases cell motility, and reduces pulmonary metastases *in vivo*. Treatment with conditioned media from autophagy-competent cells rescues the invasive capacity of autophagy-deficient cells, indicating these cells fail to secrete factors required for RAS-driven invasion. Reduced autophagy diminishes the secretion of the pro-migratory cytokine IL6, which is necessary to restore invasion of autophagy-deficient cells. Moreover, autophagy-deficient cells exhibit reduced levels of MMP2 and WNT5A. These results support a previously unrecognized function for autophagy in promoting cancer cell invasion via the coordinate production of multiple secreted factors.

**SIGNIFICANCE**

Our results delineate a previously unrecognized function for autophagy in facilitating oncogenic RAS-driven invasion. We demonstrate that an intact autophagy pathway is required for the elaboration of multiple secreted factors favoring invasion, including IL6.

## INTRODUCTION

The RAS proteins are members of a family of small GTPases critical in mediating cellular responses following activation by upstream extracellular signals, such as growth factors. Oncogenic mutations in RAS, which result in constitutive activation, are found in approximately 30% of human cancers; they are highly prevalent in several carcinomas, including lung, pancreas, and colon (1, 2). Notably, oncogenic RAS drives diverse cellular programs-proliferation, cell survival, migration, invasion and alterations in differentiation-that support tumor initiation and progression. Such mutations present a formidable therapeutic obstacle, because patients harboring mutant KRAS are refractory to most available systemic therapies and exhibit extremely poor survival (2). Hence, identifying new processes to target cancer cells with hyperactive RAS remains a question of immense clinical significance. One such pathway may be macroautophagy (autophagy), a tightly controlled lysosomal degradation process that promotes cell survival during nutrient starvation and stress. Recent evidence indicates that basal autophagy levels are enhanced upon oncogenic RAS activation and support RAS-driven transformation and tumorigenesis (3-7).

The tumor promoting functions of autophagy are largely ascribed to its importance as a survival pathway in response to diverse environmental stresses (8, 9). For example, enhanced autophagy is observed in poorly perfused, hypoxic tumor regions and loss of autophagy is associated with increased necrosis (10). Autophagy also promotes tumor cell survival in response to various cytotoxic and targeted chemotherapies (11). Importantly, studies of oncogenic RAS transformation have revealed that the pro-tumor effects of autophagy are not limited to increased survival of cancer cells under duress; rather, autophagy contributes to the metabolic fitness of the entire tumor population (3-6). Because strong oncogenic insults, such as RAS activation, are

marked by profound metabolic alterations that drive both energy production and biosynthetic capacity in rapidly proliferating cells, it has been hypothesized that autophagy maintains key metabolic pathways in RAS-transformed cells. In support, a growing body of work has unveiled a requirement for autophagy in driving proliferation as well as sustaining multiple core metabolic functions in RAS-transformed cells (3-7). These results are not unique to oncogenic RAS activation, as deletion of *RB1CC1/FIP200*, a mediator of autophagosome initiation, inhibits polyoma middle T driven mammary cancer, due to reduced proliferation and glucose metabolism (12).

In addition to its effects on proliferation and metabolism, oncogenic RAS drives diverse aggressive cellular behaviors that support tumor progression and metastasis; importantly, RAS-transformed epithelial cells exhibit highly invasive behavior associated with an epithelial-to-mesenchymal transition (EMT) (13). Here, in epithelial cells transformed with oncogenic RAS, we demonstrate that autophagy facilitates extracellular matrix (ECM) invasion, tumor cell motility, and pulmonary metastasis in vivo. Using a three-dimensional (3D) culture system, we uncover that autophagy inhibition restricts RAS-driven cell invasion and restores several aspects of normal epithelial architecture, including the polarized deposition of basement membrane and cell-cell junctional integrity. Furthermore, autophagy is required for the production of multiple secreted factors in RAS transformed cells, including interleukin-6 (IL6), matrix metalloproteinase 2 (MMP2), and WNT5A, which altogether facilitate cancer cell invasion.

## RESULTS

### Autophagy promotes invasion driven by oncogenic RAS in 3D culture.

To elucidate how autophagy impacts the cellular behavior of RAS-transformed epithelial cells, we utilized the MCF10A 3D epithelial culture system to interrogate how autophagy affects the growth and morphogenesis of cells expressing oncogenic RAS (14). We generated stable pools of MCF10A human mammary epithelial cells expressing a control vector (BABE) or an oncogenic form of HRAS ($HRAS^{V12}$) that enhances basal autophagy and elicits robust anchorage independent transformation (3). When cultured on laminin-rich ECM, control MCF10A cells formed hollow, spherical acini (Fig. S1A) (15). In contrast, $HRAS^{V12}$ transformed cells produced grossly aberrant structures notable for extensive protrusions that invaded the surrounding extracellular matrix. Individual $HRAS^{V12}$ structures formed these invasive protrusions as early as 3-5 days, ultimately producing disorganized networks of cells intermingled with large cell clusters after 8 days in 3D culture (Fig. 1A and B, left columns). The 3D morphology we observed using $HRAS^{V12}$ MCF10A cells resembles that reported for mouse mammary cells expressing oncogenic RAS and grown in a 3D collagen matrix (16).

To inhibit autophagy in this experimental system, we stably expressed unique short-hairpin RNAs (shRNA) against two autophagy genes (ATGs)—*ATG7* (shATG7-1 and shATG7-2) or *ATG12* (shATG12) in MCF10A cells expressing $HRAS^{V12}$. ATG7 or ATG12 knockdown decreased target protein levels, reduced basal and starvation (HBSS) induced autophagy, and increased protein levels of the autophagy substrate p62/SQSTM1 (Fig S1B-E). In 3D culture, the invasive protrusions observed with oncogenic RAS activation were profoundly attenuated in ATG deficient cells. Instead, $HRAS^{V12}$ shATG structures were spherical in morphology, similar to non-transformed BABE controls (Fig. 1A-B). Decreased invasive protrusions following autophagy inhibition were also observed upon stable *ATG3* knockdown (shATG3), and upon treatment with chloroquine or bafilomycin A, two lysosomal inhibitors that block the late steps

of autophagy (Fig. S1F). Importantly, ATG knockdown in $HRAS^{V12}$ cells did not affect RAS expression or activation associated phosphorylation of the major downstream effector MAPK/ERK (Fig. S1G). Thus, the reduction in 3D invasive protrusions following ATG knockdown is not due to decreased expression or activity of oncogenic RAS.

The disruption of basement membrane integrity is a hallmark of carcinoma invasion *in vivo* (14). To corroborate whether the protrusions we observed in $HRAS^{V12}$-transformed 3D cultures represented invasive behavior, we first evaluated basement membrane integrity by examining the expression and localization of the basement membrane protein LAMA5 (laminin 5) in $HRAS^{V12}$-derived acini. Consistent with previous reports, control non-transformed MCF10A acini (BABE) displayed polarized deposition of LAMA5 onto the basal surface (Fig. 2A, left panels) (15). In contrast, the expression of $HRAS^{V12}$ resulted in cytosolic accumulation of LAMA5, with no evidence of polarized deposition at the cell-ECM interface. Notably, this aberrant cytosolic staining pattern was especially prominent in the protrusions of $HRAS^{V12}$ cultures. Correlating with the decreased formation of invasive protrusions, ATG knockdown restored polarized LAMA5 secretion; based on this marker, most individual structures in ATG deficient $HRAS^{V12}$ cultures were encompassed by an intact basement membrane (Fig. 2A). Hence, in addition to restricting the formation of invasive protrusions, autophagy inhibition restored polarized basement membrane secretion typically absent in $HRAS^{V12}$ shCNT structures.

To extend these results, we evaluated ECM proteolytic activity in control and autophagy-deficient $HRAS^{V12}$ cultures by assessing fluorescence emanating from the proteolytic cleavage of dye-quenched collagen IV (COL4). In control non-transformed acini (BABE), we observed a faint ring of fluorescence surrounding each structure, corresponding to COL4 degradation due to the normal outgrowth of acini during 3D morphogenesis. On the other hand, $HRAS^{V12}$ shCNT-

expressing structures exhibited high levels of fluorescence that extended well beyond the immediate vicinity of individual structures (Fig. 2B). Notably, streaks of fluorescence connecting adjacent structures were frequently observed in $HRAS^{V12}$ shCNT cultures (Fig. 2B), which resembled the networks of invasive protrusions (Fig 1B). In contrast, $HRAS^{V12}$ shATG-derived structures exhibited a ring-like COL4 degradation pattern that was restricted to the cell-ECM interface, similar to that observed in non-transformed controls (Fig. 2B). Thus, the absence of morphological protrusions in ATG deficient $HRAS^{V12}$ cultures was associated with the restoration of basement membrane integrity and reduced ECM proteolytic activity. Together, these findings corroborate that autophagy supports RAS-driven invasion in 3D culture.

**ATG depletion in $HRAS^{V12}$ structures does not promote apoptosis or proliferation arrest in 3D culture.**

We next evaluated the impact of autophagy inhibition on oncogenic RAS-driven proliferation and cell survival. During normal MCF10A acinar morphogenesis, autophagy inhibition results in the enhanced apoptosis of cells occupying the luminal space (17). To test whether autophagy deficiency similarly impacted apoptosis in $HRAS^{V12}$ structures, we immunostained structures with an antibody against cleaved CASP3 (caspase-3). In contrast to the robust luminal apoptosis observed in control acini (BABE), only isolated cleaved CASP3 positive cells were observed in $HRAS^{V12}$ shCNT structures, consistent with the ability of oncogenic RAS to promote cell survival in 3D culture (Fig 3A). Upon enumerating cleaved CASP3 positive cells from these 3D cultures, we found that ATG knockdown did not significantly impact apoptosis in comparison to shCNT cultures (Fig. 3A). To assess whether autophagy inhibition potentially impacted non-apoptotic death processes, we also stained day 8

3D cultures with ethidium bromide (EtBr), an intravital dye that is incorporated into all dying cells. Whereas acini derived from non-transformed (BABE) cells displayed high levels of EtBr staining corresponding to luminal cell death (Fig. 3B), $HRAS^{V12}$ structures displayed only occasional EtBr cells scattered throughout the structures. Although ATG knockdown in $HRAS^{V12}$ cultures resulted in spherical structures that lacked invasive protrusions, we did not observe any increase in EtBr staining in these cultures (Fig. 3B). Thus, in contrast to normal and oncogenic PIK3CA MCF10A acinar morphogenesis, autophagy inhibition does not promote apoptosis in RAS-transformed 3D structures (17, 18).

To evaluate the effects of autophagy inhibition on the proliferative capacity of $HRAS^{V12}$ structures, we immunostained cultures with the proliferation marker Ki67 on day 8, a timepoint at which normal MCF10A acini exhibit reduced proliferation (19). As expected, low levels of Ki67 positive cells were observed in BABE structures (Fig 3C, left panels). However, both control and autophagy deficient $HRAS^{V12}$ structures displayed high levels of Ki67 positive cells (Fig 3C). Overall, these results indicate that although autophagy deficiency potently restricts $HRAS^{V12}$ driven invasion, it does not universally suppress the diverse oncogenic effects of $HRAS^{V12}$ in 3D culture, including the ability of activated RAS to inhibit apoptosis and sustain proliferation.

**Autophagy supports oncogenic RAS-driven cell migration in vitro and pulmonary metastasis in vivo.**

Because defects in invasive capacity are often associated with diminished cell motility, we next measured cell migration in autophagy competent and deficient epithelial cells. Upon ATG depletion, $HRAS^{V12}$ MCF10A cells demonstrated an approximately 30% reduction in

migratory capacity in a monolayer wound-healing assay of cell migration (Fig. 4A). Similar results were obtained using a transwell migration assay, which demonstrated a significant decrease in migration of ATG knockdown cells (Fig. 4B). We further corroborated these results using MDA-MB-231 cells, a highly migratory, KRAS mutant breast cancer cell line. siRNA-mediated knockdown of either ATG7 or ATG12 in MDA-MB-231 cells resulted in reduced LC3-II formation (Fig. S1H) as well as decreased wound closure (Fig. 4C, left). A similar decrease in MDA-MB-231 migration was also observed in the presence of the lysosomal inhibitor bafilomycin A (Fig. 4C, right). Therefore, in addition to supporting invasion of $HRAS^{V12}$ MCF10A cells in 3D culture, autophagy facilitates the migration of cells expressing oncogenic RAS in monolayer culture. Finally, we utilized an experimental metastasis assay to evaluate whether the effects of autophagy inhibition on invasion and migration correlated with changes in metastatic capacity in vivo; in support, the ability of $HRAS^{V12}$ MCF10A cells to produce pulmonary metastases was reduced upon ATG knockdown (Fig 4D).

**Altered differentiation of $HRAS^{V12}$ MCF10A cells upon autophagy inhibition.**

Constitutive RAS activation alters epithelial differentiation by driving an epithelial-mesenchymal transition (EMT) (20, 21), a process associated with increased invasive and migratory capacity *in vitro* and with metastatic capacity *in vivo* (13). Therefore, we evaluated how autophagy inhibition affects protein expression changes associated with RAS-induced EMT. We isolated BABE, $HRAS^{V12}$ shCNT and $HRAS^{V12}$ shATG expressing cells from day 8 3D cultures and determined the protein expression of a panel of EMT associated genes by immunobloting. In comparison to nontransformed BABE acini, $HRAS^{V12}$ shCNT structures displayed decreased KRT14 (keratin 14), an epithelial marker, and a corresponding increase in

the mesenchymal protein VIM (vimentin) (Fig S2A). ATG knockdown reversed these $HRAS^{V12}$ -driven changes in differentiation, resulting in an increase in KRT14 protein levels and a corresponding decrease in VIM levels compared to $HRAS^{V12}$ shCNT cells isolated from 3D culture (Fig. S2A). However, autophagy inhibition had minimal effects on other EMT markers that were altered by oncogenic RAS expression. Only a slight increase in CDH1 (E-cadherin) was observed in shATG cells, decreased FN1 (fibronectin) was only observed in shATG7-1 expressing cells, and CDH2 (N-cadherin) levels were unchanged following ATG knockdown (Fig. S2A).

During EMT, cells commonly lose the ability to form cell-cell junctions (22). Therefore, we analyzed the effects of autophagy inhibition on cell-cell junctional integrity in $HRAS^{V12}$ 3D structures by immunostaining for CTNNB1 (β-catenin). Normal MCF10A acini (BABE) displayed strong β-catenin staining at cell-cell contacts, indicating intact adherens junctions, whereas the expression of $HRAS^{V12}$ resulted in a near-complete loss of β-catenin junctional staining; in these cultures, only isolated focal areas of junctional β-catenin staining were observed (Fig. S2B). Upon ATG knockdown in $HRAS^{V12}$ structures, both the expression and junctional localization of β-catenin were significantly restored (Fig. S2B). Based on these results, we conclude that autophagy inhibition modulates certain aspects of mesenchymal differentiation in RAS-transformed cells in 3D culture, most notably the suppression of VIM, as well as the restoration of KRT14 expression and epithelial cell-cell contacts. Nonetheless, autophagy deficiency does not broadly suppress RAS-driven EMT.

**ATG knockdown in $HRAS^{V12}$ cells inhibits the production of pro-invasive secreted factors in 3D culture.**

Cell migration and invasion involves the secretion of multiple factors that cooperate to promote motility and to degrade the surrounding ECM (23, 24). To ascertain if defects in RAS-driven invasion observed following autophagy suppression were the result of decreased production of pro-invasive factors, we performed a co-culture assay in which $HRAS^{V12}$ shATG7-1 cells (co-expressing GFP for tracking purposes) were combined with $HRAS^{V12}$ shCNT cells at a ratio of 3:1, respectively. Whereas $HRAS^{V12}$ shATG7-1-GFP cells cultured alone grew as spherical structures (Fig. 5A, left panels), upon co-culture with $HRAS^{V12}$ shCNT cells, $HRAS^{V12}$ shATG7-1-GFP structures became dispersed and formed invasive protrusions (Fig. 5A, right panels). Hence, we hypothesized that factors from neighboring $HRAS^{V12}$ shCNT cells are sufficient to rescue *in trans* the invasion defect in $HRAS^{V12}$ shATG7-1 cells. To further test this prediction, we grew $HRAS^{V12}$ shATG cells in 3D culture for 3 days and subsequently treated these structures with conditioned media (CM) produced from either BABE or $HRAS^{V12}$ shCNT cultures. $HRAS^{V12}$ shATG structures remained as compact spheres following treatment with BABE CM (Fig. 5B, Fig. S3A). In contrast, CM from $HRAS^{V12}$ shCNT cultures elicited invasive protrusions at 24h following treatment, which became fully evident by 72h (Fig. 5B, Fig. S3A); notably, CM addition did not induce invasion in non-transformed BABE acini (Fig. S3B). Furthermore, basement membrane integrity was lost in $HRAS^{V12}$ shATG cells treated with $HRAS^{V12}$ CM (Fig. 5C). These findings demonstrate that autophagy inhibition in $HRAS^{V12}$ cells inhibits the production of secreted factors required for RAS-driven invasion in 3D culture.

**Diminished secretion of IL6 contributes to reduced invasion in autophagy deficient $HRAS^{V12}$ cells.**

During RAS-induced senescence, ATG depletion inhibits IL6 production following acute oncogenic RAS activation in IMR90 fibroblasts, indicating autophagy supports the production of IL6 in response to oncogenic RAS activation (25). Because IL6 has been demonstrated to support RAS-driven tumorigenesis, promote migration and invasion, and also drive epithelial-mesenchymal transition (26-28), we tested whether IL6 levels were altered in $HRAS^{V12}$ shATG 3D cultures. Analysis of IL6 in conditioned media collected from 3D cultures by ELISA indicated a significant reduction in secreted IL6 levels in $HRAS^{V12}$ shATG-expressing cultures compared to $HRAS^{V12}$ shCNT cultures (Fig. 6A). Furthermore, this decrease in secreted IL6 was not the result of reduced *IL6* gene expression; in fact, qPCR analysis revealed that *IL6* transcript levels in $HRAS^{V12}$ shATG cells were increased, rather than decreased, in comparison to $HRAS^{V12}$ shCNT cells (Fig 6B). Notably, studies of RAS-induced senescence similarly demonstrated that autophagy deficient cells exhibit reduced IL6 protein levels due to impaired translation, rather than transcription (25, 29). In contrast, we uncovered that ATG depletion did not attenuate IL6 protein levels in RAS-transformed cells grown in 3D culture (Fig 6C). These results suggest that autophagy facilitates IL6 secretion during $HRAS^{V12}$ 3D morphogenesis.

To ascertain the functional significance of these results, we interrogated whether IL6 was necessary for $HRAS^{V12}$-driven invasion in 3D culture. First, we treated $HRAS^{V12}$ shATG structures with $HRAS^{V12}$ shCNT CM in the presence versus absence of an IL6 function-blocking antibody. The addition of IL6 function-blocking antibody attenuated the ability of $HRAS^{V12}$ shCNT CM to promote invasive protrusions in $HRAS^{V12}$ shATG cultures, whereas an IgG isotype control had no effect (Fig. 6D). In parallel, we tested how exogenous recombinant human IL6 (rhIL6) treatment affected $HRAS^{V12}$ shATG cells during 3D morphogenesis. rhIL6 addition did not affect nontransformed BABE acini (Fig. S3C) but partly restored invasion in

HRAS$^{V12}$ shATG cultures, resulting in large globular structures, increased invasive protrusions, and loss of basement membrane integrity (Fig. 6E, S3D-E). Also, rhIL6 addition partially reversed the effects of autophagy inhibition on KRT14 and VIM expression in HRAS$^{V12}$ shATG7 cells (Fig. S3F). Hence, our results suggest that autophagy promotes efficient IL6 secretion by HRAS$^{V12}$ cells in 3D culture, which is necessary for invasion.

**Autophagy facilitates *MMP2* and *WNT5A* expression by HRAS$^{V12}$ cells in 3D culture.**

In addition to identifying a defect in IL6 production following ATG knockdown, we performed a qPCR array to measure the expression levels of genes involved in EMT and invasion, and identified *WNT5A* and *MMP2* as two candidate factors whose expression was upregulated in HRAS$^{V12}$ cells relative to BABE cells but potently suppressed upon autophagy inhibition. qPCR analysis of cells collected from 3D cultures confirmed a 2-fold decrease in *MMP2* and *WNT5A* expression in HRAS$^{V12}$ shATG cells compared to HRAS$^{V12}$ shCNT (Fig. 7A and B). Notably, we also evaluated the effects of rhIL6 treatment on *MMP2* and *WNT5A* expression in shATG7-1 cultures and found this was not sufficient to rescue expression, indicating that regulation of these factors was independent of IL6 (Fig. S3G).

Because these secreted factors have been implicated in cell migration and invasion, we further evaluated whether their decreased expression following ATG knockdown also contributed to the reduced invasive potential of HRAS$^{V12}$ shATG cells. First, we utilized gelatin zymography to assess MMP2 activity in CM from 3D cultures. MMP2 activity was enhanced in HRAS$^{V12}$ cells compared to non-transformed (BABE) controls, and upon ATG knockdown in HRAS$^{V12}$ cells, this activity was reduced (Fig. 7C). The increase in MMP2 expression and secretion following constitutive RAS activation was necessary for RAS-driven invasion, as

addition of an MMP2 inhibitor, Arp-100, was sufficient to inhibit the formation of invasive protrusions in $HRAS^{V12}$ 3D cultures (Fig. 7D). Furthermore, the decrease in *WNT5A* expression correlated with a decrease in WNT5A protein levels in $HRAS^{V12}$ shATG cells isolated from 3D culture (Fig. 7E). Moreover, the addition of recombinant WNT5A to $HRAS^{V12}$ shATG7-1 3D cultures promoted the dissociation of cells within the structures and enhanced the formation of invasive protrusions (Fig. 7F). Thus, in addition to IL6, autophagy facilitates the production of multiple secreted pro-migratory and invasive factors that support RAS-driven invasion in 3D culture.

## DISCUSSION

Our results delineate a previously unrecognized function for autophagy in facilitating oncogenic RAS-driven invasion and migration. Using a 3D culture system, we demonstrate that suppression of autophagy in $HRAS^{V12}$ MCF10A cells restricts the formation of invasive protrusions, restores basement membrane integrity, and attenuates ECM proteolysis. In addition, autophagy inhibition diminishes cell migration *in vitro* and pulmonary metastasis *in vivo*. Upon treatment with conditioned media produced from autophagy-competent $HRAS^{V12}$ cells, invasion is completely restored in autophagy-deficient $HRAS^{V12}$ cultures, indicating that autophagy mediates the production of secreted factors that drive invasion in oncogenic cells. In further support, we uncover that autophagy inhibition elicits the coordinate reduction of multiple molecules favoring invasion. Overall, these findings expand our understanding of how autophagy supports cancer progression.

Although autophagy inhibition suppresses invasion in 3D culture, it does not ubiquitously revert oncogenic RAS-driven changes in cell behavior. Indeed, MAPK activation remains

unaltered following autophagy inhibition in this 3D culture model and moreover, the oncogenic activation of RAS continues to disrupt fundamental aspects of 3D morphogenesis in autophagy deficient cells. First, autophagy inhibition does not alter the ability of $HRAS^{V12}$ to suppress apoptosis in 3D culture. Moreover, autophagy inhibition does not suppress proliferation in $HRAS^{V12}$ 3D cultures; rather, the spherical structures from $HRAS^{V12}$ ATG knockdown cells remain highly proliferative over extended periods. Remarkably, both others and we have shown that ATG depletion reduces soft agar growth and attenuates the proliferation of RAS-transformed cells grown in monolayer (3-5, 30); hence, the absence of proliferative suppression in this 3D culture model may be context dependent. These results also differ from those obtained in KRAS mutant mouse cancer models in which genetic ATG deletion impairs proliferation and, in certain cases, enhances apoptosis (4, 6, 7). Certain reasons may explain these differences. First, we have only reduced ATGs using RNAi, rather than genetically eliminated these proteins. Second, the experiments here are significantly shorter duration in comparison to autophagy deficient K-Ras tumor growth *in vivo*.

Although previous studies have demonstrated that autophagy supports the invasion of glioblastoma cells, the mechanistic underpinnings remain unclear (31, 32). Cell invasion requires the production and secretion of factors that stimulate migration and degrade the surrounding ECM (24). Upon treatment of autophagy depleted $HRAS^{V12}$ cells with conditioned media produced from their autophagy competent counterparts, the ability to form invasive protrusions is completely restored, suggesting that autophagy is required for the efficient production of secreted factors that promote invasion and migration of $HRAS^{V12}$ cells. Notably, conditioned media treatment does not promote invasion in nontransformed BABE cells, indicating oncogenic Ras pathway activation is still required for invasion.

Importantly, we identify IL6 as one critical factor whose secretion is ATG dependent; our results substantiate that this pro-invasive cytokine is necessary to restore invasion in autophagy-deficient $HRAS^{V12}$ cells. They also point to a specific role for autophagy in facilitating IL6 secretion; upon ATG knockdown, RAS-transformed cells fail to secrete IL6 into the conditioned media, yet both IL6 transcription and translation remain intact. These results differ from recent studies of oncogenic RAS-mediated senescence, in which reduced IL6 secretion in autophagy-deficient cells is proposed to be secondary to decreased protein synthesis (25, 29).

Though traditionally viewed as an autodigestive process, growing evidence suggests new roles for autophagy in both conventional and unconventional secretion (33). Indeed, a genetic role for ATGs has been implicated in: 1) unconventional secretion of proteins lacking N-terminal ER signal sequences (34-37); 2) efficient egress of secretory lysosomes (38, 39); and 3) conventional secretion of growth factors (40, 41). Further dissecting how autophagy directs the secretion of IL6 and other factors during RAS transformation remains an important topic for future study. Remarkably, IL6 re-addition only partially restores invasion and mesenchymal differentiation in $HRAS^{V12}$ autophagy-deficient cultures, indicating other factors promote invasion. In support, these cells exhibit reduced levels of other pro-invasive molecules, including WNT5A and MMP2. In contrast to reduced IL6 secretion, which is likely a proximal event following ATG knockdown, these changes in WNT5A and MMP2 result from decreased gene expression, indicating that autophagy inhibition produces broader transcriptional changes contributing to reduced invasion by $HRAS^{V12}$ cells.

Recently, the deletion of *RB1CC1/FIP200*, a gene mediating autophagosome initiation, was demonstrated to reduce lung metastases in the MMTV-PyMT breast cancer model. However, since *RB1CC1* deletion profoundly restricted primary tumor growth, it was unclear

whether decreased metastasis was secondary to reduced primary tumor burden (12). In addition, although liver-specific deletion of *ATG7* or *ATG5* initiates the development of benign adenomas, these tumors are unable to progress to adenocarcinomas, suggesting that autophagy is required for advanced tumor progression (42, 43). Here, in epithelial cells transformed with oncogenic RAS, we demonstrate that defective autophagy results in decreased invasion and migration, which correlates with the reduced ability to metastasize *in vivo.* Although our results do not rule out potentially important functions for autophagy in disseminated cell survival or outgrowth at foreign tissue sites, they delineate new roles for autophagy in the control of secretion during carcinoma progression.

## EXPERIMENTAL PROCEDURES

**Cell lines.** MCF10A cells were obtained from the American Tissue Culture Collection (ATCC) and cultured as previously described (44). MDA-MB-231 cells were obtained from the ATCC and cultured in DMEM supplemented with 10% FBS, penicillin, and streptomycin. Cell lines were passaged for less than 6 months following resuscitation and were not authenticated.

**Three dimensional culture assays.** MCF10A overlay 3D culture was performed as previously described (44). As indicated, the following reagents were added to cultures: 500ng/mL WNT5A (R&D Systems), 200ng/mL IL6 (Peprotech), 25 μg/mL anti-IL6 function blocking antibody (R&D Systems), 25 μg/mL IgG control antibody (BD Biosciences), 25μM Arp-100 (Santa Cruz Biotechnology), 5μM chloroquine diphosphate salt (Sigma), and 5nM bafilomycin A (Sigma). For the 3D ECM degradation assay, human DQ-COL4 (Invitrogen) was mixed with Matrigel to a final concentration of 25μg/mL prior to plating. To collect cells for immunoblotting and RNA

isolation, cultures were incubated with 0.25% Trypsin/EDTA at 37ºC for 10 min to dissociate cells from surrounding matrix and create a single cell suspension. Cells were resuspended in media containing 20% serum and washed twice with PBS to remove residual Matrigel.

For co-culture assays, shATG7-1 was expressed in $HRAS^{V12}$ cells stably expressing pBABEhygro GFP. This GFP-labeled "target" cell line was then cultured in isolation or combined with unlabelled (pBABEhygro) $HRAS^{V12}$ shCNT cells at a ratio of 3:1 with total cell number kept constant at 7,500 cells/well. For conditioned media (CM) experiments, $HRAS^{V12}$ shATG expressing cells were grown in 3D culture for 3d; subsequently, the media was replaced with conditioned media harvested from BABE or $HRAS^{V12}$ shCNT MCF10A cells grown in 3D culture for 6-8 days. When indicated, 25 μg/mL anti-IL6 function blocking or IgG isotype control antibody was added to the CM.

**Wounding Assay.** Cells were grown to confluence in 3.5 cm dishes and incubated overnight in assay media lacking EGF for MCF10A cells or DMEM+2% FBS for MDA-MB-231 cells. Wound healing was performed in the presence of 2μg/ml mitomycin C (Sigma). Cells were wounded with a 200μl pipette tip and imaged at time of wounding (0 h) and the indicated time points. Average wound widths were measured at each time point and decreases in wound width were calculated by subtracting the average width at the final time point from the average width at 0 h using MetaMorph Software (v6.0).

**Transwell Assay.** Cells were starved overnight in assay media lacking EGF and then plated at $1.0x10^5$ in the top chamber of an 8μm Transwell filter in assay media lacking EGF. The bottom chamber was filled with assay medium containing 5 ng/ml EGF. Cells were allowed to migrate

for 24 h, after which the top of each filter was cleared of cells. Cells attached to the bottom of the filter were fixed and stained with crystal violet. Crystal violet was extracted with 10% acetic acid and the absorbance was measured at 600 nm.

**Experimental metastasis assay.** For experimental metastasis assays, cells were infected with pHIV-ZsGreen (Addgene, Cambridge, MA, plasmid 18121). $1.0x10^6$ $HRAS^{V12}$ shCNT, shATG7-1, and shATG12 cells stably expressing ZsGreen were injected into the tail vein of NOD/SCID mice. After 140 days, whole lungs were fixed and imaged to detect the number of ZsGreen positive foci per lung. All animal experiments were conducted in accordance with approved UCSF IACUC protocols.

**IL6 ELISA.** Day 5 3D cultures were washed twice with PBS and cultured for 18 h in serum-free media. Conditioned media was collected, and total protein levels were determined by BCA assay (Thermo Scientific) to normalize samples. IL6 levels were measured using the Quantikine High Sensitivity ELISA kit (R&D Systems).

**Statistical analyses.** Each experiment was repeated at least three independent times. GraphPad Prism software (v5.0b) was used for generation of graphs and statistical analysis. *P* values were determined by Student's t-test or ANOVA as stated.

**ACKNOWLEDGEMENTS**

Grant support to JD includes the NIH (R01CA126792 and –S1), the DOD BCRP (W81XWH-11-1-0130 and W81XWH-12-1-0505), Samuel Waxman Cancer Research Foundation, and the

California TRDRP (18XT-0106). RL was supported by a DOD BCRP Predoctoral Award (W81XWH-08-1-0759) and CMK by a Genentech Fellowship, University of California CRCC Fellowship, and NIH F31CA167905.

## CONTRIBUTIONS

RL, CMK, AML and JD designed the experiments. RL, CMK, AML, ES and JD carried out the experiments as well as analyzed and interpreted results. JD supervised the overall study. RL and JD wrote the paper with comments from the other authors.

## REFERENCES

1. Schubbert S, Shannon K, Bollag G. Hyperactive Ras in developmental disorders and cancer. Nat Rev Cancer. 2007;7:295-308.

2. Pylayeva-Gupta Y, Grabocka E, Bar-Sagi D. RAS oncogenes: weaving a tumorigenic web. Nat Rev Cancer. 2011;11:761-74.

3. Lock R, Roy S, Kenific CM, Su JS, Salas E, Ronen SM, et al. Autophagy facilitates glycolysis during Ras-mediated oncogenic transformation. Mol Biol Cell. 2011;22:165-78.

4. Yang S, Wang X, Contino G, Liesa M, Sahin E, Ying H, et al. Pancreatic cancers require autophagy for tumor growth. Genes Dev. 2011;25:717-29.

5. Guo JY, Chen HY, Mathew R, Fan J, Strohecker AM, Karsli-Uzunbas G, et al. Activated Ras requires autophagy to maintain oxidative metabolism and tumorigenesis. Genes Dev. 2011;25:460-70.

6. Guo JY, Karsli-Uzunbas G, Mathew R, Aisner SC, Kamphorst JJ, Strohecker AM, et al. Autophagy suppresses progression of K-ras-induced lung tumors to oncocytomas and maintains lipid homeostasis. Genes Dev. 2013;27:1447-61.

7. Rosenfeldt MT, O'Prey J, Morton JP, Nixon C, MacKay G, Mrowinska A, et al. p53 status determines the role of autophagy in pancreatic tumour development. Nature. 2013;504:296-300.

8. Kimmelman AC. The dynamic nature of autophagy in cancer. Genes Dev. 2011;25:1999-2010.

9. Chen N, Debnath J. Autophagy and tumorigenesis. FEBS Lett. 2010;584:1427-35.

10. Degenhardt K, Mathew R, Beaudoin B, Bray K, Anderson D, Chen G, et al. Autophagy promotes tumor cell survival and restricts necrosis, inflammation, and tumorigenesis. Cancer cell. 2006;10:51-64.

11. Amaravadi RK, Lippincott-Schwartz J, Yin XM, Weiss WA, Takebe N, Timmer W, et al. Principles and current strategies for targeting autophagy for cancer treatment. Clin Cancer Res. 2011;17:654-66.

12. Wei H, Wei S, Gan B, Peng X, Zou W, Guan JL. Suppression of autophagy by FIP200 deletion inhibits mammary tumorigenesis. Genes Dev. 2011;25:1510-27.

13. Polyak K, Weinberg RA. Transitions between epithelial and mesenchymal states: acquisition of malignant and stem cell traits. Nat Rev Cancer. 2009;9:265-73.

14. Debnath J, Brugge JS. Modelling glandular epithelial cancers in three-dimensional cultures. Nat Rev Cancer. 2005;5:675-88.

15. Debnath J, Mills KR, Collins NL, Reginato MJ, Muthuswamy SK, Brugge JS. The role of apoptosis in creating and maintaining luminal space within normal and oncogene-expressing mammary acini. Cell. 2002;111:29-40.

16. Oft M, Peli J, Rudaz C, Schwarz H, Beug H, Reichmann E. TGF-beta1 and Ha-Ras collaborate in modulating the phenotypic plasticity and invasiveness of epithelial tumor cells. Genes & development. 1996;10:2462-77.

17. Fung C, Lock R, Gao S, Salas E, Debnath J. Induction of Autophagy during Extracellular Matrix Detachment Promotes Cell Survival. Mol Biol Cell. 2008;19:797-806.

18. Chen N, Eritja N, Lock R, Debnath J. Autophagy restricts proliferation driven by oncogenic phosphatidylinositol 3-kinase in three-dimensional culture. Oncogene. 2012.

19. Muthuswamy SK, Li D, Lelievre S, Bissell MJ, Brugge JS. ErbB2, but not ErbB1, reinitiates proliferation and induces luminal repopulation in epithelial acini. Nature cell biology. 2001;3:785-92.

20. Thiery JP. Epithelial-mesenchymal transitions in development and pathologies. Current opinion in cell biology. 2003;15:740-6.

21. Shin S, Dimitri CA, Yoon SO, Dowdle W, Blenis J. ERK2 but not ERK1 induces epithelial-to-mesenchymal transformation via DEF motif-dependent signaling events. Molecular cell. 2010;38:114-27.

22. Xu J, Lamouille S, Derynck R. TGF-beta-induced epithelial to mesenchymal transition. Cell Res. 2009;19:156-72.

23. Scheel C, Eaton EN, Li SH, Chaffer CL, Reinhardt F, Kah KJ, et al. Paracrine and autocrine signals induce and maintain mesenchymal and stem cell States in the breast. Cell. 2011;145:926-40.

24. Friedl P, Wolf K. Tumour-cell invasion and migration: diversity and escape mechanisms. Nat Rev Cancer. 2003;3:362-74.

25. Young AR, Narita M, Ferreira M, Kirschner K, Sadaie M, Darot JF, et al. Autophagy mediates the mitotic senescence transition. Genes Dev. 2009;23:798-803.

26. Ancrile B, Lim KH, Counter CM. Oncogenic Ras-induced secretion of IL6 is required for tumorigenesis. Genes & development. 2007;21:1714-9.

27. Leslie K, Gao SP, Berishaj M, Podsypanina K, Ho H, Ivashkiv L, et al. Differential interleukin-6/Stat3 signaling as a function of cellular context mediates Ras-induced transformation. Breast Cancer Res. 2010;12:R80.

28. Sullivan NJ, Sasser AK, Axel AE, Vesuna F, Raman V, Ramirez N, et al. Interleukin-6 induces an epithelial-mesenchymal transition phenotype in human breast cancer cells. Oncogene. 2009;28:2940-7.

29. Narita M, Young AR, Arakawa S, Samarajiwa SA, Nakashima T, Yoshida S, et al. Spatial coupling of mTOR and autophagy augments secretory phenotypes. Science (New York, NY.) 2011;332:966-70.

30. Kim MJ, Woo SJ, Yoon CH, Lee JS, An S, Choi YH, et al. Involvement of autophagy in oncogenic K-Ras-induced malignant cell transformation. J Biol Chem. 2011;286:12924-32.

31. Galavotti S, Bartesaghi S, Faccenda D, Shaked-Rabi M, Sanzone S, McEvoy A, et al. The autophagy-associated factors DRAM1 and p62 regulate cell migration and invasion in glioblastoma stem cells. Oncogene. 2013;32:699-712.

32. Macintosh RL, Timpson P, Thorburn J, Anderson KI, Thorburn A, Ryan KM. Inhibition of autophagy impairs tumor cell invasion in an organotypic model. Cell Cycle. 2012;11:2022-9.

33. Deretic V, Jiang S, Dupont N. Autophagy intersections with conventional and unconventional secretion in tissue development, remodeling and inflammation. Trends Cell Biol. 2012;22:397-406.

34. Duran JM, Anjard C, Stefan C, Loomis WF, Malhotra V. Unconventional secretion of Acb1 is mediated by autophagosomes. The Journal of cell biology. 2010;188:527-36.

35. Manjithaya R, Anjard C, Loomis WF, Subramani S. Unconventional secretion of Pichia pastoris Acb1 is dependent on GRASP protein, peroxisomal functions, and autophagosome formation. The Journal of cell biology. 2010;188:537-46.

36. Manjithaya R, Subramani S. Autophagy: a broad role in unconventional protein secretion? Trends Cell Biol. 2011;21:67-73.

37. Dupont N, Jiang S, Pilli M, Ornatowski W, Bhattacharya D, Deretic V. Autophagy-based unconventional secretory pathway for extracellular delivery of IL-1beta. EMBO J. 2011;30:4701-11.

38. Ushio H, Ueno T, Kojima Y, Komatsu M, Tanaka S, Yamamoto A, et al. Crucial role for autophagy in degranulation of mast cells. J Allergy Clin Immunol. 2011;127:1267-76 e6.

39. DeSelm CJ, Miller BC, Zou W, Beatty WL, van Meel E, Takahata Y, et al. Autophagy proteins regulate the secretory component of osteoclastic bone resorption. Dev Cell. 2011;21:966-74.

40. Ebato C, Uchida T, Arakawa M, Komatsu M, Ueno T, Komiya K, et al. Autophagy is important in islet homeostasis and compensatory increase of beta cell mass in response to high-fat diet. Cell Metab. 2008;8:325-32.

41. Jung HS, Chung KW, Won Kim J, Kim J, Komatsu M, Tanaka K, et al. Loss of autophagy diminishes pancreatic beta cell mass and function with resultant hyperglycemia. Cell Metab. 2008;8:318-24.

42. Takamura A, Komatsu M, Hara T, Sakamoto A, Kishi C, Waguri S, et al. Autophagy-deficient mice develop multiple liver tumors. Genes Dev. 2011;25:795-800.

43. Inami Y, Waguri S, Sakamoto A, Kouno T, Nakada K, Hino O, et al. Persistent activation of Nrf2 through p62 in hepatocellular carcinoma cells. J Cell Biol. 2011;193:275-84.

44. Debnath J, Muthuswamy SK, Brugge JS. Morphogenesis and oncogenesis of MCF-10A mammary epithelial acini grown in three-dimensional basement membrane cultures. Methods (San Diego, Calif.) 2003;30:256-68.

**FIGURE LEGENDS**

Figure 1. **Autophagy is required for the formation of invasive protrusions mediated by HRAS$^{V12}$ in 3D culture.** (A-B) HRAS$^{V12}$ MCF10A cells stably expressing non-targeting control shRNA (shCNT) or shRNAs against autophagy genes (shATGs) were 3D cultured on Matrigel for the indicated number of days. Representative phase contrast images at the indicated magnifications are shown. Bar, 100μm.

Figure 2. **Autophagy inhibition in HRAS$^{V12}$ cells restores basement membrane integrity and restricts ECM proteolysis in 3D culture.** (A) HRAS$^{V12}$ cells expressing shCNT or shATGs were 3D cultured on Matrigel for 8 days. Structures were fixed and immunostained with antibodies against the basement membrane protein LAMA5 (human specific), counterstained with DAPI to detect nuclei, and imaged by confocal microscopy. Two representative images of each condition are shown. Bar, 50μm. (B) HRAS$^{V12}$ MCF10A cells were 3D cultured on Matrigel containing 25μg/mL fluorescein DQ-collagen IV (DQ-COL4) for 5 days. Structures were fixed, counterstained with phalloidin (to visualize F-actin) and DAPI, and imaged by confocal microscopy. Green fluorescence represents areas of proteolytic cleavage of the DQ-COL4 present in the ECM. Bar, 50μm.

Figure 3. **Autophagy inhibition in HRAS$^{V12}$ MCF10A structures does not promote apoptosis or proliferation arrest.** (A) Left: Two representative images of day 8 3D cultures of BABE and HRAS$^{V12}$ MCF10A cells expressing shCNT or shATGs immunostained with antibody against cleaved CASP3 and counterstained with DAPI to detect nuclei. Bar, 50μm. Right: Quantification

of cleaved CASP3 positive cells present within 3D cultures of each indicated cell type (mean +/- s.d., Student's t-test). (B) Representative phase (top) and corresponding wide-field fluorescence (bottom) images of BABE and $HRAS^{V12}$ cells expressing shCNT or shATGs stained with the intravital dye ethidium bromide (EtBr). Bar, 100μm. (C) Left: Two representative images of day 8 3D cultures of BABE and $HRAS^{V12}$ cells expressing shCNT or shATGs immunostained with antibody against Ki67 and DAPI counterstained. Bar, 50μm. Right: Quantification of Ki67 positive nuclei present within 3D cultures of each indicated cell type (mean +/- s.d., Student's t-test).

Figure 4. **ATG knockdown suppresses the motility and reduces the metastatic potential of cells expressing oncogenic RAS.** (A) Representative images (left) and quantification (right) of wounding assay on $HRAS^{V12}$ MCF10A cells expressing shCNT or shATGs. Confluent monolayers were scratched and wound width was measured at 0 and 6h after initial wounding to quantify the decrease in scratch width. (mean +/- s.d., Student's t-test, shCNT n=16, shATG7-2 n=8, shATG12 n=14). Bar, 100μm. (B) Transwell migration of $HRAS^{V12}$ MCF10A cells expressing shCNT or shATGs. 24h after plating, cells that migrated to the bottom of the filter were stained with crystal violet. Results are expressed as the mean crystal violet extracted from stained cells (mean +/- s.d., Student's t-test, n=9). (C) Wounding assays of MDA-MB-231 cells expressing siATGs or in presence of 10nM bafilomycin A (BafA). Graphs represent the decrease in scratch width at 10h and 9h after initial wounding, respectively (mean +/- s.d., Student's t-test, siCNT n=16, siATG7 n=16, siATG12 n=10, DMSO n=6, BafA n=6). (D) Representative images (left) and quantification (right) of ZsGreen positive metastatic foci following tail vein injection

of ZsGreen expressing HRAS$^{V12}$ shCNT, shATG7-1 or shATG12 cells (mean +/- s.e.m., shCNT n=7, shATG7-1 n=7, shATG12 n=8).

Figure 5. **ATG knockdown in HRAS$^{V12}$ cells inhibits the production of pro-invasive secreted factors in 3D culture.** (A) 3D co-culture of HRAS$^{V12}$ shATG7-1 with HRAS$^{V12}$ shCNT cells rescues invasion of HRAS$^{V12}$ shATG7-1 cells. HRAS$^{V12}$ shATG7-1 cells expressing GFP were cultured for 8 days in 3D either alone (left) or together with HRAS$^{V12}$ shCNT cells expressing an empty vector (BABE). Structures were imaged by phase contrast and wide-field fluorescence microscopy or fixed, counterstained with phalloidin (to visualize F-actin) and DAPI and imaged by confocal microscopy. Phase: Bar, 100μm. Confocal: Bar, 50 μm. (B) HRAS$^{V12}$ MCF10A cells expressing shATGs were cultured in 3D for 3d and subsequently treated with BABE or HRAS$^{V12}$ shCNT conditioned media (CM). Representative phase contrast images at 24h and 72h following the addition of CM. Bar, 100μm. (C) 3D cultures of HRAS$^{V12}$ MCF10A cells expressing shATGs were treated with BABE or HRAS$^{V12}$ shCNT CM for 72h; thereafter, cultures were fixed and immunostained with an antibody against LAMA5 (human specific) to detect basement membrane and DAPI counterstained. Two representative images per condition are shown. Bar, 50μm.

Figure 6. **Autophagy supports IL6 secretion necessary for oncogenic RAS-driven invasion in 3D culture.** (A) Levels of IL6 in conditioned media collected on day 6 from 3D cultures of the indicated cell types. (mean +/- s.d., ANOVA, BABE n=3, HRAS$^{V12}$ n=5). (B) *IL6* expression levels normalized to *GAPDH* in cells collected from day 8 3D cultures. (mean relative to BABE +/- s.d., Student's t-test, n=3). (C) IL6 protein levels in day 8 3D cultures from the indicated cell

types. (D) Representative phase contrast images of $HRAS^{V12}$ shATG 3D cultures treated for 48h with BABE CM (top) or with $HRAS^{V12}$ shCNT CM containing an IL6 function-blocking antibody (bottom) or IgG control antibody (middle). Bar, 100μm. (E) Representative phase contrast images of $HRAS^{V12}$ shATG 3D cultures grown in the presence or absence of 200ng/mL recombinant human IL6 for 7d. Bar, 100μm.

Figure 7. **WNT5A and MMP2 are reduced following autophagy inhibition in 3D culture.** (A-B) RNA was isolated from BABE, $HRAS^{V12}$ shCNT, and $HRAS^{V12}$ shATG cells cultured in 3D for 8 days. Expression levels of *MMP2* and *WNT5A* were determined by qPCR and normalized to an internal control *GAPDH*. Results represent the mean relative to BABE +/- s.d. (*MMP2,* n=4; *WNT5A*, n=3; Student's t-test). (C) Conditioned media was collected from BABE, $HRAS^{V12}$ shCNT and $HRAS^{V12}$ shATG cells grown in 3D culture. Activity levels of MMP9 and MMP2 in the conditioned media were determined by zymography. (D) $HRAS^{V12}$ shCNT cells were grown in the absence (top) or presence (bottom) of 25μm Arp-100. Left: Structures were imaged on day 8 by phase contrast microscopy. Right: Representative confocal images of structures immunostained with anti-phospho-ERM (P-ERM) to detect cell borders and counterstained with DAPI. Bars, 100μm. (E) BABE, $HRAS^{V12}$ shCNT, and HRASV12 shATG cells were collected from 3D culture on day 8, lysed, and protein levels of WNT5A were determined by immunoblot analysis. (F) $HRAS^{V12}$ shATG7-1 cells were grown in 3D for 8 days in the absence (top) or presence (bottom) of 500ng/mL WNT5A. Left: Representative phase contrast images. Right: Representative confocal images of structures immunostained with anti-phospho-ERM to detect cell borders and counterstained with DAPI. Bars, 100μm.

**Autophagy dependent production of secreted factors facilitates oncogenic Ras-driven invasion**

Rebecca Lock, Candia M. Kenific, Andrew M. Leidal, Eduardo Salas and Jayanta Debnath

## SUPPLEMENTAL EXPERIMENTAL PROCEDURES:

**Retroviral vectors and retrovirus production:** pBABEneo $HRAS^{V12}$ has been previously described (1). pBABEhygro GFP was generated from pBABEpuro GFP. For retroviral transduction, VSV-G-pseudotyped retroviruses were generated, and cells were infected and selected as previously described (2).

**shRNA and siRNA.** pLKO.1 lentiviral expression plasmids containing short hairpin RNAs against ATG7 and ATG12 were purchased from Sigma (Mission shRNA). The production of viral particles and the generation of cell lines expressing shATGs have been described (1). The target sequences for hairpins directed against human ATG7 (NM_006395) are: shATG7-1 (TRCN0000007584): GCCTGCTGAGGAGCTCTCCA; and shATG7-2 (TRCN0000007587): CCCAGCTATTGGAACACTGTA; directed against human ATG12 (NM_004707) is: shATG12 (TRCN0000007394): TGGAACTCTCTATGAGTGTTT; directed against human ATG3 (NM_022488) is: shATG3 (TRCN0000149597): CCTACCAACAGGCAAACAATT. For siRNA-mediated knockdown of autophagy genes in MDA-MB-231 cells, siGenome SMARTpool siRNAs against human *ATG7* (M-020112-01) and human *ATG12* (M-010212-02) were purchased from Dharmacon and cells were transfected as previously described (3).

**Phase and immunofluorescence image acquisition and analysis.** 3D cultures were fixed and stained as previously described (2). Phase and indirect immunofluorescent imaging were performed on an Axiovert 200 microscope (Carl Zeiss) with 4x (NA: 0.1) or 10x (NA:0.25) lenses, Spot RT camera (Diagnostic Instruments) and mercury lamp, and images were acquired using MetaMorph software (v6.0). Confocal analyses were performed using a C1Si confocal laser-scanning microscope (Nikon) with 20x (NA:0.75) or 60x (NA:1.2) lenses and images were collected using EZ-C1 software (v3.20). The following antibodies and reagents were used for staining: anti-Ki67 (Invitrogen), anti-cleaved caspase 3 (CASP3, Cell Signaling), anti-β–catenin (CTNNB1, BD Biosciences), anti-laminin 5, human specific (LAMA5, EMD Millipore), anti-phospho-ERM (Cell Signaling), phalloidin-488 and phalloidin-546 (Invitrogen), DAPI (Sigma), Alexa Fluor goat anti-mouse-488 and 568 and Alexa Fluor goat anti-rabbit-488 and 568 (Invitrogen). Quantification of invasive protrusions was performed according to a method described in (4). Briefly, 3D cultures were analyzed at 48h treatment with conditioned media or recombinant human IL6; at this time point, invasive protrusions emanating from individual globular structures were easily discernable, but complex intermingled networks between structures had not formed yet. At least 200 structures in each 3D culture assay were analyzed and the percent of structures with evidence of least one invasive protrusion was quantified; for each condition, at least 3 independent experiments were analyzed.

**Immunoblotting.** Cells were lysed in RIPA buffer plus 10mM NaF, 10 mM β-glycerophosphate, 1 mM $Na_3VO_3$, 10 nM calyculin A, and protease inhibitors. Lysates were clarified by centrifugation for 15 min at 4°C, and protein concentrations were assessed using a BCA protein assay (Thermo). Samples containing equal amounts of protein were boiled in SDS sample buffer

(15-50μg of total protein per lane), resolved using SDS-polyacrylamide gel electrophoresis (PAGE), and transferred to polyvinylidene difluoride membrane. Membranes were blocked in PBS + 0.1% Tween 20 with 5% nonfat dry milk, incubated with the primary antibodies indicated overnight at 4°C, washed, incubated with horseradish peroxidase-conjugated secondary antibodies, and analyzed by enhanced chemiluminescence. The following primary antibodies were used: anti-RAS (BD Biosciences), anti-phospho-ERK1/2 (MAPK) (Invitrogen), anti-total-ERK1/2 (MAPK, Invitrogen), anti-ATG7 (Santa Cruz Biotechnology), anti-ATG5 (Cell Signaling), anti-ATG3 (Sigma), anti-LC3 (Sigma), anti-IL6 (Abcam), anti-Keratin 14 (KRT14, Novus Biologicals), anti-vimentin (VIM, BD Biosciences), anti-E-cadherin (CDH1, BD Biosciences), anti-Fibronectin (FN1, Sigma), anti-N-cadherin (CDH2, BD Biosciences), anti-WNT5A (R&D Systems), anti-p62 (Progen Biotechnik), anti-α-tubulin (TUBA, Sigma), anti-β-actin (ACTB, Sigma), and anti-GAPDH (Santa Cruz Biotechnology). In certain experiments, a previously described anti-LC3 rabbit polyclonal antibody was used (3) which is now commercial available (EMD Millipore).

**qPCR array and qPCR.** Cells were collected from 3D on day 8 and RNA was isolated using Qiagen RNeasy kit. 50ng of total RNA was used for each reaction and cDNA synthesis and PCR amplification were performed using the Brilliant II SYBR Green qRT-PCR Master Mix Kit (Stratagene). qPCR reactions were run using a StepOnePlus thermal cycler (Applied Biosciences) and analyzed using StepOne software (v2.2). For each set of experiments samples were run in triplicate, expression levels were determined based on a standard curve run with each primer set, and levels were normalized to an internal control, GAPDH. The following are the primer sequences used: *GAPDH*; For: 5'-CATGTTCGTCATGGGTGTGAACCA-3' Rev:

5'ATGGCATGGACTGTGGTCATGAGT-3', *MMP2*; For: 5'-AGAAGGATGGCAAGTACGGCTTCT-3' Rev: 5'-AGTGGTGCAGCTGTCATAGGATGT-3', *WNT5A*; For: 5'-CGCCCAGGTTGTAATTGAAGCCAA-3' Rev: 5'-TGTCCTTGAGAAAGTCCTGCCAGT-3', *IL6*; For: 5'-TGAAAGCAGCAAAGAGGCACT-3' Rev: 5'-TGAATCCAGATTGGAAGCATCC-3'.

**Conditioned media zymography.** On day 7, 3D structures were washed twice with PBS and cultures were incubated with serum free media overnight. Conditioned media was collected, the total protein level was determined by BCA assay (Thermo Scientific), and samples were normalized accordingly. Gelatin zymography using the prepared conditioned media samples was performed as previously described (5).

**SUPPLEMENTAL REFERENCES:**


1. Lock R, Roy S, Kenific CM, Su JS, Salas E, Ronen SM, et al. Autophagy facilitates glycolysis during Ras-mediated oncogenic transformation. Mol Biol Cell. 2011;22:165-78.
2. Debnath J, Muthuswamy SK, Brugge JS. Morphogenesis and oncogenesis of MCF-10A mammary epithelial acini grown in three-dimensional basement membrane cultures. Methods (San Diego, Calif. 2003;30:256-68.
3. Fung C, Lock R, Gao S, Salas E, Debnath J. Induction of Autophagy during Extracellular Matrix Detachment Promotes Cell Survival. Mol Biol Cell. 2008;19:797-806.
4. Chatterjee S, Seifried L, Feigin ME, Gibbons DL, Scuoppo C, Lin W, et al. Dysregulation of cell polarity proteins synergize with oncogenes or the microenvironment to induce invasive behavior in epithelial cells. PLoS One. 2012;7:e34343.

5. Lengyel E, Gum R, Juarez J, Clayman G, Seiki M, Sato H, et al. Induction of M(r) 92,000 type IV collagenase expression in a squamous cell carcinoma cell line by fibroblasts. Cancer Res. 1995;55:963-7.

**SUPPLEMENTAL FIGURE LEGENDS**

Figure S1. **ATG knockdown inhibits Ras-driven invasion in 3D culture.** (A) Representative phase contrast images of MCF10A cells expressing an empty vector control (BABE) grown in 3D culture for the indicated times. Bar, 100μm. (B) Protein levels of ATG7, ATG5 (ATG5:12 complex), and ATG3 in $HRAS^{V12}$ MCF10A cells expressing shATGs. (C) Protein levels of LC3-I and LC3-II in $HRAS^{V12}$ cells expressing shATGs. (D) Levels of p62 in $HRAS^{V12}$ cells expressing shATGs collected from 3D culture on day 8. (E) Levels of LC3-I and LC3-II in $HRAS^{V12}$ shCNT or shATG expressing cells grown in full media or starved in HBSS in the presence or absence of E64d and pepstatin A (E/P). (F) Representative 3D culture phase contrast images of $HRAS^{V12}$ cells expressing shATG3 or grown in the presence of 5μM chloroquine or 5nM bafilomycin A (BafA). Bar, 100μm. (G) Levels of RAS and phosphorylated ERK1/2 in BABE, $HRAS^{V12}$ shCNT, and $HRAS^{V12}$ shATG cells collected from 3D culture on day 8. (H) Protein levels of ATG7, ATG5 (ATG5:12 complex), LC3-I and LC3-II in MDA-MB-231 cells following siRNA knockdown of ATG7 and ATG12.

Figure S2. **Effects of ATG depletion on mesenchymal differentiation and junctional integrity in $HRAS^{V12}$ MCF10A cells.** (A) Protein levels of keratin 14 (KRT14), vimentin (VIM), E-cadherin (CDH1), fibronectin (FN1) and N-cadherin (CDH2) in BABE, $HRAS^{V12}$ shCNT or $HRAS^{V12}$ shATG cells collected from 3D cultures on day 8. (B) Two representative confocal images of day 8 BABE, $HRAS^{V12}$ shCNT or $HRAS^{V12}$ shATG 3D cultures immunostained with anti-β-catenin (CTNNB1) and counterstained with DAPI. Note that only isolated focal areas of junctional β-catenin staining are detected in $HRAS^{V12}$ shCNT cultures,

whereas robust β-catenin staining is evident at cell-cell junctions throughout BABE and $HRAS^{V12}$ shATG cultures. Bar, 50μm.

Figure S3. **Effects of conditioned media treatment and recombinant human IL6 re-addition on BABE and $HRAS^{V12}$ shATG 3D cultures.** (A) Quantification of invasive protrusions in $HRAS^{V12}$ shATG cells following treatment with the indicated conditioned media (CM) for 48h; the percent of structures in a culture with one or more invasive protrusion was enumerated. **P<0.01, ***P<0.001 (Student's t test, n=3). (B) Nontransformed MCF10A cells expressing empty vector (BABE) were cultured in 3D for 3d and subsequently treated with BABE or $HRAS^{V12}$ shCNT conditioned media (CM). Representative phase contrast images at 24h and 72h following the addition of CM. Bar, 100μm. (C) Representative phase contrast images of BABE 3D cultures grown in the presence or absence of 200ng/mL recombinant human IL6 (rhIL6). Bar, 100μm. (D) 3D cultures of $HRAS^{V12}$ shATG cells were treated with 200ng/ml rhIL6, fixed and immunostained with an antibody against LAMA5 and DAPI counterstained. Bar, 50μm. (E) Quantification of invasive protrusions in $HRAS^{V12}$ shATG cells following treatment with 200ng/ml rhIL6; the percent of structures in a culture with one or more invasive protrusion was enumerated. *P<0.05, ***P<0.001 (Student's t test, n=3). (Student's t test, n=3). (F) Effects of rhIL6 treatment on keratin 14 (KRT14) and vimentin (VIM) protein levels in $HRAS^{V12}$ shCNT and $HRAS^{V12}$ shATG7-1 cells grown in 3D culture in the presence or absence of 200ng/mL recombinant human IL6 (rhIL6). (G) Fold change in *MMP2* and *WNT5A* expression in cells isolated from $HRAS^{V12}$ shATG7-1 3D cultures following treatment with 200ng/ml rhIL6. Results represent the fold change relative to untreated cultures (mean +/- s.d.). ns, nonsignificant. (*MMP2,* n=4; *WNT5A*, n=4, Student's t-test).

**Figure 1**

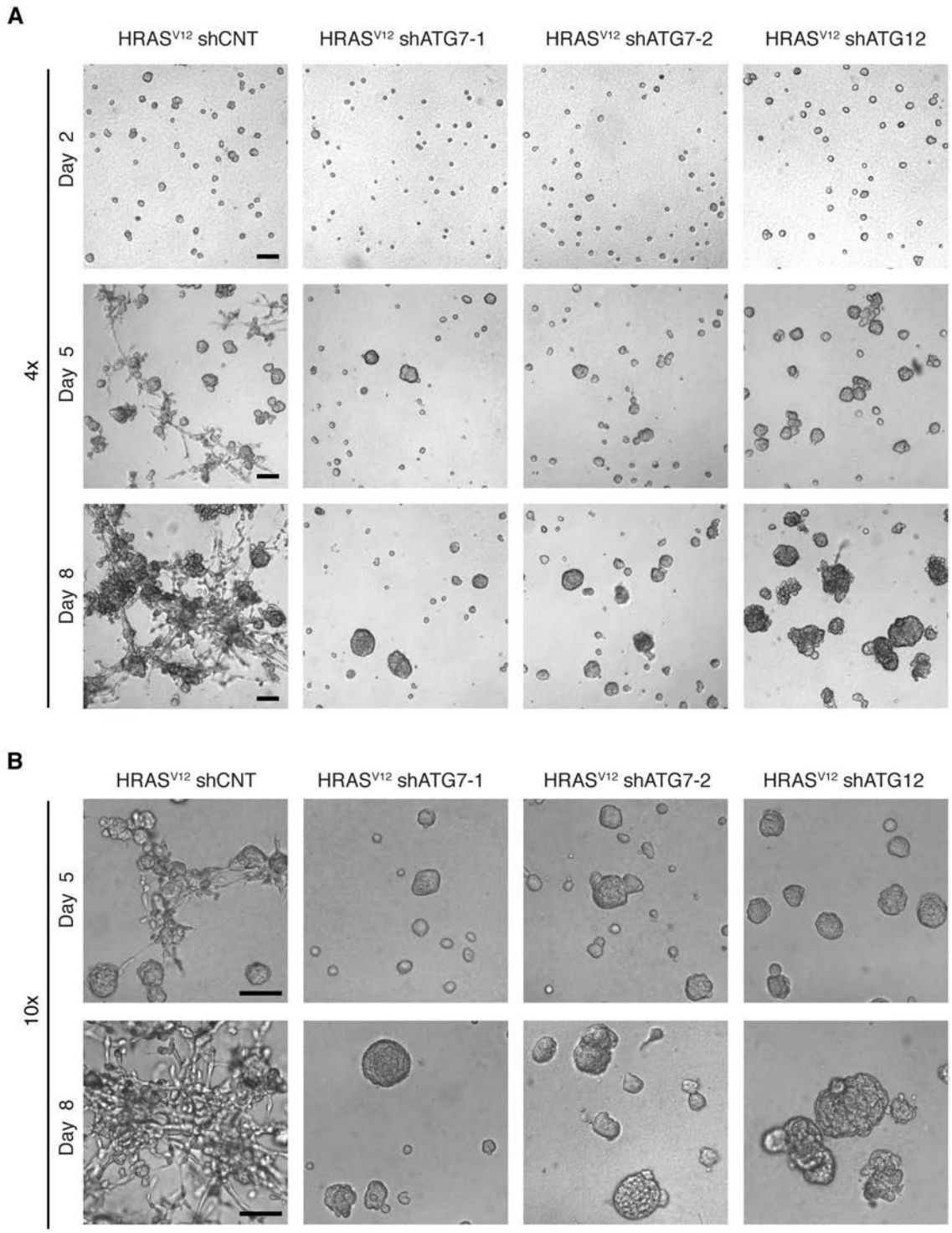
A
HRASV12 shCNT
HRASV12 shATG7-1
HRASV12 shATG7-2
HRASV12 shATG12
4x
Day 2
Day 5
Day 8
B
HRASV12 shCNT
HRASV12 shATG7-1
HRASV12 shATG7-2
HRASV12 shATG12
10x
Day 5
Day 8

**Figure 2**

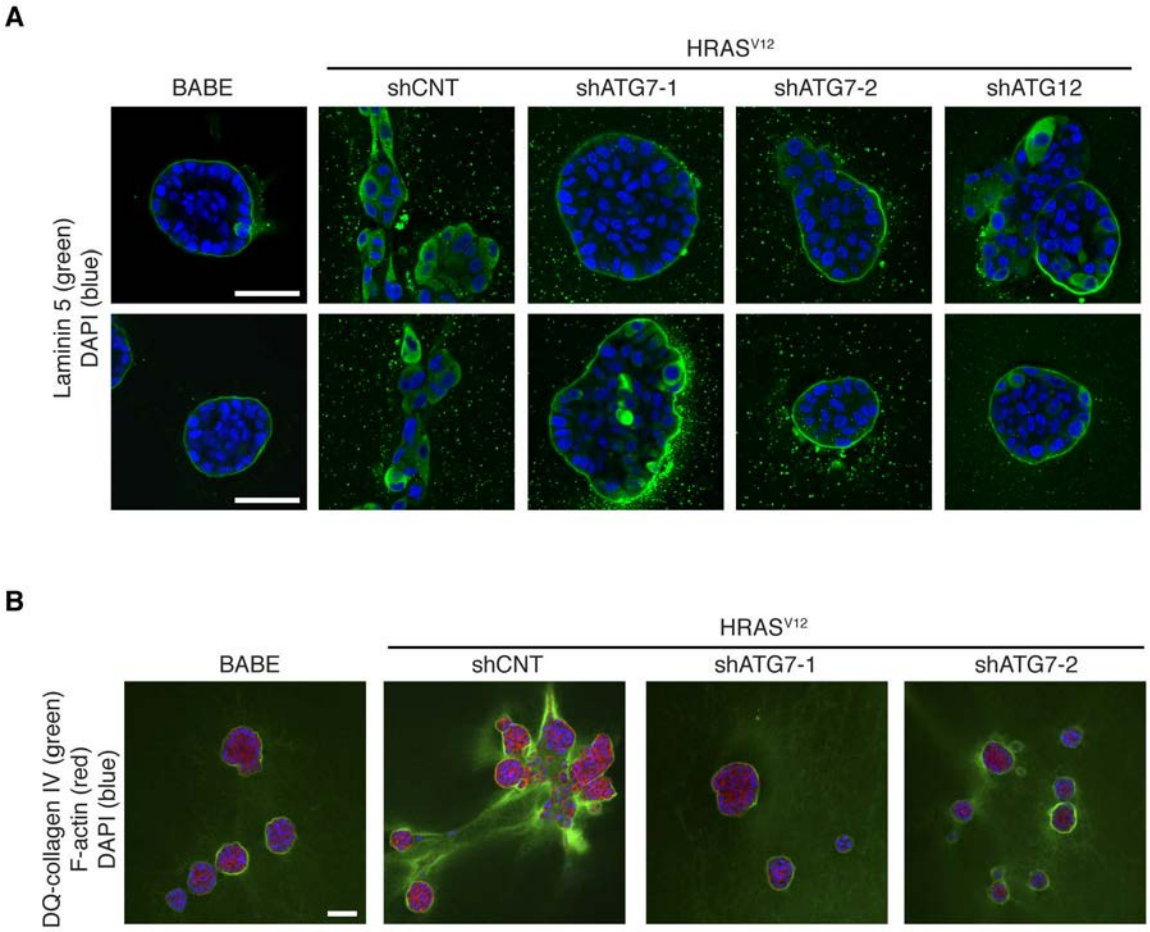
A
HRAS$^{V12}$
BABE
shCNT
shATG7-1
shATG7-2
shATG12
Laminin 5 (green)
DAPI (blue)
B
HRAS$^{V12}$
BABE
shCNT
shATG7-1
shATG7-2
DQ-collagen IV (green)
F-actin (red)
DAPI (blue)

**Figure 3**

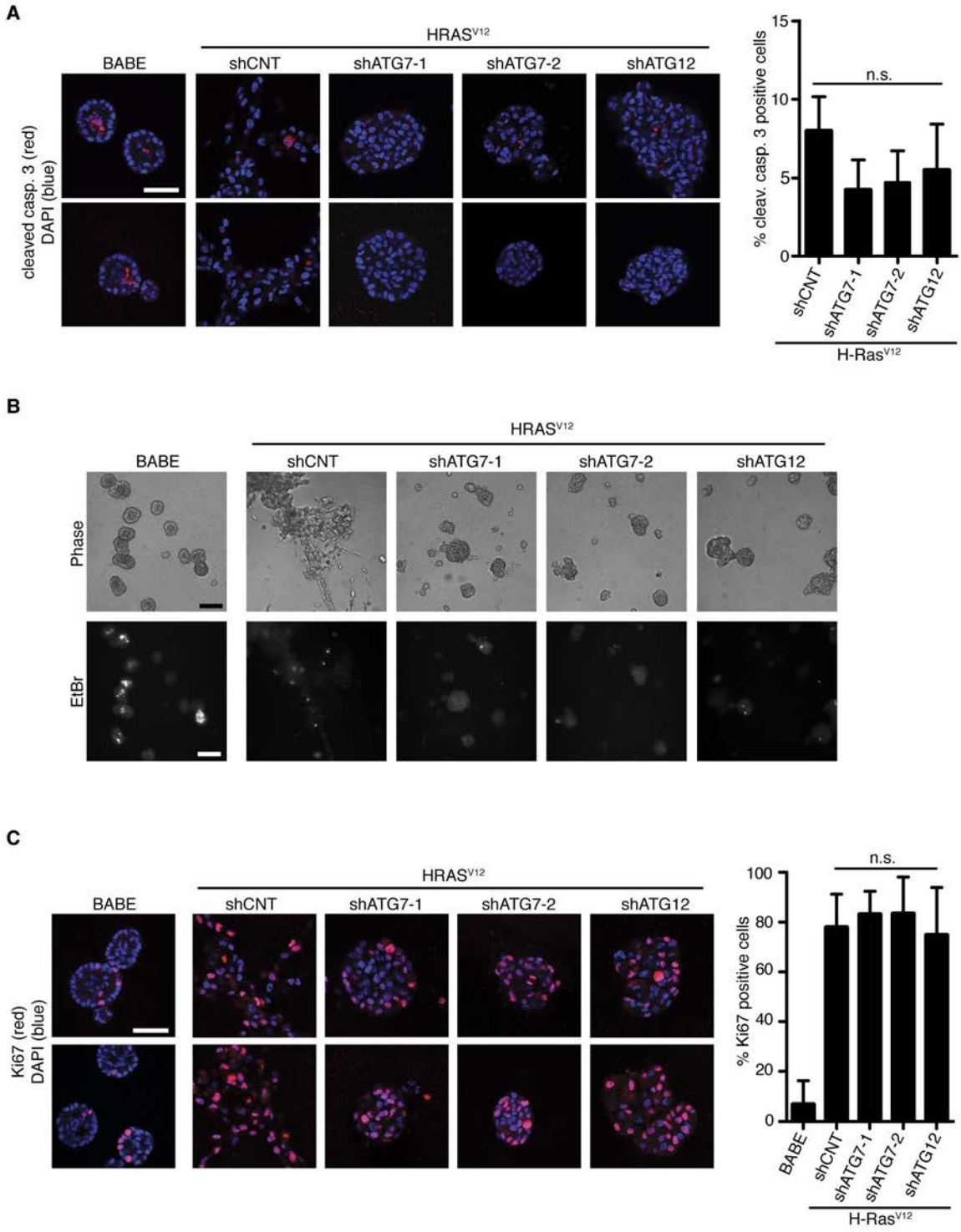
A
HRASV12
BABE
shCNT
shATG7-1
shATG7-2
shATG12
cleaved casp. 3 (red)
DAPI (blue)
% cleav. casp. 3 positive cells
n.s.
shCNT
shATG7-1
shATG7-2
shATG12
H-RasV12
B
HRASV12
BABE
shCNT
shATG7-1
shATG7-2
shATG12
Phase
EtBr
C
HRASV12
BABE
shCNT
shATG7-1
shATG7-2
shATG12
Ki67 (red)
DAPI (blue)
% Ki67 positive cells
n.s.
BABE
shCNT
shATG7-1
shATG7-2
shATG12
H-RasV12

**Figure 4**

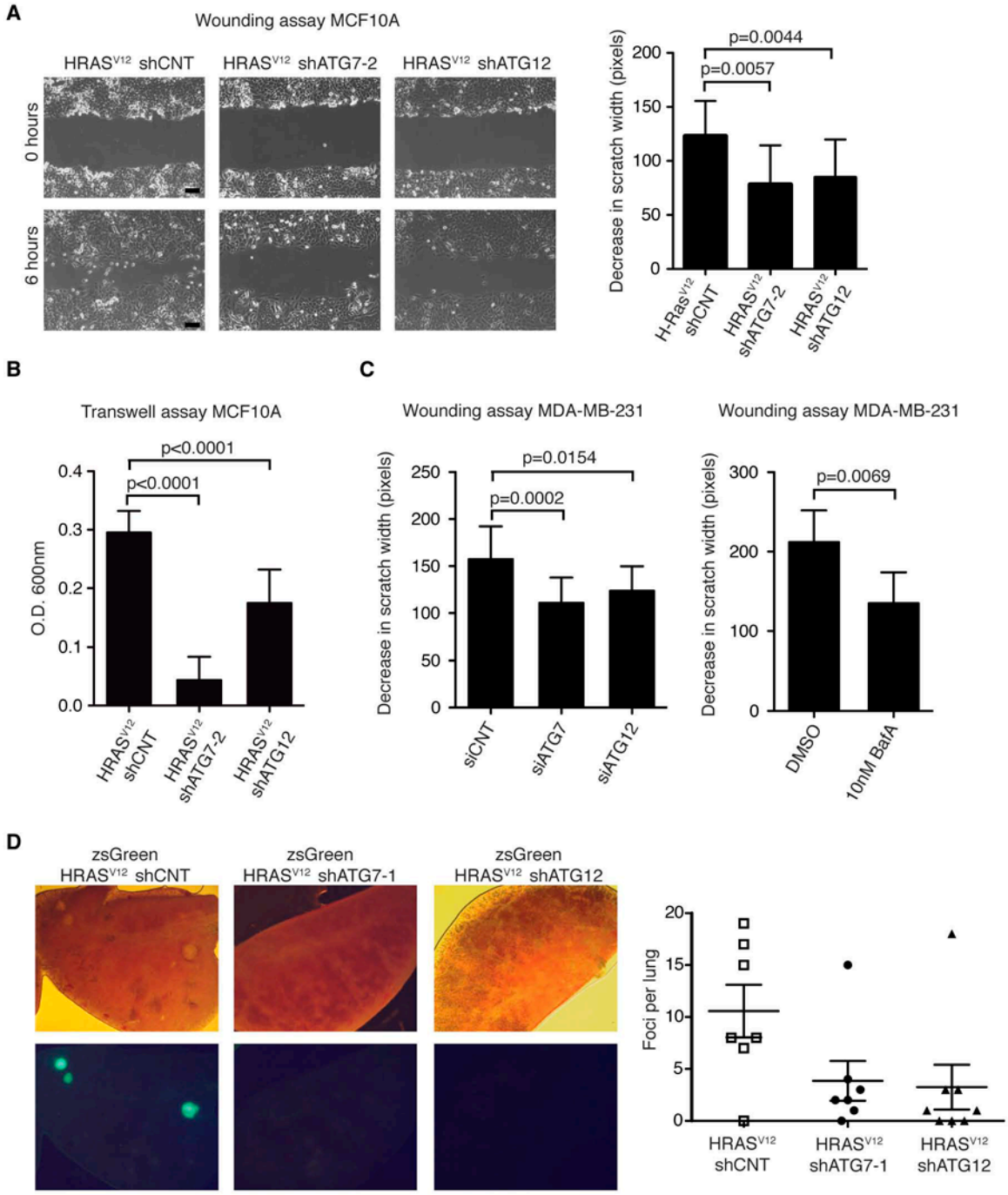
A
Wounding assay MCF10A
HRASV12 shCNT
HRASV12 shATG7-2
HRASV12 shATG12
0 hours
6 hours
Decrease in scratch width (pixels)
p=0.0044
p=0.0057
H-RasV12 shCNT
HRASV12 shATG7-2
HRASV12 shATG12
B
Transwell assay MCF10A
O.D. 600nm
p<0.0001
p<0.0001
C
Wounding assay MDA-MB-231
Decrease in scratch width (pixels)
p=0.0154
p=0.0002
siCNT
siATG7
siATG12
Wounding assay MDA-MB-231
Decrease in scratch width (pixels)
p=0.0069
DMSO
10nM BafA
D
zsGreen HRASV12 shCNT
zsGreen HRASV12 shATG7-1
zsGreen HRASV12 shATG12
Foci per lung
HRASV12 shCNT
HRASV12 shATG7-1
HRASV12 shATG12

## Figure 5

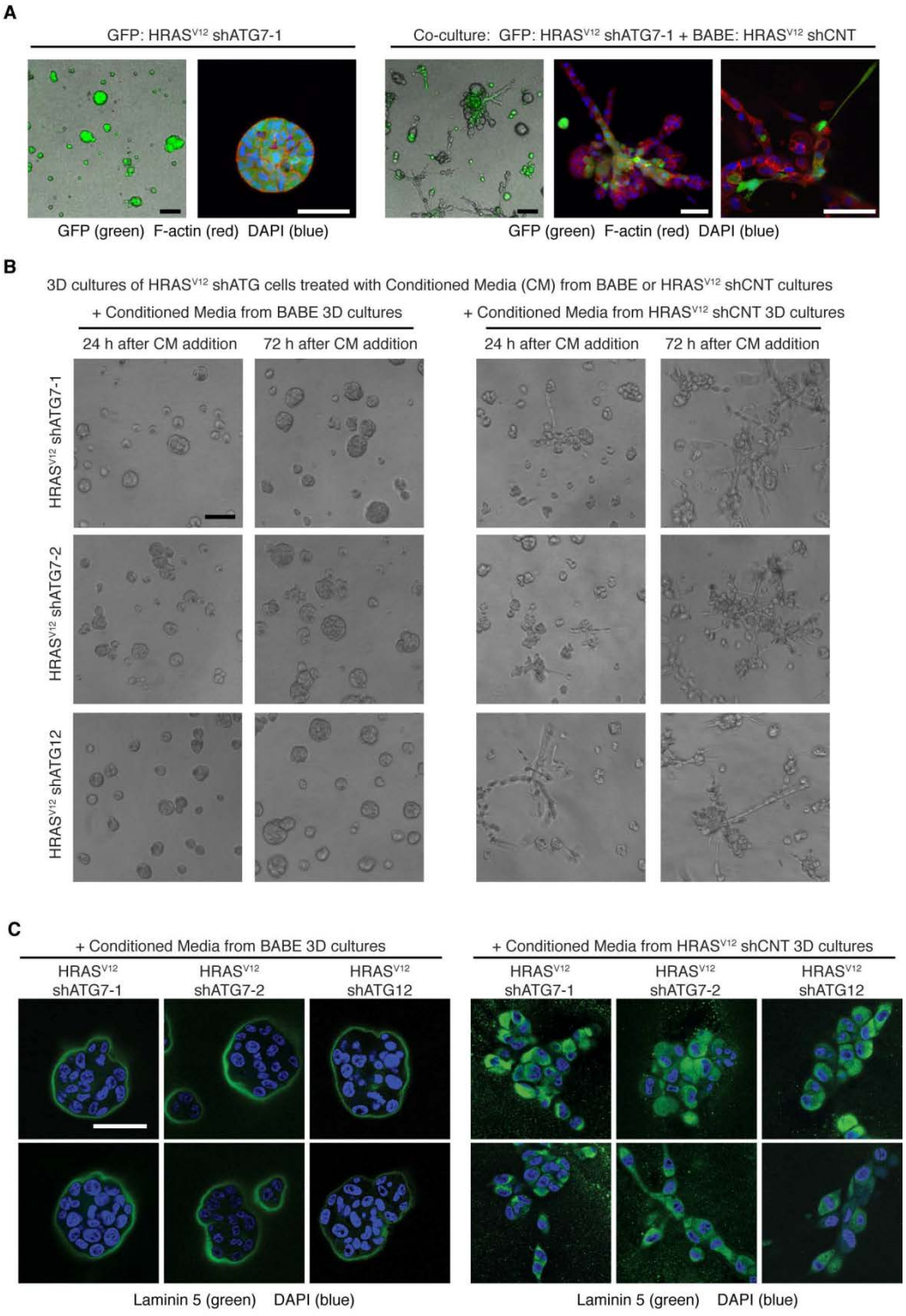
A
GFP: HRASV12 shATG7-1
Co-culture: GFP: HRASV12 shATG7-1 + BABE: HRASV12 shCNT
GFP (green) F-actin (red) DAPI (blue)
GFP (green) F-actin (red) DAPI (blue)
B
3D cultures of HRASV12 shATG cells treated with Conditioned Media (CM) from BABE or HRASV12 shCNT cultures
+ Conditioned Media from BABE 3D cultures
+ Conditioned Media from HRASV12 shCNT 3D cultures
24 h after CM addition
72 h after CM addition
24 h after CM addition
72 h after CM addition
HRASV12 shATG7-1
HRASV12 shATG7-2
HRASV12 shATG12
C
+ Conditioned Media from BABE 3D cultures
+ Conditioned Media from HRASV12 shCNT 3D cultures
HRASV12 shATG7-1
HRASV12 shATG7-2
HRASV12 shATG12
HRASV12 shATG7-1
HRASV12 shATG7-2
HRASV12 shATG12
Laminin 5 (green) DAPI (blue)
Laminin 5 (green) DAPI (blue)

**Figure 6**

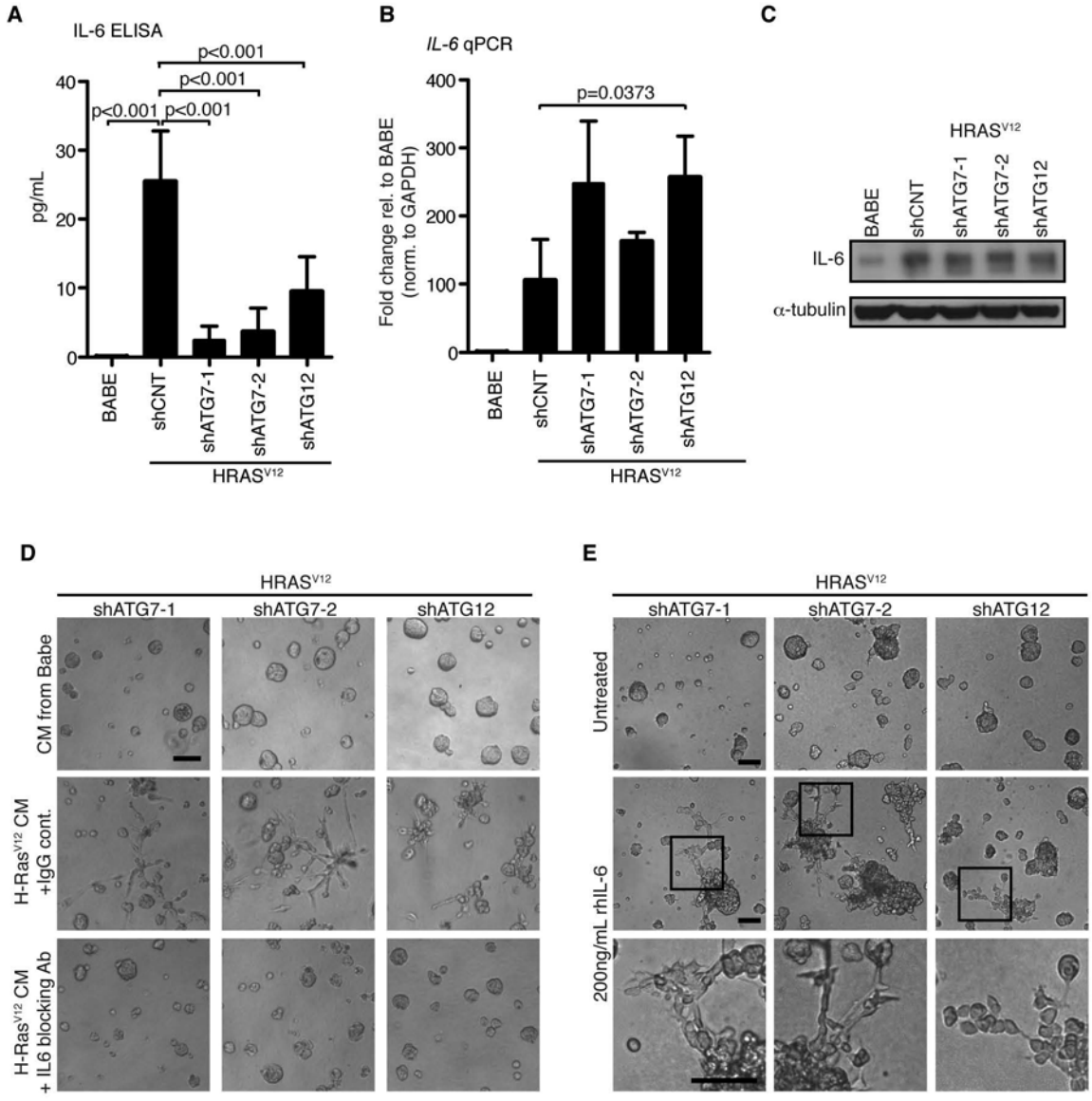
A
IL-6 ELISA
p<0.001
p<0.001
p<0.001 p<0.001
pg/mL
40
30
20
10
0
BABE
shCNT
shATG7-1
shATG7-2
shATG12
HRASV12
B
IL-6 qPCR
p=0.0373
Fold change rel. to BABE (norm. to GAPDH)
400
300
200
100
0
BABE
shCNT
shATG7-1
shATG7-2
shATG12
HRASV12
C
HRASV12
BABE
shCNT
shATG7-1
shATG7-2
shATG12
IL-6
α-tubulin
D
HRASV12
shATG7-1
shATG7-2
shATG12
CM from Babe
H-RasV12 CM +IgG cont.
H-RasV12 CM + IL6 blocking Ab
E
HRASV12
shATG7-1
shATG7-2
shATG12
Untreated
200ng/mL rhIL-6

**Figure 7**

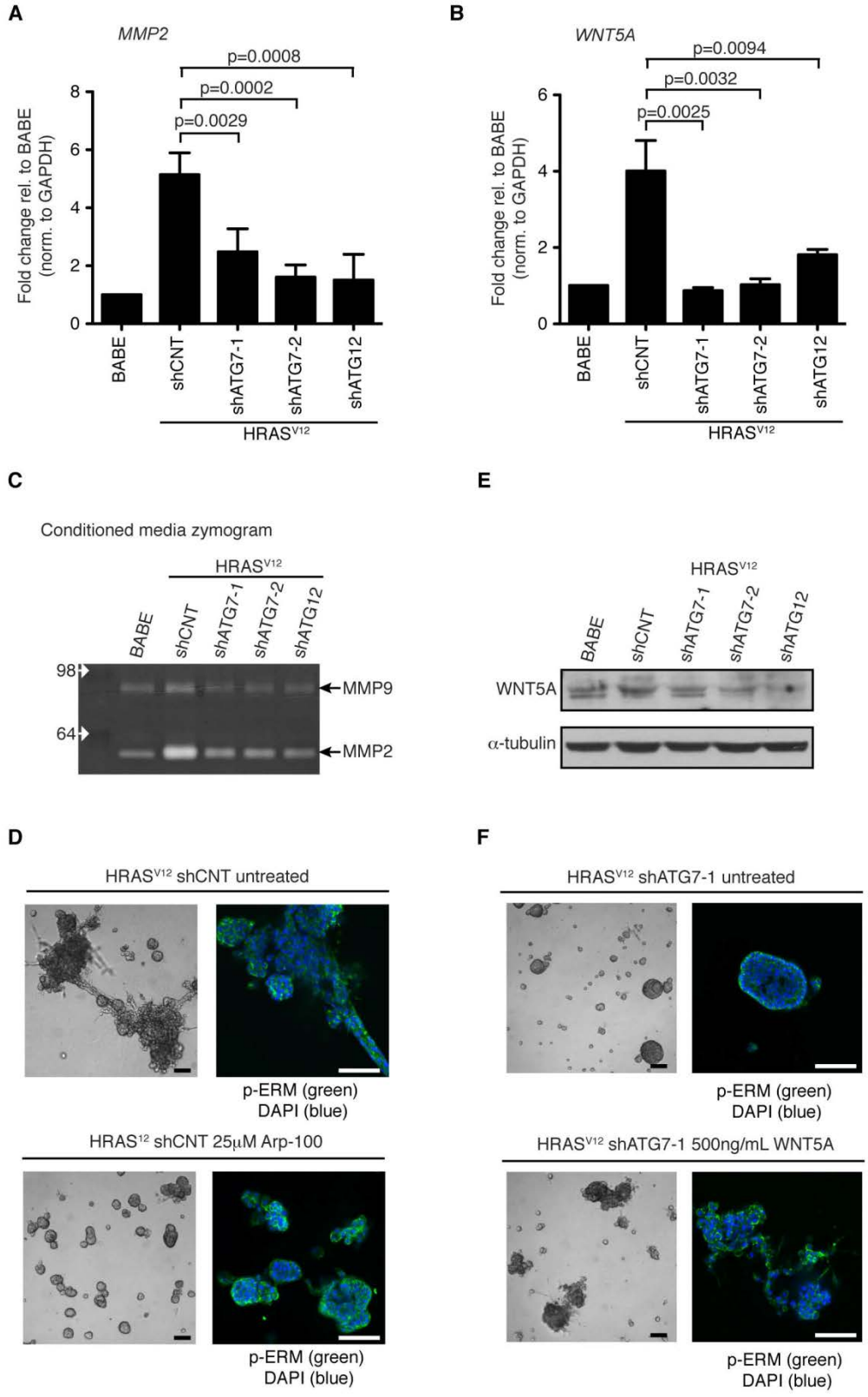
A
MMP2
p=0.0008
p=0.0002
p=0.0029
Fold change rel. to BABE (norm. to GAPDH)
BABE
shCNT
shATG7-1
shATG7-2
shATG12
HRASV12
B
WNT5A
p=0.0094
p=0.0032
p=0.0025
C
Conditioned media zymogram
98
64
MMP9
MMP2
E
WNT5A
α-tubulin
D
HRASV12 shCNT untreated
p-ERM (green)
DAPI (blue)
HRAS12 shCNT 25μM Arp-100
F
HRASV12 shATG7-1 untreated
HRASV12 shATG7-1 500ng/mL WNT5A

## Figure S1

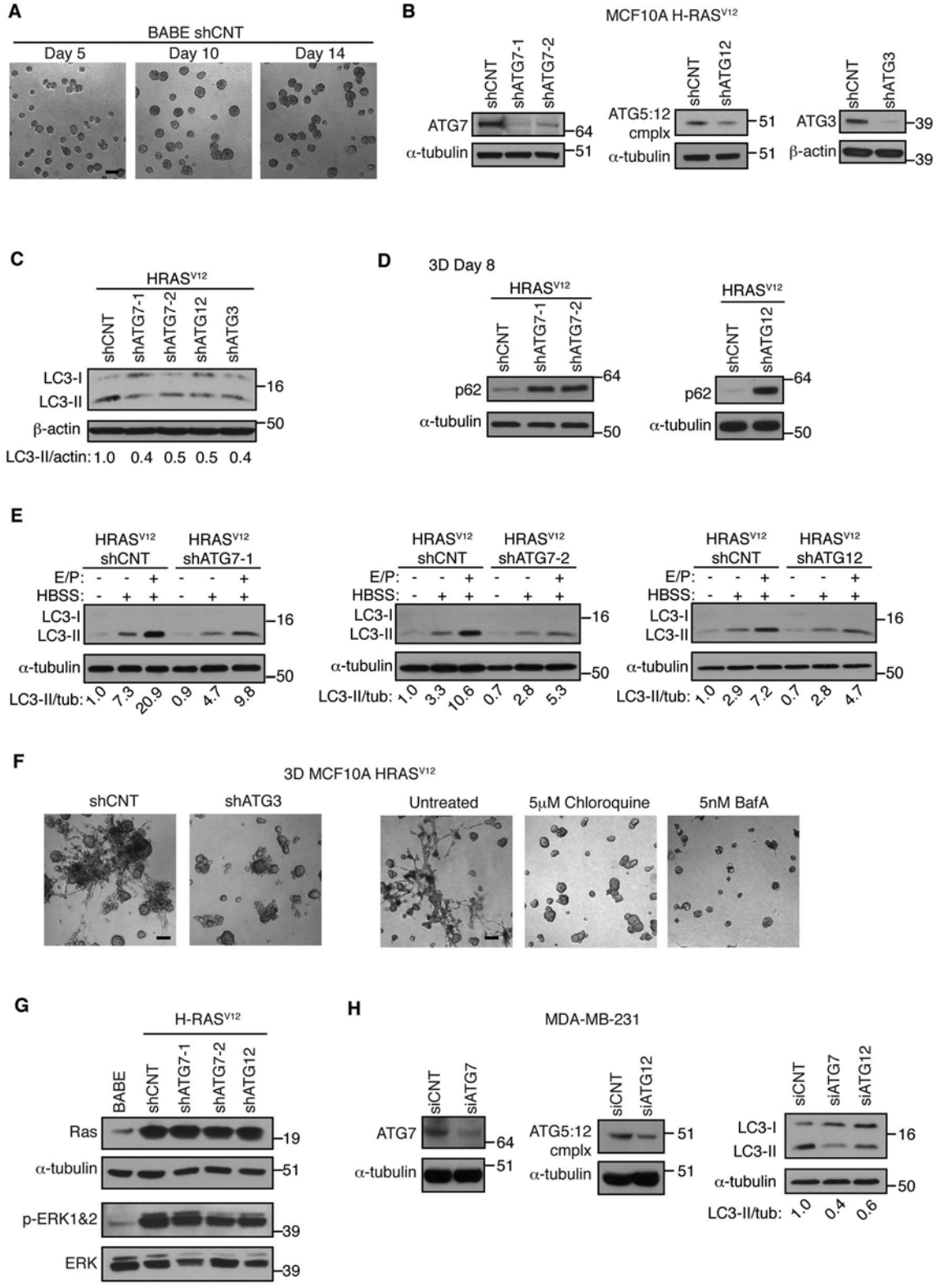
A
BABE shCNT
Day 5
Day 10
Day 14
B
MCF10A H-RASV12
shCNT
shATG7-1
shATG7-2
ATG7
α-tubulin
64
51
shCNT
shATG12
ATG5:12 cmplx
α-tubulin
51
51
shCNT
shATG3
ATG3
β-actin
39
39
C
HRASV12
shCNT
shATG7-1
shATG7-2
shATG12
shATG3
LC3-I
LC3-II
16
β-actin
50
LC3-II/actin: 1.0 0.4 0.5 0.5 0.4
D
3D Day 8
HRASV12
shCNT
shATG7-1
shATG7-2
p62
α-tubulin
64
50
HRASV12
shCNT
shATG12
p62
α-tubulin
64
50
E
HRASV12 shCNT
HRASV12 shATG7-1
E/P: - - + - - +
HBSS: - + + - + +
LC3-I
LC3-II
16
α-tubulin
50
LC3-II/tub: 1.0 7.3 20.9 0.9 4.7 9.8
HRASV12 shCNT
HRASV12 shATG7-2
E/P: - - + - - +
HBSS: - + + - + +
LC3-I
LC3-II
16
α-tubulin
50
LC3-II/tub: 1.0 3.3 10.6 0.7 2.8 5.3
HRASV12 shCNT
HRASV12 shATG12
E/P: - - + - - +
HBSS: - + + - + +
LC3-I
LC3-II
16
α-tubulin
50
LC3-II/tub: 1.0 2.9 7.2 0.7 2.8 4.7
F
3D MCF10A HRASV12
shCNT
shATG3
Untreated
5μM Chloroquine
5nM BafA
G
H-RASV12
BABE
shCNT
shATG7-1
shATG7-2
shATG12
Ras
19
α-tubulin
51
p-ERK1&2
39
ERK
39
H
MDA-MB-231
siCNT
siATG7
ATG7
α-tubulin
64
51
siCNT
siATG12
ATG5:12 cmplx
α-tubulin
51
51
siCNT
siATG7
siATG12
LC3-I
LC3-II
16
α-tubulin
50
LC3-II/tub: 1.0 0.4 0.6

**Figure S2**

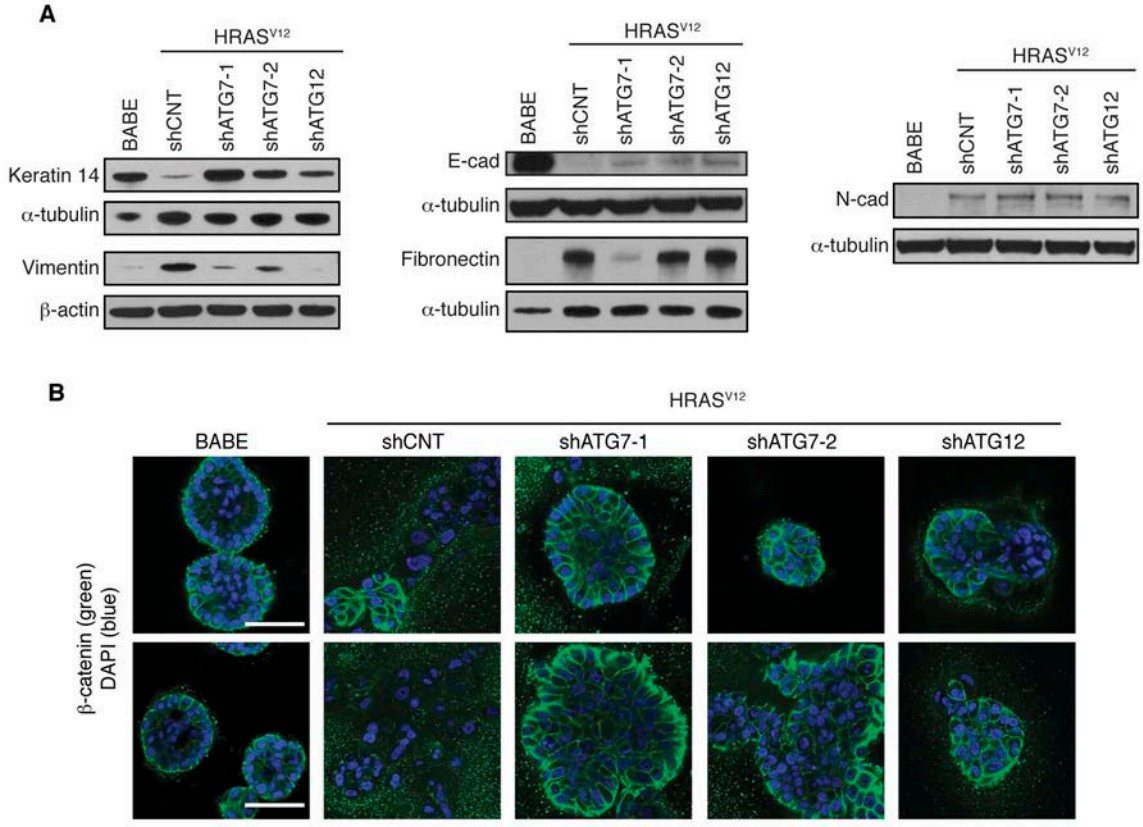
A
HRAS$^{V12}$
BABE
shCNT
shATG7-1
shATG7-2
shATG12
Keratin 14
α-tubulin
Vimentin
β-actin
E-cad
α-tubulin
Fibronectin
α-tubulin
N-cad
α-tubulin
B
HRAS$^{V12}$
BABE
shCNT
shATG7-1
shATG7-2
shATG12
β-catenin (green)
DAPI (blue)

**Figure S3**

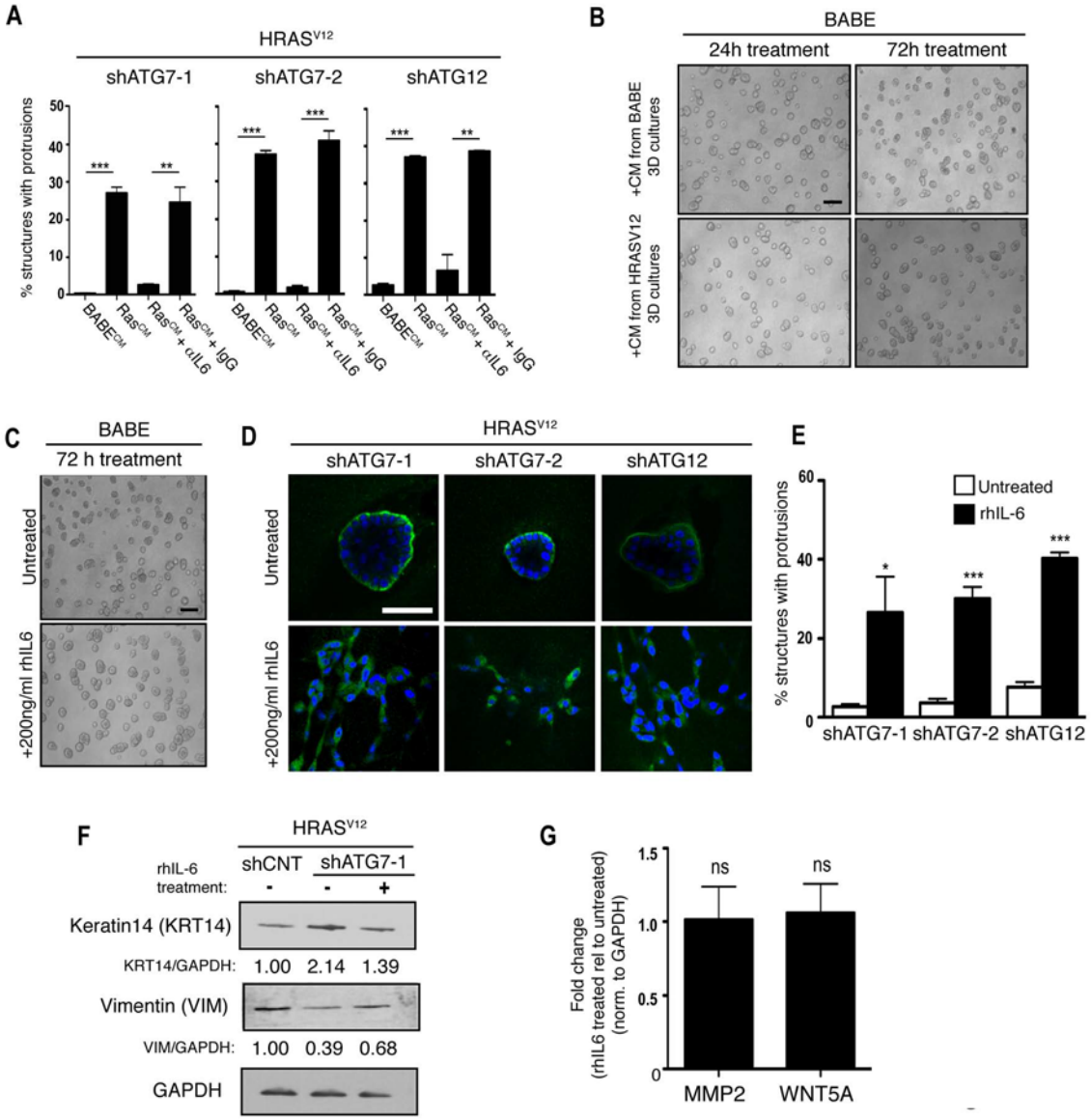
A
HRASV12
shATG7-1
shATG7-2
shATG12
% structures with protrusions
BABECM
RasCM
RasCM + αIL6
RasCM + IgG
B
BABE
24h treatment
72h treatment
+CM from BABE 3D cultures
+CM from HRASV12 3D cultures
C
BABE
72 h treatment
Untreated
+200ng/ml rhIL6
D
HRASV12
shATG7-1
shATG7-2
shATG12
Untreated
+200ng/ml rhIL6
E
Untreated
rhIL-6
% structures with protrusions
shATG7-1 shATG7-2 shATG12
F
HRASV12
rhIL-6 treatment:
shCNT
shATG7-1
Keratin14 (KRT14)
KRT14/GAPDH: 1.00 2.14 1.39
Vimentin (VIM)
VIM/GAPDH: 1.00 0.39 0.68
GAPDH
G
Fold change (rhIL6 treated rel to untreated) (norm. to GAPDH)
ns
MMP2
WNT5A

**Publishing Agreement**

*It is the policy of the University to encourage the distribution of all theses, dissertations, and manuscripts. Copies of all UCSF theses, dissertations, and manuscripts will be routed to the library via the Graduate Division. The library will make all theses, dissertations, and manuscripts accessible to the public and will preserve these to the best of their abilities, in perpetuity.*

***Please sign the following statement:***

*I hereby grant permission to the Graduate Division of the University of California, San Francisco to release copies of my thesis, dissertation, or manuscript to the Campus Library to provide access and preservation, in whole or in part, in perpetuity.*

Author Signature

8/20/15
Date